RÉPUBLIQUE FRANÇAISE
Liberté Égalité Fraternité

Université de Toulouse

Doctorat de l'Université de Toulouse

préparé à l'INSA Toulouse

Production électrochimique d'hydrogène dissous pour les bioprocédés hydrogénotrophes : stratégies pour l'électroréduction de l'eau sans bulles et le dimensionnement d'un système intégré

Thèse présentée et soutenue, le 19 décembre 2025 par

Juan Diego CARVAJALINO OLAVE

École doctorale
MEGEP - Mécanique, Energétique, Génie civil, Procédés

Spécialité
Génie des Procédés et de l'Environnement

Unité de recherche
TBI - Toulouse Biotechnology Institute, Bio & Chemical Engineering

Thèse dirigée par

Claire DUMAS et Benjamin ERABLE

Composition du jury
M. Arnaud COCKX, Président, INSA Toulouse
M. Théodore BOUCHEZ, Rapporteur, INRAE Île-de-France - Jouy-en-Josas-Antony
Mme Annemiek TER HEIJNE, Rapporteure, Wageningen University and Research
Mme Paniz IZADI, Examinatrice, Helmholtz Centre for Environmental Research
Mme Sanne DE SMIT, Examinatrice, Wageningen University and Research
Mme Claire DUMAS, Directrice de thèse, INRAE Occitanie-Toulouse
M. Benjamin ERABLE, Co-directeur de thèse, CNRS Occitanie Ouest

Electrochemical production of dissolved hydrogen for hydrogenotrophic bioprocesses: Strategies for bubble-free water electroreduction and integrated system design

Written by

Juan Diego Carvajalino Olave

Supervised by

Claire DUMAS

Benjamin ERABLE

Submitted to the doctoral school

MEGEP - Mécanique, Energétique, Génie civil, Procédés

In partial fulfillment of the requirements for the degree of

Doctor of Philosophy

Elaborated at

TBI - Toulouse Biotechnology Institute, Bio & Chemical Engineering

LGC - Institut National Polytechnique de Toulouse

Acknowledgements

I would like to express my gratitude first to my family, for being emotionally supportive during the past three years of my doctoral program and for their continued support of my professional growth, wherever the future may take me.

I also want to thank my friends in INP and TBI for the wonderful time we enjoyed together in Toulouse, for the trips, lunches, coffees and nights we shared together, these are most fond memories I will retain from my work in Toulouse as I get even older.

I extend my gratitude to my supervisors, Benjamin and Claire, for allowing me to work on this project. I am also thankful to everyone involved in the making of my experiments, the academic discussions and group meetings that contributed to my learning process.

This work has benefited from funding through the 3BCAR Institute and through a State grant managed by the National Research Agency under the 'Investissements d'Avenir' programme with the reference ANR-18-EURE-0021

Summary

The advancement of hydrogenotrophic bioprocesses, which rely on anaerobic microorganisms to convert substrates like H_2 and CO_2 into valuable chemicals such as organic acids and alcohols, is fundamentally constrained by the low solubility of H_2 in aqueous media, approximately 45 times lower than CO_2. This low solubility restricts microbial H_2 uptake kinetics and growth, as well as the production of longer-chain valuable metabolites. Consequently, large H_2 gas volumes are required during gas injection, necessitating large gas recirculation rates to overcome low H_2 solubilization efficiencies. A novel strategy to entirely bypass this gas-to-liquid mass transfer bottleneck was explored in this thesis: the direct production of dissolved H_2 via bubble-less water electroreduction. The core objective was to design and control electrochemical systems that maximize the efficiency of dissolved H_2 production by preventing H_2 bubble formation and sustaining supersaturated concentrations.

The successful implementation of this electrolytic H_2 supply mechanism requires an accurate measurement of dissolved H_2 for process monitoring and control, which was addressed in Chapter II. Upon evaluating various sensing methods, it was revealed that potentiometric measurements using a Pt wire were fundamentally limited by poor selectivity, non-linearity, and electromagnetic interference. While a commercial amperometric H_2 sensor exhibited higher selectivity and a linear response, its application was hindered by a short lifespan (~ 6 months) and electromagnetic interference with the polarized cathode. To establish reliable ex-situ measurement, a headspace gas chromatography method was successfully evaluated, achieving high precision (R^2 =0.99). For the real-time detection of H_2 bubble nucleation, an optical method using a digital camera was shown to be a reliable approach. A semiconducting metal oxide sensor only detected bubbles after they detached and transitioned to the headspace, introducing significant delays and signal saturation issues, while the optical approach provided a direct, non-invasive, and fast signal of nucleation events at the cathode surface.

The potential advantage of water electroreduction over traditional H_2 gas injection for H_2 solubilization in aqueous medium was established in a comparative study, detailed in Chapter III. In a 0.8L vessel, a solubilization efficiency of 35% was achieved by water electroreduction,

representing an 18-fold improvement compared to the 2% efficiency observed with gas injection in a single pass. A supersaturated H_2 concentration of 1.21 mmol·L^{-1} was also maintained, significantly surpassing the saturation limit of 0.78 mmol·L^{-1} achievable by gas injection at 1 bar. Furthermore, water electroreduction was demonstrated to be more energy-efficient, requiring approximately 4.6 times less energy per mole of H_2 solubilized compared to H_2 gas injection. This capacity to achieve high dissolved H_2 concentrations is essential, as high concentrations of H_2 provide the reducing equivalents necessary to enhance production rates, improve selectivity (e.g., shifting acetogenesis to solventogenesis or chain elongation), and influence microbial competition.

In Chapter IV, the necessity of preventing H_2 bubble nucleation at the cathode surface was investigated, leading to the establishment of operational constraints for bubble-free H_2 delivery. Combining experimental results with finite element simulations in COMSOL Multiphysics, it was found that nucleation must be avoided by operating at local dissolved H_2 concentrations below 5.5 mmol·L^{-1} and a local current density below 18 A·m^{-2}. Experiments utilizing linear sweep voltammetry combined with the optical detection of bubble nucleation confirmed that the use of high-surface-area cathodes delayed bubble formation. The stainless-steel porous foam exhibited the best performance, allowing the highest bubble-free current under agitation in a H_2 pre-saturated medium. Agitation was also found to be essential to counteract the effect of facilitated nucleation under H_2 pre-saturation by enhancing mass transport and removing dissolved H_2 from the electrode surface.

Building on these experimental findings, numerical simulations were done in COMSOL Multiphysics in Chapter V to determine the necessary design constraints for achieving homogeneous current distribution and efficient mass transfer within porous cathode structures. These simulation results emphasize that, to avoid hyperpolarization at electrode edges (which facilitates bubble nucleation), geometrical symmetry must be ensured, meaning the projected cathode surface area must be equal to and equidistant from the separator/counter electrode. The use of thin cathodes was favored, as this configuration leveraged the high surface area while reducing current distribution heterogeneity. Furthermore, simulations revealed that high electrolyte conductivities (e.g., 50 mS·cm^{-1}, corresponding to hypersaline media) would significantly improve current distribution homogeneity, allowing for higher imposed currents before nucleation occurs. The potential of

functionally graded electrodes (with an anisotropic polarization resistance) was also demonstrated in the context of homogenizing the current distribution. Additionally, to effectively utilize the large surface area of porous cathodes and prevent H_2 accumulation in the internal porosity, forced flow (flow-through cell design) was proposed as a superior approach to the agitation typically used in bulk electrolyzers for the efficient removal of local H_2 accumulation at the cathode surface.

Finally, a feasibility study was done in Chapter VI to dimension a continuous water electroreduction cell for providing H_2-rich water to physically decoupled hydrogenotrophic bioreactors under various H_2 uptake scenarios in a 2 L bioreactor. For a low H_2 uptake rate scenario (8.1 $mmol \cdot h^{-1}$), a single cell with a 2×15×15 cm^3 porous cathode operating at 0.77 A was found to be sufficient to maintain a dissolved H_2 concentration of 0.53 $mmol \cdot L^{-1}$ in the bioreactor while operating below the limits (local concentration and current density) of H_2 bubble nucleation in the water electroreduction cell. Conversely, it was found that physically decoupling both H_2 solubilization and biological uptake might be unfeasible for a high H_2 uptake scenario (84 $mmol \cdot h^{-1}$). An integrated microbial electrosynthesis was determined to be more adequate, employing using stacked cell designs of thin cathodes and operating under high dissolved H_2 concentrations.

The original contribution of this work is the establishment of water electroreduction as a potential tool for H_2 solubilization with superior overall efficiency. This method is particularly relevant for processes where maximizing the solubilization of H_2 is desired, such as for the production of more reduced metabolites during hydrogenotrophic bioprocesses. The core principles to enhance the solubilization of H_2 during water electroreduction were also established, leaving a roadmap for the scale-up and optimization of hydrogenotrophic bioprocesses through water electroreduction.

Résumé

L'avancement des bioprocédés hydrogénotrophes, qui reposent sur des microorganismes anaérobies pour convertir des substrats tels que H_2 et CO_2 en molécules d'intérêt (acides organiques et alcools), est fondamentalement contraint par la faible solubilité de H_2 en milieu aqueux, environ 45 fois inférieure à celle du CO_2. Cette faible solubilité restreint la cinétique d'assimilation de H_2 et la croissance microbienne, ainsi que la production de métabolites de valeur à plus longue chaîne. Par conséquent, de grands volumes de gaz H_2 sont requis lors de l'injection gazeuse, ce qui engendre des taux de recirculation de gaz élevés pour pallier les faibles rendements de solubilisation de H_2. Face à ce goulot d'étranglement du transfert de masse gaz-liquide, ce travail de thèse a exploré une stratégie novatrice : la production directe de l'H_2 dissous par électroréduction de l'eau sans bulles. L'objectif principal était de concevoir et de contrôler des systèmes électrochimiques maximisant l'efficacité de la production de l'H_2 dissous en empêchant la formation de bulles de l'H_2 et en maintenant des concentrations sursaturées.

La mise en œuvre réussie de ce mécanisme d'approvisionnement électrolytique en H_2 nécessite une mesure précise de l'H_2 dissous pour le suivi et le contrôle du procédé, un défi abordé au Chapter II. Après l'évaluation de diverses méthodes de détection, il a été démontré que les mesures potentiométriques utilisant un fil de Pt étaient fondamentalement limitées par une faible sélectivité, une non-linéarité et des interférences électromagnétiques. Bien qu'un capteur ampérométrique commercial de l'H_2 ait montré une sélectivité plus élevée et une réponse linéaire, son application était entravée par une courte durée de vie (~6 mois) et des interférences électromagnétiques avec la cathode polarisée. Pour établir une mesure ex-situ fiable, une méthode de chromatographie en phase gazeuse de l'espace de tête (headspace) a été évaluée avec succès, atteignant une grande précision (R^2 = 0,99). Pour la détection en temps réel de la nucléation de bulles de l'H_2, une méthode optique utilisant une caméra numérique s'est avérée être une approche fiable. Un capteur à oxyde métallique semi-conducteur ne détectait les bulles qu'après leur détachement et leur transition vers l'espace de tête, introduisant des retards significatifs et des problèmes de saturation du signal, tandis que l'approche optique fournissait un signal direct, non invasif et rapide des événements de nucléation à la surface de la cathode.

L'avantage potentiel de l'électroréduction de l'eau par rapport à l'injection de gaz H_2 traditionnelle pour la solubilisation de H_2 en milieu aqueux a été établi dans une étude comparative, détaillée au Chapter III. Dans un réacteur de 0,8 L, une efficacité de solubilisation de 35% a été atteinte par électroréduction de l'eau, représentant une amélioration de 18 fois par rapport à l'efficacité de 2% observée avec l'injection de gaz en un seul passage. Une concentration de H_2 sursaturée de 1,21 mmol·L−1 a également été maintenue, dépassant nettement la limite de saturation de 0,78 mmol·L−1 atteignable par injection de gaz à 1 bar. De plus, l'électroréduction de l'eau s'est révélée plus économe en énergie, nécessitant environ 4,6 fois moins d'énergie par mole de l'H_2 solubilisé que l'injection de gaz H_2. Cette capacité à atteindre des concentrations élevées de l'H_2 dissous est essentielle, car de fortes concentrations de l'H_2 fournissent les équivalents réducteurs nécessaires pour augmenter les taux de production, améliorer la sélectivité (par exemple, déplacer l'acétogenèse vers la solventogenèse ou l'élongation de chaîne) et influencer la compétition microbienne.

Au Chapter IV, la nécessité d'empêcher la nucléation de bulles de l'H_2 à la surface de la cathode a été étudiée, conduisant à l'établissement de contraintes opérationnelles pour un apport de l'H_2 sans bulles. En combinant des résultats expérimentaux avec des simulations par éléments finis dans COMSOL Multiphysics, il a été trouvé que la nucléation devait être évitée en opérant à des concentrations locales de l'H_2 dissous inférieures à 5,5 mmol·L−1 et une densité de courant locale inférieure à 18 A·m−2. Des expériences utilisant la voltampérométrie à balayage linéaire combinée à la détection optique de la nucléation de bulles ont confirmé que l'utilisation de cathodes à grande surface spécifique retardait la formation de bulles. La mousse poreuse en acier inoxydable a montré la meilleure performance, permettant le courant sans bulles le plus élevé sous agitation dans un milieu pré-saturé en H_2. L'agitation s'est également avérée essentielle pour contrecarrer l'effet de la nucléation facilitée en pré-saturation de l'H_2 en améliorant le transport de masse et en éliminant l'H_2 dissous de la surface de l'électrode.

S'appuyant sur ces découvertes expérimentales, des simulations numériques ont été menées dans COMSOL Multiphysics au Chapter V pour déterminer les contraintes de conception nécessaires à l'obtention d'une distribution de courant homogène et d'un transfert de masse efficace au sein des structures de cathode poreuses. Ces résultats de simulation ont souligné que, pour éviter l'hyperpolarisation aux bords de l'électrode (qui facilite la nucléation de bulles), la symétrie géométrique doit être assurée, ce qui signifie que la surface projetée de la

cathode doit être égale et équidistante du séparateur/contre-électrode. L'utilisation de cathodes minces a été privilégiée, car cette configuration tirait parti de la grande surface spécifique tout en réduisant l'hétérogénéité de la distribution de courant. De plus, les simulations ont révélé que des conductivités électrolytiques élevées (par exemple, 50 mS·cm−1, correspondant à un milieu hypersalin) amélioreraient significativement l'homogénéité de la distribution de courant, permettant des courants imposés plus élevés avant que la nucléation ne se produise. Le potentiel des électrodes à gradient de fonction (avec une résistance à la polarisation anisotrope) a également été démontré dans le contexte de l'homogénéisation de la distribution de courant. De plus, pour utiliser efficacement la grande surface spécifique des cathodes poreuses et empêcher l'accumulation de l'H_2 dans la porosité interne, un écoulement forcé (conception de cellule à écoulement traversant) a été proposé comme une approche supérieure à l'agitation typiquement utilisée dans les électrolyseurs en vrac pour l'élimination efficace de l'accumulation locale de l'H_2 à la surface de la cathode.

Enfin, une étude de faisabilité a été menée au Chapter VI pour dimensionner une cellule d'électroréduction de l'eau en continu fournissant de l'eau riche en H_2 à des bioréacteurs hydrogénotrophes physiquement découplés sous divers scénarios d'assimilation de l'H_2 dans un bioréacteur de 2 L. Pour un scénario de faible taux d'assimilation de l'H_2 (8,1 mmol·h−1), une seule cellule avec une cathode poreuse de 2×15×15 cm3 fonctionnant à 0,77 A s'est avérée suffisante pour maintenir une concentration de l'H_2 dissous de 0,53 mmol·L−1 dans le bioréacteur tout en opérant en dessous des limites (concentration locale et densité de courant) de nucléation de bulles de l'H_2 dans la cellule d'électroréduction de l'eau. Inversement, il a été constaté que le découplage physique de la solubilisation de l'H_2 et de l'assimilation biologique pourrait être infaisable pour un scénario de taux d'assimilation de l'H_2 élevé (84 mmol·h−1). Une électrosynthèse microbienne intégrée a été jugée plus adéquate, employant des conceptions de cellules empilées de cathodes minces et fonctionnant sous des concentrations élevées de l'H_2 dissous.

La contribution majeure de ce travail de thèse est l'établissement de l'électroréduction de l'eau comme un outil potentiel pour la solubilisation de l'H_2 avec une efficacité globale supérieure à celle de l'injection gazeuse. Cette méthode est particulièrement pertinente pour les procédés où la maximisation de la solubilisation de l'H_2 est souhaitée, comme pour la production de métabolites plus réduits lors des bioprocédés hydrogénotrophes. Les principes

fondamentaux pour améliorer la solubilisation de H_2 pendant l'électroréduction de l'eau ont également été établis, laissant une feuille de route pour la mise à l'échelle et l'optimisation des bioprocédés hydrogénotrophes via l'électroréduction de l'eau.

Table of Contents

Chapter I. Introduction 1

I-1. General overview 2

I-2. Literature review 4

I-2.1 Global energy landscape and the role of H_2 in sustainable development 4

I-2.2 Carbon Capture and Utilization prospects 6

I-2.3 Biological CO_2 fixation pathways 7

I-2.4 Hydrogenotrophic fixation of CO_2 at the thermodynamic edge of life 10

I-3. The Critical Bottleneck: H_2 solubilization is limited by mass transfer and obscured by accurate measurements 15

I-4. Overcoming slow gas-to-liquid H_2 transfer 16

I-4.1 Reactor designs for increased solubilization rate 17

I-4.2 Gas pressurization for increased H_2 solubility 19

I-5. Bypassing gas-to-liquid H_2 transfer: Electrochemical cells as a H_2 supply alternative 22

I-5.1 Electrochemical Principles of Water Electroreduction 22

I-5.2 Microbial electrosynthesis systems 28

I-6. An unexplored approach: Favoring the production of dissolved H_2 for H_2-mediated electron transfer 31

I-6.1 Evidence of H_2-mediated electron transfer as the preferred mechanism for acetogenesis 31

I-6.2 Bubble-less vs micro/nanobubbles production via water electroreduction 32

I-6.3 Avoiding bubble nucleation: theoretical insights from the Classical Nucleation Theory (CNT) 34

I-7. Practical approach to avoid bubble nucleation and favor H_2 solubilization 38

I-7.1 Interfacial tension and wettability 38

I-7.2 Decreasing local H_2 concentration near the cathode surface 39

I-7.3 Coupling water electroreduction with hydrogenotrophic CO_2 fixation 40

I-8. Main objectives of this work 41

Chapter II. Evaluation of available hydrogen sensing alternatives for the measurement of dissolved H_2 and bubble nucleation during water electroreduction 43

II-1. Introduction 44

II-2. Materials and Methods 47

II-2.1 Medium composition and reactor setup 47

II-2.2 Experimental design 49

II-3. Results 50

II-3.1 Sensors for the measurement of dissolved H_2 50

II-3.2 Sensors for the detection of H_2 bubble nucleation 59

II-4. Discussion 63

II-5. Conclusion 65

Chapter III. Electroreduction of water: A Promising Alternative to Gas Injection for the Solubilization of Hydrogen in Biological Processes Involving Hydrogenotrophs. 67

III-1. Introduction 68

III-1.1 Limitations on achieving high H_2 concentration in the liquid medium 69

III-2. Materials and methods 74

III-2.1 Reactor setup used for both H_2 solubilization techniques 74

III-2.2 Design of experiments 76

III-2.3 Solubilization rate and efficiency 76

III-2.4 Energy consumption 77

III-2.5 Modelling the thermodynamic potential of hydrogenotrophic reactions at different H_2 solubilization kinetics 79

III-3. Results 81

III-3.1 H_2 solubilization kinetics 81

III-3.2 Variation of the maximum concentration of dissolved H_2 and solubilization rate with H_2 supply rate 82

III-3.3 Energy consumed per mol of H_2 solubilized 85

III-3.4 Modelling of the effect of H_2 solubilization kinetics on hydrogenotrophic reactions 87

III-4. Discussion 93

III-4.1 Increasing the H_2 solubilization rate while maintaining high solubilization efficiency 93

III-4.2 The dissolved H_2 concentration as a selective variable for controlling competition among hydrogenotrophs and product selection 95

III-4.3 Achieving high concentrations of dissolved H_2 is technically challenging 97

III-4.4 Solubilization and energy efficiency 99

III-5. Conclusion 101

Chapter IV. Hydrogen nucleation in water electroreduction at near-neutral pH: Role of cathode structure and agitation conditions. 103

IV-1. Introduction 104

IV-2. Materials and Methods 106

IV-2.1 Medium composition and reactor setup 106

IV-2.2 Experimental design 108

IV-2.3 Electrochemical and optical setup 109

IV-2.4 COMSOL simulation 112

IV-3. Results 112

IV-3.1 Optical detection of H_2 bubble nucleation 112

IV-3.2 Current density analysis associated with bubble nucleation on different cathode materials under varying experimental conditions 115

IV-3.3 Supersaturation at the stainless-steel plate cathode surface 116

IV-3.4 Comparison of cathode materials based on the maximum current density achievable without H_2 bubble nucleation and their electrocatalytic performance 120

IV-3.5 Effect of H_2 pre-saturation and agitation on the maximum current density achieved without bubble nucleation. 123

IV-4. Discussion 125

IV-4.1 Choosing the right electrode materials to favor H_2 dissolution 125

IV-4.2 The interplay between cathode porosity, hydrodynamics and mass transfer 126

IV-4.3 Practical considerations in reactor design and bubble detection 127

IV-5. Conclusion 129

Chapter V. Numerical simulation study on the mass transfer and current distribution of different cathode geometries for the solubilization of H_2 by water electroreduction 130

V-1. Introduction 131

V-2. Methodology 134

V-2.1 Study of the current distribution of different cathode geometries during water electroreduction 134

V-2.2 Study of the H_2 mass transfer in a porous structure with different pore sizes and separation. 135

V-3. Results and discussion 138

V-3.1 Study of the current distribution of different cathode geometries during water electroreduction 138

V-3.2 Study of the H_2 mass transfer on cathodes with different porous characteristics 149

V-4. Conclusions 153

Chapter VI. Electrolytic H_2 supply for hydrogenotrophic bioreactors: A feasibility study on a coupled reactor system 155

VI-1. Introduction 156

VI-2. Methodology 157

VI-3. Results 163
VI-3.1 Reducing imposed current and recycling rate through H_2 supersaturation... 163
VI-3.2 Case 1 - Water electroreduction cell for coupling with hydrogenotrophic bioreactor at TBI (low H_2 uptake rate) 165
VI-3.3 Cases 2-5 - Effect of H_2 supersaturation ($CH2out$) and H_2 loss percentage ($sloss$) on cell dimensions at low H_2 uptake rate 169
VI-3.4 Cases 6-8 - Water electroreduction cell for coupling with hydrogenotrophic bioreactor at high biomass cell density (high H_2 uptake rate) 171
VI-4. Discussion and closing remarks 173
VI-4.1 Key findings and system feasibility 173
VI-4.2 Practical challenges and operational considerations 175
VI-4.3 Implications in a microbial electrosynthesis system (MES) setup 176
General Conclusion 178
REFERENCES 184
Supplemental Information 198
A. Headspace-gas chromatograph method 199
B. Current control interface developed for the BioLogic VSP potentiostat 202
C. Medium conductivity and H_2 solubilization 219
D. Bubble detection 221
E. O_2 crossover across the separator 224
F. Longitudinal and transverse dispersity 227

List of Figures

CHAPTER I

Fig. I.1. Approaches to accelerate the transformation towards zero carbon emissions. 5
Fig. I.2. Standard Gibbs free energy ($\Delta Gr0', pH = 7$) of common hydrogenotrophic reactions. 14
Fig. I.3. Gas concentration gradients during the dissolution of a gas bubble in a liquid medium. 16
Fig. I.4. Dissolution time (t_{life}, colored area) of different H_2 bubble radius (x-axis) at different bulk supersaturation levels (f, y-axis) as predicted by the Epstein-Plesset theory 21
Fig. I.5. Schematic diagram of a typical water electroreduction cell. 23
Fig. I.6. Depiction of the current-potential relationship of the HER and OER during water electrolysis and the involved potential losses (overpotentials). 24
Fig. I.7. Exchange current density as a function of the metal-hydrogen bond strength, E(M-H), for different metals..... 28
Fig. I.8. Schematic representation of the direct and indirect electron transfer (DET and IET) in Microbial electrosynthesis systems (MES). 29
Fig. I.9. Free energy of formation of a gas bubble. 34
Fig. I.10. Classical nucleation theory solution on the heterogeneous nucleation rate of H_2 bubbles with different supersaturation and contact angle values..... 36
Fig. I.11. Equilibrium contact angle of a pinned electrolytic H_2 bubble to the cathode surface obtained from the Lohse-Zhang diffusion model [131]. 37
Fig. I.12. Schematic representation of the basic principles followed in this work to favor the solubilization of H_2 during water electroreduction. 40

CHAPTER II

Fig. II.1. Schematic representation of the two-chamber H-type cell experimental setup for water electroreduction..... 48
Fig. II.2. Mixed potential measurements using a Pt wire electrode for Run 1 from Table II.1. 51
Fig. II.3. Effect of electromagnetic interference from the polarized cathode on the mixed potential measured by the Pt wire electrode 52

Fig. II.4. Preliminary experiments using a Pt wire as a qualitative tool to measure the mixed potential state in the liquid medium 53
Fig. II.5. Validation of preliminary experiments using a Pt wire as a qualitative tool to measure the state of H_2 saturation 54
Fig. II.6. Mixed potential measurements by a Pt wire electrode during galvanostatic experiments at 30 mA 55
Fig. II.7. Dissolved H_2 concentration measured by an amperometric H_2 sensor during galvanostatic experiments at 30 mA 56
Fig. II.8. Evaluation of the accuracy of the headspace gas chromatography (HS-GC) method for measuring dissolved H_2 concentration. 59
Fig. II.9. Semiconducting metal oxide (SMO) sensor signal and cell voltage during water electroreduction experiments at a cathodic current of 20 mA 61
Fig. II.10. H_2 bubble segmentation on single video frames of the cathode surface 62

CHAPTER III

Fig. III.1. Scheme of strategies to be used to improve electron transfer during gas fermentation. 70
Fig. III.2. Experimental setup of the two-chamber H-type cell used during (A) water electroreduction and (B) H_2 gas injection. 75
Fig. III.3. H_2 solubilization kinetics by gas injection and water electroreduction in a potassium phosphate buffered solution (0.1 M, pH = 7.2) of 0.8 L. 82
Fig. III.4. Variation of the (A) maximum dissolved H_2 concentration and (B) H_2 solubilization rate as a function of the H_2 supply rate by water electroreduction and gas injection in a potassium phosphate buffered solution (0.1 M, pH = 7.2) of 0.8 L. 83
Fig. III.5. Solubilization efficiency of dissolved H_2 by gas injection and water electroreduction in a potassium phosphate buffered solution (0.1 M, pH = 7.2) of 0.8 L. 84
Fig. III.6. H_2 Solubilization kinetics of the different H_2 supply rates tested for gas injection (solid lines) and H_2 uptake kinetics (dashed lines) 88
Fig. III.7. H_2 Solubilization kinetics of the different H_2 supply rates tested for water electroreduction (solid lines) and H_2 uptake kinetics (dashed lines) 89

Fig. III.8. Effect of low KLa to k1xX ratios and the H_2 saturation concentration (CH2sat) on the Gibbs free energy of the (autotrophic) acetogenic reaction 90
Fig. III.9. Effect of high KLa to k1xX ratios and the H_2 saturation concentration (CH2sat) on the Gibbs free energy of the ethanol production reaction 92

CHAPTER IV

Fig. IV.1. H-type reactor design for the second experimental part. (A) H-type electrolyzer design. 108
Fig. IV.2. Graphical representation of the determination of the current associated to the onset of H_2 bubble nucleation..... 110
Fig. IV.3. Graphical representation of the bubble detection algorithm. 111
Fig. IV.4. Optical features observed during image processing for H_2 bubble nucleation detection in linear sweep voltammetry (LSV) experiments conducted on different cathode materials under stirring and H_2 pre-saturation. 114
Fig. IV.5. Simulation of the experimental run with SSP cathode without agitation or H_2 pre-saturation 117
Fig. IV.6. Estimated average concentration of dissolved H_2 at the SSP cathode surface under non-agitated conditions at the onset of bubble nucleation. 119
Fig. IV.7. Electrocatalytic performance of the hydrogen evolution reaction (HER) catalyzed by stainless-steel plate (SSP), stainless-steel porous foam (SSPF), and carbon brush (CB) electrodes 121
Fig. IV.8. Effect of H_2 pre-saturation and agitation on the maximum current achieved before the onset of H_2 bubble nucleation..... 124

CHAPTER V

Fig. V.1. Schematic of a low and high ohmic resistance paths in a water electroreduction cell generated due to a nonsymmetric cathode geometry. 133
Fig. V.2. Schematic representation of the simulated geometry used for the study of the current distribution on a flat plate cathode. 134

Fig. V.3. Schematic representation of the simulated geometry used for studying the mass transfer of a porous cathode. 136
Fig. V.4. Schematic coupling of the gas fermentation reactor and the electrolyzer 137
Fig. V.5. Current distribution on the (A) electrode and the (B) electrolyte for the reference case where f_{area} = 0.127. 138
Fig. V.6. Current distribution streamlines on the electrolyte for (A) f_{area} = 2 and (B) f_{area} = 1. 140
Fig. V.7. Comparison of the effect of the total cathodic projected surface area on the maximum total current that could be imposed before nucleation (I_{bubble}) for a single parallel plate and multiple perpendicular plates. 142
Fig. V.8. Current density distribution along a perforated plate cathode. (A) Perforated plate cathode design. (B) Current density distribution across the thickness of the perforated plate. 143
Fig. V.9. Current density distribution on the electrolyte when a second separator surface is introduced. 144
Fig. V.10. Comparison of the effect of the electrolyte conductivity (κl) on the maximum total current that could be imposed before nucleation (I_{bubble}) for a single perforated plate with double separator. 145
Fig. V.11. Comparison of the effect of the exchange current density of the cathode material (J_0) on the maximum total current that could be imposed before nucleation (I_{bubble}) for a single perforated plate with double separator. 146
Fig. V.12. Effect of an anisotropic exchange current density (j_0) on the current distribution across the cathode thickness. 147
Fig. V.13. Comparison of the effect of the total cathodic projected surface area on the maximum total current that could be imposed before nucleation (I_{bubble}) for a single parallel plate, an array of perpendicular plates and a single perforated plate. 148
Fig. V.14. Spatial concentration profile of H_2 for the porous structure using 20 ppi and separation 1.1 in a cell of 25.5 mm of width. 150
Fig. V.15. Effect of the cathodic surface area on the maximum concentration of H_2 achieved in a cell with 25.5 mm of width (wide). 151
Fig. V.16. Spatial concentration profile of H_2 for the porous structure using 20 ppi and separation 1.1 1 in a cell of 7.5 mm of width. 152

Fig. V.17. Effect of the cathodic surface area on the maximum concentration of H_2 achieved in a cell with 7.5 mm of width (narrow). 153

CHAPTER VI

Fig. VI.1. Schematic of a water electroreduction cell and a hydrogenotrophic bioreactor coupling. 158
Fig. VI.2. Schematic representation of the water electroreduction cell design. 161
Fig. VI.3. Effect of the outlet concentration of dissolved H_2 ($CH2out$) on the recycling rate of electrolyte (vl) and the current applied to the water electroreduction cell (I). 164
Fig. VI.4. H_2 concentration profile and current distribution across the surface of the porous cathode for the simulation Case 1. 166
Fig. VI.5. H_2 concentration profile and current density distribution along the (A) cathode width at the exit and (B) the cathode height on the projected surface area of the porous cathode for the simulation Case 1. 168
Fig. VI.6. Fluid velocity (y- component) profile along the cell width from the middle height of the cell for the simulation Case 1. 168
Fig. VI.7. Effect of the separator-cathode spacing on the maximum local current density and local concentration of H_2. 169
Fig. VI.8. Scale factors for simulation cases with low H_2 uptake. 170
Fig. VI.9. Scale factors for simulation cases with high H_2 uptake. 172
Fig. VI.10. Current density distribution along the cathode width at the exit of the cathode for Cases 5 (cathode thickness of 2 cm) and Case 7 (stack of 6 cells with cathode thickness of 1 cm). 173
Fig. VI.11. Comparison of the dimensions of the resulting water electroreduction cells 174

SUPPLEMENTAL INFORMATION

Fig. A1. Double syringe configuration for measuring the dissolved H_2 concentration by the headspace-gas chromatography method 199

Fig. B1. Schematic representation of the proposed communication system for the current control of a potentiostat. 202
Fig. B2. Microcontroller and digital-to-analog converter (DAC) setup..... 203
Fig. B3. DB9 connection on a VSP biologic potentiostat for analog communication. (A) DB9 connector on the potentiostat. 204
Fig. B4. Modulo Bat interface on the EC-lab software. 205

Fig. C1. H_2 solubilization kinetics during water electroreduction in a carbon brush cathode with a cathodic current of 60 mA in two different liquid mediums. 220

Fig. D1.Image of the graphical interface for the bubble detection algorithm used with the stainless-steel plate (SSP) under no agitation and no H_2 pre-saturation. The plateau on the voltammogram matches with the signal increase on the bubble detection algorithm. 222
Fig. D2.Image of the (A) stainless-steel plate, SSP; (B) stainless-steel porous foam, SSPF, and (C) carbon brush, CB, at the end of the experiment in the conditions of no agitation and no H_2 pre-saturation. The electrode potentials correspond to -1.37 V, -1.53 V and -1.28 V vs SCE respectively. The separator/anode is situated to the left of the frame. 222
Fig. D3. Graphical representation of the Tafel equation for the agitated SSP setup..... 223

Fig. E1. Experimental setup to measure the O_2 crossover effect in a (A) three chamber water electroreduction cell and (B) three chamber control system. 224
Fig. E2. O_2 concentration over the left and middle chamber of the setup depicted in Fig. E1. 225

Fig. F1. Effective (A) longitudinal and (B) transverse dispersity as a function of the Péclet number (Pe). 227

SUPPLEMENTAL INFORMATION

Table A1. Validation of the dissolved H_2 concentration measured with the amperometric H_2 sensor and the headspace gas chromatography technique. 201

List of Tables

CHAPTER I

Table I.1. Seven known CO_2 fixation pathways found in nature..... 8
Table I.2. Common hydrogenotrophic reaction stoichiometries. 11
Table I.3. Additional hydrogenotrophic reactions coupled to the WL pathway for the production of longer chain molecules. 13
Table I.4. OER and HER stoichiometries at near neutral pH conditions. 22

CHAPTER II

Table II.1. Summary of experimental conditions for testing the performance of different H_2 sensing elements. 49
Table II.2. H_2 solubilization rates for water electroreduction experiments at a cathodic current of 30 mA. 56

CHAPTER III

Table III.1. Experimental conditions evaluated for each H_2 solubilization technique 76
Table III.2. Standard Gibbs Free Energy of Reaction ($\Delta Gr0'$) of different hydrogenotrophic reactions adjusted at pH = 7..... 79
Table III.3. Kinetic parameters used for the study of the two kinetic scenarios simulated 80
Table III.4. Estimation of the energy consumption per mol of H_2 solubilized for the gas injection and water electroreduction techniques. 85

CHAPTER IV

Table IV.1. HER and OER reaction stoichiometries at acidic and alkaline conditions..... 104
Table IV.2. Experimental configurations evaluated during the recording of H_2 bubble nucleation 109

Table IV. 3. Summary of the results on the determination of the cathodic current density at nucleation for the stainless steel plate (SSP), stainless steel porous foam (SSPF) and carbon brush (CB) under different conditions of agitation and H_2 pre-saturation. 116

CHAPTER V

Table V.1. Parameters used for modeling the different porous cathode structures. 136
Table V.2. Maximum local H_2 concentration achieved with different porous structures and cell width used in this work 149
Table V.3. Maximum fluid velocity inside the porous structure for different ppi values at 1.1 separation..... 153

CHAPTER VI

Table VI.1. H_2 uptake kinetic parameters at steady state of the hydrogenotrophic bioreactor to be coupled with the water electroreduction reactor..... 159
Table VI.2. Mass balances from the coupled system shown in Fig. VI.1 used to calculate $CH2in$, $CH2'$, $RH2e$ and vl 159
Table VI.3. Parameters used for the simulation of different cases for the dimensioning of the water electroreduction reactor. 160
Table VI.4. Summary of the global simulation results from the low (Cases 1-5) and high (Cases 6-7) H_2 uptake scenarios. 164

Abbreviations

3HP: 3-Hydroxypropionate bicycle

3HP/4HB: 3-Hydroxypropionate/4-hydroxybutyrate cycle

AdhE: Adlehyde-alcohol dehydrogenase pathway

AOR: Aldehyde:ferredoxin oxidoreductase pathway

ATP: Adenosine triphosphate

ADP: Adenosine biphosphate

CB: Carbon brush

CBB: Calvin-Benson-Bassham cycle

CCU: Carbon capture and utilization

CE: Counter electrode

CEM: Cation exchange membrane

CNT: Classical nucleation theory

CO: Carbon monoxide

CO_2: Carbon dioxide

CP: Chronopotentiometry (galvanostatic technique)

CSTR: Continuously stirred tank reactor

DAC: Digital-to-analog converter

DC/4HB: Dicarboxylate/4-hydroxybutyrate cycle

DET: Direct electron transfer

DSA: Dimensionally stable anode

EET: Extracellular electron transport/transfer

GHG: Greenhouse gases

H_2: Molecular hydrogen

$HCO3^-$: Bicarbonate ion

HER: Hydrogen evolution reaction

HS-GC: Headspace gas chromatography

IET: Indirect electron transfer

LSV: Linear sweep voltammetry

MES: Microbial electrosynthesis system

$NAD(P)^+$: Oxidized nicotinamide adenine dinucleotide (Phosphate)

NAD(P)H: Reduced nicotinamide adenine dinucleotide (Phosphate)

O_2: Molecular oxygen

OER: Oxygen evolution reaction

OCP: Open circuit potential

Pd: Palladium

PHB: Poly-3-hydroxybutyrate

ppi: pores per inch

Pt: Platinum

rGlyP: Reductive glycine pathway

rTCA: Reductive tricarboxylic acid cycle

RuBisCO: Ribulose-1,5-biphosphate carboxylase/oxygenase enzyme

RWGS-FT: Reverse Water Gas Shift reaction - Fisher-Tropsch process

SCE: Saturated calomel electrode

SMO: Semiconducting metal oxide

SMR: Steam methane reforming

SSP: Stainless-steel plate

SSPF: Stainless-steel porous foam

THF: Tetrahydrofolate

WE: Working electrode

WL: Wood-Ljungdahl pathway

Notations

α: Charge transfer coefficient

γ: Surface tension of the liquid

ΔG^{*}: Gibbs free energy barrier to the formation of a bubble of a critical size

ΔG_{bulk}: Gibbs free energy of dissolved gas transport from supersaturated solution to bubble

ΔG_{r}^{0}: Gibbs free energy of formation at standard conditions

$\Delta G_{r}^{0'}$: Gibbs free energy of formation at standard conditions, corrected for pH = 7

ΔG_{surf}: Gibbs free energy of gas-liquid interface formation

ΔG_{tot}: Total Gibbs free energy of bubble formation

ΔG_{v}: Gibbs free energy difference per unit of volume between dissolved and gaseous state

ΔP: Pressure drop across the porous cathode

ΔP_{frit}: Pressure drop across the glass frit during gas injection

$\in$: Energy efficiency of compression

κ_{l}: Electrolyte (ionic) conductivity

κ_{m}: Solid porous matrix (electronic) conductivity

η: Electrode overpotential

η_{C}: Cathodic overpotential

η_{A}: Anodic overpotential

Θ: Contact angle of a bubble in nucleation site

θ_{eq}: Equilibrium contact angle of a bubble in nucleation site

μ_{g}: Dynamic viscosity

ρ_{∞}: Gas density

σ: Supersaturation ratio $(C_{H_2}/C_{H_2}^{sat} - 1)$

ϕ: Wettness as a function of the contact angle of a bubble in nucleation site

a: gas-liquid interfacial area

A: Cross-sectional area of the glass frit

b: Characteristic electrode length

C: Pre-exponential kinetic nucleation factor

$C_{CO_2}^{sat}$: Dissolved CO_2 concentration at the saturation point

C_{H_2}: Dissolved H_2 concentration on the liquid bulk phase

C'_{H_2}: Inlet H_2 concentration to the hydrogenotrophic bioreactor

C''_{H_2}: Outlet H_2 concentration to the hydrogenotrophic bioreactor

$C_{H_2}^{crit}$: Critical dissolved H_2 concentration at which bubble nucleation starts

$C_{H_2}^{in}$: Inlet H_2 concentration to the water electrolyzer

$C_{H_2}^{max}$: Maximum local concentration of dissolved H_2

$C_{H_2}^{out}$: Outlet H_2 concentration from the water electrolyzer

$C_{H_2}^{sat}$: Dissolved H_2 concentration at the saturation point

C_l^b: Gas concentration in the liquid bulk phase

C_l^i: Gas concentration on the liquid interface side

C_O: Concentration of oxidized species

C_{prod}: Concentration of product

C_R: Concentration of reduced species

C_{react}: Concentration of reactants

D: Dilution rate

D_{H_2}: H_2 diffusion coefficient in water

E^0: Standard potential (vs standard hydrogen electrode, SHE) of the half redox reaction

E_{comp}: Energy of gas compression

E_{smr}: Energy consumed during the production of H_2 by steam methane reforming per mol of H_2 solubilized

E_{we}: Energy consumed per mol of solubilized H_2

f: Supersaturation ratio $(C_{H_2}/C_{H_2}^{sat})$

F: Faraday constant

f_{area}: Fraction of the projected surface area of the cathode to the separator

H: Henry's law constant

I: Current

I_{bubble}: Cathodic current imposed at the start of H_2 nucleation

J: Current density

j: Local current density

J_0: Exchange current density

j_0: Local exchange current density

J_{bubble}: Cathodic current density imposed at the start of H_2 nucleation

j^{max}: Local maximum cathodic current density

k: Darcy's permeability

k_1^x: Biomass specific H_2 uptake rate

k_g: Local mass transfer coefficient in the gas phase

k_L: Local mass transfer coefficient in the liquid phase

K_L: Overall mass transfer coefficient in the liquid phase

$K_L a$: Volumetric mass transfer coefficient in the liquid phase for H_2

$K'_L a$: Volumetric mass transfer coefficient in the liquid phase for CO_2

MI: Mixing index

M_w: Molecular weight

n: Number of electrons involved in the half reaction

N_A: Gas flux across the gas-liquid interface

n_d: Moles of H_2 dissolved in the liquid

n_s: Moles of H_2 supplied in the system

NR: Bubble nucleation rate

P_1: Inlet pressure to compressor coming from the steam methane reforming process

P_2: Pressure needed to overcome the pressure drop from the glass frit

p_{ext}: External pressure of the system

p_g^b: Gas partial pressure in the gas bulk phase

p_g^i: Gas partial pressure on the gas interface side

P_{hyd}: Hydraulic power

Q_{H_2}: Volumetric H_2 supply rate

r: radius of curvature of the bubble

R: Universal gas constant

R_{cell}: Cell resistance

$R_{H_2}^e$: Electrolytic production rate of H_2

$R_{H_2}^x$: Biological H_2 uptake rate

R_{sol}: H_2 solubilization rate

R_{sup}: Molar H_2 supply rate

R_{sup}^{V}: Volummetric H_2 supply rate

SEE: System's solubilization efficiency

s_{eff}: H_2 solubilization efficiency in percentual units

s_{loss}: Percentual H_2 lost from the flow rate exiting the electroreduction cell and the hydrogenotrophic bioreactor

T: Absolute temperature

V_c: Catholyte volume

V_{cell}: Cell voltage

v_f: Nutrient feed and purge flow rate

v_j: Stoichiometric coefficient of the specie j

v_l: Recycling flow rate between the hydrogenotrophic bioreactor and the water electroreduction cell

V_M: Molar volume

V_R: Volume of hydrogenotrophic bioreactor

Wa': Wagner number for quantify the current distribution homogeneity in 3D/porous electrodes

X: Biomass concentration

Y: Stoichiometric ratio of CO_2 to H_2 uptake

Publications and communications

J.-D. Carvajalino-Olave, L. Laguillaumie, C. Dumas, and B. Erable, “Electroreduction of water, a promising alternative to gas injection: A case on hydrogen solubilization in biological processes involving hydrogenotrophs,” *Chemical Engineering Journal*, p. 168494, Sep. 2025, doi: 10.1016/j.cej.2025.168494.

Evaluation of Different Cathode Materials on the Production of Soluble Hydrogen for Improving the Energy Efficiency of Microbial Electrosynthesis Processes (Oral Presentation). XXVIII International Symposium on Bioelectrochemistry and Bioenergetics of the Bioelectrochemical Society. Oral presentation. Alcalá de Henares, Spain. Sept 23. 2024

Chapter I.Introduction

I-1. General overview

Climate change poses a significant threat to food security, economic growth and general well-being and taking urgent action is one of the 17 integrated goals adopted by the United Nations in 2015 for achieving sustainable development [1]. The urgency of this challenge is marked by the latest United Nations Emissions Gap Report, which reveals a substantial gap between current pledges to reduce greenhouse gas (GHG) emissions and the levels required to limit global warming to well below 2°C, as stipulated in the Paris Agreement [2]. As stated by the report, even if nations were to fulfill their current commitments, the world is still projected to experience a 2.6°C increase in global temperature by the end of the century. This highlights the insufficiency of existing efforts and the need for a sixfold increase in mitigation investment to limit global warming to the critical threshold of 1.5°C. The magnitude of this challenge is further emphasized by the continued rise in global GHG emissions: they rose 0.8% annually between 2010 and 2019 while in 2023 they grew at a rate of 1.3%, reaching a record high of 57.1 $GtCO_2$ equivalents.

Carbon dioxide is recognized as a major contributor to GHG, and the imperative to mitigate its emissions has driven the development of innovative technologies. The gradual deployment of renewable energies, improved fuel efficiency, and the shift to more plant-based diets are some actions that can alleviate emissions in different sectors of the economy such as energy, transportation and agriculture [3]. For heavy industries like steel, cement, and glass manufacturing, which rely on processes that require high temperatures, the use of clean energies (e.g., solar and wind) is today prohibitively expensive [4]. While direct CO_2 capture from air offers one potential solution, carbon capture and utilization (CCU) at the source of emission presents a more targeted approach, preventing CO_2 from diluting in the atmosphere and contributing to global warming. This aligns with the growing emphasis on circular economy principles, where waste materials are repurposed and reused to minimize environmental impact.

One potential solution that falls into the category of CCU is through a process of biological CO_2 uptake called gas fermentation. This process employs microorganisms to convert gaseous substrates such as CO_2 ,CO and H_2 into valuable products such as organic acids, alcohols, methane and longer chain molecules [5]. The traditional way of processing CO_2 into chemicals

is through the reverse water gas shift reaction followed by the Fischer-Tropsch process (RWGS-FT), which requires high temperatures and pressures (150 - 350 °C, ~ 30 bar). Moreover, the chemical catalysts are susceptible to poisoning by contaminants commonly found in syngas, such as sulfur [6]. Contrary to the RWGS-FT, milder temperatures and pressures (30-37 °C, atmospheric pressure) are optimal for the growth of microorganisms during gas fermentation, which are generally more resilient to contaminants from the gas sources.

As in many biological processes operating at milder conditions, the conversion rates are usually low compared with chemical processes. In gas fermentation, autotrophic microorganisms such as acetogenic microorganisms and hydrogenotrophic archaea are the most used groups of microorganisms industrially utilized for reducing CO_2 (carbon source) in the presence of H_2 (electron source). The slow growth and substrate uptake of these microorganisms gets even more pronounced due to the necessity of first dissolving these gases into the liquid medium where these microorganisms grow. At 30° C, H_2 and CO_2 have a solubility in water of 0.78 $mmol \cdot L^{-1}$ and 35 $mmol \cdot L^{-1}$ per bar [7]. In comparison with other heterotrophic fermentation processes, glucose is used as carbon/energy source and has a solubility of 2990 $mmol \cdot L^{-1}$ [8].

Due to the slow gas-to-liquid H_2 transfer, the low H_2 solubilization rate has been recognized as the main bottleneck during gas fermentation of H_2/CO_2 gases, limiting microorganism growth, CO_2 reduction and product yield [6], [9], [10]. Most of the efforts to increase the gas-to-liquid mass transfer have focused on using special reactor designs (e.g., optimized gas spargers, bubble columns, trickle-bed reactors, membrane reactors, circulation loop reactors) and working under high pressures to shift the distribution of H_2 at equilibrium to the liquid phase [9], [11]. Another approach to circumvent the H_2 gas-to-liquid mass transfer limitation is the use of microbial electrosynthesis systems (MES) where other energy sources easily available for microorganisms can be used. Formate, a more soluble molecule that acts as an energy/carbon source (being an intermediate metabolite during the hydrogenotrophic CO_2 fixation), can be electrochemically produced by reduction of CO_2 at the expense of a higher energy input and special electrode materials [12], [13]. Direct electron transfer from cathodic surfaces to electroactive biofilms capable of reducing CO_2 has also been reported, but there is growing evidence that for scaling up the process, higher product yields are achieved when H_2 is electrochemically produced to serve as the intermediate energy source [14], [15], [16], [17], [18].

This thesis will explore a novel approach for achieving high H_2 solubilization rates in a liquid medium with the purpose of supplying H_2 to hydrogenotrophic bioprocesses. The electrochemical supply of H_2 has mostly been considered as a gas input to the gas fermentation process, which holds the mass transfer limitations mentioned before. Here, the production of soluble H_2 is achieved during water electroreduction, focusing on design and control strategies that allow the production of soluble H_2 and minimizing H_2 bubble formation.

I-2. Literature review

I-2.1 Global energy landscape and the role of H_2 in sustainable development

The global energy landscape is undergoing a profound transformation, driven by a growing energy demand and escalating concerns over climate change. In 2023, global energy demand increased by approximately 2%, with emerging markets and developing economies contributing significantly to this growth. Despite a record high in clean energy installations, fossil fuels met two-thirds of this increase in energy demand in 2023, consequently driving energy-related CO_2 emissions to another record high, with carbon dioxide levels standing at 150% above pre-industrial levels [1], [19].

The world's energy demand is projected to increase 2.0-2.5 times by 2050 [19], necessitating a drastic shift towards sustainable and carbon-neutral energy sources to mitigate the adverse effects of man-made CO_2 emissions and global warming. Despite warnings and international calls for significant cuts, such as a 55% reduction in CO_2 emissions by 2030 to limit global warming to 1.5 °C [20], the world continues to invest heavily in fossil fuel production. This necessitates diverse decarbonization strategies, such as the incorporation of solar and wind power and the use of clean fuels, particularly for hard-to-abate sectors like heavy industry, which accounts for nearly 40% of global CO_2 emissions [21].

As stated by the United Nations Environment Programme, there is not a “silver bullet” technology or approach that can be universally applied to all countries and sectors to transition into a zero-emissions scenario as shown in Fig. I.1[3]. While electricity from renewables can be better implemented in the energy sector, the beforementioned heavy industries for cement and steel could require a different approach, where carbon capture and green hydrogen might

play a bigger role [3]. For example, using H_2 instead of CO is a potential choice to reduce iron ores into metallic iron in steel making that would require tripling the global H_2 production [22].

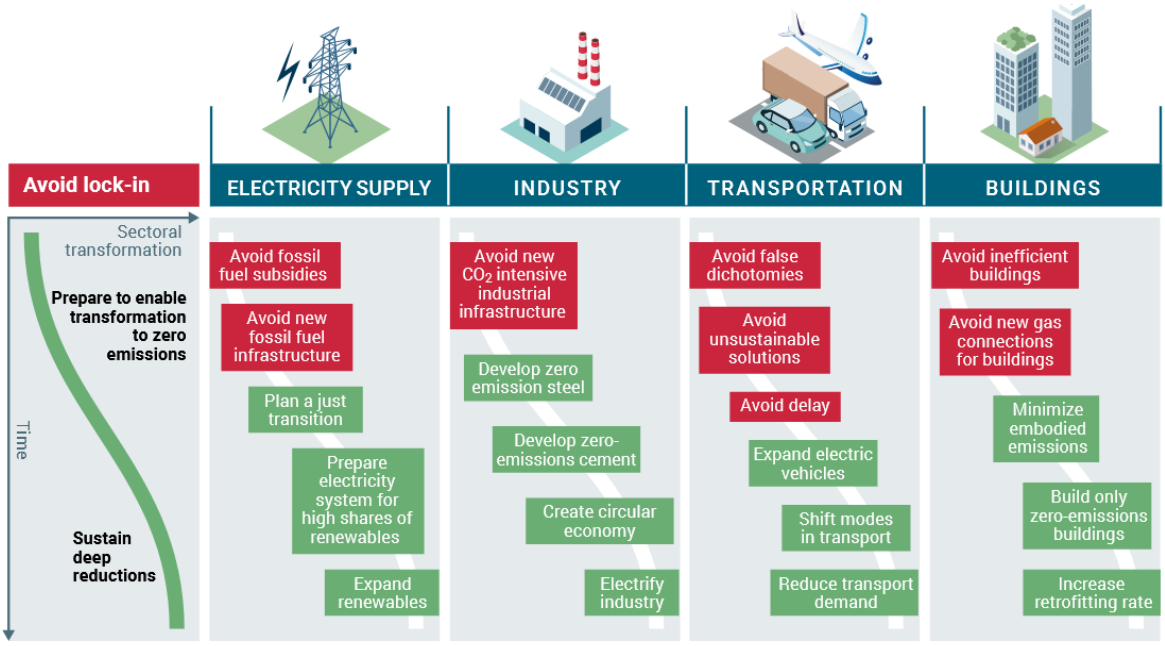

Fig. I.1. Approaches to accelerate the transformation towards zero carbon emissions. Taken from UN emissions Gap Report 2022 [3].

In a different context, H_2 emerges as a central component for sustainable energy systems due to its attributes as a clean, high-energy-density fuel and its capacity to enable sector coupling. As a clean energy carrier, hydrogen can directly substitute fossil methane for industrial process heat and feedstock, offering a zero-carbon alternative in combustion applications or through blending into existing natural gas infrastructure [21], [23], [24]. Nevertheless, the decline in the production costs of H_2 and clean energy sources might not be fast enough to push for a faster energy transition, and due to the inherent economic advantage that fossil-based industries have from years of technological optimization, many countries are still investing in fossil fuels over renewables. For example, although the US and Europe push for decommissioning of coal-fired power plants, between 2010 and 2018, India and China added significant coal-fired power capacity, with China planning on the investment of more than 140 coal-fired power plants globally [20].

The necessity of CO_2-intensive industries in a slow decarbonization scenario makes carbon capture technologies appealing for both emission-control and waste valorization. While carbon capture is not generally seen as a "game-changing strategy" for massive emission

mitigation, it complements other efforts by recycling carbon into useful products when the stored carbon is transformed into valuable products, especially if renewable energy is used for the conversion of CO_2 [20].

I-2.2 Carbon Capture and Utilization prospects

When CO_2 is captured, it can be stored in underground geological formations, depleted oil and gas reservoirs, depleted coal mines, or saline aquifers [20]. This is the most promising alternative today since the oil and gas industry already has expertise on subsurface geological characterization, drilling, and injection of CO_2 in enhanced oil recovery. Some of the challenges associated with CO_2 storage underground are the leakage back into the atmosphere (due to gradual or abrupt leakage), induction of seismicity, leakage to water bodies and long-term monitoring. Instead of storage, there is the potential for CO_2 transformation into chemicals and fuels which would close the carbon cycle (as long as carbon remains bonded in chemical products). Nevertheless, currently there are not enough proven carbon capture and utilization (CCU) technologies capable of handling the vast amounts of global CO_2 emissions. Therefore, even when carbon storage is recognized as a more urgent solution to climate change mitigation, carbon utilization research is still needed for achieving a sustainable economy in the long term.

The rapid adoption of CCU technologies will also depend on how profitable they can be, in a balance between the costs associated with CO_2 capture and transformation, and the added value of the final product (e.g., chemical or fuel). Urea is perhaps one of the most promising products with added value that can be obtained from CCU. Due to the continuous population and global economic growth, the production of urea is in demand for its use in fertilizers for agriculture. Urea can be obtained from the exothermic reaction of ammonia and CO_2 to form ammonium carbamate and its posterior dehydration to urea. Nevertheless, this process is very energy intensive, requiring temperatures around 150-250 C and 5-25 MPa [25].

Methanol, another promising product used as building block and fuel, can be obtained from the hydrogenation of CO_2. With the same principle, the use of H_2 as a reductant allows the formation of other interesting molecules such as formic acid, formaldehyde, methanol, dimethyl ether and methane through the Sabatier process; the production of higher hydrocarbons through the modified Fischer-Tropsch process from CO hydrogenation

(Anderson-Schulz-Flory hydrocarbon distribution), or higher content of gasoline/lower olefins directly from methanol hydrogenation [26], [27], [28]. Both heterogeneous and homogeneous catalysts have been reported to allow the hydrogenation reaction in gaseous and liquid phases. Cu/ZnO are common heterogeneous catalysts employed in the production of methanol at temperatures around 250 C with ~70 bars of CO_2/H_2 pressure, but Ru was also used as a homogeneous catalyst to convert CO_2 and H_2 in solution to methanol at ~120 C [29]. CO_2 hydrogenation using homogeneous catalysts (also known as molecular catalysts) although is currently done at small scale only, it is a growing field of research due to the mild temperature and pressure conditions they could operate [29].

Another CCU technology that promises CO_2 utilization at mild temperatures and pressures is the biological CO_2 fixation. Here, microorganisms can be seen as catalytic units that operate optimally at temperatures and pressures close to room conditions (20 C and 1 atm). This has the advantage of favoring the economic balance between operational cost and added value products, but at the expense of the characteristic slow kinetic of biological processes.

I-2.3 Biological CO_2 fixation pathways

The global carbon cycle fundamentally relies on the transformation of CO_2 into diverse organic compounds, a process critical for sustaining life and producing essential chemicals and energy for humanity [30]. While the Earth's autotrophic organisms collectively capture approximately 380 billion tons of CO_2 annually, their inherent fixation rates are generally insufficient to meet industrial demands, which typically require production levels significantly higher than natural processes [30]. Nevertheless, a deep understanding of natural carbon fixation mechanisms is essential for the rational design and engineering of more efficient biological CCU technologies.

Microorganisms employ a variety of complex biochemical routes to assimilate CO_2, each adapted to specific environmental conditions. These pathways can be broadly categorized based on their energy sources as shown in Table I.1. The Calvin-Benson-Bassham (CBB) cycle, the reductive tricarboxylic acid (rTCA) cycle and the 3-hydroxypropionate (3HP) bicycle use light as an energy source (photosynthetic), while the 3-hydroxypropionate/4-hydroxybutyrate (3HP/4HB) cycle, the dicarboxylate/4-hydroxybutyrate (DC/HB) cycle, the reductive glycine pathway (rGlyP) and the Wood-Ljungdahl (WL) pathway use H_2 as energy source (hydrogenotrophic) [30]. The primary energy sources (H_2 and light) on each pathway are used

to generate the reducing power and maintain the redox balance of the energy carriers ($NAD(P)H/NAD(P)^+$, ATP/ADP and Fd_{red}/Fd_{ox}).

Table I.1. Seven known CO_2 fixation pathways found in nature. Taken from Gong *et. al.* [30] with the addition of the reductive glycine pathway (rGlyP) [31].

CO_2 fixation pathway	Input	Output	Oxygen tolerance
Photosynthetic			
CBB cycle	3 CO_2, 9 ATP, 6 NAD(P)H	Glyceraldehyde-3-phosphate	Aerobic
rTCA cycle*	2 CO_2, 2 ATP, 4 NAD(P)H	Acetyl-CoA	Anaerobic
3HP bicycle	3 HCO_3^-, 5 ATP, 5 NAD(P)H	Pyruvate	Aerobic
Hydrogenotrophic			
3HP/4HB cycle*	2 HCO_3^-, 4 ATP, 4 NAD(P)H	Acetyl-CoA	Aerobic
DC/4HB cycle*	1 CO_2, 1 HCO_3^-, 3 ATP, 4 NAD(P)H	Acetyl-CoA	Anaerobic
rGlyP pathway	2 CO_2, 1 ATP, 3 NAD(P)H	Acetyl-CoA***	Anaerobic**
WL pathway	2 CO_2, 1 ATP, 4 NAD(P)H	Acetyl-CoA	Anaerobic

* Sulfur can also act as an energy source.

** Oxygen tolerant through the synthetic serine module [32].

*** Pyruvate is another end product

Due to its industrial relevance as an efficient hydrogenotrophic CO_2 fixation pathway, only the WL pathway will be presented next. The reader can find more information on the remaining six pathways in other reviews [30], [33], [34].

I-2.3.1 Wood-Ljungdahl pathway (WL)

The Wood-Ljungdahl (WL) pathway, also known as the reductive acetyl-CoA pathway, was discovered in 1972 and is particularly remarkable for its high energy efficiency, being

considered one of the most efficient non-photosynthetic carbon fixation mechanism known to date [6], [30]. This pathway is exclusively found in obligately anaerobic microorganisms, termed acetogens (type of hydrogenotrophic microorganisms, sometimes called homoacetogens), and plays a crucial role in the global carbon cycle, annually producing over 10 trillion kilograms of acetic acid [35].

The WL pathway is unique among biological CO_2 fixation routes in several aspects: it is a linear, non-cyclic pathway composed of two distinct branches: the methyl branch and the carbonyl branch [36]. It is also characterized by its use of organometallic intermediates and its ability to conserve net ATP rather than solely consuming it [37]. The pathway's central product is acetyl-CoA, which serves as a fundamental precursor for cellular biomass and other metabolic end-products.

In terms of energy supply and electron donors, the WL pathway is highly versatile. Acetogens can utilize various C1 gases, including CO_2 and CO as carbon sources, often employing molecular H_2 as an electron donor [6]. When grown autotrophically on CO, the carbon monoxide dehydrogenase enzyme can facilitate the water-gas shift reaction, generating the necessary CO_2 for the methyl branch [38]. Moreover, the growth on CO is more energetically favorable compared with H_2 , it has a higher solubility in water and a better product profile for more reduced organic molecules [6], [39], [40]. Nonetheless, its higher toxicity and carbon loss in the form of CO_2 makes the use of H_2 for CO_2 biological fixation into a desired research path for feasible scale-up [41], [42], [43].

Energy conservation in acetogens is intricately linked to the pathway, involving the generation of a sodium ion (Na^+) or proton (H^+) gradient across the cell membrane, driven by the oxidation of reduced ferredoxin through membrane protein complexes [44]. This electrochemical gradient is then utilized by ATP synthases to produce ATP. Energetically, reducing one CO_2 molecule to acetyl-CoA via this pathway requires approximately 0.5 reduced ferredoxin, 0.5 ATP, and 2 NADH as reducing equivalents/energy carriers [11]. Acetogens rely on specific membrane-bound multi-subunit structures called the Rnf and Ech complexes as well as electron bifurcation, to conserve energy and manage the balance of these reducing equivalents. For Rnf-acetogen *A. woodii*, the involved reactions are shown in equation 1-3:

$$NAD^+ + H_2 \rightarrow NADH + H^+ \text{ [45].} \qquad 1$$

$$2H_2 + Fd_{ox} + NAD^+ \rightarrow NADH + 3H^+ + Fd_{red}$$ [46]. 2

$$ADP + Pi \rightarrow ATP + H_2O$$ [47]. 3

The energy required to drive equation 3 is obtained from the ion translocation across the membrane. For example, equation 2 translocates 2 moles of Na^+ inside the membrane per mol of ferredoxin oxidized, while ATP generation translocates 3 moles of Na^+ outside the membrane per 0.9 mol of ATP in the Rnf complex [48]. While the Rnf complex can translocate sodium ions and protons across the membrane, the Ech complex only translocate protons [40].

The WL pathway is strictly anaerobic due to the oxygen sensitivity of several of its key enzymes [49]. The specific carbon compounds produced from acetyl-CoA are diverse, with acetate being the primary end-product and the reason for the name "acetogens". However, certain acetogens are also capable of producing ethanol, butyrate, butanol, hexanol, and 2,3-butanediol, expanding their utility beyond acetate [40].

The industrial applications of the WL pathway are extensive and rapidly developing. Acetogens are highly regarded as promising biocatalysts for valorizing C1 gases from industrial waste or syngas into valuable chemicals. Gas fermentation, utilizing these microorganisms, has already achieved industrial-scale production of ethanol from CO-rich steel mill waste gases [11], [50]. Despite these successes, challenges remain, particularly the low cell density and inherent energy limitations of acetogens, which operate at a thermodynamic limit, hindering commercial-scale productivity, and strategies to achieve high cell densities and high H_2 uptake rates span from reactor design to metabolic engineering [9], [40], [51].

Both the WL and the rGlyP pathways require H_2 when autotrophic growth is carried for the fixation of CO_2, and microorganisms growing in this mode are often referred as hydrogenotrophs. The categorization of hydrogenotrophs according to their industrial potential is given in the following section.

I-2.4 Hydrogenotrophic fixation of CO_2 at the thermodynamic edge of life

Hydrogenotrophs, including methanogenic archaea and homoacetogenic microorganisms, are chemolithotrophs that predominantly use H_2 as their electron donor. These organisms are

often described as living at the thermodynamic edge of life due to the inherently low energy yields of their primary metabolic reactions compared to heterotrophs. For comparison, synthesizing a 6-carbon sugar (building block for carbohydrates used in cellular synthesis) requires 2880 kJ from the reduction of CO_2 (autotrophic) while only 335 kJ from the reduction of acetate (heterotrophic) [45]. Moreover, there is a net zero ATP yield from substrate-level phosphorylation resulting from the WL pathway, and additional mechanisms such as chemiosmotic energy conservation (transmembrane ion gradients coupled with membrane-bound ATP synthases) and electron bifurcation (coupled exergonic and endergonic electron transfer) allow these microorganisms to survive in these low energy conditions [5], [44]. This energetic limitation and proteomic analysis also suggest that some metabolic regulation in these autotrophs might be dictated by thermodynamics (free energy available at a specific metabolite concentration) and not traditional protein transcription regulation, highlighting the importance of H_2 as energy source[43], [52].

Despite their energetic disadvantage, their capacity to fix different molecules such as CO_2, SO_4^{2-} or Fe^{3+} with H_2 makes them appealing for industrial applications. From the compilation of 73 different hydrogenotrophic reactions made by Thauer *et al* [53], it can be observed that the range of application of hydrogenotrophic reactions spans from the reduction of organic/inorganic carbon to produce metabolites of added value (e.g., acetogenesis, methanogenesis and solventogenesis) to the reduction of inorganic electron acceptors for remediation applications (e.g., denitrification, sulfate reduction, ferric iron reduction) as shown in Table I.2.

Table I.2. Common hydrogenotrophic reaction stoichiometries. Obtained from Thauer *et al.* [53]

Reaction	Stoichiometry	$\Delta G^{0\prime}$ [kJ/reaction]
Acetogenesis	$2CO_2 + 4H_2 \rightarrow CH_3COO^- + H^+ + 2H_2O$	-94.8
Methanogenesis	$CO_2 + 4H_2 \rightarrow CH_4 + 2H_2O$	-130.6
Solventogenesis	$CH_3COO^- + H^+ + 2H_2 \rightarrow CH_3CH_2OH + H_2O$	-9.5
Sulfate reduction	$SO_4^{2-} + 4H_2 + H^+ \rightarrow HS^- + 4H_2O$	-151.9
Ferric iron reduction	$2Fe^{3+} + H_2 \rightarrow 2Fe^{2+} + 2H^+$	-228.3

Hydrogenotrophic acetogenesis and methanogenesis reactions use the WL and a modified-WL pathway (Wolfe cycle) to produce acetate and methane from CO_2 fixation, while solventogenesis reactions extend the WL pathway through the aldehyde-alcohol dehydrogenase (AdhE) and the acetaldehyde ferredoxin oxidoreductase (AOR) pathways to produce ethanol [44]. Similarly, carboxylic acids of longer chains (e.g., n-Butyrate, propionate) can be produced by the reverse β-oxidation pathway once a carboxylate (e.g., acetate) is produced through the WL pathway [38].

As these pathways are not universally present in all hydrogenotrophic species, genetic/metabolic engineering efforts have significantly expanded the capabilities of these hydrogenotrophs for improving their product portfolio. Researchers have successfully introduced heterologous metabolic pathways into acetogens to produce a diverse range of valuable compounds not achievable in wild-type strains. For instance, butanol production, a non-native product, was demonstrated in *C. ljungdahlii* by transforming it with a plasmid expressing butanol biosynthetic genes from *C. acetobutylicum*, and subsequent studies further improved butanol production in both *C. ljungdahlii* and *C. autoethanogenum* from syngas [38], [44]. Other examples include the production of acetone and isopropanol [38] and poly-3-hydroxybutyrate (PHB) [6]. Even energy-intensive products like isoprene (C5) and mevalonate (C6), which require several molecules of ATP, have been conceptually produced in acetogens growing on gas by installing the mevalonate pathway and an isoprene synthase in *C. autoethanogenum* or *C. ljungdahlii* [6], [38]. While these are proof-of-concept productions often with low titers, they demonstrate the potential to convert C1 gases into longer carbon chain compounds, where energetic restrictions still need to be addressed.

To overcome energetic constraints in the production of these metabolites, other strategies have been adopted from a genetic perspective. For example, overexpressing four tetrahydrofolate-dependent enzymes of *C. ljungdahlii* in *A. woodii* led to a 1.1-fold increase in growth rate and a 1.2-fold increase in acetate production rate [40]. Similarly, the overexpression of native AOR in *C. carboxidivorans* demonstrated its potential to increase ethanol formation [6]. Another strategy adopted is the blocking of competing metabolic pathways to redirect carbon flux towards desired products. Inactivation of the *budA* gene (encoding acetolactate decarboxylase) in *C. autoethanogenum* eliminated 2,3-butanediol production and increased ethanol yield by 79% [38]. Similarly, disrupting the *ldhA* gene (lactate

dehydrogenase) reduced lactate production, and CRISPR-mediated downregulation of *adhE1* in engineered *C. ljungdahlii* successfully redirected carbon from ethanol to butyrate [6], [38], [40].

These energetic constraints can also be seen from an engineering point of view. As the production of longer chain molecules requires increasing quantities of reducing equivalents in the form of H_2 (see Table I.3), maintaining high concentrations of dissolved H_2 might facilitate the use of these genetically engineered strains.

Table I.3. Additional hydrogenotrophic reactions coupled to the WL pathway for the production of longer chain molecules. Obtained from Thauer *et al.* [53]

Product	Stoichiometry	$\Delta G^{0\prime}$ [kJ/reaction]
Butyrate	$2\text{Acetate}^- + \text{H}^+ + 2\text{H}_2 \rightarrow \text{Butyrate}^- + 2\text{H}_2\text{O}$	-48.1
Valerate	$\text{Acetate}^- + \text{Propionate}^- + \text{H}^+ + 2\text{H}_2 \rightarrow \text{Valerate}^- + 2\text{H}_2\text{O}$	-48.1
Caproate	$\text{Acetate}^- + \text{Butyrate}^- + \text{H}^+ + 2\text{H}_2 \rightarrow \text{Caproate}^- + 2\text{H}_2\text{O}$	-48.1
Butanediol	$2\text{Acetate}^- + 2\text{H}^+ + 3\text{H}_2 \rightarrow (2,3)\text{Butanediol} + 2\text{H}_2\text{O}$ *	+16.7

* The production of (2,3)Butanediol does not occur through the reverse β-oxidation of carboxylic acids but through the butanediol production pathway, with pyruvate as a precursor [38].

The importance of the H_2 concentration also goes beyond the product selectivity. At low H_2 concentrations, some hydrogenotrophic reactions might become thermodynamically unfavorable. For example, at standard conditions (adjusted for pH = 7), the thermodynamic potential represented by the Gibbs free energy of common hydrogenotrophic reactions calculated by equation 4.

$$\Delta G_r^{0\prime} = \Delta G_r^0 + RT\ln\left(\frac{\prod(C_{prod})^{v_j}}{\prod(C_{react})^{v_j}}\right); \qquad 4$$

Where ΔG_r^0 is the free energy of formation at standard conditions, R is the universal gas constant (8.314 $kg{\cdot}m^2{\cdot}s^{-2}{\cdot}K^{-1}{\cdot}mol^{-1}$), T is the absolute temperature, C_{prod} and C_{react} are the concentration of products and reactants and v_j is the stoichiometric coefficient of each specie. A representation of this equation at different concentrations of dissolved H_2 for some hydrogenotrophic reactions is shown in Fig. I.2.

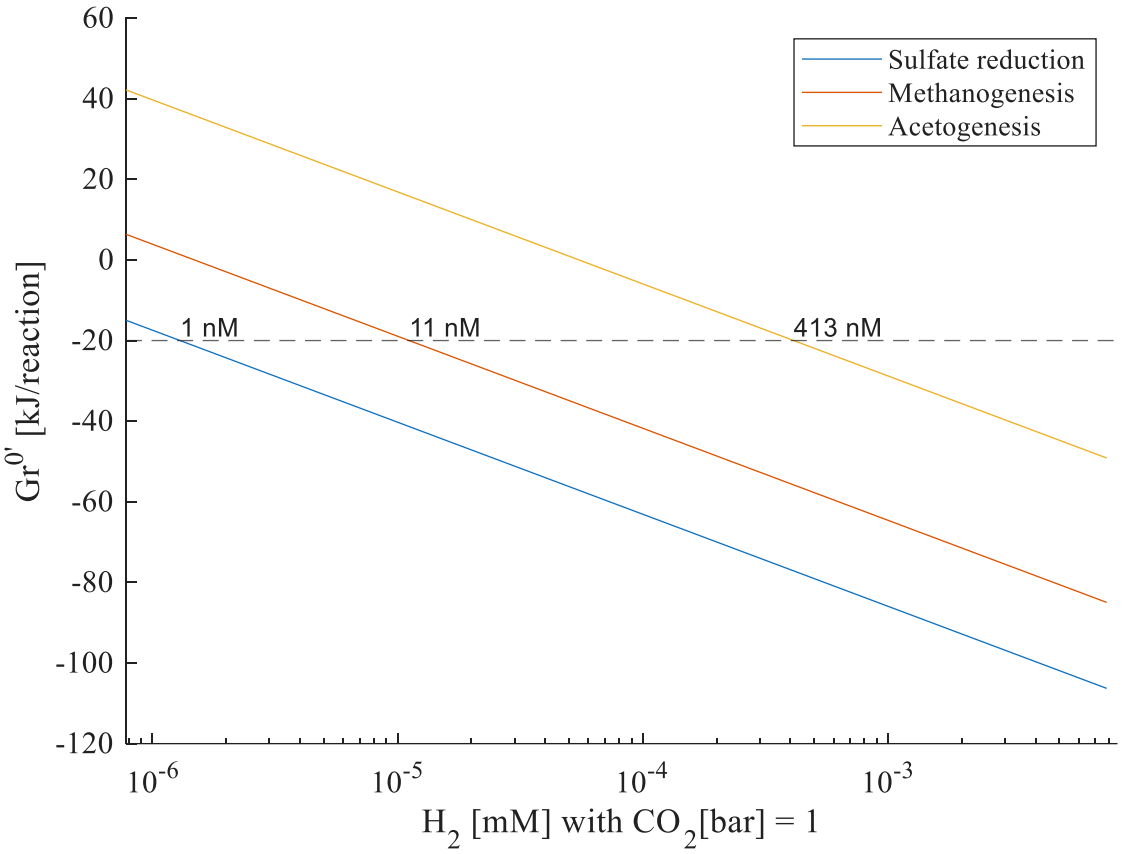

Fig. I.2. Standard Gibbs free energy ($\Delta G_r^{0\prime}$, $pH = 7$) of common hydrogenotrophic reactions. The dashed line represents the minimum $\Delta G_r^{0\prime}$ value necessary for ATP synthesis by chemiosmosis [54].

In this order, in low H_2 environments, hydrogenotrophic sulfate reducers could outcompete methanogens and the latter could also outcompete acetogens. In contrast, when the dissolved H_2 concentration is high enough to sustain different hydrogenotrophs, acetogens can kinetically outcompete other hydrogenotrophs [55], [56]. This is a very common trade-off between having a high ATP yield and maximum growth rate, or a lower substrate threshold and superior competition in low substrate environments[57], [58].

It is evident that for the fixation of CO_2 by hydrogenotrophs, the concentration of H_2 plays a fundamental role in microbial competition and product selectivity. Maintaining high concentrations of dissolved H_2 depends on the net balance between biological H_2 uptake rate and H_2 solubilization kinetics.

I-3. The Critical Bottleneck: H_2 solubilization is limited by mass transfer and obscured by accurate measurements

Gas-to-liquid mass transfer of hydrogen H_2 is widely considered the main bottleneck in hydrogenotrophic processes, primarily due to the exceptionally low solubility of H_2 in aqueous media (45 times lower than CO_2 at 1 bar and 25 C [webbook.nist.gov]) which hinders its bioavailability [9], [59], [60]. This contrasts sharply with substrates like glucose, which has a solubility of 5 $mmol \cdot L^{-1}$, while H_2 is only 0.78 $mmol \cdot L^{-1}$ [38]. This limitation implies that most hydrogenotropic bioprocesses are "liquid-phase controlled," requiring a focus on optimizing the liquid-side mass transfer coefficient [9]. Moreover, the study of the importance of dissolved H_2 becomes obscured by the fact that the liquid medium where hydrogenotrophs are is usually not at equilibrium with the gas phase, which makes real-time online measurement of dissolved H_2 concentration more challenging [61].

The current state of H_2 measurement involves taking advantage of several fundamental properties of H_2 and its interaction with other materials. For example, its high thermal conductivity compared to other gases, its exothermic reaction with O_2, its electrochemical oxidation in Pt and its adsorption on Pd has allowed the commercialization of different H_2 sensors [62]. Despite these diverse principles, significant difficulties persist, particularly for dissolved H_2 measurement in hydrogenotrophic bioprocesses. Many common H_2 sensors are unsuitable for anaerobic fermentation conditions, as they require O_2 for their detection mechanisms (e.g., catalytic combustion, thermal conductivity due to reliance on air as reference, and most metal oxide and work function sensors based on H_2 oxidation) [63]. Furthermore, cross-sensitivity to other gases (such as CO, CO_2, and H_2S) can lead to inaccurate readings or false alarms for many sensor types [63]. The complex chemical matrix of fermentation media, containing various nutrients and metabolites, intensifies interference challenges. Issues such as limited lifespan (e.g., 6 months for electrochemical sensing tips, see aquams.com/mesure-en-continu/mesure-h2-dissous), slow response times, susceptibility to poisoning, and mechanical degradation (cracking, blistering, and delamination of Pd films from

repeated H_2 exposure) further complicate the reliable, long-term, and accurate online measurement of dissolved H_2 [62], [63], [64].

I-4. Overcoming slow gas-to-liquid H_2 transfer

To improve the gas-to-liquid H_2 mass transfer during gas injection, various bioreactor designs and engineering strategies have been developed to reduce the liquid-side resistance to mass transfer between the injected bubbles and the bulk liquid.

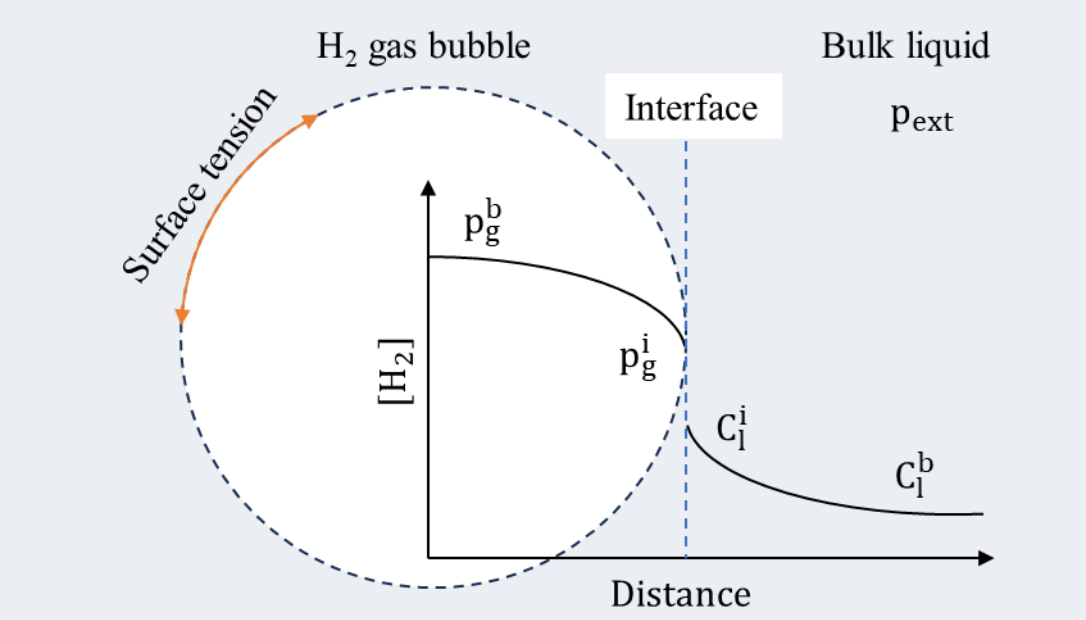

Fig. I.3. Gas concentration gradients during the dissolution of a gas bubble in a liquid medium. C_l^i and p_g^i are the gas concentration in the liquid interface side and the partial pressure at the gas interface side, and C_l^b and p_g^b are also the gas concentration and partial pressures but at their respective bulk phases; p_{ext} is the external pressure of the system.

The transfer across the gas-liquid interface (see Fig. I.3) depends on the concentration gradient of the gas between the bulk phases and their interfaces, and assuming the interface is at equilibrium, the flux of gas (N_A) can be calculated as shown in equation 5 [65]:

$$N_A = k_L\left(C_l^i - C_l^b\right) = k_g\left(p_g^b - p_g^i\right) \qquad 5$$

Where k_L and k_g are the local mass transfer coefficients in the liquid and gas phases, C_l^i and p_g^i are the gas concentration in the liquid interface side and the partial pressure at the gas

interface side, and C_l^b and p_g^b are also the gas concentration and partial pressures but at their respective bulk phases. As with other sparingly soluble gases in water, the gas-to-liquid mass transfer of H_2 is limited by the resistance at the liquid side [65], and due to the impracticability of measuring interfacial concentrations, the gas-to liquid flow rate is conveniently approximated by equation 6:

$$\frac{dC_{H_2}}{dt} = K_L a\left(C_{H_2}^{sat} - C_{H_2}\right) \quad 6$$

Where C_{H_2} is the dissolved H_2 concentration in the bulk, $\frac{dC_{H_2}}{dt}$ is the rate of H_2 solubilization, K_L is the overall liquid mass transfer coefficient, a is the gas-liquid interfacial area, and $C_{H_2}^{sat}$ is the dissolved H_2 concentration that would be at thermodynamic equilibrium with the gas phase concentration (H_2 partial pressure in the bubble). The thermodynamic equilibrium is usually described by Henry's law constant (H) and although is only ensured at the interface during mass transfer [66], it is also used for the overall approximation as shown in equation 7.

$$C_{H_2}^{*} = H \cdot p_g^b \quad 7$$

The different reactor designs and strategies target the increase of either $K_L a$ or $C_{H_2}^{*}$, and some of the most common approaches are described below.

I-4.1 Reactor designs for increased solubilization rate

I-4.1.1 Continuously stirred tank reactor (CSTR)

These reactors are commonly used at the laboratory scale due to their directly controlled mixing, and homogeneous distribution of gas substrates, temperature and pH, allowing for easy adjustment of defined reaction conditions [38]. The gas bubbles are injected and although they might have lower residence times that column reactors, the hydrodynamic shear generated by impellers in CSTRs breaks down larger bubbles into smaller ones, increasing the interfacial area available for mass transfer and, consequently, the $K_L a$ value [10]. For instance, increasing the impeller speed from 300 to 450 rpm in a synthesis-gas fermentation led to a substantial rise in $k_L a$ from 28 to 101 h^{-1} [10].However, for commercial-scale applications, the

high power-to-volume ratio required for sufficient mixing in large CSTRs makes them economically challenging, especially for low-value products like ethanol or acetic acid [44].

I-4.1.2 Bubble column

These reactors offer a more energy-efficient solution for industrial-scale gas fermentation, since mixing is achieved by the bubble dynamics and not mechanical agitation. Gas is injected at the bottom and due to the large height of the column, the residence time of the bubbles becomes larger than in CSTR. The high also aims to work with a hydrostatic pressure that aims to increase bubble pressure and minimize bubble size to maximize the gas-liquid contact area, relying on the upward flow of gas bubbles to create convection and reduce dead zones within the reactor [9]. Enhancements in bubble column design include optimizing gas diffusers, reactor geometry, and gas phase retention times. The K_La values of these reactors can range from 18 to 860 h^{-1} [67]. Industrially, bubble columns and gas-lift reactors are often preferred for hydrogenotrophic processes, as the hydrostatic pressure from the liquid column can enhance the partial pressures of gaseous substrates at the reactor's base, particularly with depths of 30 meters or more [11].

I-4.1.3 Trickle-Bed

These are packed-bed, gas-continuous reactors where the liquid phase trickles downward over a packing material [10]. These reactors are noted for their superior efficiency in addressing H_2 mass transport limitations compared to bubble columns, often requiring less energy, with reported K_La values from to 35 to 1025 h^{-1} [9]. These reactors utilize a packing material that provides a high internal surface area for the immobilization of microorganisms as a biofilm, which is specially favorable for achieving high biomass concentrations of the slow growing CO_2 fixating microorganisms [41]. Besides, the high surface area of the packing also facilitates intense contact between the solid, liquid, and gaseous phases, allowing for enhanced mass transfer. In this reactor configuration, while effective for low-energy processes, the low flow rates employed can generate concentration gradients, and establishing and maintaining stable biofilms for long-term industrial operation remains a challenge [67].

I-4.1.4 Hollow fiber membrane

These types of reactors employ a microporous hollow fiber membranes serve as gas distributors [67]. Gaseous substrates, such as H_2 and CO_2, are introduced into the lumen

(inside) of these tubular membranes, where gas molecules diffuse through the membrane to the liquid phase [9]. Compared with traditional gas spargers, the H_2 solubilization relies on a molecular diffusion principle rather than bubble dissolution, providing an extensive and well-controlled gas-liquid interface [6]. The membrane surface might also provide support for biofilm formation on the outer surface, favoring high biomass concentrations [9]. In contrast. K_La values can range from 0.4 to 1096 h^{-1} making them one of the best reactor designs for the solubilization of gases [67]. Unfortunately, the cost of membranes and biofouling remain as their biggest challenges to overcome for industrialization [9].

I-4.2 Gas pressurization for increased H_2 solubility

The reactor designs mentioned above focus on the maximization of the K_La. Nevertheless, a higher gas-to-liquid mass transfer can also be achieved by increasing $C_{H_2}^*$ by increasing the gas pressure. Traditionally, this is achieved by increasing the pressure of the whole system. When increasing the gas pressure at the headspace of the reactor, this pressure by Pascal's principle is transmitted to every point of the liquid as well, including the injected bubbles. In this case, the external pressure (p_{ext}) is equal to the internal pressure of the bubble (p_g^b), and the solubility of H_2 in the liquid phase increases proportionally. A more recent approach to increase the internal bubble of the pressure is by taking advantage of the additional forces introduced due to the surface tension of the liquid molecules in large curvatures of small bubbles [68]. This additional pressure is referred to as Laplace pressure and its contribution (right term of equation 8) to the internal pressure of the bubble can be expressed as shown in equation 8.

$$p_g^b = p_{ext} + \frac{2\gamma}{r} \qquad 8$$

Where γ is the surface tension, p_{ext} is the external pressure of the system and r is the radius of curvature of the bubble. For comparison, by using the surface tension of the water as γ = 0.072 $N \cdot m^{-1}$, the radius of the bubble would have to be of around 70 µm to reach an added pressure of 0.01 bar. In most industrial settings, the injected bubbles are of millimetric size, and the contribution of the Laplace pressure can be effectively ignored. Nevertheless, the injection of micro/nanobubble has proven to be advantageous for the solubilization of gases due to their higher internal pressure (~7 bar at 200 nm of radii [69]), increased surface area

per volume of gas, negligible buoyancy (longer residence time [70]) and coalescing resistance (by electrostatic force due to high zeta potential [71]).

The potential of these micro/nanobubbles for rapid dissolution in a liquid solution was also theoretically demonstrated by Epstein and Plesset in 1950 by the addition of the Laplace pressure as a dissolving force together with the concentration gradient in the gas diffusion of an isolated bubble in a liquid medium [72]. The Epstein-Plesset model could accurately predict the dissolution of static and isolated H_2 bubbles in a liquid medium by solving the equation

$$\frac{dr}{dt} = -D_{H_2} d \frac{1 - f + \frac{\tau}{r\rho_\infty}}{1 + \frac{2\tau}{3r\rho_\infty}} \left(\frac{1}{r} + \frac{1}{\left(\pi D_{H_2} t\right)^{0.5}} \right) \quad (9)$$

$$d = \frac{HRT}{M_w}; \; f = \frac{C_{H_2}}{C_{H_2}^{sat}}; \; \rho_\infty = \frac{p_{ext} M_w}{RT}; \; \tau = \frac{2\, M_w \gamma}{RT}$$

Where D_{H_2} is the H_2 diffusion coefficient in water (5.11×10^{-9} $m^2 \cdot s^{-1}$) , M_w is the molecular weight of H_2 (0.002 $kg \cdot mol^{-1}$), $C_{H_2}^{sat}$ is the dissolved H_2 concentration at the saturation point given by Henry's law (1.56×10^{-8} $kg \cdot m^{-3} \cdot Pa^{-1}$ at 25 C), γ is the surface tension of the liquid (0.072 $N \cdot m^{-1}$), d is the ratio of the saturated dissolved H_2 concentration to the H_2 gas density, f is the supersaturation ratio and ρ_∞ is the H_2 gas density under the same conditions of pressure and temperature with a gas-liquid interface of zero curvature ($kg \cdot m^{-3}$).

The Epstein-Plesset solution (see Fig. I.4) has been widely accepted for predicting the dissolution time of bubbles down to micrometric scale [73], which is already smaller than the millimetric bubble sizes usually generated at industrial scales [74]. The Epstein-Plesset solution plotted in Fig. I.4 also provides an interpretation on the dissolution conditions. For every supersaturation concentration, there is a critical bubble radius above which a bubble will not dissolve and grow instead. Another way of thinking into this limit case is that a bubble of a specific size will only dissolve if the supersaturation concentration around the bubble is lower than a critical supersaturation threshold. Unfortunately, the Epstein-Plesset solution fails to predict the lifetime of bubble sizes in the nanoscale, and this mismatch is what has been denominated as the Laplace Pressure Bubble Catastrophe [68]. For nanobubbles, while the theory predicts dissolution times in the millisecond range, experimental evidence shows that in the bulk liquid could last hours or even days when pinned to a surface [75], [76].

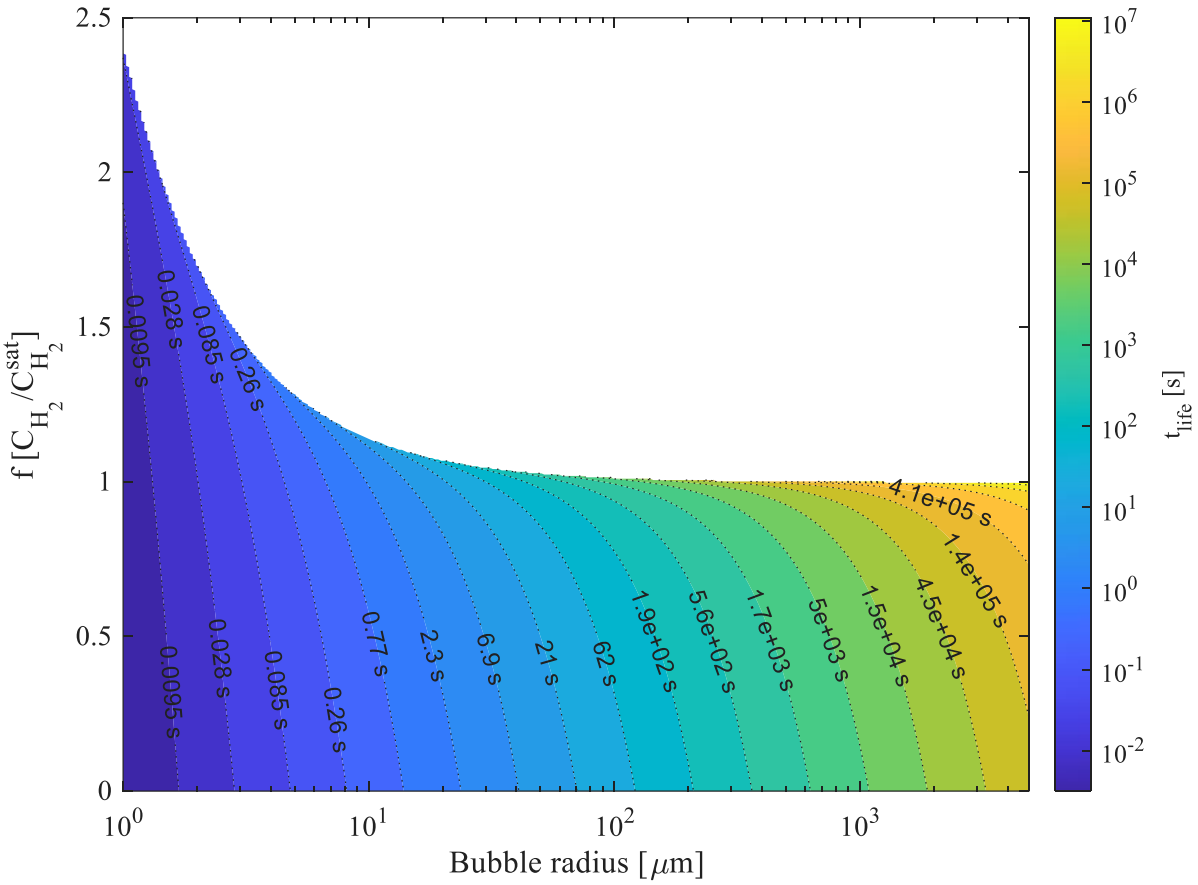

Fig. I.4. Dissolution time (t_{life}, colored area) of different H_2 bubble radius (x-axis) at different bulk supersaturation levels (f, y-axis) as predicted by the Epstein-Plesset theory [72]. The theory predicts that supersaturation of liquid solutions can only be achieved when micro/nanobubbles are injected, and their dissolution time accurately on bubbles of a few micrometers or larger [73]. Above the colored area, bubbles do not dissolve and should grow instead. Solved for H_2 at 25 C and p_{ext} = 101325 Pa.

Although there is no consensus on the mechanisms responsible for the long life of bulk nanobubbles (e.g., adsorption of contaminants and organic molecules, surface charge [77], [78]) and sometimes their existence is also debated, there is already an implementation of $H_2/CO_2/O_2$ micro/nanobubble injection for the supersaturation and metastabilization of aqueous solutions for the oxygenation in wastewater treatment, hydroponics, hypoxic tissues; CO_2 absorption for recycled cement paste, plant growth, carbon sequestration; and H_2 enrichment of gasoline and growth medium of hydrogenotrophs for CO_2 fixation [16], [79], [80], [81], [82], [83], [84], [85], [86], [87], [88], [89].

I-5. Bypassing gas-to-liquid H_2 transfer: Electrochemical cells as a H_2 supply alternative

Electrochemical cells where cathode surfaces serve as the electron donor for the direct/indirect reduction of CO_2 by hydrogenotrophs has been also proposed recently. Before expanding on the mechanisms of electron transfer between cathodes and hydrogenotrophs, some basic electrochemical principles are described first in the following section.

I-5.1 Electrochemical Principles of Water Electroreduction

The electrochemical production of H_2, predominantly through water electroreduction, is a keystone of emerging sustainable energy infrastructures. Although the vast majority of research focuses on the production of gaseous H_2 and not dissolved H_2, the thermodynamics and kinetics of the redox reactions are still applicable, as well as their derived inefficiencies.

Water electroreduction occurs in electrochemical cells made of two electrodes separated by an by an electrolyte that facilitates charge transport [90]. At the anode, water oxidation occurs, leading to the oxygen evolution reaction (OER). In parallel, at the cathode, water reduction takes place, driving the hydrogen evolution reaction (HER), which produces hydrogen gas. To ensure the efficient separation of the generated hydrogen and oxygen and to prevent their recombination, these reactions are typically confined to two distinct compartments, an anode chamber and a cathode chamber, separated by a membrane or separator, which is fundamental on allowing ion selective transport (e.g., protons or hydroxide ions) between the electrodes, maintaining charge neutrality while physically separating the gaseous products [91]. In near neutral pH[1] buffered solutions, the OER and HER can be represented by equations 10-11 as shown in Table I.4 [92]:

Table I.4. OER and HER stoichiometries at near neutral pH conditions. Standard potentials are shown against the standard hydrogen electrode (SHE).

$2OH^- \rightarrow (1/2)O_2 + H_2O + 2e^-$ (OER)	$E^0 = -0.40\ V\ (\Delta G_r^0 = 77.2\ kJ)$	10
$2H_2O + 2e^- \rightarrow H_2 + 2OH^-$ (HER)	$E^0 = -0.83\ V\ (\Delta G_r^0 = 160.2\ kJ)$	11

E^0 represents the standard potential (vs standard hydrogen electrode, SHE) of the half reaction, and is a measure of the thermodynamic potential, related to the Gibbs free energy

by

$\Delta G_r^0 = -n\,F\,E^0$; where n is the number of electrons involved in the half redox reaction (n = 2) and F is the Faraday constant (96485 C·mol-e^{-1}). A depiction of a traditional water electroreduction cell is depicted in Fig. I.5.

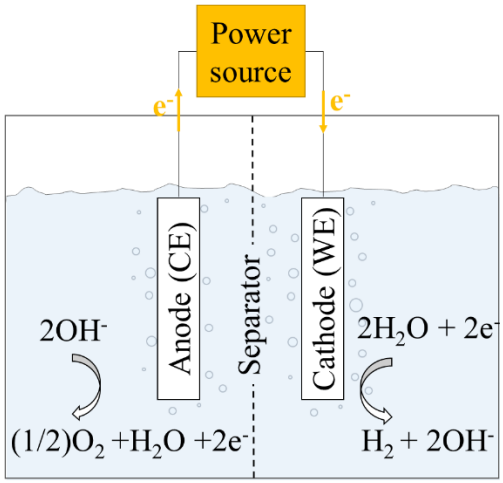

Fig. I.5. Schematic diagram of a typical water electroreduction cell. The cell consists of a power source driving the HER and OER reactions on the cathode (working electrode, WE) and anode (counter electrode, CE) surfaces. An ion exchange membrane (Separator) separates both half-reaction chambers, by allowing selectively allowing the passage of ions, in this case, represented by OH^-.

This thermodynamic potential is the electromotive force for the reaction, and in non-standard conditions, it can be expressed by Nernst equation (12), which gives the equilibrium potential at the electrode interface for reversible half-reactions at net zero current [90]:

$$E = E^0 + \left(\frac{R\,T}{n\,F}\right) \ln\left(\frac{\prod(C_O)^{v_j}}{\prod(C_R)^{v_j}}\right) \qquad 12$$

Where $(C_O)^{v_j}, (C_R)^{v_j}$ are the concentration (an approximation of their activities) of oxidized and reduced species raised to their corresponding stoichiometric coefficients. For water electroreduction, the cell potential is calculated by subtracting the cathode from the anode potential (written in reductive form), giving a cell voltage of -1.23 V. The electrode potential should be an indicative of the energy necessary to start the reaction in the production of H_2 and O_2 since they are calculated at equilibrium (zero current). Nevertheless, at a non-zero

current, the electrodes must overcome energy losses in the form of excess potential from the Nernst potential. The extra potential required to drive each redox reaction at a specific current value is called overpotential (η_C and η_A for the cathode and anode respectively), which sums the activation overpotential due to the electron transfer at each electrode surface and concentration losses due to slow reactant/product fluxes to/from the electrode surface. The total cell voltage is therefore the voltage at equilibrium with the added contributions of each electrode overpotentials and the ohmic losses ($I \cdot R_{cell}$) measured by the cell resistance, R_{cell}. These overpotentials are depicted in Fig. I.6.

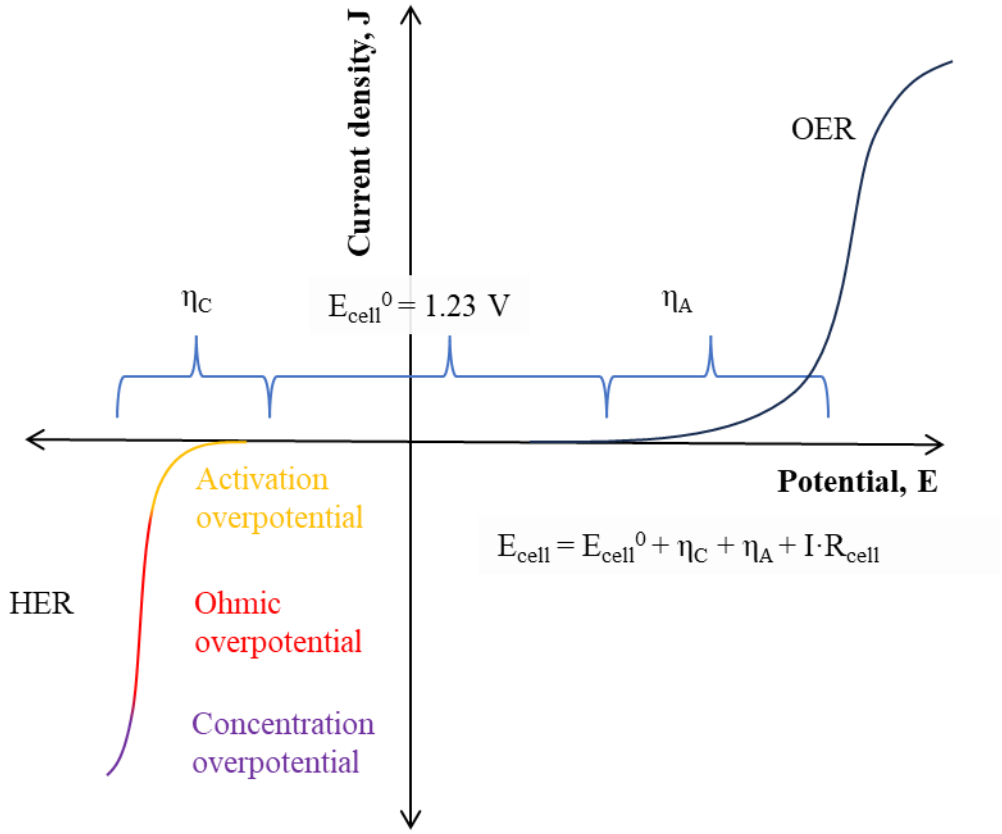

Fig. I.6. Depiction of the current-potential relationship of the HER and OER during water electrolysis and the involved potential losses (overpotentials).

The activation overpotential is defined as the deviation of the electrode potential from the equilibrium value arising from the inherent slowness of the charge exchange reaction at the interface [91], [93]. It is attributed to overcoming the intrinsic activation barriers present at both the anode and cathode during HER and OER. As the OER is a complex four-electron-proton-coupled reaction, it makes its kinetics inherently sluggish and requires significantly higher activation overpotential compared to the two-electron transfer HER [91]. The

concentration overpotential is the shift in electrode potential caused by the difference between the concentrations of reacting species at the electrode-solution interface and their concentrations in the bulk solution. This difference arises from the finite rate of mass transport, which leads to the formation and buildup of a diffusion layer near the electrode surface [93]. Ohmic overpotential, also known as the ohmic drop, represents the total voltage losses within the electrochemical cell due to parasitic resistances. These losses result from the inherent electrical resistance of the cell components, including the ionic conductivities of the electrolyte and separator, as well as the electric conductivity of current collector and electrodes [91].

The existence of these overpotentials also causes current distribution heterogeneities across the electrode surface [93]. A primary current distribution assumes the absence of both concentration and activation overpotential, and only the ohmic overpotential due to geometric factors on the current path resistance is considered. A secondary current distribution considers the activation overpotential, where the effective potential in the hyperpolarized areas due to geometric factors get reduced. Lastly, a tertiary current distribution also accounts for the concentration overpotential on top of the beforementioned overpotentials, making it the most complete and complex to simulate.

The extent of the second current distribution homogeneity in porous electrodes is usually predicted by the Wagner adimensional number (Wa'), and it takes the form of equation [93]

$$\mathrm{Wa'} = \frac{(\mathrm{d\eta/dJ})\kappa_\mathrm{l}^{*}\kappa_\mathrm{m}^{*}}{\mathrm{b}(\kappa_\mathrm{l}^{*} + \kappa_\mathrm{m}^{*})} \qquad 13$$

Where $d\eta/dJ$ is the polarization resistance (the change of the overpotential with the change of current density), b is the characteristic length of the porous electrode (e.g., electrode thickness) and κ_l^* and κ_m^* are the effective electrolyte and porous solid matrix conductivities (porosity/tortuosity corrected. Higher $\mathrm{Wa'}$ are desired to obtain more homogeneous current distributions, which result in lower local current densities where bubbles can nucleate more easily. In this sense, increasing the electric and ionic conductivities of the porous electrode and electrolyte and reducing the characteristic length of the electrode contribute to higher values of $\mathrm{Wa'}$. Additionally, it might seem surprising that larger values of $\left(\frac{d\eta}{dJ}\right)$, obtained by using poorer electrocatalytic materials (slow charge transfer), are desired to obtain more homogeneous distributions. This later principle used in electroplating is also referred to as

leveling, where *brighteners* are added into the electrolyte that preferentially adsorb at crests of the electrode (where highly localized current density might exist) and increase the local activation overpotential [93]. This is done with the purpose of achieving a more homogeneous electrodeposition over the electrode surface.

The formation of bubbles at the electrodes also contributes to energy losses included in the beforementioned overpotentials. Firstly, the continuous generation of gas at the electrode surface leads to the supersaturation of the liquid electrolyte with dissolved gas, necessitating an additional voltage to maintain these high gas concentrations [94]. This energy penalty is part of the concentration overpotential. Secondly, as bubbles nucleate and grow, they form a 'bubble curtain' that masks the catalytic surface of the electrode, physically blocking active sites [95]. This reduction in effective surface area results in an energy loss that is typically considered a component of the activation overpotential. Additionally, the inherent free energy cost of bubble nucleation and growth itself requires extra energy input, further contributing to what is often described as the catalytic overpotential also part of the activation overpotential [94], [96]. Lastly, the presence of these non-conducting gas bubbles in the inter-electrode gap decreases the effective ionic conductivity of the electrolyte, impeding ion movement and causing a voltage drop. This increased electrical resistance is a direct contributor to the ohmic overpotential [94]. Notice that in the production of dissolved H_2, the local supersaturation is to be minimized as well as bubble formation, and these bubble overpotentials become less relevant.

So far, the description of the electrochemical principles governing water electroreduction have been described according to their thermodynamics but from the depiction in Fig. I.6, it can be seen that there is a non-linear relationship between the current density and the working overpotential. The electron-transfer kinetics that describe the relationship between the current density (J) and the overpotential (η) at an electrode-electrolyte interface can be described by the Butler-Volmer equation (14) [90]:

$$J = J_0 \left[\left(\frac{C_O(0,t)}{C_O^{bulk}} \right) e^{-\frac{\alpha \eta F}{RT}} - \left(\frac{C_R(0,t)}{C_R^{bulk}} \right) e^{-\frac{(1-\alpha)\eta F}{RT}} \right] \quad (14)$$

The left term in the brackets represents the forward (reduction) reaction while the right term in the brackets represents the reverse (oxidation) reaction (e.g., H_2 oxidation and reduction), J_0 is the exchange current density, or the current density value when both the forward and reverse reaction rates are at equilibrium (when the net current is zero); $C_O(0,t)$, $C_R(0,t)$, C_O^{bulk} and C_R^{bulk} are the concentrations of the oxidized and reduced species (e.g., H_2O and H_2) at the surface of the electrode and at the bulk electrolyte, α is the charge transfer coefficient. At large values of η, for example, at negative overpotentials for HER, and well mixed solutions, the current-overpotential adopts a Tafel behavior as shown in equation 15:

$$J = J_0\left[e^{-\alpha f \eta}\right] \qquad 15$$

Or in a linearized form as shown in equation 16:

$$\eta = \frac{RT}{\alpha F}\ln(J_0) - \frac{RT}{\alpha F}\ln(J) \qquad 16$$

Which becomes useful for calculating kinetic parameters such as j_0 from experimental values of η and J. The exchange current density, J_0, also becomes a useful descriptor of the electrocatalytic activity of an electrode material. Larger values of j_0 translate into low activation overpotentials. For example, for HER, noble metals (e.g., Pt, Ir, Rh) are great catalysts with the highest exchange current density, followed by iron and coinage metals (e.g., Ni, Fe, Cu), sp-metals (e.g., Ag, Pb, Zn) and early transition metals (e.g., Ti, Mo, Ta) as it is depicted in Fig. I.7 [97].

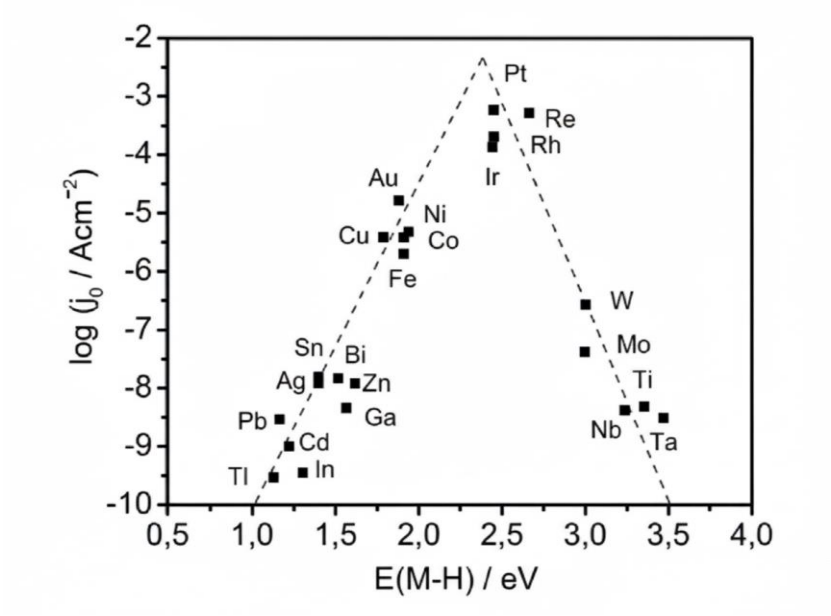

Fig. I.7. Exchange current density as a function of the metal-hydrogen bond strength, E(M-H), for different metals. Taken from Zeradjanin *et al.*, 2016. [97].

In the plot, the goodness of the HER electrocatalytic activity is shown to depend on the H-binding strength, where a balanced bond strength means a balanced between adsorption and desorption steps. In this regard, carbon materials due to their low electrocatalytic activity, are usually doped with heteroatoms to be used for HER [91]. Although this work focuses on the use of H_2 produced by water electroreduction, a saturated O_2 solution is also produced in the anodic chamber, which could equally be useful to aerobic processes. In a water electroreduction cell designed for O_2 gas to quickly nucleate and escape the system, this high-purity O_2 gas source could also be used as a supplement/replacement of O_2 source in the cement/steel making process, increasing the purity of the outlet CO_2 stream that is to be used in the hydrogenotrophic bioprocess [98].

I-5.2 Microbial electrosynthesis systems

While the H_2 gas from a traditional water electroreduction can be compressed and injected in a hydrogenotrophic bioreactor in one of the reactors designs previously described, it is also possible to include CO_2-reducing microorganisms directly in the cathodic chamber of the water electroreduction cell. These types of designs are usually referred to as microbial electrosynthesis systems (MES). Nevertheless, their initial interest came after the discovery of electrogenic microorganisms back in 1911, when M.C. Potter demonstrated that microorganisms could generate a voltage and deliver current [99]. These discovery prompted the demonstration of new devices called microbial fuel cells (MFC) in 1999 by Kim *et al*, where electroactive biofilms were used in the anode to generate a small current [100]. Later on, in 2004, it was discovered that electroactive biofilms could also act as electron acceptors [101], with concept of MES first proposed by Nevin *et al.* in 2010, focusing on the electricity-driven reduction of CO_2 to organic compounds [102].

Extracellular electron transfer (EET) from the cathode to these electrotrophic microorganisms in MES systems can occur through two primary mechanisms: direct and indirect electron transfer. Direct Electron Transfer (DET) involves physical contact between the microbial cells and the cathode, often facilitated by outer-membrane cytochromes or conductive nanowires

(pili) [103]. Indirect electron transfer (IET), also known as mediated electron transfer, relies on soluble electron shuttles or mediators, such as electrochemically produced H_2 or formate, or naturally secreted flavins or phenazines, to carry electrons between the cathode and the cells. A schematic representation of both EET mechanisms is shown in Fig. I.8 [104].

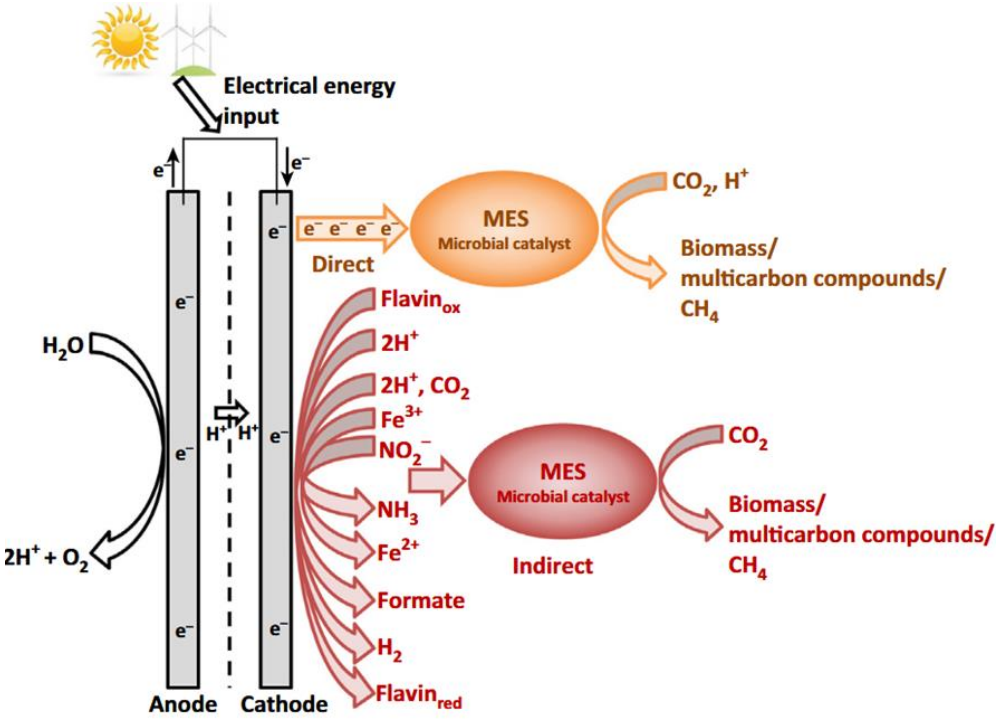

Fig. I.8. Schematic representation of the direct and indirect electron transfer (DET and IET) in Microbial electrosynthesis systems (MES). Taken from Tremblay *el al.,* 2016 [104].

The contribution of DET vs IET in the production of multicarbon products by microbial electrosynthesis remains a subject of discussion. The hypothesis of DET is frequently supported by the detection of multicarbon compounds at high cathodic overpotentials that are thermodynamically unfavorable for abiotic hydrogen evolution [105]. However, recent studies suggest that released enzymes, such as hydrogenases, can adsorb to the cathode surface and decrease the overpotential required for hydrogen evolution, where due to the resulting low H_2 production rate at the cathode, the biotic H_2 uptake could be fast enough to rapidly consume it in the biofilm, preventing its accumulation to detectable levels in the bulk electrolyte [106].

I-5.2.1 Indirect electron transfer (IET)

In IET, redox mediators are used as electron shuttles. These are molecules that can be reduced/oxidized multiple times without being consumed by microorganisms and thus remain in the liquid medium. In the case of electroactive microorganisms growing in an electrode, these mediators can get oxidized/reduced by diffusing between the electrode surface and the microorganisms inside and/or outside a biofilm.

These mediators can be either externally added (exogenous) or produced by microorganisms as metabolites (endogenous)[107]. Thionin, AQDS, neutral red, methyl viologen and ferricyanide have been reported as exogenous electron mediators [100]. The use of these "artificial" mediators might bring other problems of stability/toxicity as well as new opportunities for using different metabolic routes. For example, with the purpose of reducing acetate to longer-chain molecules, the use of methyl viologen as mediator shifted the production of butyrate/methane to ethanol in a bioelectrochemical system fed with acetate [108]. Similarly, "natural" mediators such as humic acids and cysteine were found in aquatic sediments and soils where they can also play a role in the EET of Fe(III) reduction [107].

Endogenous mediators such as flavins, phenazines, quinones and melanin have been found to mediate EET even between electron acceptors and strains that do not produce them [107]. This non-specificity expands the applicability of bioelectrochemical systems with mixed communities. Although these endogenous mediators might be naturally produced to reduce insoluble metals present in the environment, they can also be used to reduce electrode surfaces as discovered by Marsili *et al,* where *Shewanella sp.* (the most studied species regarding redox mediated EET) produced flavins that adsorbed in the anode and allowed the recovery of energy as current [109]. The study of EET using anodes as electron acceptors is more abundant than using cathodes as electron donors. Nevertheless, redox mediators such as flavins and quinones also have the capacity to be involved in electron exchange with anodic and cathodic surfaces [110], [111].

I-5.2.2 Direct electron transfer (DET)

Different from redox mediators that need to diffuse between the electron source and sink, some electroactive microorganisms can perform electronic conduction of electrons with electrodes, minerals and other microbial species. As direct contact must be established, these

species can form a biofilm when the electron source is a cathode. It has been proposed that the electron transport from the cell to outer electron acceptors occurs through c-type cytochromes (from inner to outer cell) or by nanowires, being the latter more commonly accepted to be involved in long-distance EET [112]. This was further supported by establishing the dependance of the conductivity of a *Geobacter sulfurreducens* biofilm on temperature changes. At temperatures over 0 °C, biofilms presented metallic-like conductivity, while at lower temperatures, they presented an electron-hopping behavior where the conductivity of an EET by only c-type cytochromes should be independent of temperature changes [113].

As in the case of redox mediators, most of the studies focus on anodic biofilms, and cathodic biofilms might present different EET transfer mechanisms [101]. Moreover, the mechanism involved can also depend on the biofilm population. For example, pure *Geobacter* biofilms are thinner when grown in a cathode compared to an anode, and when using a strain incapable of uptake H_2 as electron donor, they have been able to reduce fumarate to succinate at potentials high enough to prevent H_2 formation [101].

I-6. An unexplored approach: Favoring the production of dissolved H_2 for H_2-mediated electron transfer

I-6.1 Evidence of H_2-mediated electron transfer as the preferred mechanism for acetogenesis

It has been shown that in MES, extracellular enzymes as hydrogenases contribute to the reduction of the activation overpotential required for HER [114], with comparatively similar electrocatalytic activity per active site to Pt [115]. Nevertheless, several challenges associated with biofilm-driven mechanisms still limit their implementation compared with the hydrogenotrophic bioprocesses where H_2 gas is injected. The limited mass transfer due to the dense extracellular polymeric matrix, the biofilm stability over time and the low active biomass attainable are often recognized as main bottlenecks to overcome the reported low current densities of these systems [18], [89], [116], [117].

It has been suggested that a MES for CO_2 reduction with mixed cultures may work preferably with indirect electron transfer, where H_2 is still produced but quickly consumed by the biofilm.

LaBelle *et al* found that acetate yield in MES was enhanced with increasing H_2 production [118]. They also found an overexpression of genes that participate in the hydrogen evolution reaction (HER) and uptake, supporting the hypothesis of the use of H_2 as a mediator in mixed cultures. Blanchet *et al* tested a MES at two different cathodic potentials at neutral pH :-0.36 V and -0.66V vs SHE, but only at the more negative potential, acetate was detected in the medium [119]. They attributed these results since only at cathodic potentials lower than -0.41 V vs SHE H_2 could be theoretically produced, supporting again the importance of H_2 as a mediator in MES.

In these cases where the EET mechanism is H_2-mediated, a biofilm forming at the cathode surface will compete with the HER which can be undesired. It has been demonstrated that H_2 evolution may be enhanced due to metabolites, cellular debris and metals accumulating in the cathode surface [118], but impurities can also act as preferred nucleation sites due to their hydrophobic nature [74], [120]. Even in the presence of electrotrophs performing direct electron transfer in the cathode, the biomass performing CO_2 reduction is more abundant (and therefore more desirable) in the liquid medium (planktonic state) vs in the biofilm, which could explain the higher acetate yields in MES with H_2 evolution. The slow kinetics of biofilm electron uptake vs H_2-mediated electron uptake are also discussed elsewhere in favor of using planktonic microorganisms for CO_2 reduction in a MES [16].

I-6.2 Bubble-less vs micro/nanobubbles production via water electroreduction

As has been discussed so far, optimizing the efficient delivery of H_2 might be critical for increasing the low current densities achieved in H_2-mediated MES. When operating a H_2-driven electron transfer approach, the production of micro/nanobubbles is usually pursued due to their significantly increased interfacial area between the gas and liquid phases, and their smaller size that leads to longer retention times within the liquid medium, and faster H_2 solubilization rates due to their high internal pressure [16], [89]. However, others have proposed that the electrolytic production of H_2 in H_2-driven MES should disfavor the production of bubbles and instead, focus on reactor designs that avoid bubble nucleation [42]. Not surprisingly, the principles for micro/nanobubble production differ from the dissolution of H_2 without bubble nucleation . While both H_2 delivery modes require good mixing to maintain

a thin diffusion layer around the cathode surface, high local current densities are desired for micro/nanobubble nucleation, while low local current densities for the bubble-less H_2 solubilization as explained next. For the production of micro/nanobubbles, Kikuchi *et al*. proved that increasing the current density up to a current density threshold (3 $A \cdot m^{-2}$, bounded to their characteristic local mixing at the electrode surface) allowed to produce smaller bubbles of nanometric size [121], due to the high local supersaturation maintained at the electrode surface. Above this current density threshold, the H_2 supply becomes too large compared with its diffusion away to the bulk liquid through the diffusion layer and bubbles unstably grow. Following the same principle, electrolytic nanobubbles are also cleverly obtained during pulse electrolysis, where pulses with large amplitude allow high instantaneous current densities that achieve high local supersaturation, while the short duration of the pulses allows to maintain thin diffusion layers that prevent bubble growth [122], [123], [124]. In this sense, electrodes of micrometer size (small surface area) are preferred not only to achieve large current densities, but also due to their fast mass transport between the electrode surface and bulk liquid which results in thin diffusion layers [90], [125].

On the other hand, Kracke *et al.* investigated the H_2 solubilization under the principle of avoiding bubble nucleation, by utilizing 3D-printed cathodes or large specific surface area per unit of volume [42]. They also identified a critical current density (around 13 $A \cdot m^{-2}$ in their specific NiMo cathode system with *M. maripaludis*) beyond which performance declined. This decline was attributed to a combination of increased H_2 loss through bubble formation and decreased biocompatibility due to localized high pH conditions at the cathode surface, emphasizing the need to operate near this critical density for maximum production rates.

Both the production of micro/nanobubbles and the production of dissolved H_2 through bubble-free water electroreduction must have a preferred operational range that might overlap. For example, during the solubilization of H_2 on a H_2 depleted medium, working with the production of micro/nanobubbles might be initially more favorable due to their low buoyancy and fast dissolution at high current densities. On the other hand, as the medium gets saturated with H_2, the solubilization rate (and efficiency) of microbubbles might quickly decline, making the bubble-free operation more favorable. The specific operation ranges where one might be more favorable than the other should also depend on the specific

solubilization characteristics of each system (e.g., how small can bubbles be generated, how high the imposed current can be before bubble nucleation).

I-6.3 Avoiding bubble nucleation: theoretical insights from the Classical Nucleation Theory (CNT)

The nucleation of H_2 gas bubbles from a supersaturated liquid phase is fundamentally an energy-driven process, requiring an initial energy barrier to be overcome for a stable new phase to emerge. This process is well-described by classical nucleation theory (CNT), which provides a framework for understanding the energetics of bubble formation [126]. The formation of a bubble nucleus in a solution involves the competition between the energy cost for creating a new gas-liquid interface (ΔG_{surf}) against the energy gained from the liberation of dissolved gas molecules from the supersaturated liquid into the bubble (ΔG_{bulk}), where the total free energy of formation (ΔG_{tot}) is expressed as shown in equation 17 [127]:

$$\Delta G_{tot} = \Delta G_{surf} - \Delta G_{bulk} \qquad 17$$

$$\Delta G_{tot} = 4\pi\gamma r^2 + \frac{4}{3}\pi\Delta G_v\, r^3$$

Where γ is the surface tension of the liquid, r is the nanobubble radius and ΔG_v is the difference in energy per unit of volume between the dissolved and gaseous state. The contribution of each term into the total free energy of bubble formation (ΔG_{tot}) is shown in Fig. I.9.

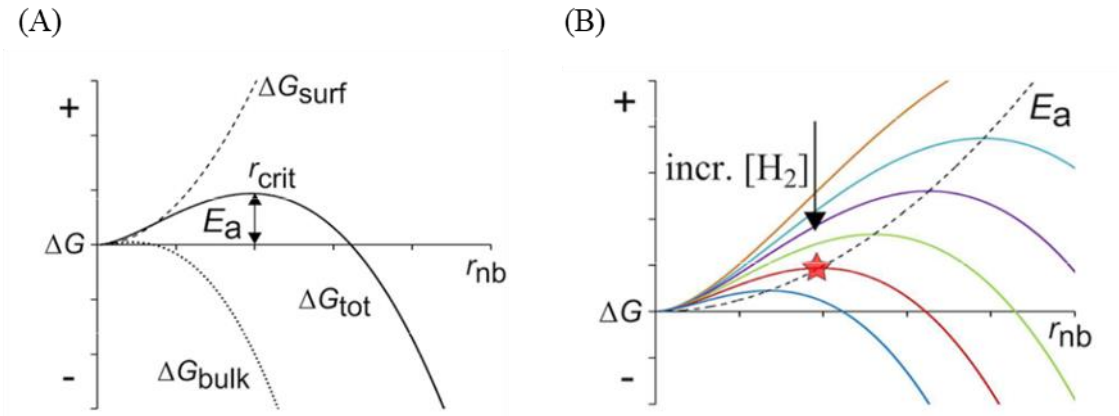

Fig. I.9. Free energy of formation of a gas bubble. (A) Contribution of ΔG_{surf} and ΔG_{bulk} to ΔG_{tot} and (B) decrease in the activation energy (E_a) and critical bubble radius for bubble

formation related to the increase in supersaturation concentration [H_2]. Taken from German *et al.* , 2016 [127].

The activation energy E_a is better known as ΔG^*, and its the energy barrier to the formation of a critical bubble size. ΔG^*depends on the surface tension of the liquid (γ), the supersaturation ratio $\left(\sigma = \frac{C_{H_2}}{C_{H_2}^{sat}} - 1 = f - 1\right)$ and $\phi(\Theta)$ which is a function of the contact angle of the bubble in the nucleation site. From the classical nucleation theory, the heterogeneous bubble nucleation rate ($NR[m^{-3}s^{-1}]$) can be expressed as a function of this nucleation barrier as shown in equation 18 [120]:

$$NR = C \exp\left(\frac{-\Delta G^*}{kT}\right) \qquad 18$$

$$NR = C \exp\left(\frac{-16\pi(\Upsilon_0 + \sigma b)^3 \phi(\Theta)}{3kT(\sigma\, p^{ext})^2}\right)$$

$$\phi(\Theta) = \frac{1}{4}(1 + \cos\Theta)^2(2 - \cos\Theta)$$

Where, C is a pre-exponential kinetic nucleation factor that describes the statistical formation of a critical nucleus, k is the Boltzmann constant (1.380649×10^{-23} [m^2 kg s^{-2} K^{-1}]), Υ_0 [$N \cdot m^{-1}$]is the surface tension (non-corrected), b [$N \cdot m^{-1} \cdot Pa^{-1}$] is a correction parameter for accounting the surface tension effect of the gas, $\phi(\Theta)$ is a wetness function of the contact angle and T [K] is the temperature of the system. In this context, the interfacial tension, the cathode wettability and the local saturation are parameters that play a significant role in the nucleation of bubbles and therefore fundamental for optimizing the beforementioned H_2 solubilization. The use of this equation nevertheless is somewhat problematic: the nucleation rate becomes extremely sensitive to the input parameters in the exponential term (e.g., contact angle, supersaturation, surface tension) [126], [128]. Moreover, although the theory predicts that the nucleation onset occurs when the supersaturation is in the thousands (see Fig. I.10), it has been experimentally found that the supersaturation ratio drops to around 300 in microelectrodes and 8 in a platinum electrode [128], [129].

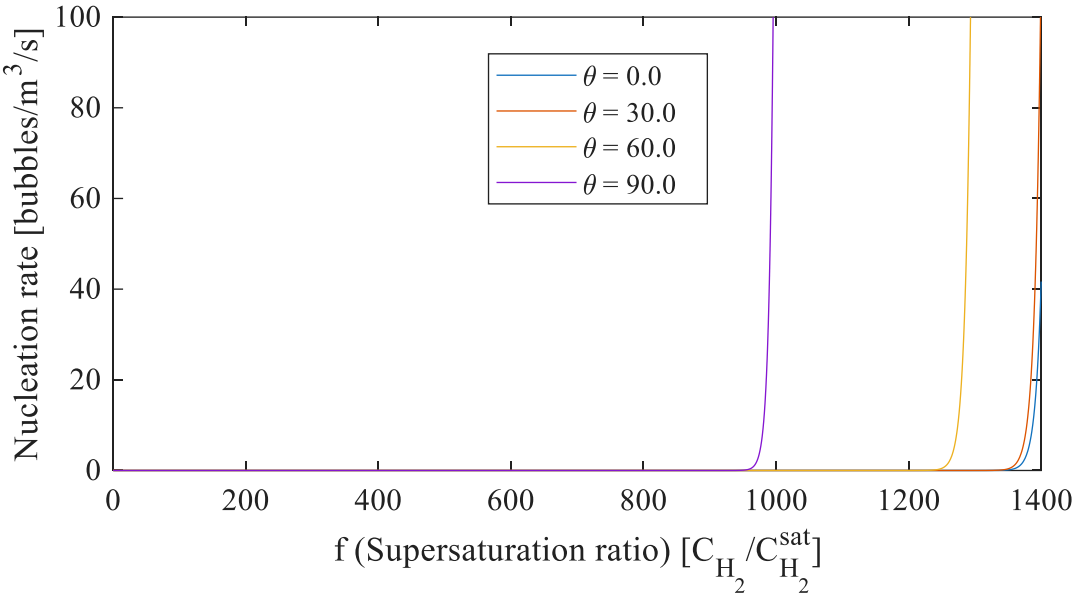

Fig. I.10. Classical nucleation theory solution on the heterogeneous nucleation rate of H_2 bubbles with different supersaturation and contact angle values. The following parameters were used: Υ_0 = 0.072 N·m^{-1}, b = -2.47×10^{-10} N·m^{-1}·Pa^{-1}, C = 1×10^{35} m^{-3}·s^{-1} and p^{ext} = 101325 Pa. When using a value of Υ_0 = 0.05 N·m^{-1} and a θ of 90°, the nucleation onset would be predicted at a supersaturation of 400.

Besides the mismatch between the supersaturation needed for nucleation in experimental settings vs the predicted by theory, there are also discrepancies in the dissolution kinetics of surface nanobubbles similar to the ones discussed for bulk nanobubbles with the Laplace catastrophe (although with solid evidence of the existence of surface nanobubbles) [69], [127], [130]. The mechanisms for the experimental slow dissolution observed in surface nanobubbles has been aborded from different mathematical models by expanding the Epstein-Plesset theory (e.g., pinning-oversaturation, traffic jam, dynamic equilibrium model)[77]. Moreover, further expanding the pinning mechanism, Lohse and Zhang developed a diffusion controlled model applicable to macroelectrodes that predicts when pinned electrolytic bubbles change from a stable pinning contact angle to an unstable growth at a threshold current density [131]. The solution to this model is shown in equation 19:

$$J = \frac{4D_{H_2}C^{sat}_{H_2}\Upsilon_0 \sin(\theta_{eq})}{LHp^{ext}}\left[1 - \frac{L(1-\cos(\theta_{eq}))}{4H\sin(\theta_{eq})}\right]^{-1} \qquad 19$$

Where θ_{eq} is the stable bubble contact angle at the electrode surface, L is the pinning length and H is the height of the cell where the concentration varies linearly from the electrode surface to the equilibrium concentration at p^{ext}. The solution of this equation is shown in Fig. I.11.

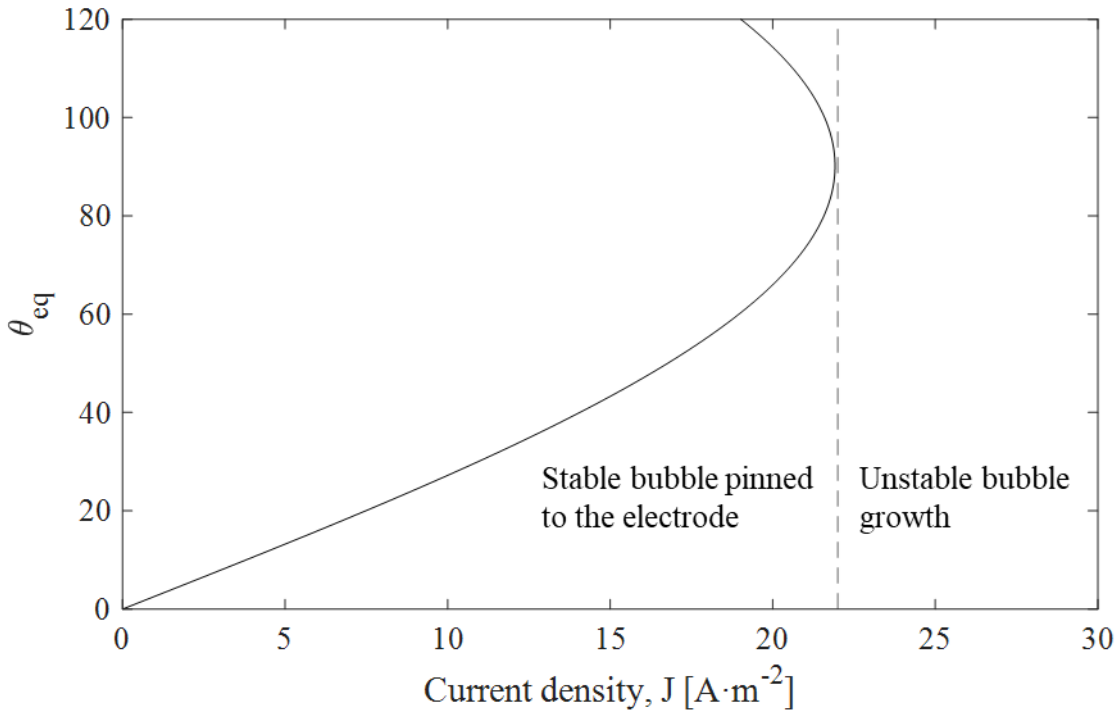

Fig. I.11. Equilibrium contact angle of a pinned electrolytic H_2 bubble to the cathode surface obtained from the Lohse-Zhang diffusion model [131]. The model was solved for H = 100 µm, L = 1 µm, p^{ext} = 101325 Pa, Υ_0 = 0.072 N·m^{-1}, $C_{H_2}^{sat}$ = 0.78 mmol·L^{-1}, D_{H_2} = 5.11 ×10^{-9} m^2·s^{-1}.

Although the validation and consolidation of the theoretical background for surface nanobubbles still needs further research, the theoretical models and experimental evidence suggests that for the electrolytic production of H_2 during water electroreduction, there must be a threshold H_2 supersaturation that induces nucleation and a threshold current density that promotes the growth of nucleated nanobubbles, both of which should be avoided to favor the production of dissolved H_2.

I-7. Practical approach to avoid bubble nucleation and favor H_2 solubilization

To efficiently deliver H_2 to hydrogenotrophic microorganisms, it is essential to favor the dissolution of H_2 over the formation of gas bubbles at the cathode surface. Two primary strategies for achieving this are related to the thermodynamic principles that govern bubble nucleation: controlling the physicochemical properties of the system and manipulating the local H_2 concentration. While the former involves factors like interfacial tension and wettability, this thesis focuses on the latter as its core methodology.

I-7.1 Interfacial tension and wettability

During the hydrogenotrophic CO_2 reduction process, extracellular proteins and CO_2 might contribute to a reduction in the interfacial tension of the medium. From the classical nucleation theory, the Epstein-Plesset based models (e.g., Lohse-Zhang model) before mentioned and experimental evidence, a decrease of the surface tension should result in a decrease on the supersaturation and current density thresholds [132], [133], which is unfavorable for the solubilization of H_2. Paradoxically, although nucleation can be favored, the stability of these small bubbles under low surface tension might be improved [134], which together with biomass, salts, alcohol content and other fermentation components, can result in larger gas-to-liquid mass transfer [135].

On the other hand, from the CNT, increased wettability (proportional to $\phi(\theta)$) should disfavor the nucleation of bubbles. However, during H_2-gas producing water electroreduction cells, efforts focus on favoring bubble nucleation and fast departure. In abiotic experiments. the increase of bubble coalescence and formation of large bubbles was favored when the surface of a nickel foam cathode was coated with PTFE due to the decrease in wettability [136]. Similarly, the same increase in bubble size was found in cathode surfaces with increased hydrophobicity due to micro-patters at their surface [137].In the context of gas fermentation, strategies for increasing the wettability of the cathodic surface should be implemented instead.

I-7.2 Decreasing local H_2 concentration near the cathode surface

By maintaining a low concentration of dissolved H_2 near the cathode surface, the produced H_2 dissolution should be favored over the nucleation and growth. This implies both working with low local current densities and improved mixing to promote H_2 transport from the diffusion layer to the bulk liquid. Low local current densities can be obtained by working with high surface area cathodes, where its volumetric compactness should also help to the prevention of local supersaturation as well as proper mixing [42], [117], [138]. Perhaps not broadly discussed is the effect that the geometrical configuration of the cell components (e.g., electrodes, membranes) have on the local current density. Ideally, the current distribution should be as homogeneous as possible, to avoid hyperpolarized cathode areas where the local current density is significantly larger than the rest of the electrode. Besides ensuring high ionic conductivity on the electrolyte, avoiding sharp edges on electrodes, working with symmetric components (e.g., equidistant separator/electrodes) and an overall small characteristic length of the system (e.g., thickness) is recognized to homogenize the current distribution [93]. These principles for favoring the solubilization of H_2 during water electroreduction are represented in Fig. I.12 and are to be the basis for the development of this work.

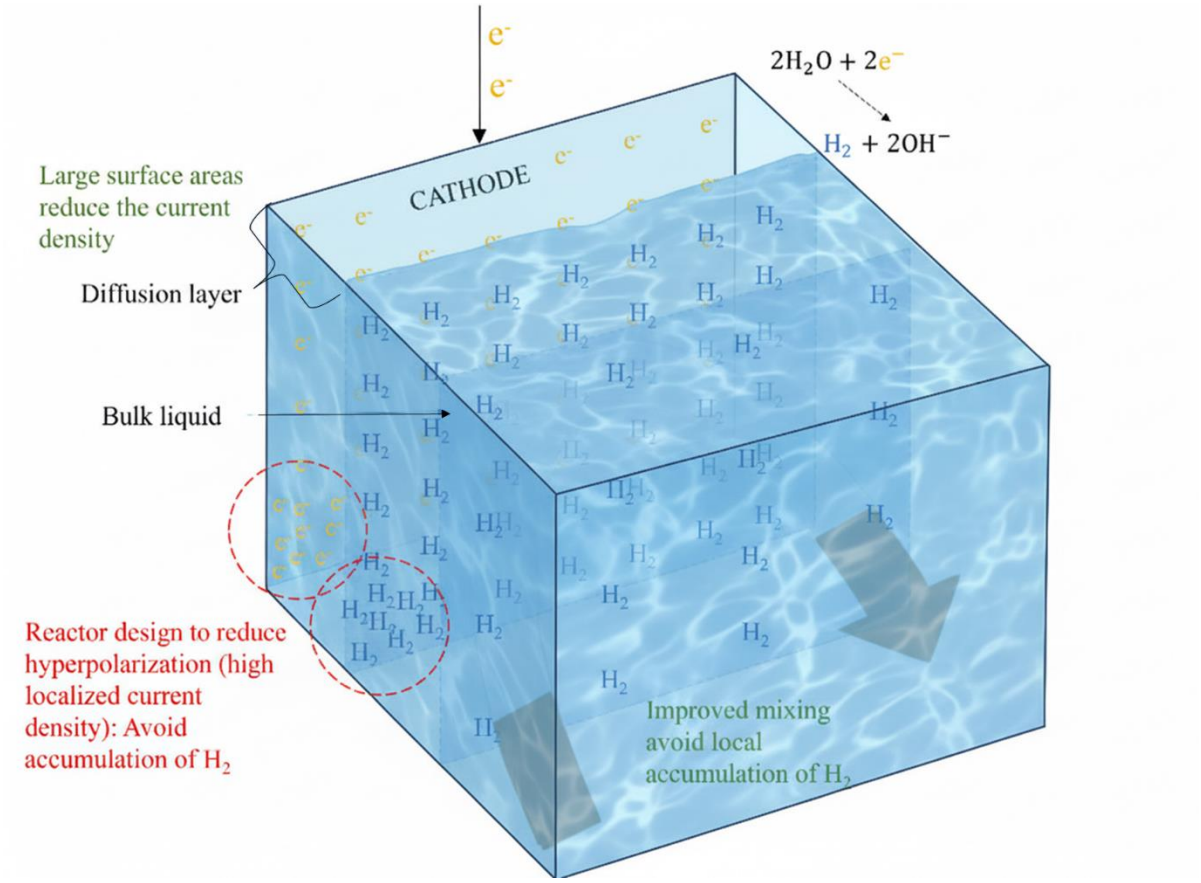

Fig. I.12. Schematic representation of the basic principles followed in this work to favor the solubilization of H_2 during water electroreduction.

I-7.3 Coupling water electroreduction with hydrogenotrophic CO_2 fixation

The design and operational considerations mentioned above for the coupling of both H_2 solubilization by water electroreduction and H_2 uptake by CO_2-fixating hydrogenotrophs can be implemented either in a single reactor as in a MES, or in physically separated compartments. In a MES configuration where the H_2 is produced and consumed at the same time, H_2 degassing could be less of a problem compared with the physically separated approach, where the recycling flow and the use of pumps, pipes and joints might trigger bubble nucleation and gas leaks if the whole system is not pressurized. Nevertheless, the MES configuration also opens the possibility for biofilm colonization on the cathode surface, which becomes a competing reaction for HER. This issue can be circumvented in a separated system by adding a proper biomass recycling (e.g., membrane separation) mechanism, that contains the solid biomass in the bioreactor only. Therefore, for operating the reactor at elevated H_2

concentrations, it might be more favorable to use a MES configuration assuming biofilm formation can be avoided. On the other hand, if H_2 concentrations are below the saturation point where degassing is not an issue, a physically separated approach might be more practical.

I-8. Main objectives of this work

In short, the critical bottleneck during the hydrogenotrophic fixation of CO_2 is the slow H_2 solubilization rate, which severely limits microorganism growth, CO_2 reduction, and overall product yield due to the low solubility of H_2 in aqueous media. This thesis addresses this challenge by exploring a novel approach: achieving high H_2 solubilization rates through direct production of dissolved H_2 via water electroreduction. Here, the focus is shifted to avoiding H_2 bubble formation by targeting the maintenance of a low local H_2 concentrations near the cathode surface through optimized cathode design for homogeneous current distribution and low current density, and efficient mixing to prevent high local H_2 supersaturation and subsequent bubble nucleation. This is aborded through the following objectives:

1. Choosing the right H_2 sensing technologies for the measurement of dissolved H_2 and H_2 bubble detection during water electroreduction (Chapter II): This objective involves assessing potentiometric, amperometric, and headspace gas chromatography methods for dissolved H_2 measurement and exploring optical and other methods for detecting H_2 bubble nucleation, to establish suitable potential methodologies for real-time water electroreduction control.

2. Exploring the potential of the production of dissolved H_2 by comparative evaluation of water electroreduction and gas injection for H_2 solubilization (Chapter III): This objective focuses on quantifying H_2 solubilization rates, efficiencies, and maximum achievable dissolved H_2 concentrations for both water electroreduction and gas injection techniques, while also analyzing the energy consumption per mole of solubilized H_2.

3. Investigating the role of cathode design and hydrodynamics on bubble-free H_2 production (Chapter IV): This objective aims to determine the critical current density for bubble nucleation on various cathode materials (plate, porous foam, brush) and quantify the impact of H_2 pre-saturation and mechanical agitation on nucleation.

4. Numerical simulation study on the mass transfer and current distribution of different cathode geometries for the solubilization of H_2 by water electroreduction (Chapter V): This objective involves simulating current distribution and mass transfer in porous cathodes to guide the design of water electroreduction cells for efficient bubble-free H_2 production by establishing a local current density and H_2 concentration thresholds.

5. Dimensioning an optimal water electroreduction cell for coupling with hydrogenotrophic bioreactors (Chapter VI): This objective focuses on modeling cell design based on H_2 uptake rates, H_2 losses, and supersaturation levels for both low and high H_2 uptake scenarios and evaluating the influence of cell stacking and cathode thickness on overall system performance and practicality of the coupled system.

Chapter II. Evaluation of available hydrogen sensing alternatives for the measurement of dissolved H_2 and bubble nucleation during water electroreduction

ABSTRACT

The mass transfer limitations during H_2 gas injection due to the low solubility of H_2 is the primary bottleneck in bioreactors using hydrogenotrophs. In this context, water electroreduction emerges as a potential alternative to gas injection for the supply of H_2 to hydrogenotrophic bioreactors. Unfortunately, the difficulties on measuring the dissolved H_2 concentration overshadows the possible alternatives and approaches to overcome this limitation. It is therefore essential to ask: What are the limitations of existing sensing technologies for monitoring dissolved H_2 concentrations and bubble nucleation events during water electroreduction? and what are the most suitable technologies for real-time H_2 sensing to be implemented in the control of a water electroreduction cell?

To answer these questions, the methodology involved evaluating different in-situ and ex-situ sensing technologies using a two-chamber H-type cell during water electroreduction. From the different sensing techniques tested here, potentiometric measurements with a platinum (Pt) wire showed poor selectivity, a non-linear response, and significant electromagnetic interference. On the contrary, a commercial amperometric H_2 sensor offered higher selectivity and a linear response, with a rapid response time, but with still electromagnetic interference and a limited lifespan of approximately 6 months. Alternatively, a headspace gas chromatography (HS-GC) method was developed, achieving high precision for dissolved H_2 concentration (R^2=0.99), although it still requires further efforts to reduce liquid sampling volumes (50 mL) and automatization.

For the detection of H_2 bubble nucleation, a semiconducting metal oxide (SMO) sensor in the headspace was inadequate because it only detected bubbles after they detached from the

electrode surface, introducing a delay in the detection. The sensor also exhibited signal saturation around 1.4 V (corresponding to approximately 1000 ppm H_2). In contrast, an optical method using a digital camera offered a promising, non-invasive, and real-time solution. Image analysis successfully highlighted nucleation events, on graphite and carbon brush electrodes, showing bubble presence and prompting its further use in following chapters.

II-1. Introduction

Mass transfer is a primary bottleneck in bioreactors utilizing hydrogenotrophs due to the low solubility of gaseous substrates. For this reason, significant efforts have focused on engineering bioreactor design and operation to overcome gas uptake kinetic limitations [38]. Consequently, the measurement and precise control of dissolved H_2 gas concentration and its solubilization rate are fundamental for achieving optimal process operation. The inability to effectively manage these parameters can lead to operational instability and sub-optimal performance.

For example, in bioreactors with a continuous gas supply, significant fluctuations in H_2 uptake can occur, which demands an adaptable H_2 solubilization rate. During the exponential growth phase, where substrates are consumed at an increased rate, the implementation of an increasing substrate feed rate (fed-batch) is a recognized strategy to avoid substrate inhibition, while maintaining high cell density [139]. Even after reaching a steady state in continuous reactors, oscillations in H_2 and CO uptake rates (termed "crash-recover cycles") have been reported in chemostats with *C. autoethanogenum* [52]. These oscillations were not caused by changes in gene/protein expression but were linked to imbalances in intracellular redox ratios, regulated by the thermodynamic feasibility of crucial metabolic reactions. Similarly, metabolic shifts in *C. autoethanogenum*, such as the change in product selectivity from acetate to ethanol, were found to be strongly influenced by H_2 supplementation and linked to the thermodynamic potential of metabolic pathways [43]. These examples indicate that the solubilization and control of H_2 are not only critical for maximizing gas uptake but also for maintaining metabolic stability and steering product selectivity in hydrogenotrophic systems.

Achieving high concentrations of dissolved H_2 is essential for optimal bioreactor operation, which is traditionally accomplished through reactor pressurization. This method helps overcome the low solubility of H_2 in liquid media. While high pressures are required for this purpose (with partial pressures up to 15 bar being used for the production of acetic acid in a

mixed culture [140]), high pressures can also cause significant growth inhibition. For example, pressures as low as 4 bar already severely inhibited the growth of *C. ljungdahlii* with a H_2/CO_2 gas mixture [141]. In this case, the author suggested that direct pressurization was a possible cause of the early inhibition, and subsequent studies by the same author, which used a slow pressurization rate, reported effective operation at 4 bar with no growth inhibition [142]. The mechanisms responsible for H_2 inhibition at high concentrations of H_2 (and therefore high H_2 uptake rates) can be pinpointed to the role of the energy conserving complexes in different hydrogenotrophs that are ATP limited. In *A. woodii* (Rnf complex, Na^+ dependent), as the driving force for ATP generation is the Na^+ transmembrane gradient, the ATP-consuming formate condensation rate cannot keep up with the CO_2 reduction of formate step driven by the direct H_2 uptake, which results in the toxic accumulation of formate [143]. In *C. autoethanogenum* (Rnf complex, H^+ dependent), the high H_2 uptake and high acetate production rate directly disrupts the proton motive force of the Rnf complex due to a higher intracellular acetic acid dissociation, which results in an unsustainable higher ATP demand and metabolic crash [144]. In other microorganisms employing the Ech-complex (e.g, *M thermoacetica),* the higher extracellular H_2 concentration can also acts as a thermodynamic backpressure against the intracellular escape of H_2 generated by the Ech complex [145].

In this work, water electroreduction is explored as an alternative to gas injection and reactor pressurization to achieve high H_2 solubilization rates and high dissolved H_2 concentration. During water electroreduction, high inhibitory H_2 concentrations could potentially be reached due to the supersaturated conditions present in the electrolyte [146], [147] and therefore, its measurement and control becomes even more critical than with traditional gas injection methods where supersaturation is not reached.

Measuring dissolved H_2 during water electroreduction presents challenges not encountered with H_2 gas injection. In traditional hydrogenotrophic processes where H_2 gas is injected, H_2 from an enriched gas phase (bubbles and headspace) is continuously transferred to the liquid phase, approaching thermodynamic equilibrium. In these reactors, strategies such as agitation and bubble size reduction are used to quickly achieve equilibrium between the two phases. Under near-equilibrium conditions, the dissolved gas concentration can be readily estimated by measuring the H_2 gas fraction in the headspace. This estimation, however, becomes less reliable in hydrogenotrophic chemostats once sufficient cell biomass is attained [61]. In

contrast, when water electroreduction is used as the H_2 supply, the liquid phase is enriched with H_2 first, and the subsequent transfer of H_2 to the gas phase (via bubble nucleation or diffusion to the headspace) is therefore undesired. Since the equilibration of these phases is to be avoided, estimating the dissolved H_2 concentration from the headspace H_2 fraction becomes highly inaccurate. Nonetheless, various sensing technologies have been developed that allow the measurement of the dissolved H_2 concentration. Membrane-coated electrochemical H_2 sensors are the most popular for measuring dissolved H_2 due to their commercial availability, low power and H_2 consumption, fast response, small size, and room-temperature operation. These advantages are particularly notable when compared to other sensors based on H_2 absorption/adsorption on palladium, such as fiber Bragg gratings and microcantilevers [62], [64]. In the case of electrochemical H_2 sensors, they can be either potentiometric or amperometric according to their detection principle. Potentiometric sensors rely on the adsorption of active redox species (e.g., H+, H_2, O_2) on a working electrode (e.g., platinum) that generates a measurable, concentration dependent Nernst potential of logarithmic nature. In contrast, amperometric sensors operate by imposing a constant potential on the working electrode, generating a diffusion-limited current that linearly depends on the oxidizing species concentration. Although amperometric H_2 sensors are preferred due to their higher selectivity to H_2 (not all redox species are active at a specific potential) and linear response, their short lifespan (~6 months) and price prevent their widespread use. Alternatively, traditional H_2 gas sensors can be employed, provided the H_2 from liquid samples is first equilibrated with a sampling headspace. The H_2 gas fraction in this headspace can then be analyzed using techniques such as gas chromatography or conductivity sensors [63].

Beyond measuring the dissolved H_2 concentration, the detection of H_2 bubble nucleation is also of interest during the production of dissolved H_2 via water electroreduction, since the generation of bubbles signifies a decrease in the solubilization efficiency. Kempler *et al.* compiled a comprehensive list of different electrochemical, optical and non-optical methods that have been used for the study of bubbles at electrode surfaces [148]. For the precise study of nucleation events, some methods rely on complex laboratory setups, which are not compatible with industrial applications, the use of H_2 producing microelectrodes or the detection of high-frequency impedance changes in macroelectrodes resulting from the

aggregated effect of many nucleation events. Among the techniques suitable for studying early nucleation at macroelectrodes, optical methods are highlighted for their simplicity of interpretation and implementation, as they allow the imaging of large-scale surfaces while being non-intrusive [149], [150], [151].

This chapter addresses the critical need for effective monitoring of hydrogen delivery in water electroreduction systems used for hydrogenotrophic processes. The main questions that are boarded in this chapter are: What are the limitations of existing sensing technologies for monitoring dissolved H_2 concentrations and bubble nucleation events during water electroreduction? and what are the most suitable technologies for real-time H_2 sensing to be implemented in the control of a water electroreduction cell? To answer these questions, an evaluation on several in-situ and ex-situ sensing technologies for both dissolved hydrogen concentration and hydrogen bubble nucleation is done, encompassing their potential use on a water electroreduction cell. Specifically, the limitations of potentiometric measurements using a Pt (platinum) wire are assessed, highlighting their poor selectivity and non-linear response to hydrogen concentration. The performance of a commercial amperometric H_2 sensor and a headspace gas chromatography (HS-GC) method is also investigated, with the trade-offs between accuracy, lifespan, and operational complexity identified. To address the issue of H_2 solubilization efficiency, methods for detecting bubble nucleation are explored, concluding that optical methods, such as those employing a digital camera with a suitable bubble detection algorithm, offer a promising, non-invasive, and real-time approach compared to headspace gas analysis with a semiconducting metal oxide (SMO) sensor. The experiments performed here establish the most suitable methodologies for real-time control of the electrolyzer based on these two key parameters.

II-2. Materials and Methods

II-2.1 Medium composition and reactor setup

A minimum salt medium was used as electrolyte based on a gas fermentation reactor operated previously at TBI [152]. Stock solutions A, B and C were prepared first according to the composition described next. Solution A: NH_4Cl, 20 $g \cdot L^{-1}$. Solution B: $MgCl2 \cdot 6H_2O$, 2 $g \cdot L^{-1}$; $CaCl_2 \cdot 2H_2O$, 1 $g \cdot L^{-1}$. Solution C: $FeCl_2 \cdot 4H_2O$, 200 $mg \cdot L^{-1}$; H_3BO_3, 10 $mg \cdot L^{-1}$; $ZnCl_2 \cdot 7H_2O$ 10 $mg \cdot L^{-1}$; $CuCl_2 \cdot 2H_2O$, 8 $mg \cdot L^{-1}$; $MnCl_2 \cdot 4H_2O$, 20 $mg \cdot L^{-1}$; $H_{24}Mo_7N_6O_{24}$, 7 $mg \cdot L^{-1}$; $CoCl_2 \cdot 6H_2O$, 60 $mg \cdot L^{-1}$;

$NiCl_2$, 20 mg·L^{-1}. For the preparation of the medium, 50 mL of solutions A and B were mixed with 20 mL of solution C, and distilled water was used to complete one liter of medium solution. The pH and ionic conductivity of the medium were 6.7 units and 2.4 mS·cm^{-1}. Prior to the electrolysis experiments, the liquid medium was sparged with N_2 gas using a glass frit (VitraPOR Micro-immersion-filter Por 2, Robu, Germany) of 10 mm of diameter and 4 mm of thickness, to remove traces of dissolved gases such as H_2 and O_2.

A two-chamber H-type cell was used as a reactor, with a working volume of 800 mL on each chamber and separated by a cation exchange membrane of 5 cm of diameter (CMI 7000S, Membranes International Inc, USA). For the counter electrode (i.e., anode here) DSA® plate of 2.5×5.3×0.1 cm (projected area: 13.25 cm^2; Di Noer Technology Co. Ltd, China) was used while two different working electrodes (i.e., cathodes here) were tested: a graphite electrode of 2.5×2.5×1.0 cm^3 (Goodfellow, France) was used as a cathode for bubbling conditions and a carbon brush (6TMIC Ing,. France) occupying a diameter of 5 cm and 4 cm of height (projected surface area: 20 cm^2, bulk volume: 79 cm^3). Titanium rods were used as current collectors and a saturated calomel electrode (SCE, Hg/Hg_2Cl_2 in saturated KCl, +0.241 V vs SHE) was used as a reference electrode. A schematic representation of the reactor setup is shown in Fig. II.1.

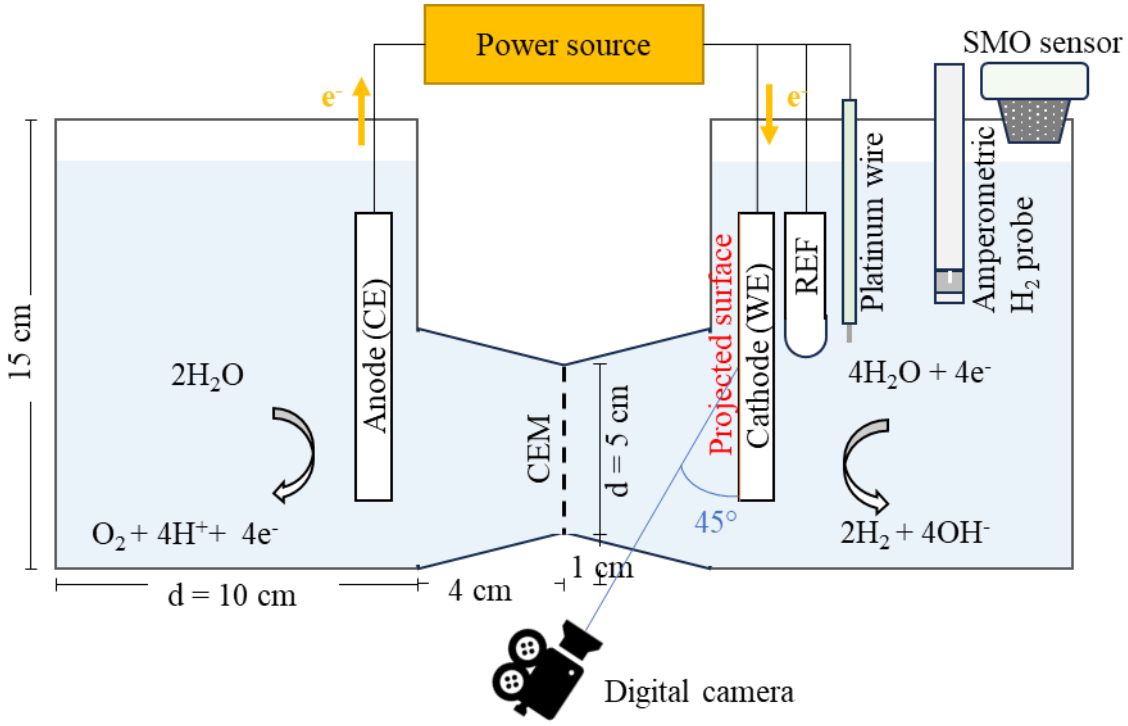

Fig. II.1. Schematic representation of the two-chamber H-type cell experimental setup for water electroreduction. CE: counter electrode; WE: working electrode; REF: reference

electrode; CEM: cation exchange membrane. The setup was used to evaluate various H_2 sensing elements. For dissolved H_2 concentration sensing, a Pt wire, an amperometric H_2 sensor, and a headspace gas chromatography (HS-GC) method (not shown in the figure) were used. For detecting H_2 bubbles, a digital camera and a semiconducting metal oxide (SMO) sensor were employed.

A Pt wire electrode of 5 mm exposed length and 1 mm diameter (Heraeus, Germany) was used to measure the mixed potential of the electrolyte vs the reference electrode. An amperometric H_2 sensor (MS08 Aquams, France) was used to directly measure the dissolved H_2 concentration, coupled with a msBox and an Arduino UNO for data logging. A gas chromatograph (Trace 1300, Thermo Scientific) was used for the measurement of the H_2 fraction for the HS-GC method (see Supplemental Information A for details of the method). A SMO sensor (MQ-8 Flying-fish, China) was positioned at the gas outlet of the cathodic chamber with a water retention filter in between to avoid humidity interference. A digital camera (Digital microscope 12M, RS PRO, France) was used to record the projected surface of the cathode pointing at the cathode surface at a 45° angle of incidence. For the shaking of the carbon brush electrode, a continuous servo motor (Parallax, USA) coupled with a microcontroller Arduino UNO (Arduino, Italy) was used to apply a back-and-forth (oscillatory) movement on the electrode. A potentiostat (VSP, BioLogic) was used as a power source to perform the galvanostatic experiments through a chronopotentiometry (CP) technique, applying a constant current at the working electrode for the production of dissolved H_2 through water electroreduction.

II-2.2 Experimental design

The conditions for the galvanostatic experiments done in this chapter are summarized in Table II.1. The H_2 solubilization rates reported from the amperometric H_2 sensor were calculated by calculating dissolved H_2 concentration change from 0 and 100 minutes and reporting the mean and standard deviation of the replicates of each mixing condition.

Table II.1. Summary of experimental conditions for testing the performance of different H_2 sensing elements. Pt: Platinum wire; SMO: Semiconducting metal oxide; A-H_2 sensor:

Amperometric H_2 sensor. Runs 1-3 were done once, while the rest of the runs were done by duplicate.

Run	Current [mA]	Cathode material	Sensors tested	Mixing conditions
1	20	Graphite	Pt	Agitated
2	20	Graphite	Pt, SMO, camera	Agitated
3	20	Carbon brush	Pt, SMO, camera	Agitated
4	30	Graphite	Pt, A-H_2 sensor	Agitated
5	30	Carbon brush	Pt, A-H_2 sensor	Agitated
6	30	Carbon brush	Pt, A-H_2 sensor	None
7	30	Carbon brush	Pt, A-H_2 sensor	Shaken cathode
8	30	Carbon brush	Pt, A-H_2 sensor	Agitated, shaken cathode

II-3. Results

II-3.1 Sensors for the measurement of dissolved H_2

II-3.1.1 Potentiometric and amperometric H_2 sensing

This subsection aims to evaluate the efficacy of potentiometric and amperometric methods for measuring dissolved H_2 concentration. The primary objective was to assess the reliability, selectivity, and response time of a Pt wire electrode as a potentiometric sensor compared to a commercial amperometric sensor. A key challenge was distinguishing the Pt wire's response to dissolved H_2 from its response to other redox species (O_2) and electromagnetic interference from the cathode. The method involved monitoring the potential of the Pt wire and the concentration measured by the amperometric sensor in a two-chamber H-type cell under various conditions, including N_2 purging and different cathode materials and mixing conditions

II-3.1.1.1. Sensibility of the Pt wire to H_2, O_2 and interference with polarized cathode

During the N_2 purging done prior the polarization of the cathode, the Pt wire's potential as a redox indicator dropped from ~0.3 V to ~0.1 V over 150 minutes as oxygen was removed from the medium by N_2 purging, as shown in Fig. II.2A. This corresponded to a decrease in oxygen concentration from 8.6 to 0.3 mg $O_2 \cdot L^{-1}$ as measured by a separate O_2 sensor. Nevertheless, this potential change took approximately 100 minutes, while the O_2 sensor showed that most of the dissolved O_2 was already stripped out in about 15 minutes. The Pt potential dropped

further to -0.17 V in just 20 minutes when a cathodic current of 20 mA was applied to the graphite electrode, as shown in Fig. II.2B.

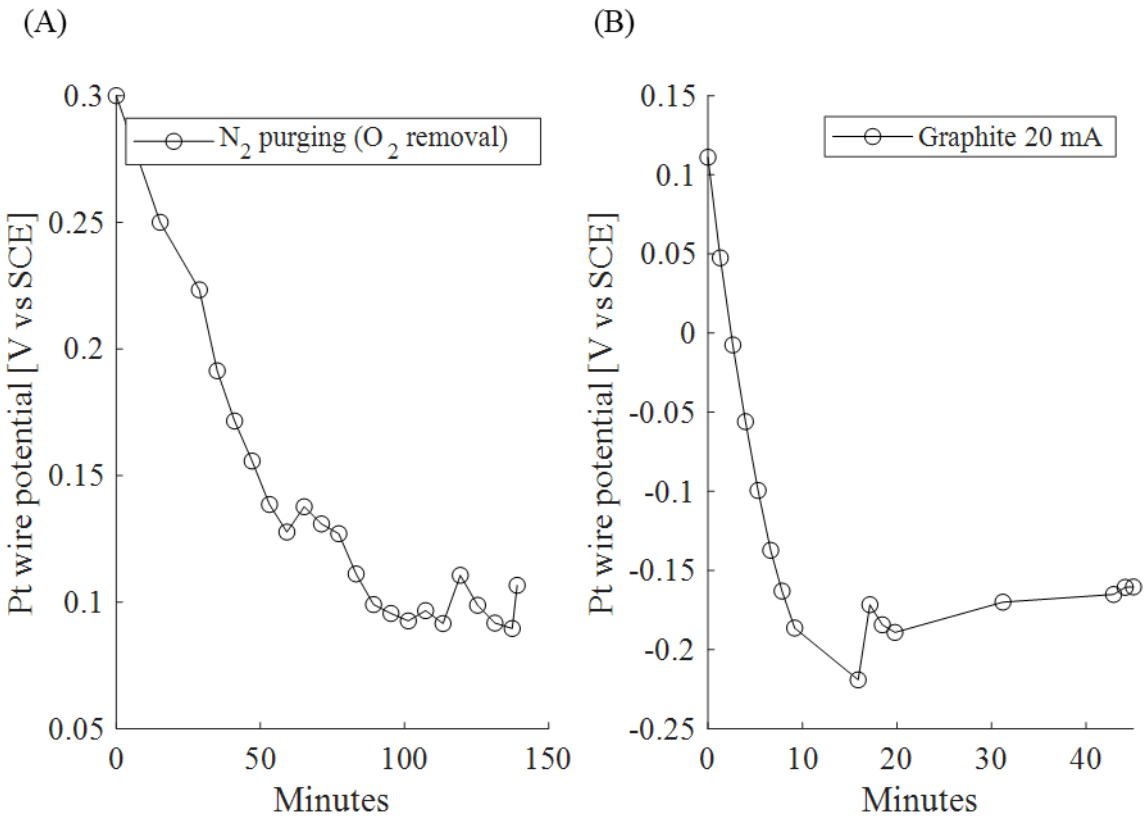

Fig. II.2. Mixed potential measurements using a Pt wire electrode for Run 1 from Table II.1. Graph (A) shows the change in Pt wire potential during N2 purging to remove dissolved O2. Graph (B) shows the potential drop when a cathodic current of 20 mA was applied to a graphite cathode. All potentials are measured against a saturated calomel electrode (SCE).

Before stopping the polarization experiment, it was also found that positioning the Pt wire close to the graphite cathode (both sharing the same port from the screw cap) affected the Pt potential, making it more positive than when the cathode polarization was off, as shown in Fig. II.3. This offset was reduced from 0.15 V to 0.10 V by positioning the Pt wire in a separate port, 3.5 cm away from the polarized cathode.

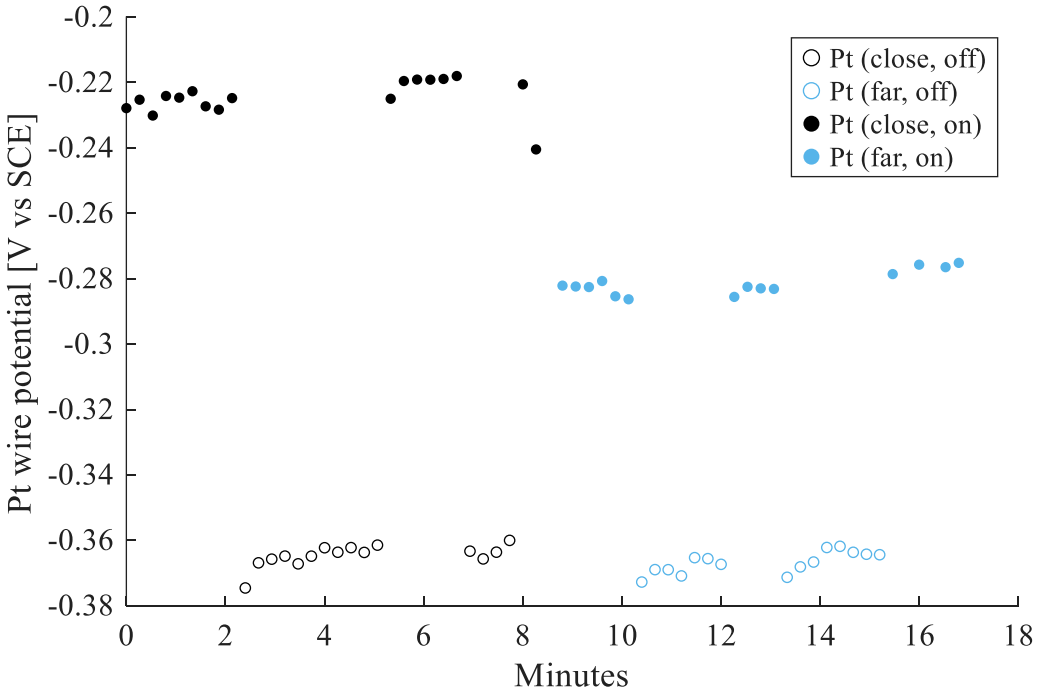

Fig. II.3. Effect of electromagnetic interference from the polarized cathode on the mixed potential measured by the Pt wire electrode for Run 1 from Table II.1. The graph compares Pt wire potential measurements when the wire is positioned close to (cathode and Pt wire on same port) and far from the cathode (cathode and Pt wire on different ports, 3.5 cm of distance), both with the cathode polarization on and off.

Despite the need for an offset correction due to the electromagnetic interference from the polarized cathode, this potential could still be useful for obtaining some information on the state of change of redox species such as dissolved H_2. For example, Fig. II.2B shows that the mixed potential measured by the Pt wire reached a plateau after 20 minutes of polarization at a cathodic current of 20 mA, which could be related to how fast a state of equilibrium of the dissolved redox species is reached. It could be expected that in different H_2 solubilization conditions, this plateau is reached first on setups that solubilize H_2 at a higher rate, reaching the H_2 solubility limit first. This idea will be further explored next.

II-3.1.1.2. Mixed potential changes measured when using a bubbling (graphite) and non-bubbling (carbon brush) cathode

Under the same cathodic current, it could be expected that an electrode that produces H_2 in the absence of bubbling has a higher H_2 solubilization rate than an electrode with vigorous bubbling, which could be qualitatively tested by following the Pt wire potential. To test this

idea, the Pt wire potential was measured during the imposition of a cathodic current of 20 mA on two different cathode materials, as shown in Fig. II.4.

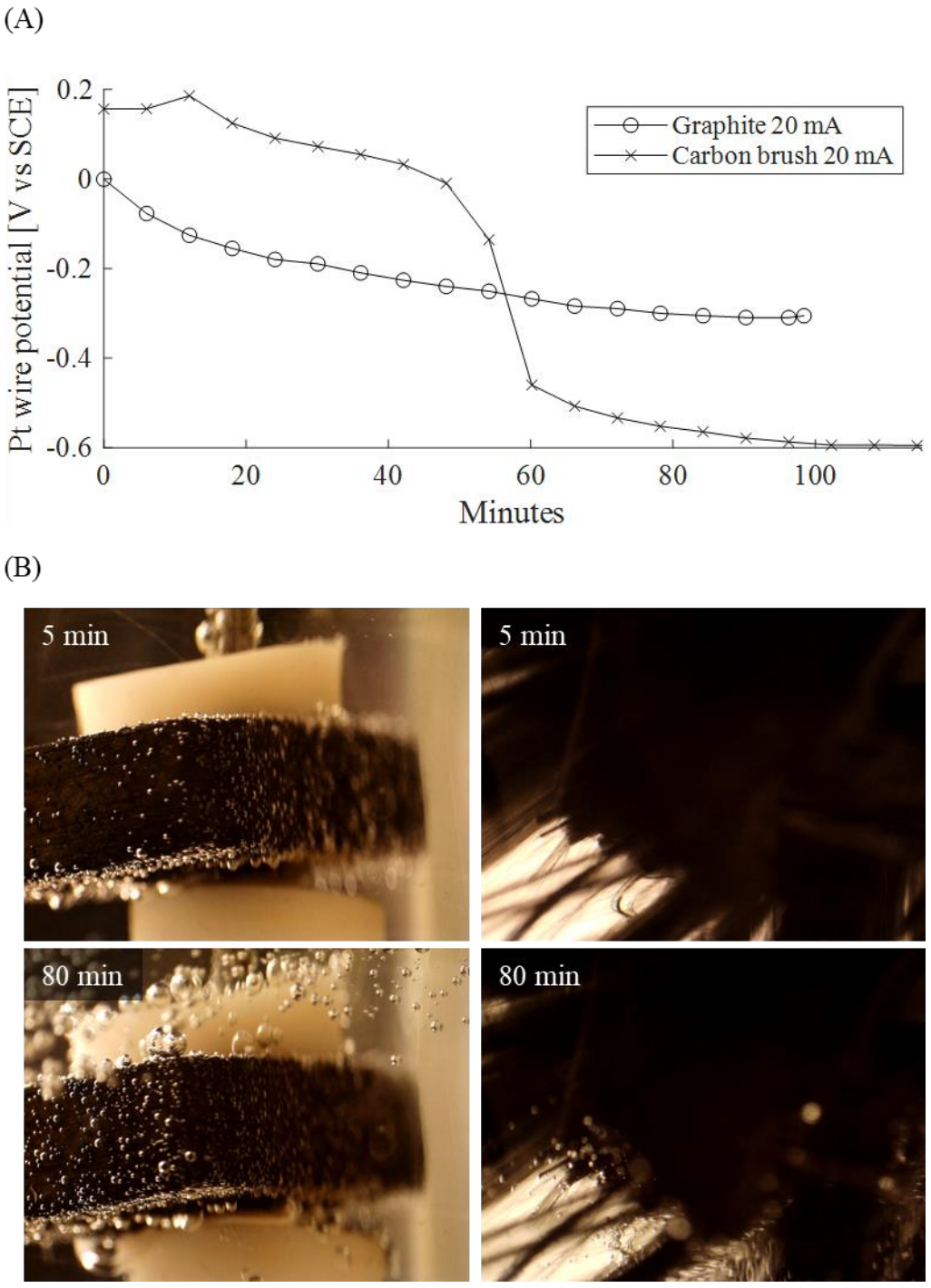

Fig. II.4. Preliminary experiments using a Pt wire as a qualitative tool to measure the mixed potential state in the liquid medium for Runs 2 and 3 from Table II.1. (A) Shows the Pt wire potential change during the imposition of a 20 mA cathodic current on a graphite and a

carbon brush cathode. (B) Displays video recordings of the cathode surfaces at 5 and 80 minutes, illustrating the difference in H_2 bubble nucleation between the two materials.

Fig. II.4A shows that while the Pt wire potential curve showed a delayed drop, it eventually reached an apparent equilibrium at a lower potential. These characteristics may be due to the different bubbling regimes achieved with both electrodes. For the carbon brush, it took around 80 minutes to observe the start of H_2 bubble nucleation attached to the carbon brushes, while the graphite quickly reached a state of vigorous bubbling on its surface, as shown in Fig. II.4B. The difference in the time required for the start of nucleation shows that the carbon brush was more effective in distributing the electrons and produced H_2 over the volume of the catholyte compared to the graphite cathode, which prevents the rapid local supersaturation necessary for the start of nucleation (the nucleation onset on different cathode structures is further studied in Chapter IV).

The initial redox state given by the Pt potential after deaeration differed by 0.16 V between both electrodes, although the final Pt potential differed by 0.3 V. The experiment was run again in duplicate at 30 mA, as shown in Fig. II.5. In this case, the shape and final Pt potential difference were preserved, though both cases reached a more negative potential, possibly due to a higher concentration of dissolved H_2. The faster change in the Pt wire potential change for the graphite cathode was possibly due to the convection induced by bubbling, which helped to dissipate faster the dissolved H_2 from the cathode surface into the bulk liquid.

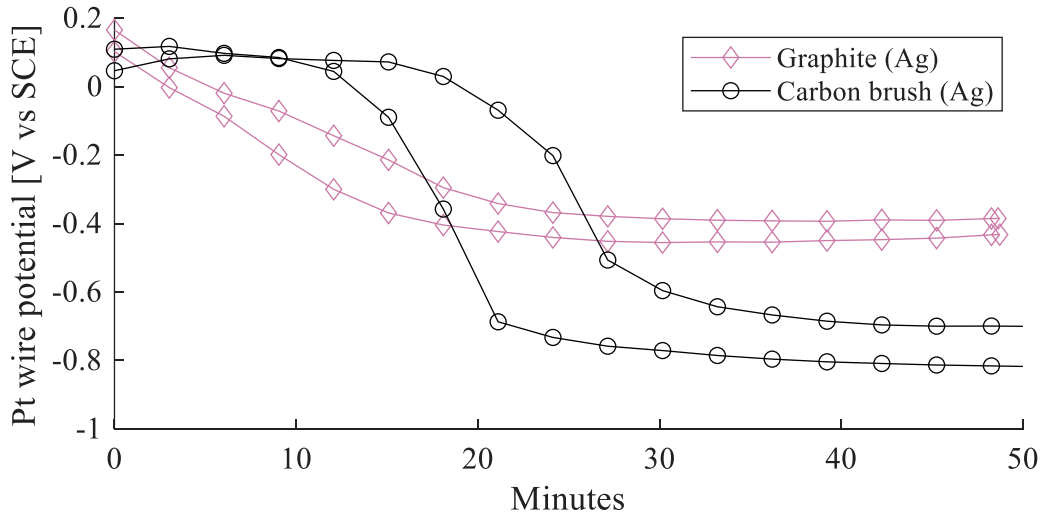

Fig. II.5. Validation of preliminary experiments using a Pt wire as a qualitative tool to measure the state of H_2 saturation for Runs 4 and 5 from Table II.1. This figure shows the

mixed potential measured by a Pt wire electrode during galvanostatic experiments at a higher current of 30 mA. The graph compares the potential changes during water electroreduction using a graphite cathode and a carbon brush, further demonstrating the difference in H_2 nucleation characteristics between the two materials.

The lower Pt potential achieved by the carbon brush indicates that the medium could be holding a higher concentration of dissolved H_2 due to the absence of vigorous bubbling. Although there was no bubble nucleation at the beginning of the polarization experiments for the carbon brush, bubbles still nucleated eventually at the surface of the brushes, where agitation alone was not sufficient to remove them from the surface. To establish different conditions at which bubbling might be affected on the surface of the carbon brush, four configurations were tested: the cathode was either agitated by stirring (Ag), shaken (Sh), a combination of both (Ag-Sh), or neither, as shown in Fig. II.6.

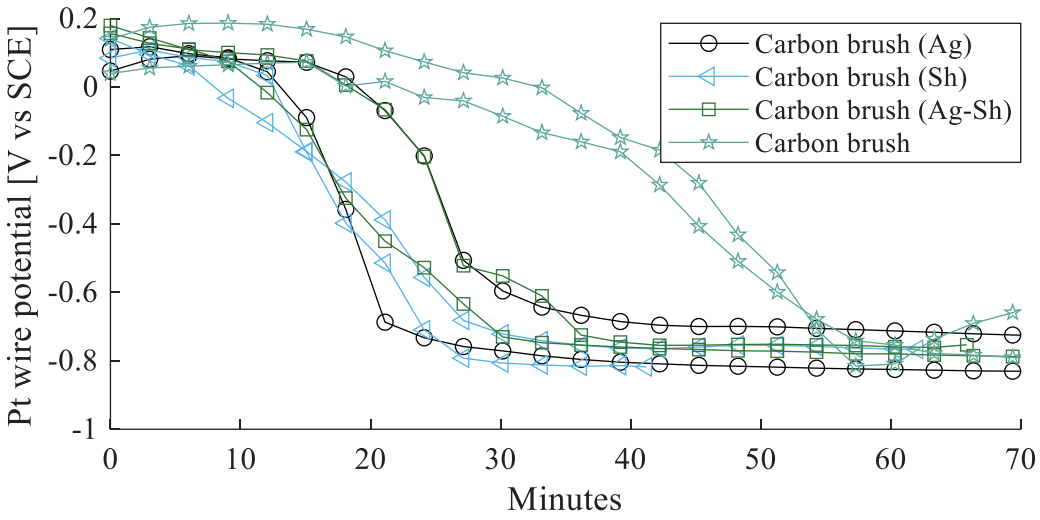

Fig. II.6. Mixed potential measurements by a Pt wire electrode during galvanostatic experiments at 30 mA for Runs 5-8 from Table II.1. The graph shows the potential changes during water electroreduction using a carbon brush under four different mixing conditions: agitated medium (Ag), shaken cathode (Sh), a combination of both (Ag-Sh), and neither.

At first glance, the figure indicates that the experimental setups where the medium was agitated or the cathode shaken allowed a Pt potential to be reached much faster than in the absence of agitation or shaking. Here, the lowest potential achieved seemed to reach a minimum value around -0.8V. Nevertheless, this minimum value does not seem to correspond

to a H_2 saturation limit, since different dissolved H_2 concentrations were directly measured with an amperometric H_2 sensor, as shown in Fig. II.7.

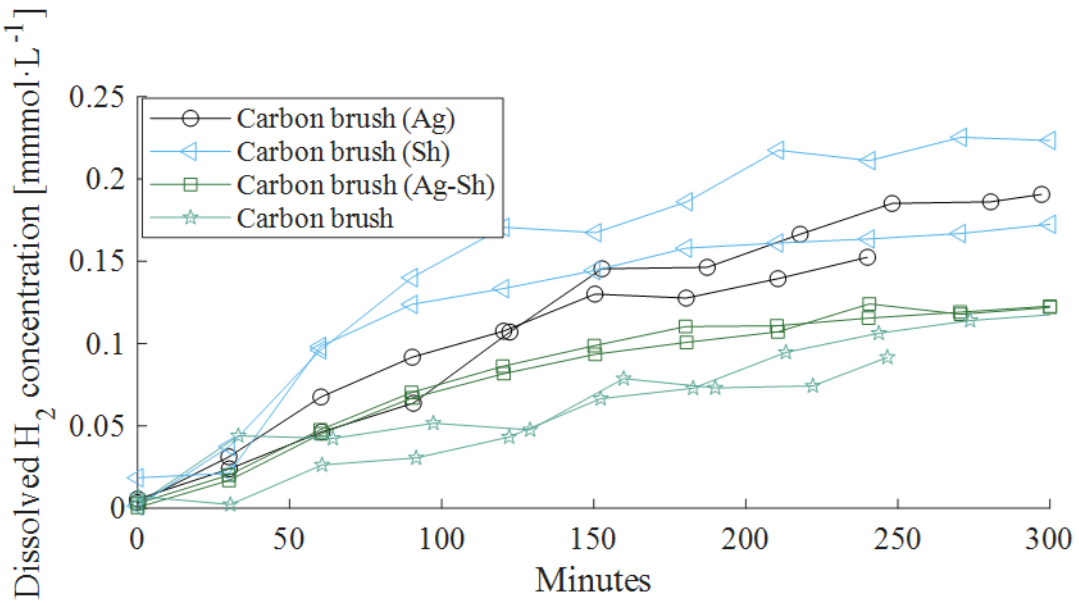

Fig. II.7. Dissolved H_2 concentration measured by an amperometric H_2 sensor during galvanostatic experiments at 30 mA for Runs 5-8 from Table II.1. The graph shows the potential changes during water electroreduction using a carbon brush under four different mixing conditions: agitated medium (Ag), shaken cathode (Sh), a combination of both (Ag-Sh), and neither.

The differences between each condition became more evident by comparing the H_2 solubilization rates summarized in Table II.2.

Table II.2. H_2 solubilization rates for water electroreduction experiments at a cathodic current of 30 mA. The table presents the calculated rates under different mixing conditions: agitated (Ag), shaken (Sh), a combination of both (Ag-Sh), and neither. The solubilization rates were calculated from the data contained in Fig. II.7, using the dissolved H_2 concentrations at 0 and 100 minutes and reporting the mean and standard deviation of the replicates of each mixing condition.

Mixing condition	H_2 solubilization rate [mmol·L^{-1}·h^{-1}]
None	0.0249 ± 0.0086
Agitated medium (Ag)	0.0518 ± 0.0092
Shaken cathode (Sh)	0.0842 ± 0.0140

Agitated and Shaken (Ag-Sh)	0.0441 ± 0.0017

The highest solubilization rate was achieved by the shaken cathode, followed by the setup with the agitated medium, the shaken cathode and agitated medium setup, and the non-agitated and non-shaken setup. In contrast to the Pt wire potential, which became invariant after 60 minutes, the H_2 concentration did not achieve a saturation value in the tested time frame of approximately 250 minutes. While this could suggest a slow response from the amperometric H_2 sensor, this was quickly discarded after a separate test showed a response time of a few seconds in a pre-saturated H_2 medium. The pH of the catholyte rose by around 2 units during the course of the experiment, which accounts for a Pt potential reduction of around 0.1 V according to the Nernst equation. At this pH, if the H_2/H^+ pair were the only redox couple interacting with the Pt wire, a plateau potential of around -0.8 V would be reached when the dissolved H_2 concentration was saturated at 0.78 $mmol \cdot L^{-1}$. Nevertheless, the dissolved H_2 concentration, as measured by the amperometric H_2 sensor, was much lower than the saturation value, suggesting either interference from other redox species or a surface saturation on the Pt wire that prevented it from reacting to further changes in dissolved H_2 concentration. One possible hypothesis to the Pt wire potential reaching exactly the potential at which H_2 is saturated could be due to the absence of a membrane coating (silicone in the amperometric H_2 sensor), micro/nano bubbles generated in the cathode could reach and mask the Pt surface, giving an apparent H_2 saturation concentration.

The use of a Pt wire with a reference electrode proved to be an unreliable indicator of dissolved H_2 concentration, due to the non-linear response of the mixed potential to the concentration of the H_2/H^+ pair and the poor selectivity of the H_2 measurement. While the Pt wire potential reacts to the adsorption of redox species on its surface, the amperometric H_2 sensor measures the kinetic rate of H_2 oxidation by operating at a constant working potential, which adds selectivity for H_2 oxidation. Unfortunately, the lifetime of the amperometric H_2 sensor was only 6 months as reported by the manufacturer. Common degradation reasons include membrane fouling and aging, internal electrolyte degradation, and electrode poisoning. This rapid degradation necessitates a continuous and expensive replacement of the sensor. Moreover, the amperometric H_2 sensor also presented electromagnetic interference with the polarized cathode, which requires either sampling and external measurement of the dissolved H_2 concentration outside the cathodic chamber or the application of a constant current to the

cathode for potential offset correction during in-situ measurements. Because these difficulties, another methodology for measuring the dissolved H_2 concentration was tested: the headspace gas chromatography (HS-GC) method, which will be discussed in the next section.

II-3.1.2 Headspace gas chromatography (HS-GC)

The objective of this subsection was to develop and evaluate a reliable method for measuring dissolved H_2 concentration by analyzing the headspace gas of a sampled aliquot. The main challenge was to carefully extract the dissolved H_2 of the liquid sample into a headspace, to be injected later into the gas chromatograph, without losing the quality of the sample. The method involved preparing liquid samples with varying dissolved H_2 concentrations in an arrangement of two syringes interconnected with a 3-way valve, and establishing a possible correlation between the readings of the H_2 fractions from the gas chromatography with the dissolved H_2 concentration.

A linear relationship can be observed between the dissolved H_2 concentration of five different samples and the H_2 fraction in the headspace (Fig. II.8). By comparing the expected H_2 fraction calculated by Henry's law and the reading from the gas chromatography, a high coefficient of determination of $R^2 = 0.99$ was established, validating the precision of the sample dilution, H_2 equilibration and measurement.

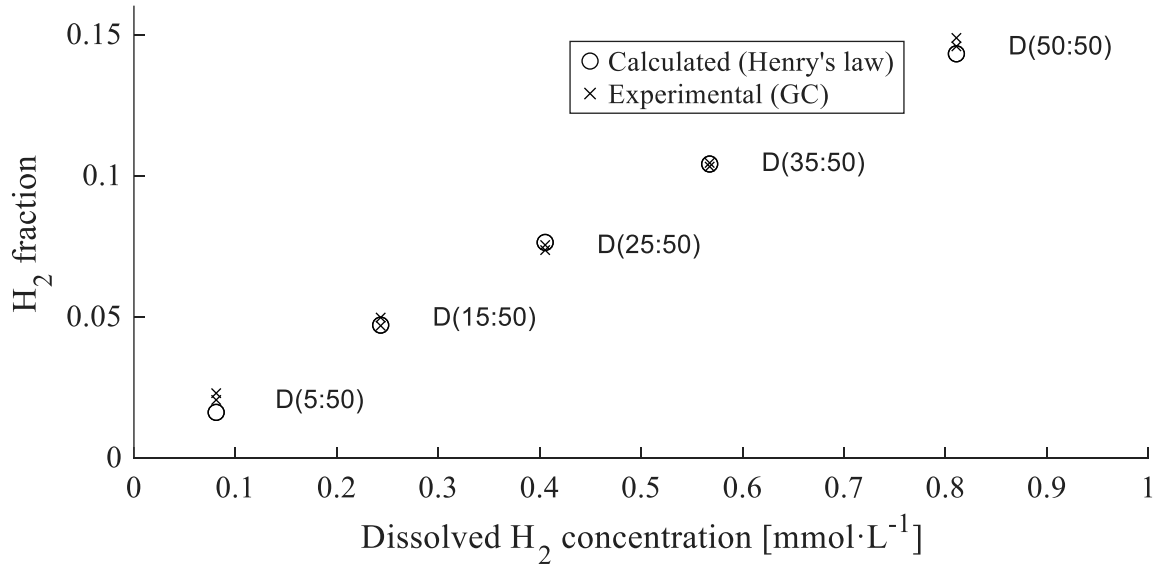

Fig. II.8. Evaluation of the accuracy of the headspace gas chromatography (HS-GC) method for measuring dissolved H_2 concentration. The method uses a syringe system with a 50 mL liquid sample and a 5 mL headspace. The linear relationship between the expected dissolved H_2 concentration and the measured H_2 fraction in the headspace demonstrates the precision of the method, with a coefficient of determination of $R^2 = 0.99$.

Compared with the amperometric H_2 sensor, there is no need for frequent replacement of the sensing elements for the gas chromatograph, but its sampling and measurement becomes more cumbersome, as an automated setup, while possible, is also harder to build. Moreover, the method developed here required 50 mL liquid samples (phase ratio of 5:50 v/v), which can have a large effect on lab-scale experiments, especially when a high sampling and data measurement frequency is needed. This method was further corroborated by comparing the readings obtained with this method with the readings from the amperometric H_2 sensor at different experimental conditions explored in Chapter III. It was also used in Chapter IV to validate the H_2 saturation in H_2 pre-saturated experiments.

II-3.2 Sensors for the detection of H_2 bubble nucleation

This subsection aimed to explore alternative methods for detecting H_2 bubble nucleation events, which signify a decrease in solubilization efficiency and should be avoided. The detection of these nucleation events is particularly useful for process control: if the electrolyzer is coupled with a gas fermentation reactor where the maximum H_2 uptake rate is greater than the maximum H_2 solubilization rate, the electroreduction cell could be operated at the maximum current that avoids nucleation. This would allow the detection of nucleation to be used alone to control the imposed current. A primary challenge was to find a method that could quickly detect nucleation in real-time. The methods tested were a semiconducting metal oxide (SMO) sensor placed in the headspace to detect increases in H_2 concentration due to bubble release, and a digital camera used to record the cathode surface and identify nucleation events through image analysis.

II-3.2.1 Semiconducting metal oxide sensor (SMO)

The first alternative for the detection of nucleation on the cathode surface is the measurement of changes in the gas phase. While the slow measurement/detection time of a gas chromatograph makes the method impractical, other fast-responding sensors could be

employed. For example, during the polarization of the carbon brush shown in Fig. II.4, an SMO sensor was placed at the open outlet of the cathodic chamber of the headspace to record changes in the sensor's voltage output due to the increase of H_2 concentration caused by the generation of bubbles. As seen in Fig. II.9A, the graphite cathode produces H_2 bubbles from the start of the galvanostatic experiment, and the microconvection generated by the bubbles is reflected in the increase of the cell voltage (less negative). In parallel, the fast production and release of bubbles from the graphite surface quickly raise the H_2 concentration in the headspace, which is consequently quickly detected by the SMO sensor. After 60 minutes of operation, the SMO signal can be seen to saturate at around 1.4 V, which can be expected when the headspace H_2 concentration surpasses the detection limit of the sensor (~1000 ppm, 0.1 %). In contrast, in Fig. II.9B, the SMO signal and cell voltage of the carbon brush have a much different time profile due to its reduced H_2 nucleation. Before the visual confirmation of bubbles at the carbon brush (< 80 minutes), the cell voltage remained close to -6.8 V, and the SMO signal increased steadily from 0.36 V to 0.86 V. This increase can be attributed to the detection of H_2 in the headspace coming from the desorption from the liquid phase. In the 80-150 minute interval, bubbles kept accumulating and growing on the carbon fibers, and the cell voltage began to decrease further to around -7.1 V, which is attributed to the gas masking of the electrode surface area, which in turn reduces the electroactive surface area available for the hydrogen evolution reaction (HER). Nevertheless, as bubbles were still attached to the electrode surface, the steady increment in the SMO signal continued up to 1 V. After 105 minutes, it was visually confirmed that some of the bubbles attached to the carbon fibers were released due to increasing buoyant force, which, besides introducing microconvection around the carbon fibers, unmasked part of the area available for HER. This sudden release of bubbles was also detected by a sudden increase of the cell voltage together with a sudden spike in the SMO signal. After the sudden release, bubbles started to grow again on the surface area to be later released in a cyclic fashion, which gave a sawtooth shape to the cell voltage and the SMO signal. Here, the measurement of the SMO signal in the headspace only detected bubbling when bubbles were released from the cathode surface and not as soon as they nucleated on it. Moreover, the signal of the tested SMO sensor also seems to approach a saturation limit, at which the detection of bubble release would become infeasible.

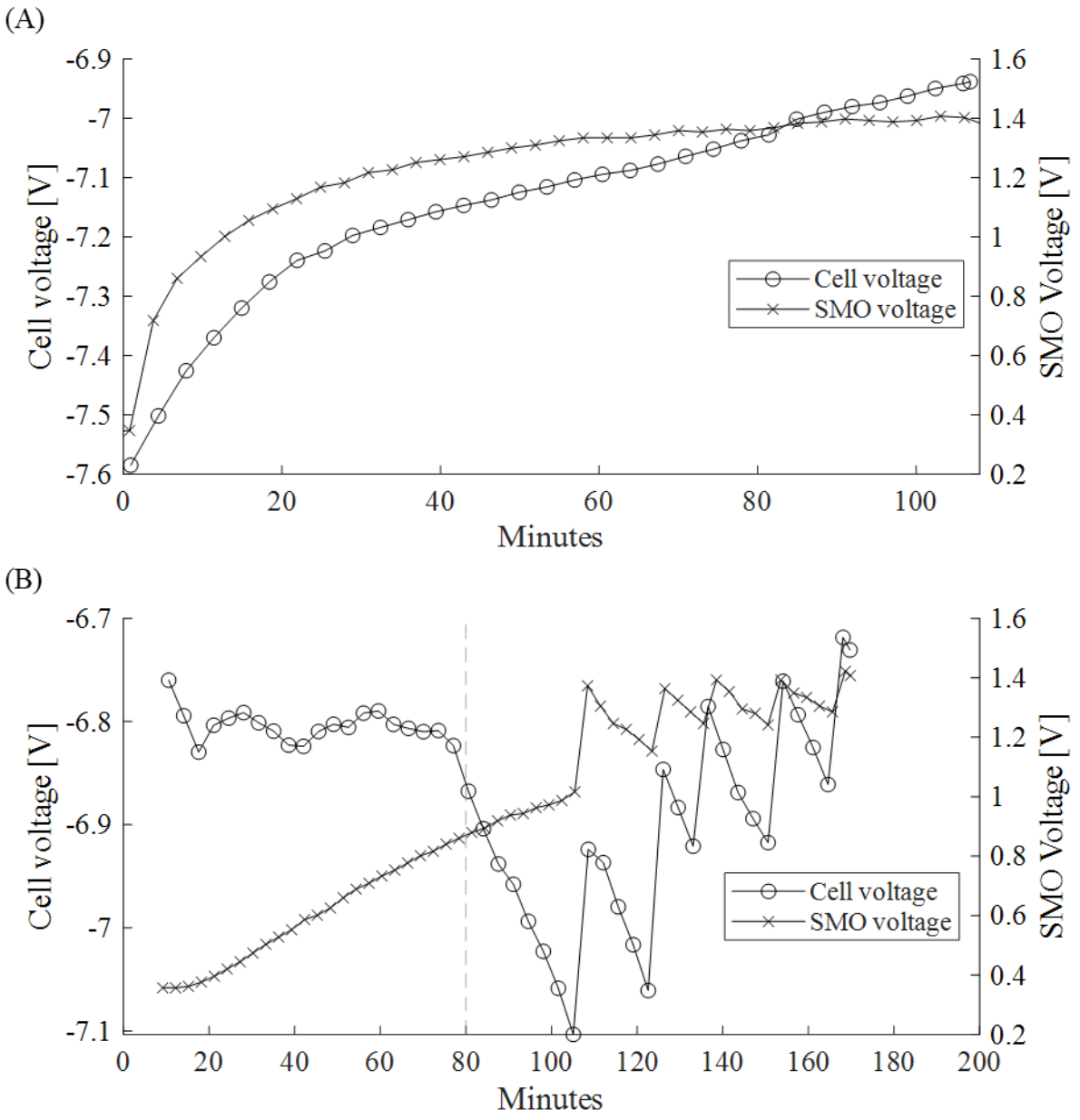

Fig. II.9. Semiconducting metal oxide (SMO) sensor signal and cell voltage during water electroreduction experiments at a cathodic current of 20 mA for Runs 2 and 3 from Table II.1. The graphs show the response for a (A) graphite electrode and (B) carbon brush electrode, illustrating the distinct time profiles based on their H_2 nucleation characteristics.

II-3.2.2 Digital camera

Another tool tested for the detection of nucleation is the use of a digital camera. Although this approach requires an appropriate algorithm for the detection of nucleation, the physical setup can be non-invasive and more straightforward compared with the SMO sensor. During the video recording of a cathodic surface, the intensity change in the pixels of each recorded frame

could be used as a detection method for nucleation. For example, video recordings from the cathodes shown in Fig. II.4A were analyzed, and pixels with an intensity increase (relative to a non-polarized state) were colored in magenta using the MATLAB function *imfuse*, as shown in Fig. II.10.

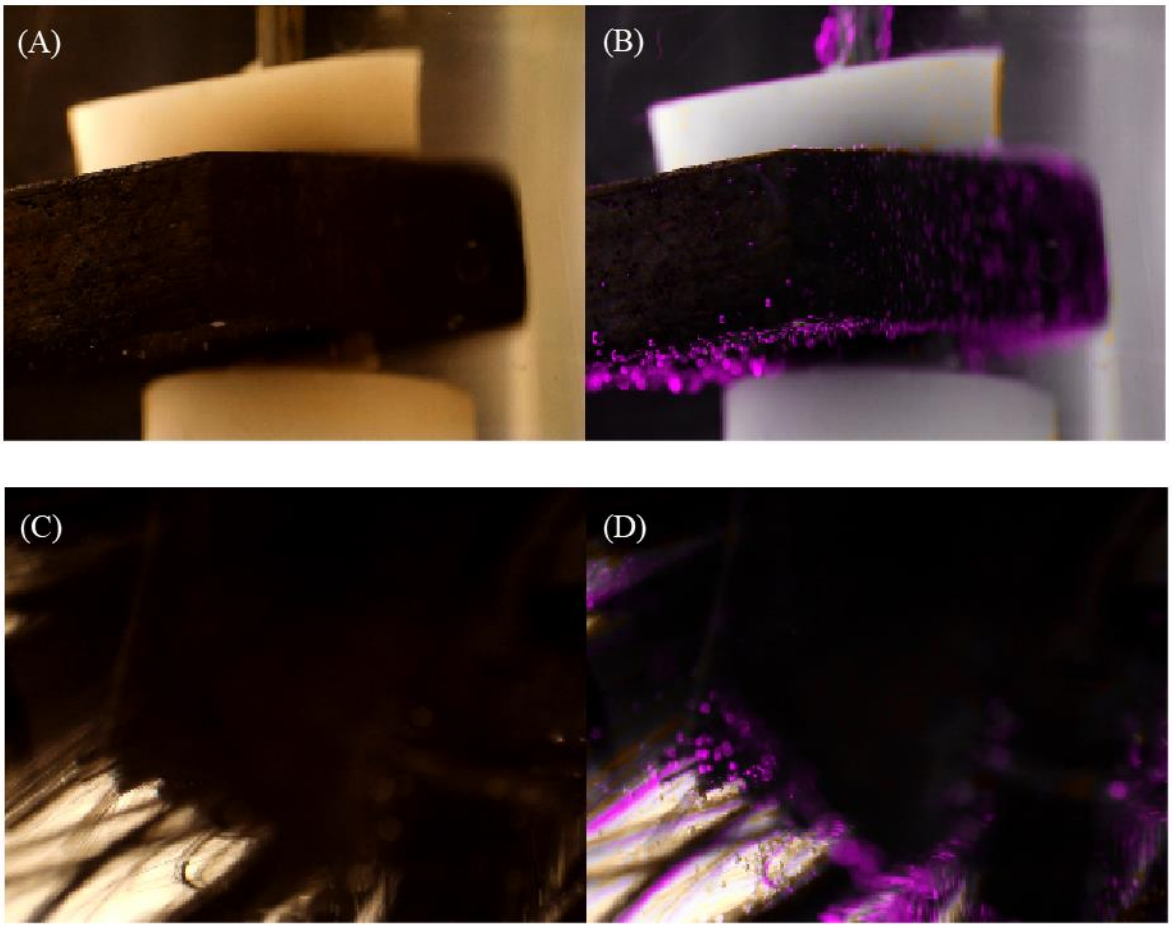

Fig. II.10. H_2 bubble segmentation on single video frames of the cathode surface of Runs 2 and 3 from Table II.1. Frames (A) and (B) show a graphite electrode before and after bubble nucleation, with magenta pixels highlighting the bubbles. Frames (C) and (D) show a carbon brush electrode before and after bubble nucleation, with magenta pixels indicating the bubbles. This method was used to quantify bubble formation through image analysis

In Fig. II.10A the graphite electrode is shown before nucleation started, and in Fig. II.10B, after nucleation started, where 7% of the total pixels of the frame are colored magenta due to the apparition of bubbles. Similarly, in Fig. II.10C and Fig. II.10D, the frames before and after nucleation are shown where the magenta pixels account for a 21% of the total pixels. By tracking the increase in the value of pixels with a specific intensity change threshold, it would

be possible to detect the nucleation of H_2 bubbles in the cathode. This approach is further explored and detailed in Chapter IV.

II-4. Discussion

The use of a Pt wire electrode as an indicator of the H_2 concentration level proved to be impractical based on the many controlled conditions that would be necessary to be implemented according to the results presented in this chapter. First, it is worth noting that the potential measured by the Pt wire was a “mixed potential” with a non-linear response to all of the possible sensor effective redox couples and not an exclusive Nernstian potential of the H_2/H^+ redox pair. In a complex biological growth medium, other redox pairs such as Fe^{2+}/Fe^{3+}, Mn^{2+}/Mn^{4+} or O_2/H_2O [153]. Here, it was proven that the Pt wire potential dropped when oxygen was being removed at a much slower rate than the expected, based on individual measurements of dissolved O_2 concentrations. This could be due to the fact that the oxygen redox reactions is kinetically slow, requiring long times to reach and measure an equilibrium potential [153]. On the contrary, the Pt electrode reached an equilibrium potential during the electrolysis step at a much shorter time than the one measured with the amperometric H_2 sensor. Besides the interference with other redox couples that could be affecting the mixed potential, the Pt wire electrode is not an indifferent electrode, due to capacity to adsorb species such as oxygen, hydrogen, humic acids, sulfide compounds, chloride and carbonate ions which can quickly turn into electrode poisoning of sites for electron exchange [153], [154], [155]. Moreover, a fast pseudo-equilibrium in the Pt wire potential measured at increasing H_2 bulk concentrations has also been observed by others [156], which confirms that the plateau reached on the Pt potential from this work was not a plateau reached in the dissolved H_2 concentration. Moreover, in a potential application in fermentation-spent medium, the presence of other redox active species could also affect the potentiometric measurement.

The amperometric H_2 sensor seemed to be the easiest solution to measure dissolved H_2 concentrations. Although an electromagnetic interference with the polarized cathode was also observed similar to the one presented in this chapter for the Pt electrode, this could be easily bypassed by doing an offset correction previous before the start of the galvanostatic experiment. Moreover, its higher selectivity makes it more applicable to fermentation-spent medium. The main drawback of this sensor was the fast degradation of the sensing element,

which required frequent replacement (6 months), increasing operational costs. Similarly, the HS-GC method proved to have great potential for the accurate measurement of dissolved H_2, although the setup implemented here required careful manipulation. Contrary to the amperometric H_2 sensor, the HS-GC detection has a long delay (~10 minutes after sampling) which although is useful for obtaining reliable measurements, it can be unfeasible for its industrial application in a control loop where fast responses are required. Similarly, a quick estimation in our group (data not shown) showed that frequent GC sampling could even be more expensive that the replacement of the sensing element of the amperometric H_2 sensor.

The use of gas-tight instruments and the automation of sampling extraction and equilibration could be implemented for a more robust method that gets rid of the manipulation expertise required in the manual alternative. More importantly, an implementation of the HS-GC with an N2 gas headspace would also be useful for detecting other important dissolved gases in the fermentation medium such as O_2 and CO_2.

In the detection of H_2 nucleation, measuring the concentration of the headspace of the cathodic chamber also proved to be inadequate in the water electroreduction setup (here measured with a semiconducting metal oxide sensor, SMO), as reaching the H_2 liquid-gas phase equilibrium is undesired. Moreover, bubbles were detected only when they were detached from the electrode surface which adds a delay in the effective detection. A more promising alternative is the use of a digital camera for the detection of bubble nucleation on the cathode surface. This method, besides having little detection delay, is also easy to implement. Nonetheless, a proper algorithm for the detection of bubbles needs to be implemented, which is further explored in Chapter IV. With the digital camera, only the projected surface area is recorded since it is where the highest current density is expected and therefore the start of nucleation. Nonetheless, it would be necessary to also detect possible bubble formation inside the porosity of the cathode or in turbid medium, for which other techniques such as operando high frequency impedance measurements might be also implemented for a more robust detection [157].

The measurement of dissolved H_2 concentration and/or H_2 bubble nucleation its necessary due to the expected variable H_2 uptake rates of the coupled hydrogenotrophic processes. In consequence, this requires also variable H_2 production rates, which are achieved by a control system on the imposed current. Matching the applied current to the H_2 uptake rate during

operation can be used to avoid local H_2 accumulation and therefore nucleation, but also to maximize coulombic efficiency, CO_2 utilization and help to stabilize pH when also using optical density as a control parameter [158]. The avoidance of bubble nucleation by current control becomes even more relevant by the fact that pre-existing gas cavities are the main cause for bubble nucleation and growth[159]. This was demonstrated by showing that bubble-free H_2 supersaturation (> 25-times the saturation concentration) near the cathode surface occurs only in the absence of pre-existing H_2 gas pockets generated during water electroreduction at larger currents, and only bringing the current back to almost zero could deplete these gas pockets and restore the supersaturation behavior before bubble nucleation [160]. Moreover, the control of the imposed current on a potentiostat based on external sensors such as a digital camera is not well documented. A proof of concept developed and tested is described for the galvanostatic control of a VSP potentiostat, described in the Supplemental Information B.

Future experiments in this manuscript were done using a potassium phosphate buffered media (pH = 7.2, 0.1M) due to the more realistic ionic conductivity that the catholyte of a water electroreduction cell might have (compatible with acetogens as used by LaBelle *et. al.* [17]) and the better H_2 solubilization kinetics obtained with an electrolyte of higher conductivity (see Supplemental Information C). Although the optimization of the medium composition or the role of the conductivity was not further addressed experimentally in this manuscript, in Chapter V, some insights of the effect of the ionic conductivity of the catholyte on the H_2 solubilization are given by means of a Multiphysics simulation.

II-5. Conclusion

This work demonstrates the critical need for robust and reliable H_2 sensing technologies to optimize hydrogen delivery from water electroreduction for hydrogenotrophic processes. Here, it was determined that the potentiometric H_2 measurements done by a Pt wire electrode, are fundamentally limited by issues of selectivity, linearity, and signal interference. While the amperometric H_2 sensor and HS-GC provide accurate dissolved H_2 data, their individual operational constraints (short sensor lifespan and manual labor, respectively) hinder their utility for continuous, in-situ control. Developing a more robust and automated HS-GC method would be a great tool for the implementation of measuring dissolved H_2 (and other

dissolved gases such as CO_2, CO or O_2) in a fermentation medium for hydrogenotrophic bioprocesses.

It could be established that monitoring the headspace gas of the cathodic chamber (here done with an SMO sensor) is not an effective approach for the detection of bubble nucleation at the electrode surface, reinforcing the distinction between hydrogen solubilization and gas evolution. The most compelling finding is the potential of optical methods, such as a digital camera, to provide a direct, non-invasive, and timely signal for bubble nucleation events. This optical approach could serve as a feedback mechanism, enabling the real-time control of the imposed current to maintain bubble-free conditions and maximize solubilization efficiency. In the following chapters, the H_2 solubilization of water electroreduction vs gas injection was studied using an amperometric H_2 sensor, while an algorithm for the detection of bubble nucleation at the cathodic surface was developed with the use of a digital camera as data input.

Chapter III. Electroreduction of water: A Promising Alternative to Gas Injection for the Solubilization of Hydrogen in Biological Processes Involving Hydrogenotrophs.

Published article: https://doi.org/10.1016/j.cej.2025.168494

ABSTRACT

Hydrogenotrophic microorganisms reduce organic or inorganic molecules coupled with the oxidation of H_2, for the production of valuable products such as carboxylic acids, methane, and ethanol, as well as the reduction of sulfates, nitrates or iron for remediation applications. H_2 is usually dissolved by gas injection but the low gas-to-liquid mass transfer limits its biotic uptake. This chapter proposes water electroreduction as an alternative to gas injection for dissolving H_2. To evaluate this new approach, the following questions are approached in this chapter: How do water electroreduction and traditional gas injection compare in terms of H_2 solubilization rate, maximum concentration achieved in the medium and energy consumption per mole of H_2 solubilized?

The two H_2 solubilization techniques were evaluated in a 0.8 L potassium phosphate buffered medium (0.1 mol·L^{-1}, pH = 7.2) used as a representative medium for the enrichment and study of hydrogenotrophic microorganisms. Although the H_2 production rate of water electroreduction was around 18 times lower than the H_2 supply rate used during gas injection, both techniques achieved similar H_2 solubilization rate but different solubilization efficiencies. To reach a solubilization rate of 0.67 mmol·L^{-1}·h^{-1} by water electroreduction, 1.87 mmol·h^{-1} of H_2 were produced, yielding a 35% solubilization efficiency. In contrast, achieving a comparable solubilization rate of 0.79 mmol·L^{-1}·h^{-1} via gas injection required an injection of 42 mmol·h^{-1}, corresponding to a solubilization efficiency of only 2%. Moreover, the maximum concentration of dissolved H_2 reached (0.62 mmol·L^{-1}) by gas injection was limited by the saturation concentration at 1 bar (0.78 mmol·L^{-1}), while by water electroreduction it reached 1.21 mmol·L^{-1}. The potential of this high concentration of dissolved H_2 achieved by water

electroreduction is also discussed in terms of its potential to enhance metabolite production rates and selectivity during hydrogenotrophic bioprocesses.

III-1. Introduction

Hydrogenotropic microorganisms can reduce a wide variety of substrates such as carboxylic acids, aldehydes, alcohols and inorganic molecules by using dissolved H_2 as electron source. From the compilation of 73 different hydrogenotrophic reactions made by Thauer *et al* [53], it can be observed that the range of application spans from the reduction of organic/inorganic carbon to produce metabolites of added value (e.g., acetogenesis, methanogenesis and solventogenesis) to the reduction of inorganic electron acceptors for remediation applications (e.g., denitrification, sulfate reduction, ferric iron reduction) [53], [145], [161], [162], [163], [164].

Controlling the H_2 concentration is fundamental for selecting specific strains within bioreactors with a mixed consortium of microorganisms, due to their specific kinetics, thermodynamics and energetics. As noted by Muñoz *et al*, strains with highest H_2 thresholds (minimum H_2 concentration required for making the H_2 uptake thermodynamically feasible) such as *Clostridium sp.* (threshold range: 2000-15000 $nmol \cdot L^{-1}$) are usually enriched in consortia with high H_2 concentrations, while at *Sporomusa sp.* (threshold range: 40-100 $nmol \cdot L^{-1}$) are enriched at low H_2 concentrations, in hand with methanogens [58].As an example, working at low H_2 concentrations would help favoring the competition of methanogens [55], [165].

In bioreactors where low H_2 concentrations are not needed to favor strains with high affinity for soluble H_2 (i.e. low H_2 thresholds), working at high H_2 concentrations might also favor high product yields and their selectivity. Muñoz *et al* found that different species of hydrogenotrophic acetogens (*Clostridium sp, Sporomusa sp* and *Acetobacterium sp*) were not inhibited by high concentrations of H_2 up to saturation concentration, (just below 0.78 $mmol \cdot L^{-1}$ at 1 bar of H_2) and its H_2 consumption rate followed first-order kinetics [166]. Besides favoring the production rate of metabolites, additional reducing equivalents in the form of H_2 are required to shift acetogenesis into solventogenesis with capable strains. Stoichiometrically, 4 moles of H_2 are needed to reduce 2 moles of CO_2 into 1 mol of acetate (H_2:CO_2 = 2:1), but 2

additional H_2 moles are needed to reduce 1 mole of acetate into ethanol (H_2:CO_2 = 3:1). The addition of reducing equivalents in the form of H_2 for solventogenesis was also demonstrated by Valgepea *et al* when the addition of 3 moles of H_2 per mol of CO in the gas feed allowed to increase the ethanol/acetate product ratio 5 times when working with *C. autoethanogenum* [43].

In summary, maintaining high concentrations of H_2 has an effect on the competition of hydrogenotrophic species (favoring the ones with high H_2 thresholds/affinities) and on the selection of other metabolites (making the production of alcohols and long chain carboxylic acids thermodynamically feasible), while still maintaining high H_2 uptake rates (not limited by the classical substrate saturation found in Monod-like growth kinetics). In practice, maintaining high concentrations of H_2 in the liquid medium is technically challenging. The limitations and their workarounds are described in the following sections.

III-1.1 Limitations on achieving high H_2 concentration in the liquid medium

The traditional approach to supply H_2 in bioreactors is to inject H_2 gas. Around two thirds of the total H_2 production in 2023 came from steam methane reforming (SMR), with water electrolysis accounting for less than 1% of the global production [167]. The main drawback of using gas injection is the slow gas-to-liquid mass transfer of H_2 due to the low solubility of H_2 in water [38] (45 times lower than CO_2 at 1 atm and 25 C [webbook.nist.gov]). In processes where hydrogenotrophs are involved, H_2 becomes the limiting substrate since only dissolved H_2 becomes bioavailable. Two different approaches have been found in literature so far to overcome this limitation: 1) Increasing the gas-to-liquid H_2 transfer by improving the reactor design or 2) bypassing the gas-to-liquid mass transfer by avoiding the use of gaseous H_2. These two approaches are depicted in Fig. III.1.

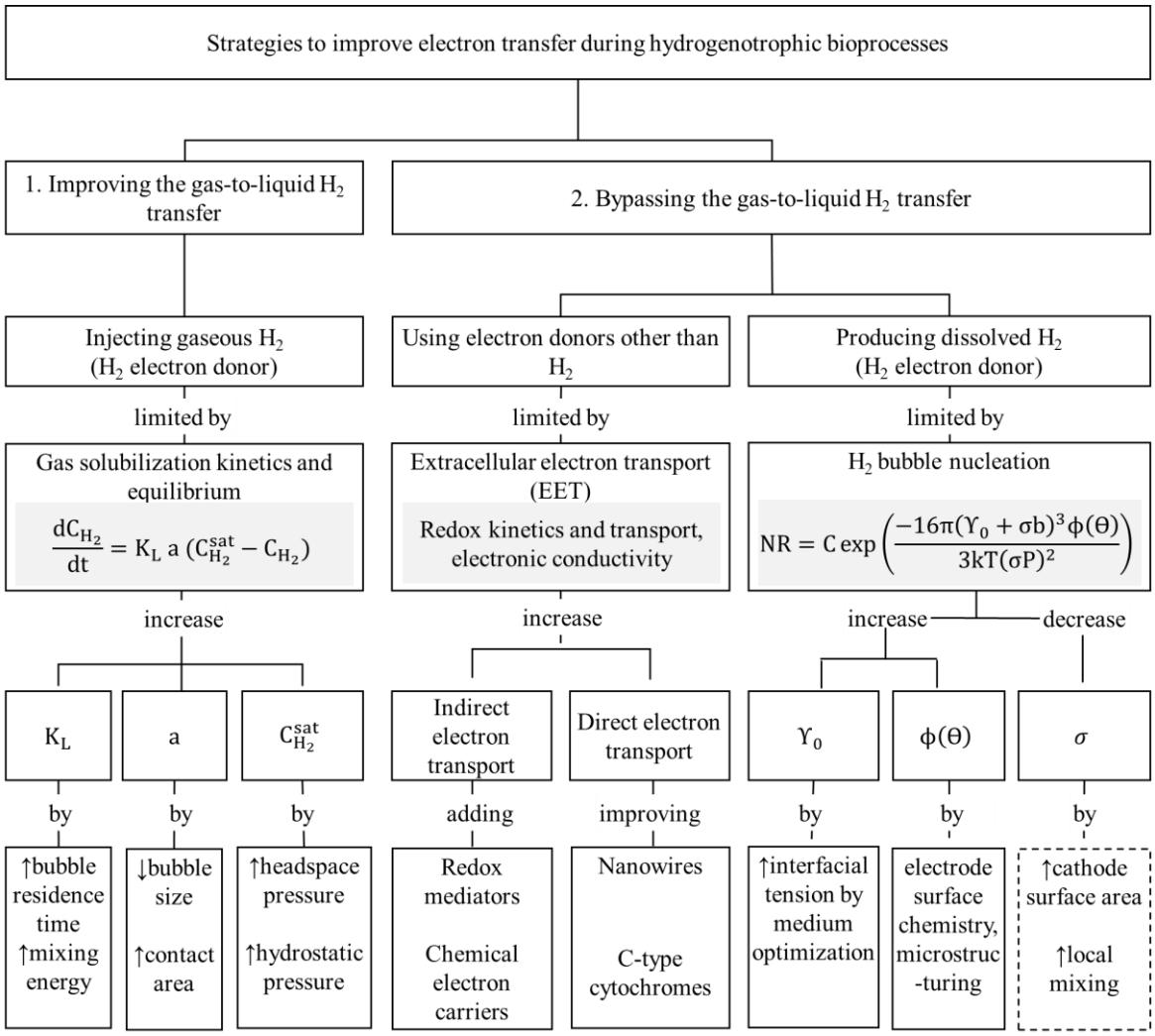

Fig. III.1. Scheme of strategies to be used to improve electron transfer during gas fermentation. The approach delimited by a dashed line is proposed here in this article.

III-1.1.1 First approach: Improving the gas-to-liquid H_2 transfer.

In practical applications where gas is injected through coarse/fine gas spargers, the resulting injected bubbles usually have diameters in the millimeter range. The solubilization rate of these millimetric bubbles is commonly described by equation 6, where the rate of H_2 solubilization is a function of characteristic parameters: K_L (overall mass transfer coefficient in the liquid phase), a (gas-liquid interfacial area) and $C_{H_2}^{sat}$ (dissolved H_2 concentration at saturation). Increasing either K_L, a or $C_{H_2}^{sat}$ results in an increased solubilization rate. K_L can be increased by the energy inputs such as agitation in the medium and the increase of bubble residence time such as in tall bubble columns[168], [169]. On the other hand, producing a large number of bubbles of small diameter is desired to increase the interfacial surface area,

which can be achieved using gas spargers with small orifices. Unfortunately, spargers with small orifices are more prone to get clogged by biomass, particulate organic matter and salt precipitates from the liquid medium, which may require often maintenance. Additionally, if orifices are too close to each other, bubbles may coalesce more easily (increasing bubble size) before departing the sparger surface [169]. Other approaches less stablished such as hollow membranes, trickle-bed reactors and nanobubble production also aim to increase the interfacial area and are already being used in bioprocessing studies [16], [170]. Lastly, higher $C_{H_2}^{sat}$ values can be obtained by increasing the gas pressure in contact with the liquid as shown in equation 7 representing Henry's law.

Although this can be achieved either using tall columns with higher hydrostatic pressure, increasing the headspace pressure in pressurized reactors is also done for this purpose with the disadvantage of the operational and safety complexities that brings the working with pressurized reactors. Another approach to increase the saturation concentration would be the injection of fine/ultrafine bubbles that should solubilize due to high internal pressures [72]. Nevertheless, working with nano/micrometric size bubbles is not common in the industry.

III-1.1.2 Second approach: Bypassing the gas-to-liquid H_2 transfer

In the second approach, the gas-to-liquid mass transfer limitation is bypassed by replacing H_2 gas injection with: A) electron sources other than H_2 and B) electrochemical production of dissolved H_2.

III-1.1.2.1. Using electron sources other than H_2

Some microorganisms can perform extracellular electron transport (EET) with conductive solid surfaces and molecules outside the cell membrane such as electrodes and redox mediators. These "electroactive" bacteria can either perform a direct or indirect EET. In direct electron transport, a biofilm forms on the electrode surface where the relay of electrons occurs through conductive "nanowires" or by membrane-bound cytochromes[103]. In indirect electron transport, redox mediators such as methyl viologen (externally added) and flavins (produced biologically in-situ) get continuously oxidized/reduced between the electrode and the microorganisms [107]. Other molecules such as formate, ammonia and Fe^{2+} can be electrochemically produced and used as soluble electron carriers during the fermentation of

gases, but reported product yields from Fe^{2+}/NH_3 oxidizers have been comparatively lower than using H_2 by hydrogenotrophic acetogens/methanogens [13], [171].

When electrodes (cathodes) work as electron donors for electroactive bacteria, the bioprocess is commonly called microbial electrosynthesis (MES) [18]. Similarly to common hydrogenotrophic bacteria, acetate, methane and alcohols are also the main products usually targeted [172]. While some hydrogenotrophic acetogens have been reported to be able to perform EET in electroactive biofilms attached to the electrode, the reduced spatial distribution of cells in contact with the electrode surface might limit the electron transfer [40]. It has been suggested that a MES for CO_2 reduction with mixed cultures may work preferably with indirect EET, where H_2 is produced but quickly consumed by the surrounding hydrogenotrophs. LaBelle *et al* found that acetate yield in MES was enhanced with increasing H_2 production at low cathodic potentials [118]. Blanchet *et al* tested a MES at: -0.36 V and -0.66V vs SHE as fixed cathodic potentials, but acetate was produced only at -0.66V [119]. They attributed the electron uptake and production of acetate being mediated by H_2, which is theoretically produced at potentials lower than -0.41 V vs SHE. The slow kinetics of biofilm electron uptake vs H_2-mediated electron uptake are also discussed elsewhere in favor of using planktonic bacteria for CO_2 reduction in a MES [16].

III-1.1.2.2. Production of dissolved H_2

The produced H_2 in a cathodic surface by water electroreduction does not immediately evolves into the gas phase. H_2 molecules are first produced and dissolved in the liquid phase. The first requisite for the bubble evolution is to surpass a certain concentration threshold, which is larger than the saturation concentration (therefore, bubble nucleation occurs at a local supersaturation of H_2). The rate of bubble nucleation can vary according to cathode irregularities and its surface chemistry, and the interfacial tension between the gas-liquid phase [120] as shown described by the CNT. The nucleation of bubbles reduces the solubilization efficiency which is undesirable for hydrogenotrophic processes. To reduce the bubbling rate, it would be possible to increase the interfacial tension, the wettability, or reduce the local supersaturation near the cathodic surface.

Increasing the surface tension of a liquid might be harder to achieve than reducing it using surfactants. Surfactants tend adsorb at the cathode surface which in turn reduce the current necessary to start the nucleation of bubbles [132], [133]. Wettability has also been studied in

abiotic electrolyzers with the goal of fast H_2 gas formation and removal. For example, the increase of bubble coalescence and formation of large bubbles was favored when the surface of a nickel foam cathode was coated with PTFE due to the decrease in wettability [136]. The local concentration of dissolved H_2 can be decreased in reactors when the current density is homogeneously distributed on the cathode surface. This can be achieved by using porous electrodes with large surface area per occupied volume. Also, efficient mixing of the catholyte should reduce the local accumulation of H_2 near the cathode surface. In a MES where methane is targeted as the main product from the oxidation of electrochemically produced H_2 and the reduction of CO_2 by *M. maripaludis*, using 3D-printed electrodes with large surface area per volume allowed to reduce the H_2 waste due to the absence of bubble nucleation, and therefore the production of methane was increased [42].

Although MES can involve an electron-carrying H_2 intermediate, the electrochemical production of dissolved H_2 by water electroreduction has not been extensively considered to physically decouple the electrolytic H_2 saturation of the liquid medium from the biotic H_2 uptake in hydrogenotrophic processes. To evaluate the potential advantages/disadvantages of water electroreduction over gas injection, it could be interesting to answer: How do water electroreduction and traditional gas injection compare in terms of H_2 solubilization rate, maximum concentration achieved in the medium and energy consumption per mole of H_2 solubilized?

The present work focuses on the comparison of the H_2 solubilization in a potassium phosphate buffer solution by 1) water electroreduction and 2) H_2 gas injection. Both solubilization techniques were evaluated based on the maximum achieved dissolved H_2 concentration, the H_2 solubilization rate, the H_2 solubilization efficiency and the energy consumption. Lastly, an analysis on how the distinct kinetics of H_2 solubilization can influence the competition between hydrogenotrophs as well as the product selectivity, is done based on the thermodynamic potential of common hydrogenotrophic reactions measured by the Gibbs free energy of reaction.

III-2. Materials and methods

III-2.1 Reactor setup used for both H_2 solubilization techniques

A potassium phosphate buffer solution was used as liquid medium (electrolyte) containing 10.7 $g \cdot L^{-1}$ of K_2HPO_4 and 5.2 $g \cdot L^{-1}$ of KH_2PO_4 (pH = 7.2, 12.7 $mS \cdot cm^{-1}$) to simulate the buffering capacity of a growth medium used for acetogenesis in a microbial electrosynthesis cell [17]. The liquid medium was sparged with N_2 gas for 10 minutes using a glass frit (VitraPOR Micro-immersion-filter Por 2, Robu, Germany) of 10 mm of diameter and 4 mm of thickness, prior to the start of each experiment to remove traces of dissolved gases such as H_2 and O_2. A two-chamber H-type cell (Duran Schott GLS 80® with side connection) was used as a reactor with a 4-port screw cap (Duran GLS 80 ® 4-port EPDM seal), with a working volume of 0.8 L on each chamber and separated by a cation exchange membrane of 5 cm of diameter (CMI 7000S, Membranes International Inc, USA) as shown in Fig. III.2A. The liquid medium was agitated with a magnetic stirrer at 370 rpm in both H_2 solubilization techniques. The dissolved H_2 concentration was measured using an amperometric H_2 probe (MS08, Aquams, France). The H-type cell was open to air through one of the screw cap ports to avoid the impact of different headspace pressures on the solubilization of H_2. Therefore, a small ingress of oxygen to the liquid could be expected (and get reduced in the catholyte) but its concentration does not interfere with the H_2 sensor readings (although a diminished solubilization efficiency during water electroreduction could be expected). At the end of each experiment, the dissolved H_2 concentration of a liquid sample of 50 mL was measured by equilibrating the aliquot with a 5 mL headspace and further analyzed with the headspace gas chromatography method (See Supplemental Information A for further details).

For the water electroreduction technique, a DSA® plate of 2.5×5.3×0.1 cm (projected area: 13.25 cm^2; Di Noer Technology Co. Ltd, China) was used as a counter electrode (i.e., anode here). A carbon brush (6TMIC Ing,. France) occupying a diameter of 5 cm and 8 cm of height (projected surface area: 40 cm^2, bulk volume: 157 cm^3) was used as a working electrode (i.e., cathode here, Fig. III.2C). Prior to the use of the electrodes, the carbon brush was thermochemically treated by thermal activation in a muffle furnace at 380 C for 2 hours. Afterwards, the carbon brush was cleaned by successively immersion in the following solutions under stirring: Ethanol:Acetone (1:1) for 20 minutes, distilled water for 20 minutes, 1 M HCl

for 1 hour, distilled water for 20 minutes, 1 M NaOH for 1 hour, and distilled water for 20 minutes. The DSA anodes are cleaned by applying an anodic current density of 250 $A \cdot m^{-2}$ in a 0.1 $mol \cdot L^{-1}$ sulfuric acid solution for 5 hours. A titanium and stainless-steel rod were used as current collectors respectively for the working and counter electrodes.

For the H_2 gas injection technique, no electrodes were submerged in any compartment. Instead, a glass frit (VitraPOR Micro-immersion-filter Por 2, Thermo Fisher Scientific, France) was used for the H_2 gas injection as shown in Fig. III.2B.

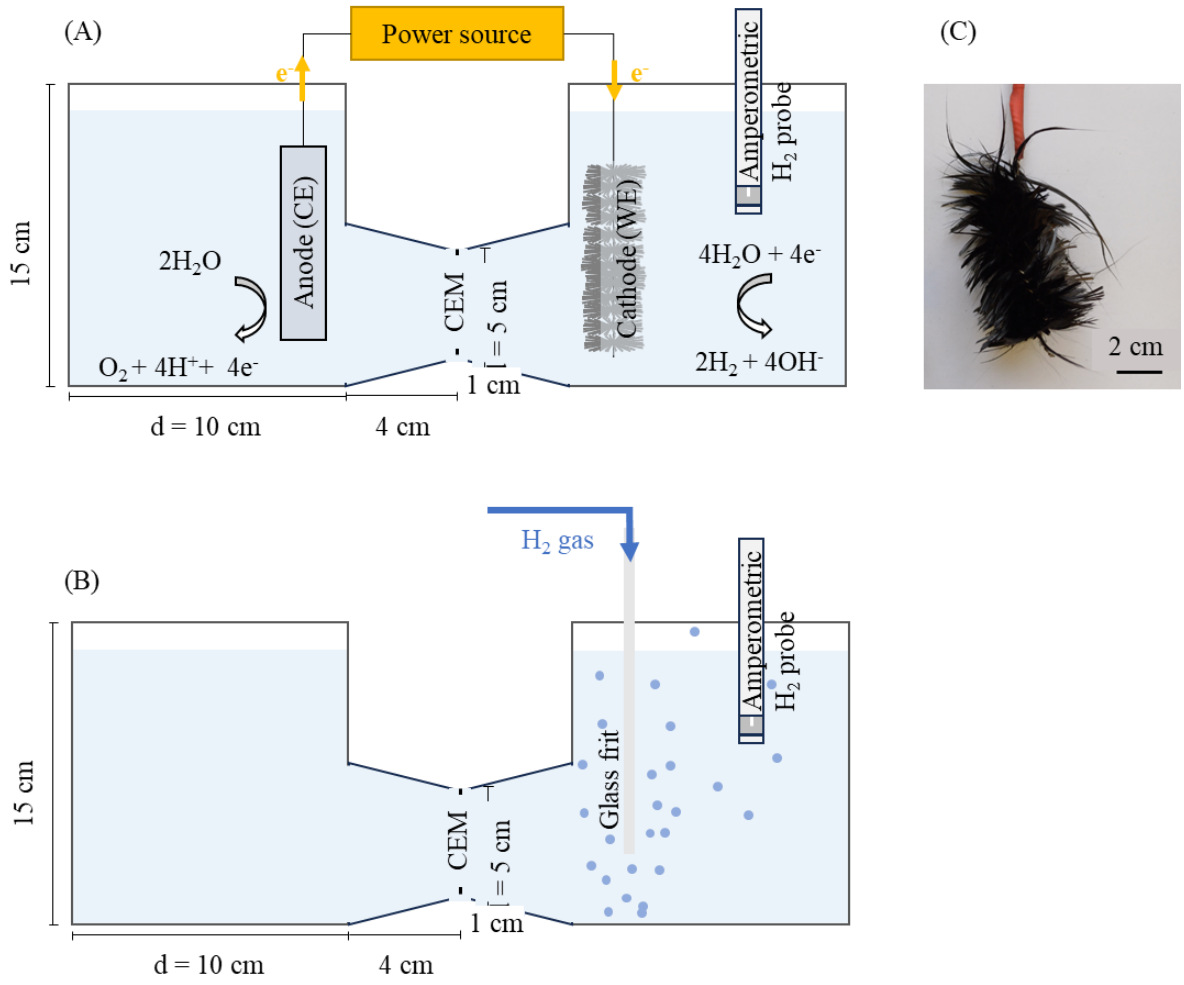

Fig. III.2. Experimental setup of the two-chamber H-type cell used during (A) water electroreduction and (B) H_2 gas injection. The cathode material used during water electroreduction is shown in (C). CE: Counter electrode (DSA anode); WE: Working electrode (Carbon brush cathode); CEM: Cation exchange membrane.

III-2.2 Design of experiments

Three different H_2 supply rates were used for each one of the H_2 solubilization techniques evaluated. The values of each H_2 supply rate and their corresponding fixed current and gas injection rates are summarized in Table III.1.

Table III.1. Experimental conditions evaluated for each H_2 solubilization technique

H_2 solubilization technique	H_2 supply rate [mmol·h^{-1}]
Water electroreduction	
20 mA	0.37
60 mA	1.12
100 mA	1.87
H_2 gas injection	
1 L·h^{-1}	42
2 L·h^{-1}	83
3 L·h^{-1}	125

A potentiostat (VSP, BioLogic) was used as a power source to perform chronopotentiometry (CP) for applying a constant current, between 20-100 mA, at the working electrode during the production of dissolved H_2 through water electroreduction. The lowest current applied, 20 mA, was chosen due to allowing to reach a steady state concentration in around 5 h (smaller currents could take longer, making the experiment unnecessarily long), while 100 was the maximum current it could be imposed before reaching the cell voltage security limits (10 V) in the H-type cell. For H_2 gas injection, a mass flow meter (Bronkhorst EL-FLOW select, France) was used to set the H_2 supply rate between 1 L·h^{-1} (minimum to overcome the glass frit pressure drop) and 3 L·h^{-1} (maximum allowed by the flow meter).

III-2.3 Solubilization rate and efficiency

The H_2 solubilization rate in mmol·L^{-1}·h^{-1}, was calculated by dividing the concentration change by the time it takes to increase the concentration of dissolved H_2 from 0 to 0.5 mmol·L^{-1} per liter of liquid medium. Values larger than 0.5 mmol·L^{-1} were not used for the calculation since

the H_2 solubilization rate with gas injection quickly drops at larger values due to approaching the saturation concentration.

The percentual solubilization efficiency (s_{eff}) was calculated for every point in time as shown in equation 20:

$$s_{eff}(t) = 100 \cdot \frac{n_d(t)}{n_s(t)} \qquad 20$$

$$n_d(t) = \frac{V_c \cdot C_{H_2}(t)}{M_w}$$

$$n_s(t) = \frac{Q_{H_2} \cdot t}{V_M}$$

Where n_d are the moles of H_2 dissolved in the liquid (mmol·L^{-1}); n_s are moles of H_2 supplied in the system (by gas injection or water electroreduction) (mmol·L^{-1}); V_c is the volume of the catholyte (0.8 L); C_{H_2} is the measured dissolved H_2 concentration (mg·L^{-1}); M_w is the molar weight of H_2 (2 mg·mmol^{-1}), Q_{H_2} is the volumetric H_2 supply rate (nL·h^{-1}); t is the time of measurement (h); and V_M is the molar volume (0.024 L ·mmol^{-1} at room conditions).

For the H_2 solubilization kinetics comparison between the biological uptake rate and the solubilization rate, the datapoints from dissolved H_2 concentration vs time were first smoothed through a median filter (*medfilt1* MATLAB's function). The solubilization rate was then calculated using the gradient of the concentration over time (*gradient* MATLAB's function) and finally, a linear model was fitted between the solubilization rate and the dissolved H_2 concentration (*fitlm* MATLAB's function).

III-2.4 Energy consumption

The energy consumption was calculated using the solubilization rate measured between 0-0.5 mmol·L^{-1} as described above. The energy consumption is expressed as MJ per mol of solubilized H_2. For water electroreduction, the energy consumed per mol of solubilized H_2 (E_{we}) is calculated as shown in equation 21:

$$E_{we} = (V_{cell} \cdot I)\frac{1}{V_c \cdot R_{sol}} \cdot \left(\frac{1\ MJ}{1x10^6\ J}\right) \qquad 21$$

Where V_{cell} (V) is the cell voltage, I (A) is the imposed current and R_{sol} (mol·m^{-3}·s^{-1}) is the H_2 solubilization rate. For the calculation of the energy consumption, the first approximation was to include the energy consumed during the production of H_2 with the energy consumed during the compression. The energy consumed during the production per mol of H_2 solubilized (E_{smr}) was calculated based on a life cycle analysis done on the steam methane reforming process, using the total energy used by the system (natural gas and non-feedstock): 183.2 MJ/kg H_2 [173] and using it in equation 22:

$$E_{smr} = 183.2 \frac{MJ}{kg\ H_2} \cdot \left(\frac{0.002\ kg\ H_2}{1\ mol\ H_2}\right) \cdot \frac{R_{sup}}{V_c \cdot R_{sol}} \quad 22$$

Where R_{sup}(mol·s^{-1}) is the molar H_2 supply rate. To calculate the compression energy, it was calculated first the required pressure to overcome the pressure drop from the glass frit (ΔP_{frit} , Pa) using Darcy's law in equation 23:

$$\Delta P_{frit} = \frac{R_{sup}^{V} \cdot \mu_g \cdot L}{k \cdot A} \quad 23$$

Where R_{sup}^{V} (m^3·s^{-1}) is the H_2 supply rate in volumetric units, μ_g (8.9×10^{-6} Pa·s) is the dynamic viscosity of H_2, L (0.004 m) is the glass frit thickness, k (2.9×10^{-11} m^2) is Darcy's permeability of the glass frit, and A (7.85×10^{-5} m^2) is the cross-sectional area of the glass frit. The energy of compression per mol of H_2 solubilized (E_{comp}) can be calculated using equation 24:

$$E_{comp} = \left(\frac{R_{sup}}{Vol \cdot R_{sol}}\right) \cdot \left(\frac{1}{\in} \cdot R \cdot T \cdot \ln\left(\frac{P_2}{P_1}\right)\right) \cdot \left(\frac{1\ MJ}{1x10^6\ J}\right) \quad 24$$

Where $\in$ [0.8 unitless] is the energy efficiency of compression, P_2 (Pa) is the pressure needed to overcome the pressure drop from the glass frit and P_1 (Pa) is the inlet pressure to the compressor coming from the steam methane reforming process. A quick calculation ΔP_{frit} for the case where H_2 is supplied at a rate of 125 mmol·h^{-1} (R_{sup}^{V} = 8.3×10^{-7} m^3·s^{-1}) would result in a very small ΔP_{frit} = 13 Pa. Even assuming a large compression work from 1 bar to 250 bar (high pressure H_2 gas cylinder), this would result in the energy of compression being around 5% of the energy used during the H_2 production by steam methane reforming. Therefore, the calculations for energy consumption in gas injection only consider the energy associated with the H_2 production by steam methane reforming.

A third hypothetical case was evaluated where H_2 was produced with an ideal water electrolyzer at 1.48 V [174] producing H_2 gas with a solubilization efficiency of 1.5 % (based on the experimental results obtained here for gas injection). Assuming all of the electric current imposed is converted to H_2 gas, the solubilization rate can be expressed as $\mathrm{R_{sol}} = (0.015) \cdot \mathrm{I}$ to calculate the energy consumption by using equation 21.

III-2.5 Modelling the thermodynamic potential of hydrogenotrophic reactions at different H_2 solubilization kinetics

A comparison of the thermodynamic potential (feasibility) of different hydrogenotrophic reactions as a function of the H_2 concentration is done based on their Gibbs free energy change as shown in Table III.2.

Table III.2. Standard Gibbs Free Energy of Reaction ($\Delta G_r^{0\prime}$) of different hydrogenotrophic reactions adjusted at pH = 7.

Reaction	Stoichiometry	$\Delta G_r^{0\prime}$ [kJ/reaction][1]
Sulfate reduction	$SO_4^{2-} + 4H_2 + H^+ \rightarrow HS^- + 4H_2O$	-94.8
Methanogenesis	$CO_2 + 4H_2 \rightarrow CH_4 + 2H_2O$	-131
Acetogenesis	$2CO_2 + 4H_2 \rightarrow CH_3COO^- + H^+ + 2H_2O$	-152
Ethanol production	$CH_3COO^- + H^+ + 2H_2 \rightarrow CH_3CH_2OH + H_2O$	-9.51

[1] The values of $\Delta G_r^{0\prime}$ were calculated by adjusting to pH = 7, the ΔG_r^0 obtained from the energies of formation compiled in the NBS tables [175].

To establish the feasibility at operational conditions during hydrogenotrophic processes, the following mass balance on the H_2 and CO_2 concentration was solved at steady state $\left(\frac{dC_i}{dt} = 0\right)$: to simulate a continuous bioreactor where H_2 and CO_2 are consumed by hydrogenotrophic acetogens:

$$\frac{dC_{H_2}}{dt} = -k_1^x X\left(C_{H_2}\right) + K_L a\left(C_{H_2}^{sat} - C_{H_2}\right) \quad 25$$

$$\frac{dC_{CO_2}}{dt} = -\frac{k_1^x X}{Y}\left(C_{H_2}\right) + K_L' a\left(C_{CO_2}^{sat} - C_{CO_2}\right) \quad 26$$

Where k_1^x is the biomass specific H_2 uptake rate, X is the biomass concentration, $C_{H_2}^{sat}$ and $C_{CO_2}^{sat}$ are the gas saturation concentrations characteristic of the solubilization technique, Y is the

stoichiometric ratio of CO_2 to H_2 uptake and K_La and K'_La are the overall mass transfer/solubilization coefficients of H_2 and CO_2. The values taken for these parameters were chosen to represent the two scenarios under different H_2 solubilization limitations, and their values are tabulated in Table III.3.

Table III.3. Kinetic parameters used for the study of the two kinetic scenarios simulated

Scenario	K_La [h^{-1}]	k_1^x [$h^{-1}\cdot(g_{dw}\cdot L^{-1})^{-1}$]	X [$g_{dw}\cdot L^{-1}$] at steady state	K_La to k_1^xX ratio	
				Calculated	Range
(1) Slow H_2 solubilization	0.062 [89]	60.93 [166]	1.4 [43]	7.27×10^{-4}	1×10^{-4} to 1×10^{-1}
(2) Fast H_2 solubilization	2280 [9]	8.19 [166]	0.5 [43]	557	1×10^{0} to 1×10^{3}

In the first scenario, it is assumed that the process is limited by the H_2 solubilization rate, characterized by low K_La to k_1^xX ratios, while the second scenario assumes that there is no limitation by H_2 solubilization, characterized by larger K_La to k_1^xX ratios (a reciprocal of the Damköhler number I), with the purpose of shifting acetate production to ethanol. For both scenarios, Y was taken as 2 (see stoichiometry of acetogenesis at Table 3) and $\frac{K'_La}{K_La}\sqrt{\frac{D_{CO_2}}{D_{H_2}}} = 0.65$ [9] were used for a system at steady state at 1 bar and 298 K. $C_{H_2}^{sat}$ was varied from 0.78 mmol·L^{-1} (characteristic of gas injection at 1 bar) to 5.5 mmol·L^{-1}, the latter corresponding to the supersaturation concentration experimentally found in microelectrode described by Lubetkin during water electroreduction [129].

Once the steady state concentrations of H_2 and CO_2 are obtained from the different kinetic scenarios described above, the ΔG_r of Acetogenesis and Ethanol production is calculated using equation 4.

All calculations and simulation scenarios were performed in MATLAB R2024a (MathWorks Inc., Natick, Massachusetts, United States, RRID:SCR_001622).

III-3. Results

III-3.1 H_2 solubilization kinetics

The kinetics of H_2 solubilization obtained for each one of the techniques listed in Table 1 are shown in Fig. III.3. At first sight, although the gas injection curves reached their saturation concentration faster than with water electroreduction, the maximum concentration of dissolved H_2 achieved was lower than the maximum concentration obtained during water electroreduction. For the three H_2 supply rates used for gas injection, the maximum dissolved H_2 concentration achieved varied from 0.58 mmol·L^{-1} to 0.62 mmol·L^{-1}, which was just below the theoretical equilibrium concentration of 0.78 mmol·L^{-1}. On the contrary, the maximum concentration of dissolved H_2 greatly varied with the H_2 supply rate during water electroreduction, from 0.51-1.21 mmol·L^{-1}, surpassing the equilibrium concentration of 0.78 mmol·L^{-1}. These supersaturation concentrations fall into the range previously reported by Kikuchi *et al.,* where dissolved H_2 concentrations of 0.9-1.25 mmol·L^{-1} were obtained at the outlet of water electroreduction cells operated with a continuous fresh electrolyte flow [75], [121]. They reported that the maximum concentration of dissolved H_2 achieved was limited at high current densities due to the accumulation of a high bubble population density and high bubble growth rate, which quickly transported the dissolved H_2 into the gas bubbles.

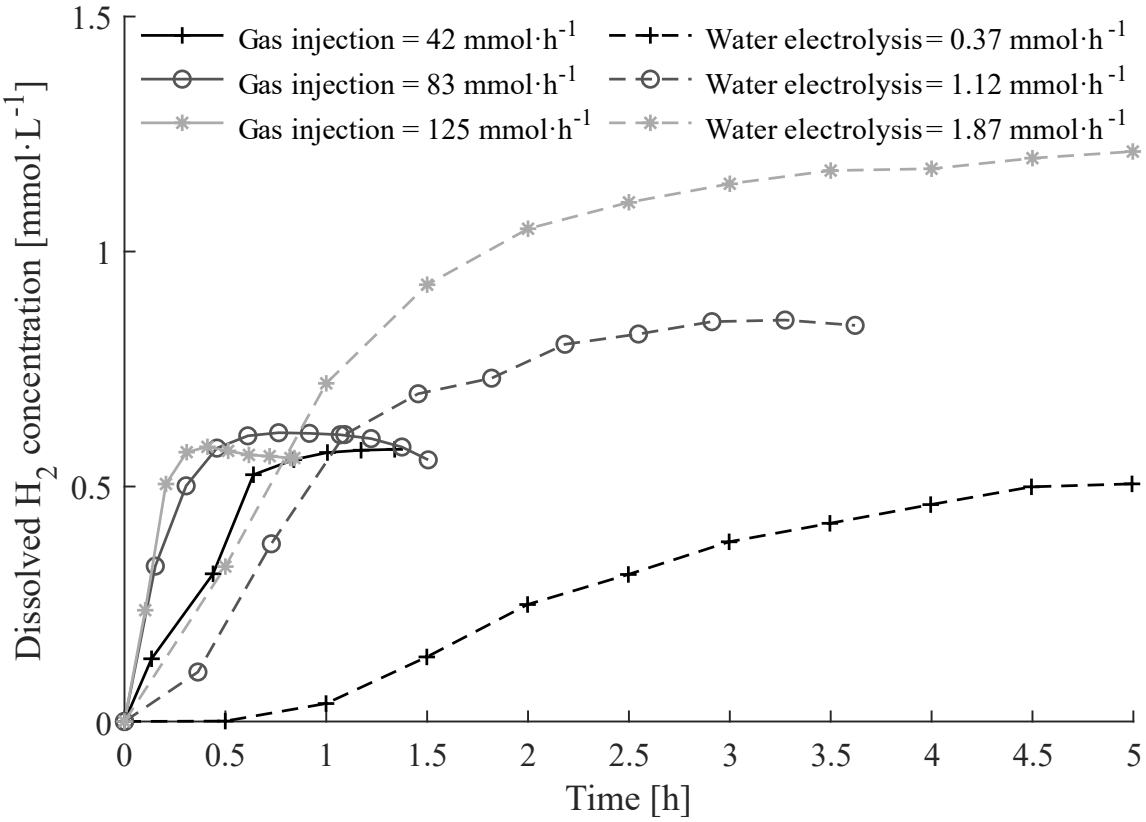

Fig. III.3. H_2 solubilization kinetics by gas injection and water electroreduction in a potassium phosphate buffered solution (0.1 M, pH = 7.2) of 0.8 L. Three different H_2 supply rates were used in each case: For gas injection, 1 $L \cdot h^{-1}$ (42 $mmol \cdot h^{-1}$), 2 $L \cdot h^{-1}$ (83 $mmol \cdot h^{-1}$), and 3 $L \cdot h^{-1}$ (125 $mmol \cdot h^{-1}$); for water electroreduction, 20 mA (0.37 $mmol \cdot h^{-1}$), 60 mA (1.12 $mmol \cdot h^{-1}$), and 100 mA (1.87 $mmol \cdot h^{-1}$).

III-3.2 Variation of the maximum concentration of dissolved H_2 and solubilization rate with H_2 supply rate

The large variation of the maximum concentration of dissolved H_2 as a function of the H_2 supply rate can be better observed in Fig. III.4A.

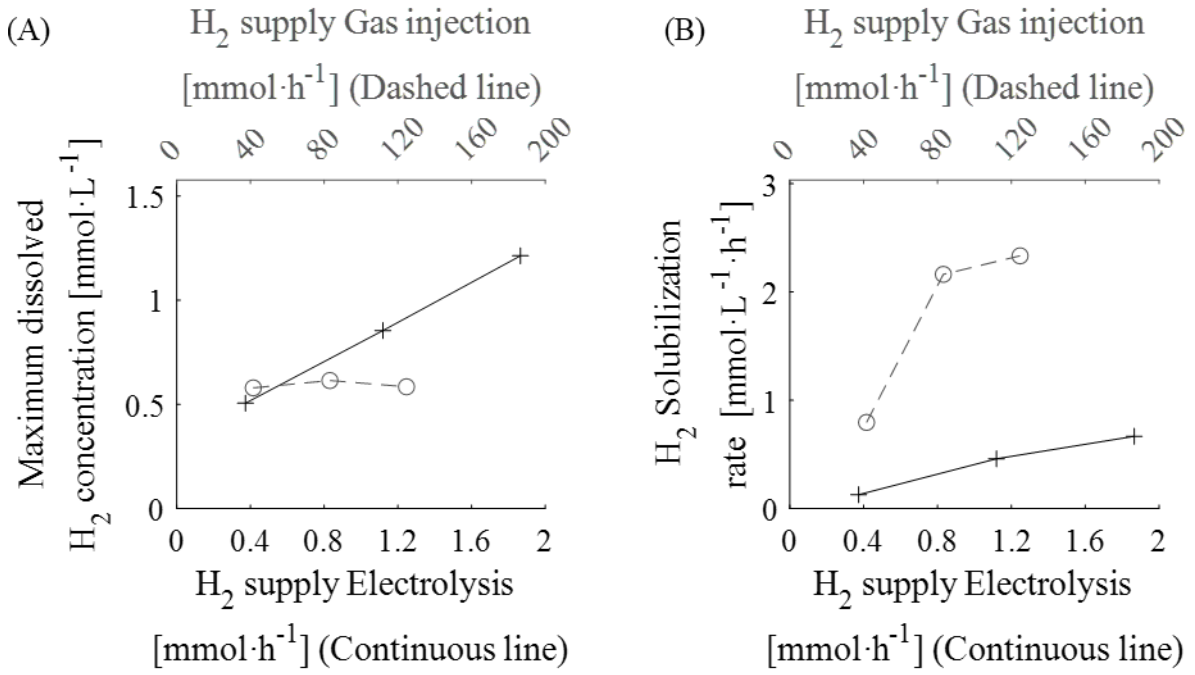

Fig. III.4. Variation of the (A) maximum dissolved H_2 concentration and (B) H_2 solubilization rate as a function of the H_2 supply rate by water electroreduction and gas injection in a potassium phosphate buffered solution (0.1 M, pH = 7.2) of 0.8 L. The solubilization rate was measured from the time required to increase the concentration from 0 to 0.5 mmol·L^{-1}.

The fact that higher H_2 supply rates during water electroreduction lead to proportionally higher maximum dissolved H_2 concentrations opens up a new avenue for H_2 solubilization. Unlike gas injection, water electroreduction is not constrained by the H_2 saturation concentration achieved by the dissolution of H_2 bubbles, which could be advantageous for processes where besides having high H_2 solubilization rates, supersaturated concentrations of H_2 are also favorable. Although a higher concentration of dissolved H_2 was achieved during water electroreduction, the time it took to solubilize the same quantity of H_2 was faster for gas injection. This can be better observed by comparing the different solubilization rates as shown in Fig. III.4B. Despite the ~2 orders of magnitude difference in H_2 supply rates, the H_2 solubilization rates obtained during water electroreduction were closely below those obtained during gas injection. For example, during water electroreduction at 1.87 mmol·h^{-1}, the H_2 solubilization rate obtained was 0.67 mmol·L^{-1}·h^{-1}, while during gas injection at 42 mmol·h^{-1} it was 0.79 mmol·L^{-1}·h^{-1}.

It is important to notice that even with the large difference in H_2 supply rates used in both techniques (around 20 times) the solubilization rates obtained were not largely different. It is

expected therefore to have largely different H_2 solubilization efficiencies between gas injection and water electroreduction. The different solubilization efficiencies achieved can be seen in Fig. III.5. Overall, the H_2 solubilization efficiency by gas injection was ~2 %, much lower than the ~35 % reached by water electroreduction. The maximum solubilization efficiency achieved by water electroreduction at 1.12 mmol·h^{-1} was 41% after 1 hour of operation, which was around 20 times larger than the maximum achieved by gas injection, around 2% after 10 minutes with a H_2 supply of 83 mmol·h^{-1}. When comparing both techniques at similar solubilization rates, i.e., water electroreduction at 1.87 mmol·h^{-1} and gas injection at 42 mmol·h^{-1}, the solubilization efficiency difference is of 18-fold.

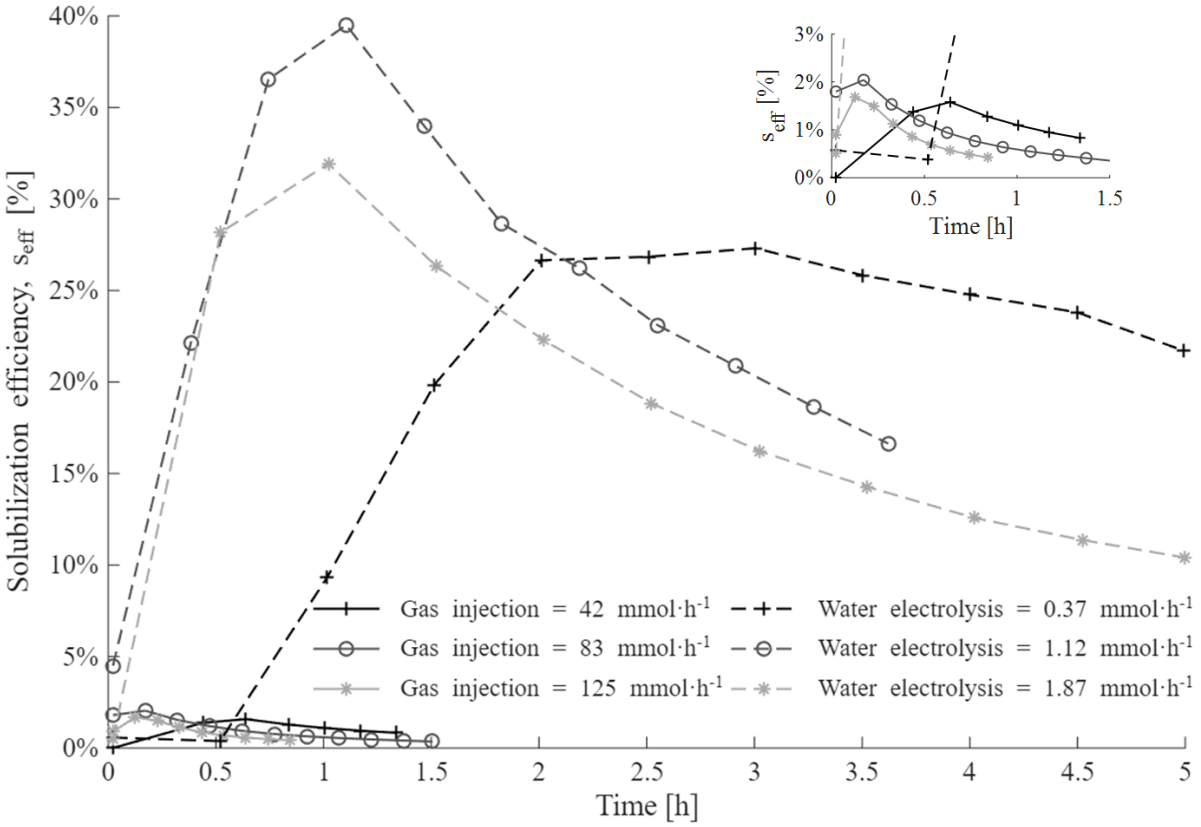

Fig. III.5. Solubilization efficiency of dissolved H_2 by gas injection and water electroreduction in a potassium phosphate buffered solution (0.1 M, pH = 7.2) of 0.8 L. Three different H_2 supply rates were used in each case: For gas injection, 1 L·h^{-1} (42 mmol·h^{-1}), 2 L·h^{-1} (83 mmol·h^{-1}), and 3 L·h^{-1} (125 mmol·h^{-1}); for water electroreduction, 20 mA (0.37 mmol·h^{-1}), 60 mA (1.12 mmol·h^{-1}), and 100 mA (1.87 mmol·h^{-1}).

Nevertheless, the release of H_2 bubbles was also observed after some time in the cathodic surfaces of the water electroreduction technique. For example, after 22 minutes at 1.87 mmol·h^{-1}, H_2 bubbles started to slowly nucleate and get pinned at the outer region of the

carbon brush. Afterwards, the rate of bubble nucleation kept increasing until the rate of H_2 loss by nucleation (and H_2 loss through the liquid-headspace interface) matches the rate of H_2 solubilization and the concentration stabilizes at the maximum value. It is worth noting that bubbles observed did not correspond to the first nucleation events (which should form nanobubbles, invisible to the naked eye) which the CNT tries to predict, but the pinned and stable bubbles, more closely represented by the diffusion-controlled growth of electrolytic bubbles described by the Lohse-Zhang model which occurs after the nanobubble nucleation event. Based on the Epstein-Plesset model presented in section I-4.2 (although not considering the enhanced dissolution due to the kinetic energy of the bubble), these observed bubbles should be large enough to not dissolve in the bulk liquid and instead grow at H_2 supersaturated concentrations. Nevertheless, as H_2 supersaturation was still maintained, reinforcing the hypothesis that the nucleation rate at the high current density evaluated was still low enough to allow supersaturation to be maintained through the balance between the electrolytic production of H_2 and its diffusion away from the electrode surface.

To avoid larger losses of H_2 due to a more extensive nucleation rate at higher currents and therefore limit the maximum concentration achieved in the bulk, the current density should be maintained low by using larger surface areas, while maintaining sufficient mixing at the electrode surface.

III-3.3 Energy consumed per mol of H_2 solubilized

It is now useful to compare how the 18-fold difference in solubilization efficiency translates into energy efficiency. It is commonly accepted that electrolyzer are more energetically demanding for producing H_2 than the traditional steam methane reforming when considering the production of gaseous H_2. As hydrogenotrophic reactions require dissolved H_2, the energy consumption of each technique is normalized per each mol of H_2 solubilized and shown in Table III.4.

Table III.4. Estimation of the energy consumption per mol of H_2 solubilized for the gas injection and water electroreduction techniques.

H_2 solubilization technique	H_2 supply rate [$mmol \cdot h^{-1}$]	Solubilization rate [a] [$mmol \cdot L^{-1} \cdot h^{-1}$]	Energy per mol of H_2 solubilized [$MJ \cdot mol^{-1}$]
Gas injection	42	0.79	23.92 [b]
Gas injection	83	2.16	17.60 [b]
Gas injection	125	2.33	24.47 [b]
Water electroreduction	0.37	0.13	2.04 [c]
Water electroreduction	1.12	0.46	3.20 [c]
Water electroreduction	1.87	0.67	5.16 [c]
Ideal water electroreduction with H_2 gas production	35[d]	0.67[d]	18.65[e]

[a] Calculated from the concentration change at 0 and 0.5 $mmol \cdot L^{-1}$ of dissolved H_2 in the 0.8 L liquid medium. [b] Calculated from the production of H_2 by steam methane reforming, using the total energy used by the system (natural gas and non-feedstock): 183.2 MJ per kg H_2 [173]. [c] Calculated with the cell voltage at 0.5 $mmol \cdot L^{-1}$ of dissolved H_2 which corresponded to 2.92, 5.45 and 7.66 for the H_2 supply rates [$mmol \cdot h^{-1}$] of 0.37, 1.12 and 1.87. [d] The solubilization rate was assumed to be the same as for water electroreduction at the highest supply rate, but the supply rate was calculated based on a 1.5% solubilization efficiency (obtained in this work for gas injection).[e] Calculated with a water electroreduction cell voltage of 1.48 V [174].

At a H_2 supply rate of 42 $mmol \cdot h^{-1}$ by gas injection and 1.87 $mmol \cdot h^{-1}$ by water electroreduction, the energy required for solubilizing 1 mol of H_2 by water electroreduction was around 4.6-times lower than the energy required by gas injection if the H_2 gas was produced by SMR 3.6-times lower if it was produced by an ideal water electroreduction cell

operating. This highlights the potential of water electroreduction as an efficient technique for the production of dissolved H_2.

III-3.4 Modelling of the effect of H_2 solubilization kinetics on hydrogenotrophic reactions

For each H_2 solubilization technique, the highest rate of H_2 solubilization rate is obtained when the liquid medium is initially free of dissolved H_2. This solubilization rate then gradually decreases, eventually reaching zero, as the concentration of dissolved H_2 approaches the maximum amount that each system can hold. As the solubilization rate becomes a unique function of the dissolved H_2 according to the solubilization technique used, it becomes necessary to contrast the H_2 solubilization kinetics of each technique with the expected H_2 uptake kinetics for some hydrogenotrophic reactions to obtain information about the dissolved H_2 concentration that could be maintained at each case. In a continuous bioreactor working with a single strain where H_2 is being solubilized along with its biotic consumption, the steady state dissolved H_2 concentration in the bioreactor is established once the H_2 solubilization and uptake rate become equal. In Fig. III.6 the H_2 solubilization kinetics by gas injection is compared with slow H_2 uptake kinetics (as in *C. ljungdahlii*) and a fast H_2 uptake kinetics (as in *C. autoethanogenum*) based on the uptake rates obtained from Muñoz *et al* at low biomass concentrations (~0.1 g dry weigh·L^{-1})[166]. Although the first-order kinetics of hydrogenotrophs were only evaluated up to the saturation concentration, here it was

extrapolated past this value to elucidate any possible effects on working with supersaturated concentrations.

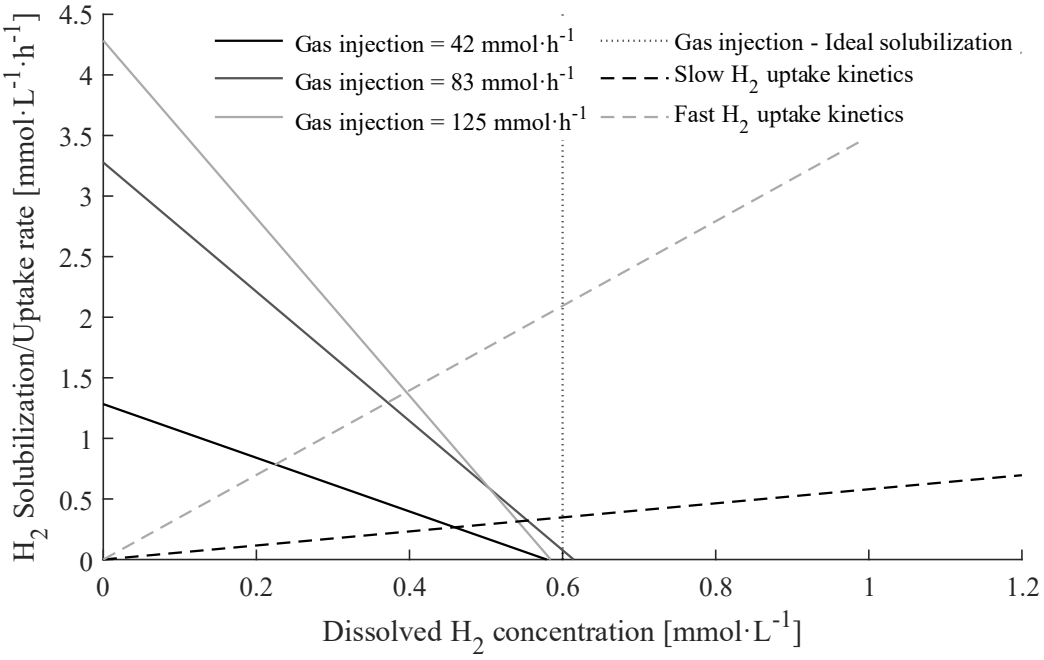

Fig. III.6. H_2 Solubilization kinetics of the different H_2 supply rates tested for gas injection (solid lines) and H_2 uptake kinetics (dashed lines) based on the kinetic experiments reported by Muñoz *et al* [166]. The dotted vertical line represents an ideal gas injection setup where the H_2 gas is instantaneously solubilized (here, 0.6 mmol·L^{-1} was chosen based on the experimental concentration at saturation point).

The higher H_2 supply rates in gas injection allowed decrease the slope of the solubilization kinetics but pivoted close to the saturation concentration. By using the highest injection rate of H_2 gas tested in this work (125 mmol·h^{-1}), it would be possible to maintain a bioreactor working with slow H_2 uptake kinetics at an uptake rate of 0.32 mmol·L^{-1}·h^{-1} with a steady concentration of dissolved H_2 of 0.55 mmol·L^{-1}. For a bioreactor working with fast H_2 uptake kinetics, the maximum uptake rate and dissolved H_2 concentration would be 1.37 mmol·L^{-1}·h^{-1} at 0.39 mmol·L^{-1}. In a system where the H_2 gas injected would instantaneously dissolve but still limited by the saturation concentration (ideal gas sparger, represented by the vertical dotted line), the maximum H_2 uptake rates that could be achieved in the bioreactor for both cases would be 0.35 mmol·L^{-1}·h^{-1} and 2.09 mmol·L^{-1}·h^{-1} respectively. In bioreactors where gas is injected with bubbles larger than a few micrometers, the H_2 uptake rate and concentration of dissolved H_2 would be always limited by the saturation concentration.

Similarly, both H_2 solubilization and biotic uptake kinetics for the case of water electroreduction are shown in Fig. III.7.

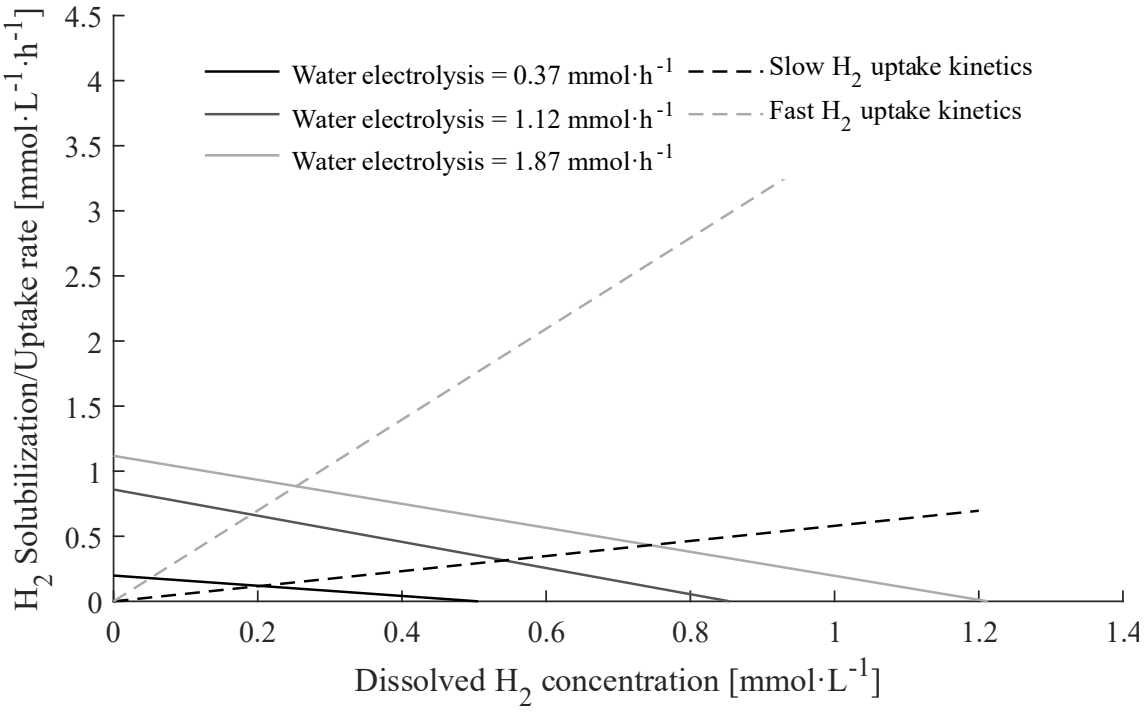

Fig. III.7. H_2 Solubilization kinetics of the different H_2 supply rates tested for water electroreduction (solid lines) and H_2 uptake kinetics (dashed lines) based on the kinetic experiments reported by Muñoz *et al* [166].

In water electroreduction, the kinetics of solubilization are not pivoted around the saturation concentration, which allows to have different steady states for the H_2 uptake rate and dissolved concentrations. This is observed on how the solubilization kinetics translate without a pivoted point at different H_2 supply rates. By using the highest rate of H_2 production tested in this work (1.87 mmol·h^{-1}), it would be possible to maintain a bioreactor working with slow H_2 uptake kinetics at an uptake rate of 0.43 mmol·L^{-1}·h^{-1} with a steady concentration of dissolved H_2 of 0.74 mmol·L^{-1}. For a bioreactor working high H_2 uptake kinetics, the steady state H_2 uptake rate and dissolved H_2 concentration would be 0.87 mmol·L^{-1}·h^{-1} at 0.25 mmol·L^{-1}. Even if compared with an ideal gas sparger with instantaneous H_2 solubilization, the water electroreduction technique would be easily more advantageous for bioreactors working with microorganisms characterized by a low H_2 uptake rate. As different H_2 solubilization kinetics result in different dissolved H_2 concentrations, it can be expected that some hydrogenotrophic reactions become more thermodynamically favorable than others. Assuming -20 kJ/mol as the minimum free

energy change required for ATP synthesis by chemiosmosis (through translocation of 1 mol of H^+ across the cytoplasmic membrane [54]) and solving equation 4 at standard conditions (adjusted for pH = 7), acetogens would require a minimum concentration of dissolved H_2 of ~400 nmol·L^{-1} to overcome this thermodynamic limit, while for methanogens it would be ~11 nmol·L^{-1}. This means that when concentrations fall between these two values, methanogens would outcompete acetogens due to a thermodynamic limitation on the growth of acetogens.

The actual concentration of the species involved in the hydrogenotrophic reactions such as H_2 and CO_2 depends on the balance between the substrate uptake and supply in the bioreactor. In this work, two scenarios with (1) slow H_2 solubilization and (2) fast H_2 solubilization kinetics relative to the H_2 uptake kinetics were evaluated in terms of the thermodynamic potential of a hydrogenotrophic reaction. The results of the modeling of the first scenario are shown in Fig. III.8.

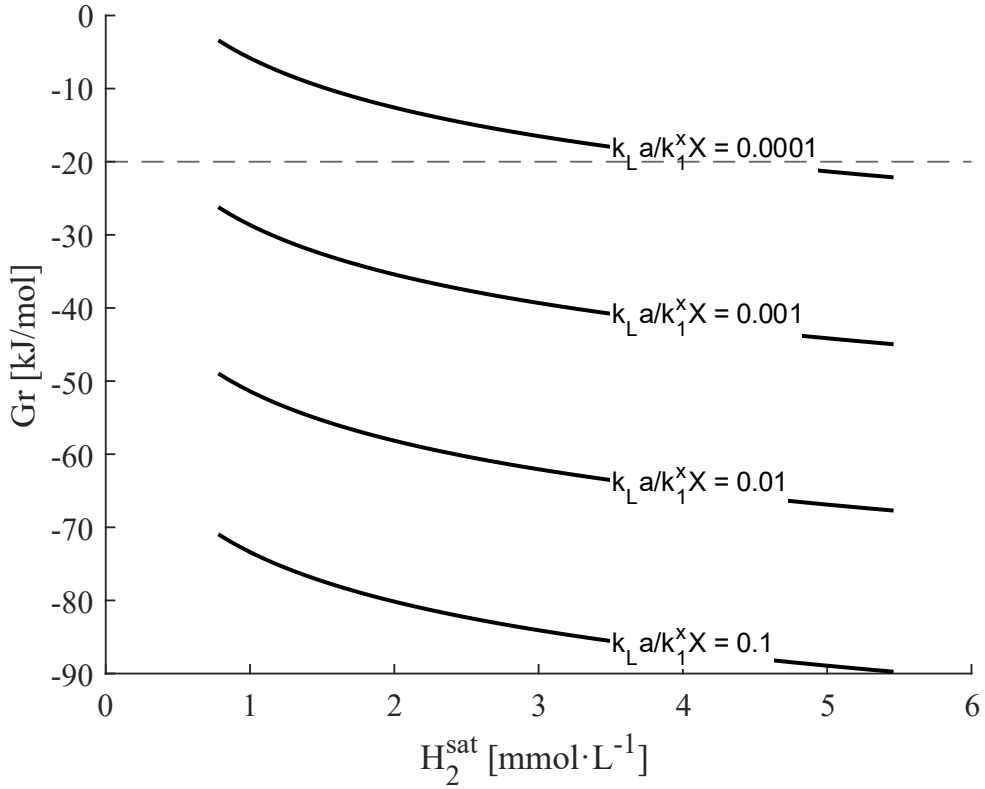

Fig. III.8. Effect of low $K_L a$ to $k_1^x X$ ratios and the H_2 saturation concentration ($C_{H_2}^{sat}$) on the Gibbs free energy of the (autotrophic) acetogenic reaction $2CO_2 + 4H_2 \rightarrow CH_3COO^- + H^+ + 2H_2O$. The CO_2 and H_2 concentrations were obtained at steady state from the solution

of equations 20) and 21) for an acetogenic reaction, while the rest of species were maintained at standard conditions.

The lowest $K_L a$ to $k_1^x X$ evaluated, with a ratio of 1×10^{-4} resulted in a steady state concentration of $C_{H_2} = 78\ \mathrm{nmol \cdot L^{-1}}$ and $C_{CO_2} = 34.4\ \mathrm{mmol \cdot L^{-1}}\ (0.98\ \mathrm{bar})$ at the conditions of gas injection ($C_{H_2}^{sat} = 0.78\ \mathrm{mmol \cdot L^{-1}}$). In this case, not enough energy would be available for acetogens overcome the ΔG_r = -20kJ/reaction needed for growth and outcompete methanogens and sulfate reducers, which would have more favorable thermodynamic potentials of -40 kJ/reaction and -60 kJ/reaction respectively if calculated. In fact, sulfate reducers and methanogens would have always a ΔG_r < -20 kJ/reaction at the conditions evaluated in this work. In other words, acetogens would be able to outcompete others hydrogenotrophs due to their larger specific growth rates, only when they are not thermodynamically limited [55]. The best strategy here to favor the thermodynamic potential of acetogenesis is to increase $k_L^{H_2} a$. While working at elevated $C_{H_2}^{sat}$ concentrations (e.g., by bioreactor pressurization or supersaturation by water electroreduction) would have a less important effect. It is worth noting that the C_{CO_2} values obtained at steady state in the simulation were close to the saturation concentration, which highlights the higher relevance of controlling the H_2 concentration over the CO_2 concentration. The C_{CO_2} at steady state varied between 88-98% of its saturation concentration, while the C_{H_2} at steady state varied between 0.1-10% of its saturation concentration.

For the second scenario, higher $K_L a$ to $k_1^x X$ ratios were used to obtain the steady state concentrations of H_2 and CO_2. As the acetogenic reaction becomes always thermodynamically feasible (with ΔG_r < -70kJ/reaction), it is more interesting to calculate the conditions at which ethanol production would become feasible. The effect of different $C_{H_2}^{sat}$ values at high $K_L a$ to $k_1^x X$ ratios on the ΔG_r of ethanol production from acetate is shown in Fig. III.9.

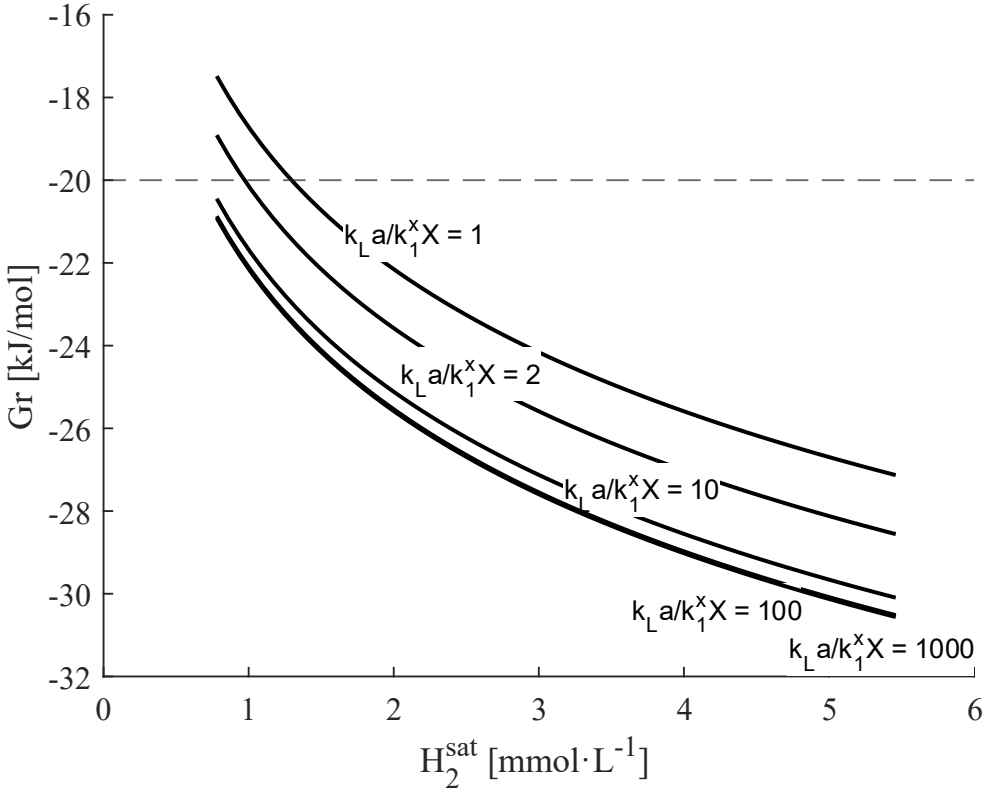

Fig. III.9. Effect of high $K_L a$ to $k_1^x X$ ratios and the H_2 saturation concentration ($C_{H_2}^{sat}$) on the Gibbs free energy of the ethanol production reaction $CH_3COO^- + H^+ + 2H_2 \rightarrow CH_3CH_2OH + H_2O$. The CO_2 and H_2 concentrations were obtained at steady state from the solution of equations 20) and 21) for an acetogenic reaction, while the rest of species were maintained at standard conditions.

As opposed to the scenario 1, the best strategy would be to work at supersaturation levels where $C_{H_2}^{sat}$ is greater than 0.78 mmol·L^{-1}. For example, if working at a total pressure of 1 bar, the lowest ΔG_r value that could be obtained with a $K_L a$ to $k_1^x X$ ratio greater than 10 seems to reach a minimum of -21 kJ/reaction (the curves at 100 and 1000 ratios are superimposed at the axis scales shown). This is because at a ratio of 10, the dissolved H_2 concentration is already at the 90 % of the saturation value (0.78 $mmol \cdot L^{-1}$) and higher ratios only logarithmically approach to 100% of the saturation value. Nevertheless, if water electroreduction is used, the same value of ΔG_r = -21 kJ/reaction could be obtained with only a $K_L a$ to $k_1^x X$ ratio of 2 and $C_{H_2}^{sat}$ = 1.21 mmol·L^{-1}. This is consistent with what is shown in Fig. III.6 and Fig. III.7, where for a low H_2 uptake rate relative to the solubilization rate (large $K_L a$ to $k_1^x X$ ratio), even an

instantaneous solubilization by gas injection with $C_{H_2}^{sat}$ = 0.78 mmol·L^{-1} would maintain a lower growth rate than a system where supersaturation ($C_{H_2}^{sat}$ > 0.78 mmol·L^{-1}) is achieved.

III-4. Discussion

III-4.1 Increasing the H_2 solubilization rate while maintaining high solubilization efficiency

Overcoming H_2 solubilization limitations should be the first step when working with bioreactors involving hydrogenotrophs. In both gas injection and water electroreduction, larger solubilization rates were achieved by increasing the H_2 supply rate. Nevertheless, for H_2 gas injection, the H_2 supply rate did not linearly increase the H_2 solubilization rate. At increasing H_2 supply rates, it can be expected that the interfacial area (the 'a' in K_La) also increases as long as bubbles do not coalesce. At the highest H_2 supply rate used here, it is hypothesized that a higher bubble coalescence was occurring during the injection (which also reduces the bubble residence time and consequently, the H_2 solubilization rate). While small pores produce bubbles with small diameters, they are also more prone to bubble coalescence. Therefore, although there is a proportionality of $K_La \propto d_b^{-1}$ where d_b is the bubble diameter, this proportionality can drop to $K_La \propto d_p^{-0.1}$ when considering the pore diameter d_p of spargers in bubble columns [169]. When using gas sparger, the pore size and distribution must be carefully selected to avoid excessive bubble coalescence at high H_2 supply rates. In bubble columns and stirred tank reactors operating at high gas flowrates, bubble coalescence becomes rather unavoidable, and achieving proper bubble breakup and dispersion (e.g., by impeller design, mechanical energy input or induced turbulence) plays a more important role on achieving high k_La values [169].

In water electroreduction, other challenges arise when working at high currents. The first challenge to overcome is due to the high internal resistance of the cell which translates into high energy costs. Optimal reactor designs with low internal resistance (with low interelectrode gap) should be used to avoid large cell voltages. The H-type cell configuration, although useful for studying electrode reactions, is impractical for electrolysis scale-up. The large cell voltage (around 7V for 100 mA) in the experiments was mainly attributed to the internal resistance of the H-type cell, while the overpotential associated with the HER reaction

alone was less than 2V (data not shown), limiting the maximum current that could be applied. The second challenge at high currents comes with maintaining local and homogeneously distributed low current densities to avoid bubble nucleation. Similar to how bubble coalescence reduces the solubilization efficiency during gas injection, large current densities facilitate bubble nucleation during water electroreduction, also reducing the solubilization efficiency and therefore the solubilization rate.

To avoid bubble nucleation, electrode designs with large surface areas should be used instead. The use of large cathodic surface areas helps to avoid large local supersaturation of dissolved H_2 in the cathode surface, which is the first requirement for bubble nucleation. In this sense, while high dissolved H_2 concentrations are desired in the bulk phase and not in the localities of the cathode surface, the cathode design and the hydrodynamic flow in the cathodic chamber should also be optimized to allow the easy removal of dissolved H_2 out of the cathode surface into the bulk phase. In this regard, some strategies should be explored such as improved passive transport (by capillary effect) or by active transport by mechanical convection (by agitation), and flow-through porous electrodes.

Passive transport utilizing the capillary effect, particularly through the use of hydrophobic porous membranes such as expanded polytetrafluoroethylene like Gortex ® membranes, has been recently proposed as a promising strategy to remove dissolved H_2 out of the cathode surface in a configuration called “bubble-free” electrolysis [96]. Electrodes incorporating PTFE-based Gortex ® gas diffusion layers coated with catalysts have demonstrated besides achieving low cell onset potentials, the elimination of bubble nucleation, at least to the naked eye. The operational principle relies on the aerophilic nature of the PTFE material, which exhibits a strong affinity for gases. It is suggested that as soon as H_2 gas is produced at the cathodic surface, by its hydrophobic nature, it preferentially adsorbs and transversally transports the H_2 molecules through the PTFE surface away the catalyst layers due to its strong capillary force [94].

Instead of a passive transport by capillary force, an active transport of dissolved H_2 out of the cathode surface can be used during water electrolysis at high currents. Instead of applying a mixing force to agitate the whole bulk liquid around the cathode surface as in H-type cells, the fluid can also be forced through the porosity or the 3D geometry of the cathode in what is commonly known as flow cells. Although flow cells are less used in laboratory setups

compared to H-type cells, their higher area to volume ratios and enhanced mass transfer could be more suited for preventing the accumulation of dissolved H_2 near the cathode surface [176]. The enhanced mass transfer is primarily driven by an efficient convective transport, which supplements the slower process of molecular diffusion.

III-4.2 The dissolved H_2 concentration as a selective variable for controlling competition among hydrogenotrophs and product selection

Different concentrations of dissolved H_2 may favor certain hydrogenotrophic microorganisms over others depending on the energetic gain and metabolic pathways used at each concentration of dissolved H_2. Comparing hydrogenotrophic microorganisms by the Gibbs free energy change of the catabolic reaction, sulfate reducers should have an energetic advantage for growth ($\Delta G^{0'}$= -152.2 kJ/mol from sulfate to sulfide), followed by methanogens ($\Delta G^{0'}$= -131 kJ/mol from CO_2 to methane) and finally acetogens ($\Delta G^{0'}$= -95 kJ/mol from CO_2 to acetate) [177].

However, the Gibbs free energy of the catabolic reaction alone is insufficient to determine the energetic gain or ATP gain for each microorganism and accurately predict competitive advantages. Muñoz *et al* found experimentally that hydrogenotrophs performing the same acetogenic reaction have different H_2 thresholds spanning from 44×10^{-6} mmol·L^{-1} to 15×10^{-3} mmol·L^{-1} and which are proportional to ATP gains [58]. They also found that while ATP gains were genus-specific, H_2 uptake rates were strain-specific, suggesting that growth kinetic differences could originate from enzymes involved in the energy conservation mechanisms coupled with the Wood-Ljungdahl pathway [166].

In bioreactors limited by a slow H_2 solubilization rate, low concentrations of dissolved H_2 dictate the competition among hydrogenotrophs, where only microorganisms with lower H_2 thresholds thrive. In a bioreactor with a H_2 solubilization rate large enough to maintain dissolved H_2 concentrations above common H_2 thresholds, hydrogenotrophic microorganisms using metabolic pathways with high specific H_2 uptake rates may outcompete the ones using metabolic pathways with low specific H_2 uptake rates. For single strains capable of switching metabolic pathways according to the substrate concentration, high concentrations of dissolved

H_2 might favor the use of metabolic pathways with high H_2 uptake rates even if they allow lower ATP gains as described by the resource allocation theory [178].

The shift on metabolic strategies and fluxes in acetogens are dictated by the thermodynamics of these metabolic fluxes, more than the common gene-regulation found in other microorganisms [179]. The thermodynamic potential of each metabolic flux depends on the balance of its involved redox pairs (NADPH/$NADP^+$, NADG/NAD^+, Fd_{red}/Fd_{ox}) and the concentration of intermediate metabolites (e.g., acetate) [179]. As the H_2 is involved in the balance of these redox pools, different dissolved H_2 concentrations should also affect the flux of these metabolic pathways and therefore the product selectivity. In *C. autoethanogenum*, the shift from acetate to ethanol formation at high dissolved H_2 concentrations occurs when sufficient H_2 supply leads to high biomass and undissociated acetic acid concentrations in a bioreactor. The resulting intracellular acetate accumulation disrupts ATP homeostasis, and ethanol production via the aldehyde:ferredoxin oxidoreductase (AOR) pathway helps restore balance [144], [180]. In mixed cultures, chain elongation likely occurs by the coupling of the Wood-Ljungdahl pathway where acetate and ethanol is generated first and then cyclically elongated to medium-chain carboxylic acids by the fatty acid biosynthesis pathway and the reverse β-oxidation pathway, where maintaining high concentrations of dissolved H_2 (or reducing equivalents) avoids the oxidation of the elongated carboxylic acids [181], [182], [183]. Similarly, excessive ethanol oxidation (EEO, present in some hydrogenotrophs) is a competing metabolic pathway against alcohol production where the most common approach to suppress EEO is to work at high concentrations of dissolved H_2 to maintain the EEO reaction thermodynamically unfeasible [184].

High concentrations of dissolved H_2 also influence the competitive dynamics between Rnf- and Ech- acetogens. These organisms use the Rnf or Ech membrane-bound enzymatic complex to couple electron transport with ion translocation across the membrane, a process which is ultimately responsible for ATP synthesis. In Rnf-acetogens, the end product of respiration is NADH, which can be redirected into other NADH-reducing metabolic pathways. In contrast, Ech-acetogens produce H_2 as a respiration product [145]. As a result, high concentrations of dissolved H_2 can create a thermodynamic backpressure, potentially inhibiting Ech-acetogens over Rnf-acetogens. Furthermore, high concentrations of dissolved H_2 can also cause direct metabolic inhibition. For instance, in *A. woodie*, biomass growth and acetate production

declined when the H_2 partial pressure of the inlet gas increased from 0.4 bar to 1.4 bar and 2.1 bar. This decline was accompanied by an accumulation of formate (a key precursor in the Wood-Ljungdahl pathway) [143]. Similarly, in a genetically engineered strain of *M. thermoacetica* designed for ethanol production, high concentrations of H_2 inhibited its growth, which was not observed in the wild-type strain. This inhibition was linked to the disruption of the NAD^+/NADH redox balance, which could be mitigated by the introduction of an external electron acceptor [185].

These findings highlight the importance of controlling the dissolved H_2 concentration in hydrogenotrophic processes. Maintaining an optimal concentration of H_2 is essential not only for regulating microbial growth and interspecies competition, but also for maximizing product yields. Moreover, operating across a wider range of dissolved H_2 concentrations could expand the spectrum of viable metabolic fluxes in hydrogenotrophic systems.

III-4.3 Achieving high concentrations of dissolved H_2 is technically challenging

Operating at high concentrations of dissolved H_2 is industrially relevant for achieving high growth and production rates, and for potentially shifting metabolic pathways towards long-chain metabolites. However, achieving such high concentrations presents significant technical challenges. In this work, the maximum concentration of dissolved H_2 achieved by gas injection, regardless of the H_2 supply rate, consistently remained below 0.78 $mmol \cdot L^{-1}$, which is the H_2 saturation concentration at 1 bar and 25 C.

Higher hydrostatic pressures in tall columns or operating with pressurized reactors increase the H_2 saturation concentration, in accordance with Henry's law. Demler *et al.* observed that the cell-specific productivities for hydrogenotrophic acetate production by *A. woodii* increased linearly with increasing H_2 partial pressures (0.4 - 1.7 bar, corresponding to 0.3-1.3 $mmol \cdot L^{-1}$ of dissolved H_2) in the reactor headspace [186]. Stoll *et al.* similarly reported increased cell and product concentrations when increasing the total pressure from 1 to 4 bar in a syngas-fed reactor ($H_2/CO/CO_2/N_2$: 48/16/16/20). However, a negative effect was observed at 7 bar, which they attributed to the pressurization rate not being sufficiency slow to allow for cell adaptation [142]. For comparison, a partial H_2 pressure of 1.55 bar would be required for gas injection to match the 1.21 mmol $H_2 \cdot L^{-1}$ achieved by water electroreduction at 1 bar of total

pressure. Achieving this H_2 partial pressure by gas injection would require a total reactor pressure of 2 bar in a reactor using a gas mixture of high purity at H_2:CO_2 of 3:1; or 7.75 bar with a gas mixture containing 20% H_2. Alternatively, the internal bubble pressure can also be increased by producing bubbles of smaller sizes (micro/nanobubbles), owing to the Laplace pressure. It can be roughly estimated that H_2 bubbles of 30 µm of diameter would have to be injected to reach a dissolved H_2 concentration of just 15% above the H_2 saturation concentration at 25 C in water, according to the Epstein-Plesset solution for the dissolution of H_2 bubbles [72]. However, the practical size of generated bubbles is restricted by sparger fouling; in industrial settings, coarse gas spargers typically produce bubbles with diameters larger than 1 mm [187].

A more effective approach for injecting H_2 microbubbles into the liquid medium can be also achieved by water electroreduction. In this case, high current densities are used to initiate bubble nucleation, yielding significantly smaller bubbles compared to those produced by traditional gas spargers. Gao *et al.* managed to produce microbubbles with diameters below 150 µm using a CoP-NiF electrode, maintaining a dissolved H_2 concentration of 0.63 $mmol \cdot L^{-1}$ in the presence of hydrogenotrophic methanogens [188]. Cui *et al.* generated bubbles ranging from 25 to 750 µm using an inexpensive stainless-steel felt band as an electrode, achieving a H_2 supersaturation concentration of 1 $mmol \cdot L^{-1}$ and proving its applicability within a MES producing acetate [16]. Commercial devices capable of producing micro/nanobubbles from gas injection are also available. For example, Moleaer nanobubble injector (www.moleaer.com) can produce nanobubbles with a mean bubble diameter of ~120 nm. Micro/nanobubble production and stability represent a growing research field, although its applicability to processes involving hydrogenotrophs requires further validation.

When using water electroreduction for the production of dissolved H_2, the maximum concentration of dissolved H_2 achievable in the bulk liquid is ultimately limited by the local concentration at which the dissolved H_2 nucleates on the cathodic surface. In this study, a maximum concentration of 1.21 $mmol \cdot L^{-1}$ was achieved at the highest electrochemical H_2 supply rate. The concentration at the bulk liquid is expected to be lower than the local concentration at the cathode surface (the upper limit). The proximity of the dissolved H_2 concentration in the bulk liquid to this upper limit depends on the rate at which the dissolved H_2 is transported away from the cathode surface. Using equation 18 from the classical

nucleation theory, it can be estimated that a local supersaturation approximately 1450-fold is required initiate bubble nucleation, assuming a zero contact angle at the nucleation site (as in homogeneous nucleation) [120]. Nevertheless, this value does not account for surface heterogeneities on the cathode that could alter the contact angle at the nucleation site. For platinum nanoelectrodes of varying sizes (radii = 7-41 nm), a local supersaturation of approximately 300-fold was found to be necessary for the start of H_2 bubble nucleation. This corresponds to a dissolved H_2 concentration of 230 $mmol \cdot L^{-1}$ on the cathode surface with a contact angle of 150°, a value specific to the extent of surface heterogeneities and cathode's hydrophilicity [128]. In this study, although the local critical concentration for nucleation was not estimated, it is safe to assume that the maximum dissolved H_2 concentrations achievable in the bulk liquid were not limited by the local supersaturation concentration. This observation arises from the linear relationship obtained between the H_2 supply rate (imposed current) and the maximum dissolved H_2 concentration, suggesting that even higher concentrations in the bulk liquid could be potentially achieved as long as proper mixing is ensured. This linear relationship was also observed by others in a continuous water electroreduction cell, where the effect of working at high electrolyte flow rates (improved mixing) eclipsed the negative effects of the electrode roughness on achieving high dissolved H_2 concentrations [138].

It is worth noting that using the electrolyte supersaturated in H_2 as a growth medium for hydrogenotrophic bioprocesses can bring additional challenges. The reduction of water in the cathodic chamber can increase the pH of the medium if the pH is not adequately controlled. Moreover, the solid biomass and inorganic particles can act as potential nucleation sites when the solution is supersaturated with H_2. Other soluble compounds with surfactant activity (e.g., dissolved CO_2, extracellular proteins) that could be inevitably present in the cathodic chamber may also facilitate the nucleation of bubbles at the cathode surface. Future research on the extent of degassing should be further tested in a hydrogenotrophic spent medium.

III-4.4 Solubilization and energy efficiency

Different strategies must be implemented to improve the solubilization efficiency according to the solubilization technique used. For gas injection, improving energy efficiency is linked to enhancing the solubilization efficiency. Gas recirculation is employed to prolong the bubble

residence time within the liquid medium, thereby increasing solubilization. However, this solubilization efficiency can decrease if the population of bubbles becomes too large, potentially promoting coalescence. Larger coalesced bubbles have larger volumes and thus higher rise velocities, paradoxically leading to a decrease in the overall residence time and consequently affecting solubilization efficiency [169]. It is worth noting that tall columns and large gas recirculation fractions are commonly used to achieve high biologic H_2 conversion percentages, and the low solubilization efficiency found here is due to the short height of the reactor and lack of gas recirculation, which highlights the intrinsic slow mass transfer of H_2 gas bubbles.

For water electroreduction, the first step to improve the energy efficiency should come from the use of cell designs with low internal resistance and cell voltage. Reducing the cell by using a cell with a low interelectrode gap could significantly improve energy efficiency. Similarly, it would be convenient to work with electrolytes with high ionic conductivity to reduce the internal resistance of the cell. Although this is usually achieved by increasing the salinity of the electrolyte, high concentrations of ions such as Na^+ can disfavor the growth of non-halophilic microorganisms [189].

The choice of cathode material is also fundamental to achieving lower cell voltages. While noble metals such as platinum and rhodium exhibit the highest electrocatalytic activity for HER [190], their high cost renders their use economically unfeasible in applications with low-value products, such as in hydrogenotrophic processes. Transition metals such as nickel and iron have high electrocatalytic activity for HER, but at a significantly reduced cost. Nickel alloys (e.g., Ni-Mo, Ni-Fe) are most commonly used due to their high electrocatalytic activity and corrosion resistance. Finally, carbon-based materials are also employed due to their high surface area and corrosion resistance, although they are typically doped with heteroatoms or combined with transition metals to enhance their electrocatalytic activity [191].

The next step towards improving energy efficiency during water electroreduction involves minimizing the formation of H_2 bubbles at the cathode surface. This can be achieved by using cathode materials with optimized structures, such as porous and 3D electrodes, that prevent H_2 accumulation at their surface. Moreover, cell designs such as the use of thin electrodes in flow through cells should be investigated on their current distribution homogeneity. The efficient use of the cathode surface by homogeneous current distributions should also bring a

reduction in the local maximum current density and therefore (by avoiding bubble formation) a better solubilization/energy efficiency.

The inherent advantage in energy efficiency obtained by water electroreduction for dissolved H_2 production stems from the fact that the H_2 produced does not necessarily form a separate gas phase before dissolving. This is reflected in an 18-fold higher solubilization efficiency compared to gas injection. If the water electroreduction cell were designed to produce gaseous H_2 for subsequent injection and solubilization in a separate step, water electroreduction would require approximately 1.8 times more energy than if it was produced via SMR.

III-5. Conclusion

The findings of this chapter demonstrate that water electroreduction offers a clear advantage over traditional H_2 gas injection for providing dissolved H_2 in bioprocesses. This superiority is evidenced by several key metrics. Notably, water electroreduction achieved a H_2 solubilization efficiency of 35%, an 18-fold improvement compared to the 2% efficiency observed with gas injection. This high efficiency allowed for the generation of a supersaturated H_2 concentration of 1.21 $mmol \cdot L^{-1}$, whereas gas injection was limited to a maximum dissolved H_2 concentration of 0.62 $mmol \cdot L^{-1}$ (close to saturation concentration of 0.78 $mmol \cdot L^{-1}$). Furthermore, even with an H_2 production rate approximately 18 times lower than that of gas injection, water electroreduction achieved a comparable H_2 solubilization rate of 0.67 $mmol \cdot L^{-1} \cdot h^{-1}$, aligning closely with the 0.79 $mmol \cdot L^{-1} \cdot h^{-1}$ rate obtained via gas injection. These results highlight the potential of water electroreduction as an effective method for providing the high H_2 concentrations required to optimize processes involving hydrogenotrophs, where supersaturation can significantly influence product selectivity and microbial competition.

Chapter IV. Hydrogen nucleation in water electroreduction at near-neutral pH: Role of cathode structure and agitation conditions.

ABSTRACT

The mass transfer of H_2 gas into a liquid medium is the main limitation on bioreactors involving hydrogenotrophic reactions, as in the production of organic acids and solvents. This chapter addresses the limitation by investigating the potential optimization of dissolved H_2 production via water electroreduction, focusing on preventing bubble nucleation. The main questions This chapter investigates the optimization of dissolved H_2 production by evaluating the role of cathode design and agitation in preventing H_2 bubble nucleation during water electroreduction. Consequently, the following questions are developed in this chapter: How agitation and the accumulation of dissolved H_2 affect the nucleation events at different cathode structures? And what are the estimated local supersaturation concentration and current density thresholds that should not be reached to operate under a bubble-free regime?

To answer these questions, experiments were conducted using a two-chamber H-type cell with three cathode materials: Stainless-steel plate (SSP), stainless-steel porous foam (SSPF), and carbon brush (CB). These cathode materials were compared under different conditions of electrolyte agitation and H_2 pre-saturation. Linear sweep voltammetry combined with video recording, and an image processing algorithm determined the maximum current density achievable before the onset of bubble nucleation. Results showed that under agitated and H_2 pre-saturated conditions, the SSPF allowed the highest current density before nucleation (-42.38 ± 14.77 $A \cdot m^{-2}$), followed by CB (-25.22 ± 4.07 $A \cdot m^{-2}$) and SSP (-18.32 ± 1.24 $A \cdot m^{-2}$). While H_2 pre-saturation decreased the nucleation threshold, agitation significantly counteracted this effect, particularly for the SSPF, highlighting the importance of convection in mitigating local supersaturation and diffusion limitations within porous structures. In conclusion, high-surface-area cathodes combined with effective mixing strategies are key to maximizing bubble-free H_2

solubilization by water electroreduction, offering a promising approach to improve hydrogenotrophic reactors.

IV-1. Introduction

The increasing global demand for energy, along with the pressing need to reduce greenhouse gas emissions, is driving a fundamental transformation of the energy sector. Central to this transition is the development of clean and sustainable energy carriers capable of replacing fossil fuels in both centralized and decentralized applications. Hydrogen has emerged as a particularly promising candidate due to its high gravimetric energy density (140 $MJ \cdot kg^{-1}$), which is more than twice that of conventional hydrocarbon fuels, and its clean oxidation pathway, which yields only water as a byproduct [192], [193]. These characteristics position hydrogen not only as a zero-emission fuel, but also as a key enabler of sector coupling in future energy systems.

Among the various H_2 production routes, water electroreduction (commonly referred to as water electrolysis) stands out as a mature, scalable, and environmentally friendly technology. When powered by renewable electricity sources such as solar or wind, it enables the generation of high-purity H_2 with minimal environmental impact. In an electrolyzer, water molecules are split into oxygen and hydrogen via the oxygen evolution reaction (OER) at the anode and the hydrogen evolution reaction (HER) at the cathode. These half-reactions are typically separated by an ion-exchange membrane that selectively transports charge carriers such as protons (H^+) in acidic media or hydroxide ions (OH^-) in alkaline media. The half reactions involving these charge carriers are shown in Table IV.1 and described by equations 27-30 [194]:

Table IV.1. HER and OER reaction stoichiometries at acidic and alkaline conditions

Acidic conditions		
$H_2O \rightarrow (1/2)O_2 + 2H^+ + 2e^-$	$E^0 = -1.23\ V$	27
$2H^+ + 2e^- \rightarrow H_2$	$E^0 = \ 0.00\ V$	28
Alkaline conditions		
$2OH^- \rightarrow (1/2)O_2 + H_2O + 2e^-$	$E^0 = -0.40\ V$	29
$2H_2O + 2e^- \rightarrow H_2 + 2OH^-$	$E^0 = -0.83\ V$	30

Conventional electrolyzers generally operate under strongly acidic or alkaline conditions to benefit from high ionic conductivity and well-established reaction kinetics. However, these harsh environments accelerate corrosion of cell components, necessitating the use of expensive and chemical resistant materials. In contrast, operation at near-neutral pH offers significant practical advantages. The lower concentration of aggressive H^+ or OH^- ions reduces material degradation, thereby enabling the use of less costly construction materials and broadening the choice of compatible electrodes and membranes [192], [195]. Furthermore, near-neutral conditions are essential for integrating water electroreduction with bioelectrochemical systems, such as microbial electrosynthesis, where hydrogen-consuming microorganisms (hydrogenotrophs) convert dissolved hydrogen into value-added chemicals, including carboxylic acids and alcohols [196].

Despite these advantages, HER at near-neutral pH is significantly less efficient than under acidic or alkaline conditions due to a combination of increased overpotentials. These include activation overpotentials resulting from slow water dissociation kinetics, concentration overpotentials due to limited buffer diffusion or ion accumulation near the electrode surface, and ohmic overpotentials arising from the reduced ionic conductivity of neutral electrolytes [91], [92], [197]. In addition to these thermodynamic and kinetic constraints, a major challenge in near-neutral water electroreduction is gas bubble formation at the electrode surface. Bubble nucleation and growth introduce complex phenomena that further degrade electrochemical performance. Prior to detachment, gas bubbles partially block the electrode surface, hindering charge transfer and mass transport, while also locally increasing the electrical resistance of the electrolyte due to their non-conducting nature [94], [96]. In applications where dissolved H_2 is the desired product, such as in bioelectrochemical systems or bubble-free electrolyzers, the formation of bubbles is particularly detrimental, as it not only decreases the dissolved H_2 availability but also imposes additional energetic penalties associated with bubble re-solubilization. Therefore, controlling and ideally preventing bubble formation is essential to maintain high reaction efficiency under bubble-free conditions.

Theoretical descriptions based on classical nucleation theory (CNT) show that bubble nucleation is influenced by surface properties (e.g., hydrophilicity), local supersaturation levels of dissolved H_2, and the presence of surface imperfections acting as nucleation sites [120], [198]. The CNT predicts that the nucleation onset occurs when the supersaturation is in the

thousands, but it has been experimentally found that the supersaturation ratio drops to around 300 in microelectrodes and 8 in a platinum electrode [128], [129]. In practice, the bubble formation threshold can be altered by tailoring electrode materials and morphology, as well as optimizing electrolyte flow and agitation to promote H_2 removal from the interface before reaching the supersaturation threshold [94], [129]. Moreover, the Lohse-Zhang theory establishes that for every electrode surface, there must be a critical current density threshold at which nucleated bubbles unstably grow instead of dissolve into the liquid medium [131] contributing to a form of hydrogen loss in the system.

In the context of avoiding H_2 nucleation to maximize its solubilization during water electroreduction, it is therefore of high relevance to answer: How agitation and the accumulation of dissolved H_2 affect the nucleation of H_2 bubbles at different cathode structures? And what are the estimated local supersaturation concentration and current density thresholds that should not be reached to operate under a bubble-free regime?

In this chapter, the influence of cathode structure on hydrogen bubble nucleation during water electroreduction was explored. Three distinct electrode designs were evaluated: planar, porous, and brush-type, regarding their ability to delay or suppress bubble formation. In this chapter, using a transparent three-electrode electrochemical cell and optical imaging under potentiostatic control, the critical current density at which the first bubble nucleates under varying hydrodynamic conditions (stagnant vs stirred) and hydrogen concentrations (H_2-free vs H_2 pre-saturated catholyte) was determined. By correlating electrode structure, electrolyte agitation, and supersaturation effects with the onset of bubble formation, this chapter provides new insights into the rational design of bubble-free electrolyzers optimized for near-neutral pH operation.

IV-2. Materials and Methods

IV-2.1 Medium composition and reactor setup

A potassium phosphate buffer solution was used as liquid medium (electrolyte) at 0.1 M and pH of 7.2 (12.7 $mS \cdot cm^{-1}$). The medium was sparged with N_2 overnight using a glass frit (VitraPOR Micro-immersion-filter Por 2, Thermo Fisher Scientific, France) prior to the start of each experiment with the purpose of removing the soluble oxygen from the medium and

avoiding the oxygen reduction reaction signal from the voltammograms. A two-chamber H-type cell was used for electrolysis with a working volume of 0.8 L as shown in Fig. IV.1A,C. To control the working electrode potential, a saturated calomel electrode (SCE, Hg/Hg_2Cl_2 in saturated KCl, +0.241 V vs SHE) was used as a reference electrode. A titanium and stainless-steel rod were used as current collectors for the working and counter electrode Three different working electrodes, i.e. cathodes here, were used during water electroreduction (see Fig. IV.1B): A stainless-steel plate, SSP, (AISI 316; Goodfellow, England) of 2.5×1.0×0.1 cm^3 (projected area: 2.5 cm^2, volume: 0.25 cm^3); a stainless-steel porous foam, SSPF, (AISI 316, 24 pores·cm^{-1}; Goodfellow, England) of 3.0×1.0×0.5 cm^3 (projected area: 3 cm^2, bulk volume: 1.5 cm^3); and a carbon brush, CB, (6TMIC Ingénieries, France) occupying a diameter of 5 cm and 4 cm of height (projected surface area: 20 cm^2, bulk volume: 79 cm^3). As cathodes with different sizes are compared in this section, the current density is calculated based on the projected area.

Prior to the use of the electrodes, a pretreatment for each was followed as described next. For the SSP and SSPF, successive immersion in the following solutions under stirring: Ethanol:Acetone (1:1) for 20 minutes, a 2/20% solution of fluorhydric/nitric acid for 20 and finally thorough cleaning with distilled water. The CB was thermochemically treated by thermal activation in a muffle furnace at 380 C for 2 hours. Afterwards, the CB was cleaned by successive immersion in the following solutions under stirring: Ethanol:Acetone (1:1) for 20 minutes, distilled water for 20 minutes, 1 M HCl for 1 hour, distilled water for 20 minutes, 1 M NaOH for 1 hour, and distilled water for 20 minutes. The DSA anodes are cleaned by applying an anodic current density of 250 A·m^{-2} in a 0.1 mol·L^{-1} sulfuric acid solution for 5 hours.

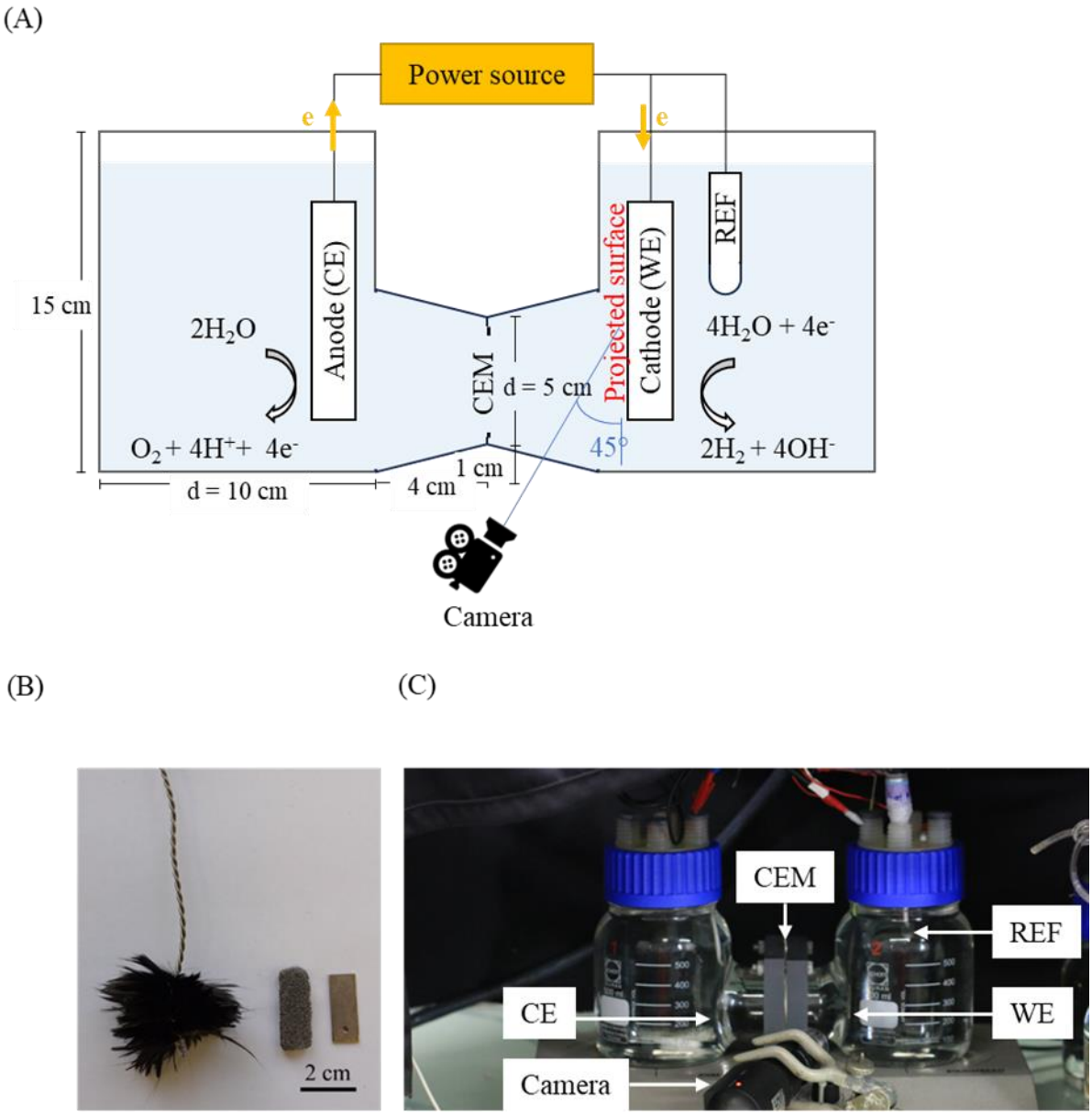

Fig. IV.1. H-type reactor design for the second experimental part. (A) H-type electrolyzer design. CE: Counter electrode (DSA anode); WE: Working electrode (Cathode); REF: Reference electrode (Saturated calomel electrode); CEM: Cation exchange membrane. (B) Working electrodes used in this part: Carbon brush (CB, left), stainless-steel porous foam (SSPF, middle), stainless-steel plate (SSP, right). (C) Photography of experimental setup

IV-2.2 Experimental design

Three different configurations were evaluated (by duplicate) during the recording of H_2 bubble nucleation, based on two conditions as shown in Table IV.2.

Table IV.2. Experimental configurations evaluated during the recording of H_2 bubble nucleation

Configuration	Conditions	
	H_2 pre-saturation	Agitation
1	No	No
2	No	Yes
3	Yes	Yes

A magnetic stirrer (370 rpm) was used to agitate the medium at the configurations 2 and 3. The H_2 pre-saturation condition was achieved by injecting H_2 gas bubbles through a glass frit (VitraPOR Micro-immersion-filter Por 2) at a rate of 9 $L \cdot h^{-1}$(375 $mmol \cdot h^{-1}$) during 1h. After the H_2 pre-saturation, the dissolved H_2 concentration was measured by stripping the H_2 out of a sample and measuring the gas phase concentration with gas chromatography (see Supplemental Information A). The H_2 pre-saturated samples achieved saturation concentration (0.78 $mmol \cdot L^{-1}$) with an estimated margin of error of 6%.

IV-2.3 Electrochemical and optical setup

Linear sweep voltammetry (LSV) was carried out to obtain the J=f(E) curve for the electroreduction reaction of water to H_2 happening on the working electrodes. The LSV was performed from the working electrode OCP to -2V versus the working electrode OCP. The scan rate used was 1 $mV \cdot s^{-1}$. While LSV was being performed, the projected surface of the cathode was video recorded using a digital 12M pixels camera with ×230 Optical zoom (Digital microscope 12M, RS PRO) with an embedded LED light, pointing at the cathode surface at a 45° angle of incidence as shown in Fig. IV.1C. Although the videos were recorded at ~20 frames per second, to reduce the file size and image processing time, 50 frames are skipped between every frame recorded, meaning that 1 frame is used every 2 seconds of video recorded. Considering the focal length between camera and the projected surface of the cathode, it was estimated that each pixel should roughly correspond to a bubble size of 18 µm. This was obtained by dividing a known length on the frame (e.g., the height of the stainless-steel plate, 2.5 cm) into the number of pixels that corresponded to that length in the recorded frame (e.g., 1410 pixels of cathode height).

By synchronizing the LSV voltammogram and the sequence of frames (images) recorded by the camera, it was possible to detect at which current during the J=f(E) curve the H_2 nucleation started as depicted in Fig. IV.2.

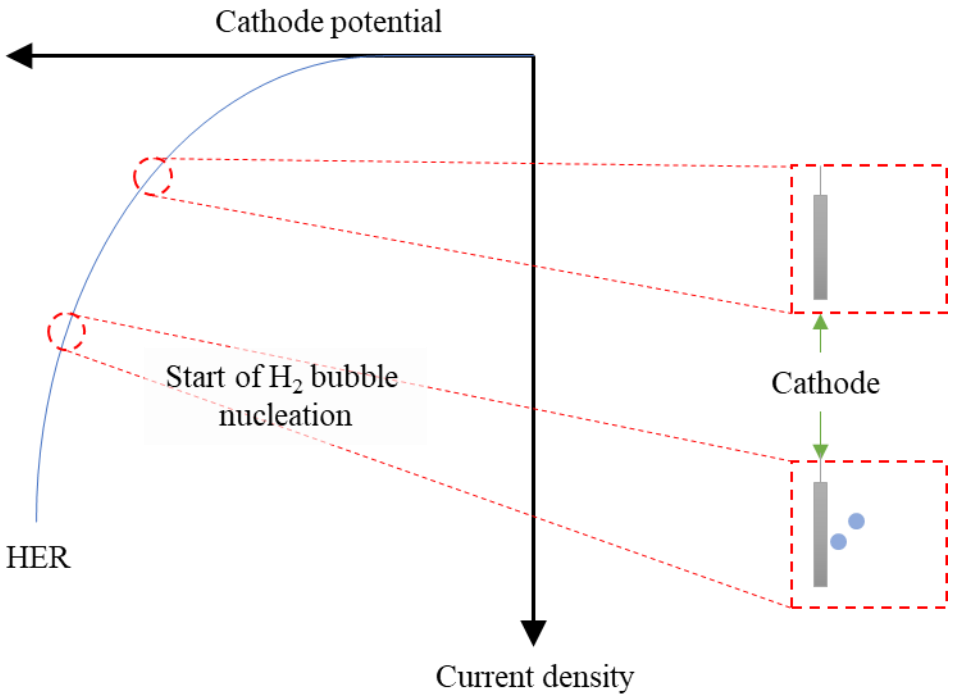

Fig. IV.2. Graphical representation of the determination of the current associated to the onset of H_2 bubble nucleation.

The sequence of frames corresponding to each video recording was saved and analyzed for image processing using MATLAB R2023a (The MathWorks Inc. 2022, version: 9.14.0.2206163) to detect the presence of H_2 bubbles at each frame. A graphical representation of the bubble detection algorithm is shown in Fig. IV.3 and described below.

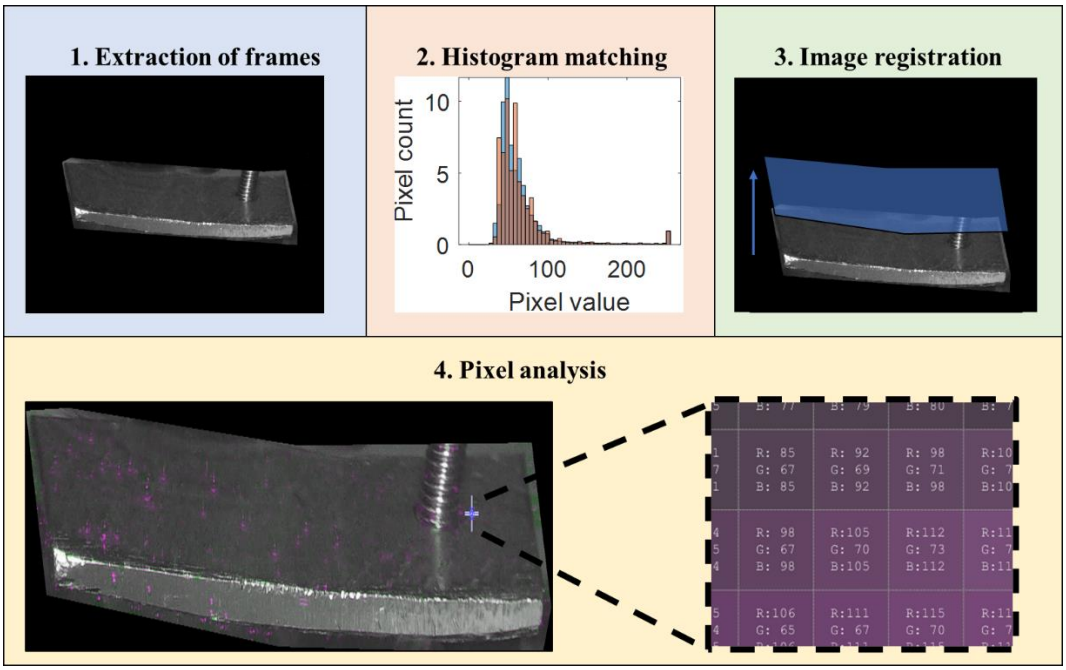

Fig. IV.3. Graphical representation of the bubble detection algorithm.

The sequence of images is first extracted from the video recorded. The first frame of the sequence is used as reference frame, at which the cathode is at OCP just before the start of the LSV. For every frame extracted, a current and cathode potential value is found based on the time each point during the LSV is recorded and the corresponding time each frame was captured. Then, for the following frames, each frame's histogram was adjusted to match the histogram of the reference frame. As the cathode's position might slightly move due to the agitated media, the cathode position at each frame was adjusted (image registration) to its position on the reference frame if necessary. Image registration was not done during when using the cathode brush with agitated media since each brush hair may move independently.

Based on the fact that the presence of a bubble changes the brightness of the pixels where the bubble is located, two different criteria were used to determine if bubbles were present: the first criterion denominated "absolute brightness", counts the number of pixels that are brighter than a threshold value and the second criterion, "relative brightness", counts the number of pixels where there is a considerable change of brightness (pixel-wise) compared with their individual pixel value at the reference frame. The number of pixels for both criteria is lastly divided by the total number of pixels analyzed in the picture. For the "absolute brightness" criterion, the threshold is chosen manually based on the pixel intensity of the cathode surface before bubbling (at the reference frame) and after bubbling (last frame during

LSV). For the “relative brightness” criterion, each frame is ‘fused’ with the reference frame using the MATLAB function *imfuse*, where brighter and darker pixels are colored magenta and green, while identical pixels are colored grey. Pixels were counted for the detection of bubbles if the intensity of the red channel is at least 1.5-times brighter/darker than on green channel and if the red or green channel has an intensity greater than 8% of the saturation value. These parameters were adjusted based on the apparition of bubbles on the stainless steel plate, since the nucleation onset on its projected surface was homogeneous enough to rapidly mask its surface, producing a clear plateau signal on its voltammogram. An example of this plateau and the graphical interface of the bubble detection algorithm can be found in Supplemental Information D.

IV-2.4 COMSOL simulation

To simulate the current distribution and the H_2 concentration, COMSOL Multiphysics 6.1 with the Secondary Current Distribution model and Transport of Diluted Species in the cathodic chamber using a half cell model where the total current was imposed (galvanostatic boundary). While half cell (cathodic) mode with a galvanostatic boundary allows to calculate the current density distribution on the cathode surface and mass transfer on the cathodic chamber, the absence of an anode in the simulation impedes any conclusions on absolute values of electric potential (or energy) in the cathode or electrolysis cell [199]. The mesh was automatically generated by COMSOL through the physics-controlled option, where a triangular mesh is used with automatic size refinement near the boundaries. Only the stainless-steel plate under no agitation was simulated, and the LSV data was entered as function in time of the total current imposed in the cathode. The electrode reaction was modeled using Butler-Volmer kinetics with an anodic/cathodic transfer coefficient of $\alpha = 0.5$. The electrolyte conductivity (κ_l) and the exchange current density (J_0) used were 12.7 $mS \cdot cm^{-1}$ and 23.13 $A \cdot m^{-2}$ (See Fig. D3) as measured experimentally.

IV-3. Results

IV-3.1 Optical detection of H_2 bubble nucleation

The accurate and early detection of H_2 bubble nucleation on electrode surfaces is critical for understanding and optimizing electrolysis processes, particularly in the context of designing

bubble-free systems. A key challenge in optical detection lies in differentiating true bubble formation from optical artifacts arising from electrode characteristics and experimental setup. This subsection addresses the question of how different cathode material structures influence the efficacy of optical bubble detection methods. The objective is to evaluate two primary optical criteria, where the absolute and relative brightness of the video frames are analyzed, and to identify their advantages and limitations when applied to electrodes with similar structures as the SSP, SSPF and CB cathode tested here.

The two criteria employed for detecting bubble nucleation (absolute and relative brightness, see section IV-2.3) exhibited distinct advantages and limitations according to the structural characteristics of the cathode materials (SSP, SSPF and CB). These differences arise from the presence or absence of specific optical features during video acquisition for each material, as illustrated in Fig. IV.4.

During the recording of the SSP cathodic surface shown in Fig. IV.4A, the electrode was securely fastened to the current collector, which minimized movement during agitation. This stability facilitated bubble detection using the relative brightness criterion, as minimal image registration was required to correct for electrode displacement. Additionally, the flat geometry of the SSP allowed for relatively homogeneous illumination across the surface, enabling the effective application of the absolute brightness criterion through the selection of a consistent threshold. These conditions allowed for the accurate detection of bright bubbles (labeled ‘a’ and visualized in violet in Fig. IV.4A), with minimal interference from background brightness fluctuations. The only limitation observed was a mild distortion of the electrode shape, attributed to optical deformation caused by the cylindrical walls of the electrochemical chamber (indicated by ‘b’). However, this did not significantly hinder the analysis of bubble nucleation.

In contrast, the recording of the SSPF surface (Fig. IV.4B) presented additional challenges. Alongside the cylindrical wall-induced deformation (‘b’), the porous structure of the SSPF led to increased motion during agitation, due to insufficient mechanical fixation to the current collector. As a result, image registration became essential for effective bubble detection using the relative brightness criterion. Moreover, the electrode’s porosity caused uneven illumination of the projected surface, creating alternating bright and dark regions. This heterogeneity in brightness produced instances where bubbles appeared as darker regions

(labeled ‘c’ and shown in green), complicating the application of the absolute brightness criterion.

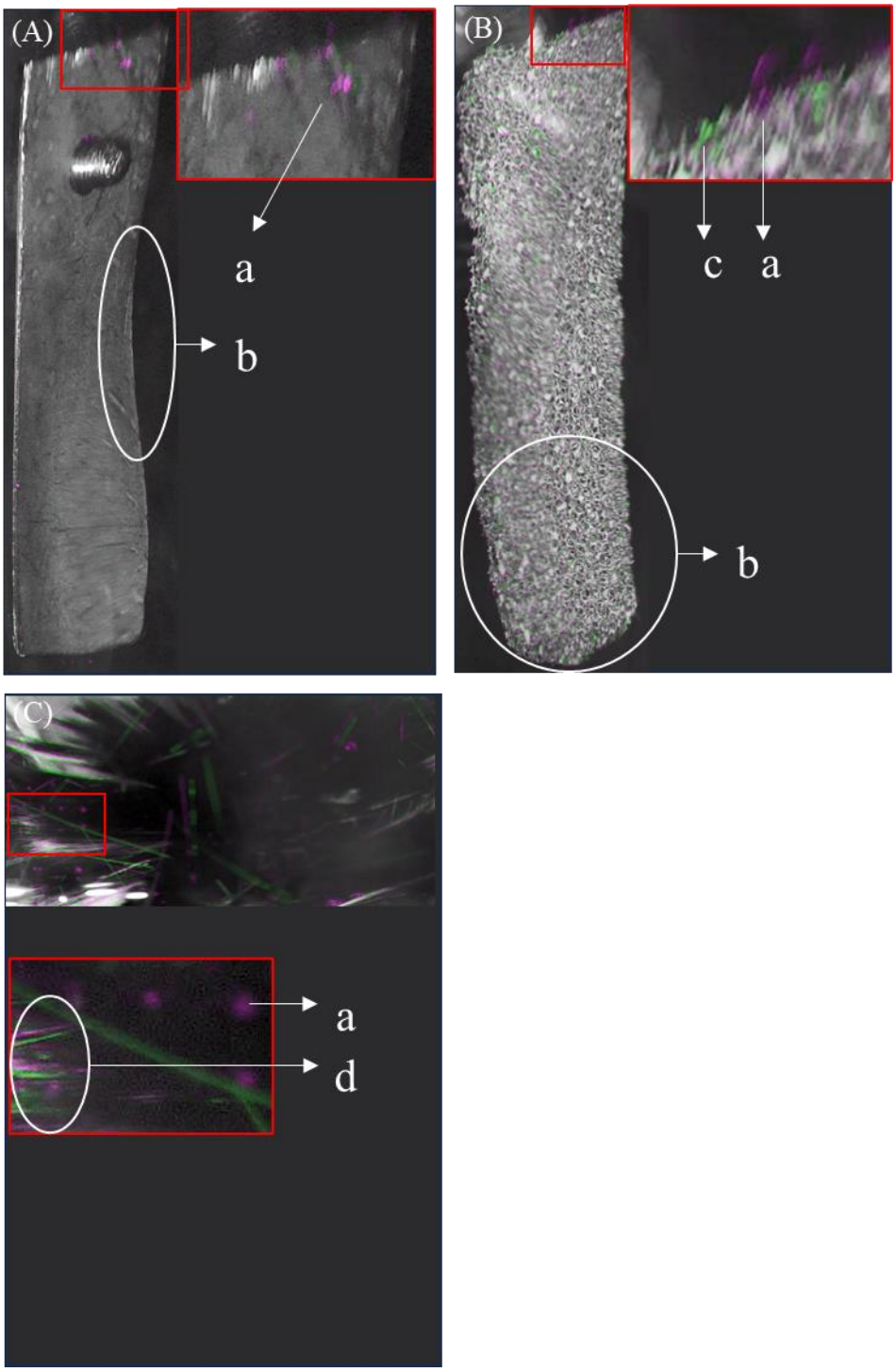

Fig. IV.4. Optical features observed during image processing for H_2 bubble nucleation detection in linear sweep voltammetry (LSV) experiments conducted on different cathode materials under stirring and H_2 pre-saturation. The cathode materials tested were: (A)

stainless-steel plate (SSP); (B) stainless-steel porous foam (SSPF); and (C) carbon brush (CB). The optical features identified during the analysis are marked with white letters: (a) and (c) indicate bubble detection based on brightness variations (increase and decrease, respectively); (b) corresponds to shape deformation caused by the use of cylindrical-walled vessels; and (d) refers to brightness changes resulting from deformation of the overall cathodic geometry.

For the CB cathode shown in Fig. IV.4C, although the bubbles remained optically distinguishable from the darker electrode background (allowing identification of bright bubbles, 'a'), the free movement of the electrode during agitation severely limited the use of the relative brightness criterion. Electrode displacement introduced brightness variations unrelated to bubble nucleation, thereby compromising the reliability of both detection methods and necessitating manual classification of bubbles.

Despite these challenges, it was proved that the digital camera employed had enough resolution to enable early-stage detection of bubble nucleation events (as demonstrated by the matching of the bubble detection optical signal with the cathode masking signal in the voltammogram, see Fig. D1), Moreover, it was successfully employed in complex geometries such as the porous foam and brush, underscoring its usefulness as a bubble nucleation sensor for water electroreduction.

IV-3.2 Current density analysis associated with bubble nucleation on different cathode materials under varying experimental conditions

Understanding the electrochemical conditions that conduce to H_2 bubble nucleation is essential for controlling gas evolution during water electroreduction. This subsection investigates the key question of how current density, electrolyte pre-saturation with H_2, and agitation influence the onset of bubble nucleation on various cathode materials. A significant challenge is to precisely correlate the observed nucleation events with specific current densities and to systematically quantify the individual and combined effects of mass transport parameters. The objective is to determine the cathodic current density at which the first observable bubble nucleation event occurs for SSP, SSPF, and CB electrodes under different

experimental conditions. The analytical approach involves identifying nucleation events from kinetic current-potential (J = f(E)) curves and systematically varying agitation and H_2 pre-saturation to elucidate their impact on nucleation behavior. This approach enabled the correlation between electrochemical behavior and gas evolution dynamics. Furthermore, the influence of two key experimental parameters, the pre-saturation of the electrolyte with dissolved hydrogen and the application of mechanical agitation, was systematically evaluated in terms of their effects on mass transport and nucleation behavior.

A summary of the results obtained under each experimental condition is provided in Table IV. 3.

Table IV. 3. Summary of the results on the determination of the cathodic current density at nucleation for the stainless steel plate (SSP), stainless steel porous foam (SSPF) and carbon brush (CB) under different conditions of agitation and H_2 pre-saturation.

Cathode design	Projected surface area [cm^2]	Agitation	H_2 pre-saturation	Current density at nucleation [$A \cdot m^{-2}$]
SSP	2.5	No	No	-17.56 ± 2.15
		No	Yes	-9.10 ± 3.88
		Yes	Yes	-18.32 ± 1.21
SSPF	3	No	No	-26.12 ±1.06
		No	Yes	-14.88 ± 5.73
		Yes	Yes	-42.38 ± 14.78
CB	20	No	No	-29.60 ± 4.94
		No	Yes	-15.54 ± 6.12
		Yes	Yes	-25.23 ± 4.07

IV-3.3 Supersaturation at the stainless-steel plate cathode surface

Knowing the maximum local concentration of dissolved H_2 at the electrode surface that can be held before H_2 bubble nucleation is essential for the design and operation of bubble-free water electroreduction cells. A critical question arises concerning the extent of supersaturation required for nucleation and how it correlates with experimental observations, especially given the complexities of mass transport at macroelectrodes. A key challenge is to accurately estimate this localized supersaturation, which is often difficult to measure directly,

and to reconcile any discrepancies between theoretical predictions and experimental data. This subsection aims to estimate the dissolved H_2 concentration and corresponding supersaturation ratio at the SSP cathode surface at the onset of bubble nucleation under non-agitated conditions. The analytical approach combines experimental determination of nucleation current densities with finite element simulations to resolve the spatial distribution of dissolved H_2 and current density at the critical nucleation point. An example of the simulated current density distribution at the nucleation onset, corresponding to the experimental condition without agitation or H_2 pre-saturation for one of the replicates is presented in Fig. IV.5.

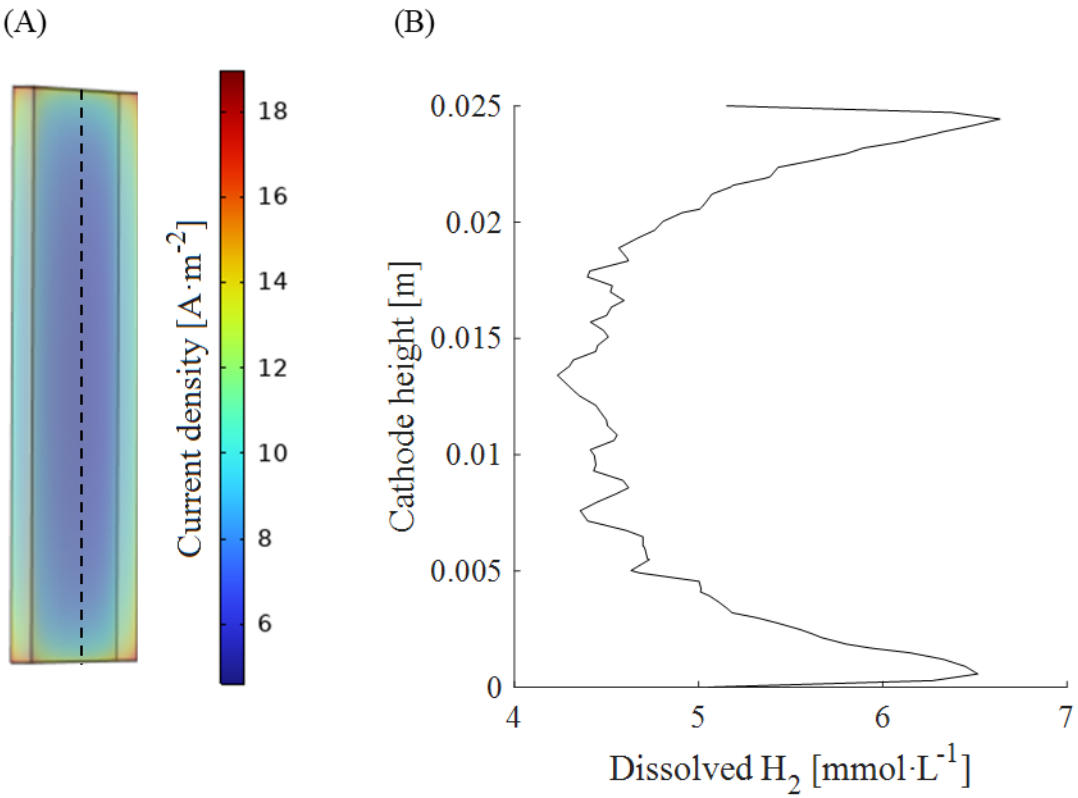

Fig. IV.5. Simulation of the experimental run with SSP cathode without agitation or H_2 pre-saturation for one of the replicates. (A) Simulated cathodic current distribution at the start of H_2 nucleation (t = 1104 s of the linear sweep voltammetry). The dashed vertical line is used as a measuring path for plotting the (B) dissolved H_2 concentration measured at the cathodic surface. The noise present in (B) is due to the solution being plotted without any post-processing tool used in (A).

As shown in Fig. IV.5A, the simulated current density is primarily localized at the edges of the cathodic surface. However, within the resolution limits of the optical detection method

employed, bubble nucleation was observed to initiate preferentially at surface pits and imperfections, as confirmed by visual inspection of the recorded videos (see example in Supplemental Information D). These surface defects were not incorporated into the simulation geometry, which may explain the discrepancy between the predicted and observed nucleation sites.

Despite this limitation, Fig. V.5B provides useful insight into the concentration of dissolved H_2 at the moment of nucleation. By averaging the maximum and minimum concentrations along the measurement path, the local dissolved H_2 concentration is estimated at approximately 5.5 $mmol \cdot L^{-1}$. The corresponding local supersaturation ratio at the onset of nucleation is thus estimated to be $\sigma = 6.1$ according to the finite element simulation. It is worth noting that due to the low resolution of the camera, the threshold current measured here do not correspond to the first nanobubble nucleation event but could more closely relate to the threshold current density at which the pinned bubbles quickly grow to a micrometer scale and get detected by the camera.

The same approach of combining current density distribution and estimation of local dissolved H_2 concentration was applied to the remaining experimental runs conducted with the SSP cathode under non-agitated conditions. The resulting averaged H_2 concentrations are presented in Fig. IV.6, plotted as a function of the corresponding current density values normalized to the projected cathodic surface area. It can be observed that, under H_2 pre-saturation conditions, the maximum current density achievable prior to the onset of nucleation was reduced. This limitation, in turn, led to lower levels of local supersaturation at the cathodic surface, consistent with the suppressive effect of dissolved H_2 on further bubble formation.

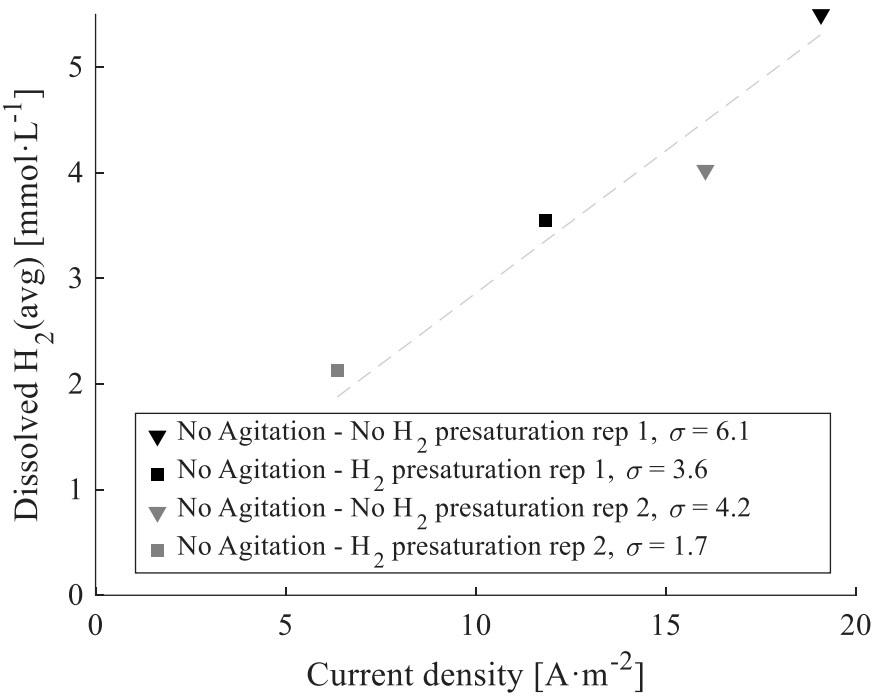

Fig. IV.6. Estimated average concentration of dissolved H_2 at the SSP cathode surface under non-agitated conditions at the onset of bubble nucleation. The values on the y-axis represent the average concentration, calculated as the mean of the maximum and minimum concentrations along the measurement path indicated by the dashed line in Fig. IV.5A.

The Cottrell equation (31) is commonly used in ultramicroelectrodes to represent the linear relationship between the current at which nucleation occurs and the local H_2 concentration at the electrode surface [90]:

$$I_{crit} = 4nFD_{H_2}C_{H_2}^{crit}r_e \qquad 31$$

Where I_{crit} is the current at the point of bubble formation, n is the number of electrons involved in the reduction reaction, F is the Faraday number, D_{H_2} is the diffusion coefficient of H_2 and r_e is the radius of the ultramicroelectrode tip. This equation arise from the solution of the diffusion problem in a disk ultramicroelectrode, and describes current-time behavior under diffusion-limited conditions and is particularly applicable to ultramicroelectrodes which is not the case here (with at least one dimension < 25 µm) [90]. This framework is frequently employed in studies using nanoelectrodes to capture peak current signals associated with bubble nucleation events [128], [200]. In the present study, the estimated maximum local supersaturation was approximately σ = 6. This value is two orders of magnitude lower than the theoretical maximum predicted by classical nucleation theory, and one order of magnitude

below the values typically reported in nanoelectrode-based experiments [128]. However, it is comparable to the lower bound of supersaturation values (σ = 8) observed in studies using microelectrodes, as previously described in the literature [129]. This discrepancy between theoretical predictions and experimental values has been attributed to several factors, including the effective surface area of macroelectrodes, the presence of surface artifacts or defects, and the influence of the electric field on surface tension within the electric double layer [201], [202]. In this case, the pronounced effects of both H_2 pre-saturation and mechanical agitation on the maximum current density and local supersaturation at the nucleation onset highlight the critical role of mass transport limitations and the structure of the diffusive boundary layer. These findings highlight that, beyond reaching a critical concentration of dissolved H_2 at the electrode surface, the dynamics of the surrounding electrolyte and the properties of the interfacial region significantly influence the nucleation process.

IV-3.4 Comparison of cathode materials based on the maximum current density achievable without H_2 bubble nucleation and their electrocatalytic performance

For the development of efficient bubble-free electrolysis systems, it is relevant to identify cathode materials that can besides sustain high current densities without initiating H_2 bubble formation, are also good electrocatalysts of the HER. In this subsection, the kinetic current-potential (J = f(E)) curves were analyzed to calculate the cathodic power densities for each material at a representative current density for the three cathodes tested.

To evaluate the capacity of different cathode materials to sustain hydrogen evolution without bubble formation, their performance was compared by their kinetic curves (J = f(E)) as presented in Fig. IV.7.

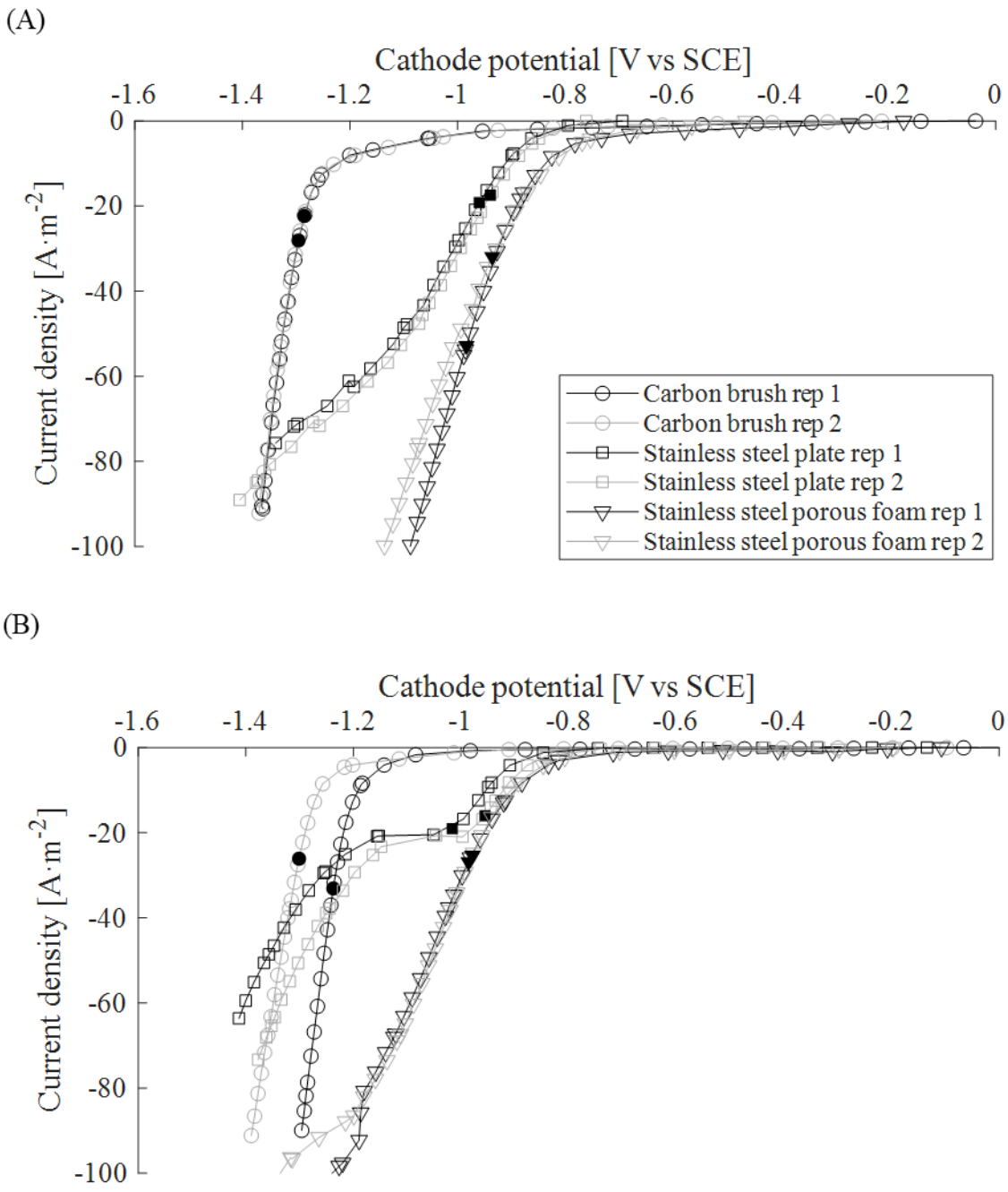

Fig. IV.7. Electrocatalytic performance of the hydrogen evolution reaction (HER) catalyzed by stainless-steel plate (SSP), stainless-steel porous foam (SSPF), and carbon brush (CB) electrodes in a medium subjected to (A) agitation and H_2 pre-saturation and (B) no agitation and no H_2 pre-saturation. Filled black markers indicate the point of H_2 bubble nucleation detection.

In Fig. IV.7A, which more closely resemble actual operation conditions, a clear shift in the J = f(E) curves can be observed for the CB electrode compared to the stainless-steel electrodes,

particularly at current densities below -70 $A \cdot m^{-2}$. This shift reflects the relatively lower catalytic activity of carbon-based electrodes for HER, which translates into higher overpotentials at a given current density. In practical terms, this implies higher energy consumption for equivalent hydrogen production rates.

For instance, to impose a current density of -30 $A \cdot m^{-2}$ using each of the three cathode materials, the corresponding cathodic power densities (calculated as P = J·E) required to sustain HER are: 29.91 ± 0.04 $W \cdot m^{-2}$ for the SSP, 22.45 ± $W \cdot m^{-2}$ for the SSPF and 31.76 ±0.33 $W \cdot m^{-2}$ for the CB. These values highlight not only the differences in catalytic performance but also the potential trade-offs between material structure, efficiency, and operational cost in the design of bubble-free electrolysis systems. Moreover in Fig. IV.7A, the stainless-steel plates showed a clear overpotential after bubble nucleation, and in Fig. IV.7B, this becomes more evident achieving a characteristic overpotential due to the initial masking of the electrode area due to bubbling and posterior bubble release and demasking at higher current densities. A similar overpotential is also observed in Fig. IV.7B at a current density below -90 $A \cdot m^{-2}$ for the stainless-steel porous foam, where mass transfer becomes more evidently limited. Due to the small surface area of the stainless-steel plate, the nucleated bubbles end up masking a large proportion of the cathodic surface, having a noticeable effect on the J = f(E) curves. It is also worth noting that at the end of the experiment, the nucleation of bubbles at the CB happened mostly either in the current collector contact and on the CB tips that were closer to the separator/anode (see Fig. D2 from Supplemental Information), which is common of an uneven current distribution across the cathode surface. In the context of H_2 solubilization, although bubbling is presented at high current densities, it might be favorable to work as such high currents when the dissolved H_2 concentration is still much lower than the saturation concentration, given that gas cavities can be removed when a lower current density mode is to be operated near the saturation limit with the purpose of favoring the production of dissolved H_2. For example, when examining one of the repetitions for the non-agitated and non-pre-saturated, the bubbles pinned to the SSP surface at the end of the experiment had diameters of around 0.2-0.6 mm (), while on the CB were 0.2-0.8 mm (bubble sizes at the SSPF were not estimated since the porosity impeded a clear measurement at the low image resolution acquired). While the bubble size might be insufficient to achieve supersaturation, a

static bubble of 0.4 mm should still dissolve around 26-times faster than a static bubble of 2 mm according to the Epstein-Plesset theory.

IV-3.5 Effect of H_2 pre-saturation and agitation on the maximum current density achieved without bubble nucleation.

Mass transport phenomena, specifically the accumulation of dissolved H_2 at the electrode-electrolyte interface, plays a big role in the onset of bubble nucleation during water electroreduction. Moreover, in the practical use of a water electroreduction, it is possible that high bulk concentrations of dissolved H_2 are needed to be maintained to drive other hydrogen-consuming processes such as hydrogenotrophic bioreactors. This subsection focuses on how electrolyte H_2 pre-saturation and mechanical agitation individually and synergistically impact the maximum current density achievable before bubble formation. A significant challenge lies in quantifying the specific contributions of these parameters to mitigating or promoting nucleation across different electrode architectures. The main objective here is to evaluate the combined and individual effects of H_2 pre-saturation and agitation on the nucleation threshold for SSP, SSPF, and CB cathodes. The analytical approach involves comparing the maximum current densities achieved under various conditions (non-agitated/non-pre-saturated, non-agitated/pre-saturated, agitated/pre-saturated) to elucidate the roles of convection and dissolved H_2 accumulation. The results for each electrode are summarized in Fig. IV.8.

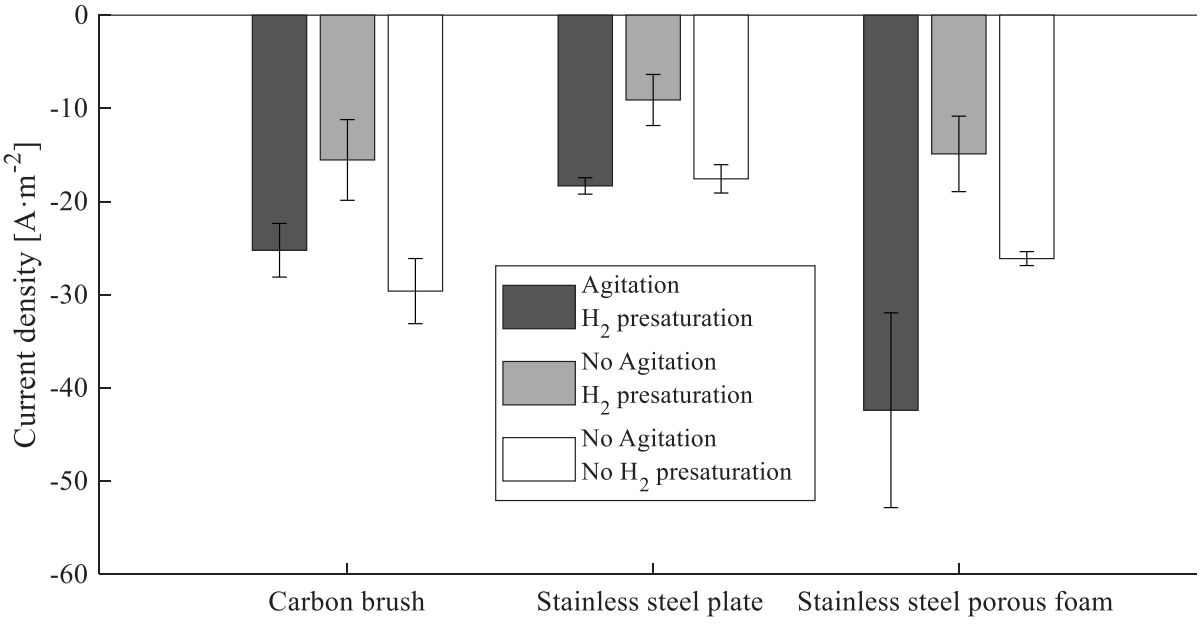

Fig. IV.8. Effect of H_2 pre-saturation and agitation on the maximum current achieved before the onset of H_2 bubble nucleation on a stainless-steel plate (SSP), stainless-steel porous foam (SSPF) and carbon brush (CB).

Among the materials tested, the SSPF exhibited the highest current density before nucleation, reaching -42.38 $A \cdot m^{-2} \pm 14.77$ under agitation and H_2 pre-saturation. This was followed by the CB at -25.22 $A \cdot m^{-2} \pm 4.07$, and the SSP at -18.32 $A \cdot m^{-2} \pm 1.24$ ($p = 0.025$). These conditions are representative of systems designed to produce dissolved hydrogen or operate under bubble-free electrolysis modes and clearly demonstrate the superior performance of the porous foam in terms of both reduced bubble formation and lower cathodic power density required for HER.

To better understand the respective roles of convection and dissolved H_2 accumulation, the impact of agitation and pre-saturation was analyzed for each electrode. H_2 pre-saturation alone significantly reduced the maximum current achievable before bubble formation ($p = 0.017$), while agitation of the pre-saturated medium partially restored this threshold ($p = 0.002$).

Due to its planar geometry, the SSP likely benefits from more favorable mass transport by diffusion and advection, reducing local H_2 buildup. However, its low surface area results in higher local current densities, promoting earlier nucleation. For the SSP, H_2 pre-saturation reduced the nucleation threshold by approximately a factor of 1.9, which was almost fully recovered (increased by a factor of 2) with agitation. This two-fold change serves as a useful reference for comparing electrodes with more complex structures.

In the case of the CB, H_2 pre-saturation also reduced the nucleation threshold by a factor of 2, but agitation restored it only by a factor of 1.62. This partial recovery suggests that magnetic stirring was insufficient to fully mitigate local H_2 accumulation within the brush's fibrous structure.

In contrast, for the SSPF, H_2 pre-saturation reduced the nucleation current by a factor of 1.7, while agitation increased it by a factor of 2.8. The more pronounced effect of agitation on the SSPF compared to the SSP implies that the foam was already experiencing diffusion limitations even in the absence of H_2 pre-saturation. Agitation not only counteracted the effects of pre-

saturation but also alleviated inherent mass transport limitations due to the foam's porous geometry. This explains why the SSPF outperformed the CB only under agitated conditions.

IV-4. Discussion

IV-4.1 Choosing the right electrode materials to favor H_2 dissolution

The successful advancement of hydrogenotrophic bioreactors relies on the efficient solubilization of H_2. Achieving this when using water electroreduction as H_2 source, particularly under high currents necessary for viable practical applications, relies fundamentally on two primary strategies: strategically selecting electrode materials and optimizing the hydrodynamic environment. The initial consideration involves choosing cathode materials that inherently discourage the nucleation of bubbles, and that can operate at higher thresholds of H_2 supersaturation before nucleation starts. Classical nucleation theory offers a guiding framework for achieving this by optimizing the electrode's surface chemistry and the composition of the medium. For instance, engineering electrode surfaces to be more hydrophilic, increasing the energy barrier required for nucleation. In parallel, the electrolyte medium composition must be also considered, specifically by avoiding surfactants that tend to decrease surface tension and facilitate nucleation. Beyond surface properties, the magnitude of the electrochemical active surface area is also fundamental. Materials possessing high surface areas facilitate the distribution of the total imposed current across a larger active region, which effectively maintains low local current densities at the individual reaction sites. This current distribution results in lower local rates of H_2 accumulation, successfully preventing the localized gas oversaturation that would otherwise initiate bubble formation, even when the overall macroscopic current is high. Here, the CB and the SSPF obtained a higher current density threshold than the stainless-steel plate, supporting the importance of the use of electrodes with high surface area. Nonetheless, the effective use of the surface area should be ensured by achieving even current distribution over the electrode surface, which requires careful dimensioning and design of these porous/3D electrodes.

In addition to the effect of the electrode material on bubble nucleation, the energetic costs related to HER kinetics represent an equally important aspect influencing both cathode material selection and the eventual reactor configuration. Here, it was observed that despite the theoretical benefit of the large surface area achieved with the CB to avoid nucleation, it

presented the highest overpotential required for HER initiation according to the J = f(E) curves. This disparity indicates that while surface area is an important component, the intrinsic catalytic activity of the chosen material cannot be ignored. This insight aligns with known challenges associated with carbon-based electrodes, which often exhibit poor inherent electrocatalytic activity for HER despite their vast surface areas, necessitating common modifications like doping with heteroatoms or combining them with transition metals to enhance performance [191]. In contrast, transition metals such as iron (Fe) and nickel (Ni), are well-established as effective HER catalysts, second only to noble metals like platinum (Pt) [190]. Nickel and its alloys (e.g., Ni-Mo, Ni-Fe, Ni-Co) are particularly notable also for their affordable commercial price.

IV-4.2 The interplay between cathode porosity, hydrodynamics and mass transfer

The second critical component for preventing bubble formation involves optimizing the hydrodynamic flow dynamics immediately surrounding the cathode surface. This optimization is indispensable for the efficient mass transport of dissolved H_2, enabling its transport from the thin diffusion layer where it is generated and into the bulk electrolyte where planktonic hydrogenotrophs are. Here, it was shown that agitation alleviated the H_2 pre-saturation conditions by allowing a higher current density threshold compared with the no agitation scenario. Also, the analysis of the H_2 concentration over the SSP surface revealed that a local supersaturation value of approximately $\sigma = 6$ could be achieved under simple agitation, even without deliberate optimization of surface chemistry or medium composition. This value establishes an upper boundary for the bulk H_2 concentration attainable before bubble nucleation inevitably occurs. Optimizing the hydrodynamics to allow for a faster removal of H_2 out of the electrode surface is also relevant for configurations where micro/nanobubbles are deliberately produced. The formation of these smaller bubbles often requires high local supersaturation levels (i.e., high current densities) while maintaining slow growth rates in bubble size. By enhancing the removal of dissolved H_2 from the diffusion layer into the bulk liquid, the growth rates of these bubbles can be decreased [121], [203], [204], potentially improving the control and utility of these micro/nanobubble systems. Here, the bubbles pinned to the electrode surface had diameter in the micrometer range at the highest current

density evaluated at the end of the experiment. An initial production of microbubbles bubbles can also be a good strategy to allow the use of higher currents, especially when the dissolved H_2 concentration is still low, where the dissolution rate of these microbubbles is expected to be large.

The results from this chapter suggest that the porosity of the stainless-steel porous foam could be a potential limiting factor in preventing bubble formation, paradoxically, despite its large overall surface area. This observation resonates with findings from Rocha *et al.* , where by using nickel foams (high surface-to-volume ratios) of different porosities in alkaline water electroreduction, foams with smaller pore sizes yielded the highest electrochemical active surface areas [205], but not necessarily the best overall performance, presenting larger overpotentials. This was attributed to bubble entrapment within very small pore sizes, a direct consequence of poor electrolyte flow and inefficient mass transfer within the intricate porous structure of the electrode.

IV-4.3 Practical considerations in reactor design and bubble detection

Accurate and reliable bubble detection is needed for the study and optimizing bubble-free H_2 production. In this work, a relatively simple optical detection method was successfully employed to identify the onset of bubble nucleation across various cathode structures and agitation conditions. It was found that a pixel-wise comparison method proved particularly effective when the cathode was rigidly fixed in space. However, its utility was significantly limited for electrodes prone to movement, such as the CB under agitation, where consistent spatial referencing becomes challenging. Another certain limitation of the optical detection used here is that only the projected area of the cathode was being recorded. For the porous foam and brush cathodes used here, it means that possible bubbling inside the pores of the foam or deep in the brush was not captured. Although it could be expected that the cathodic surface area closer to the projected surface contains most of the current distribution (see Chapter V) where nucleation starts, it can be hypothesized that this limitation is also responsible for the variability of the measured current density at nucleation. Moreover, the exponential increase of the current density with time (through the linear sweep voltammetry experiment) also meant that the current recorded varied faster at larger current. This means that for large current densities, a larger variability of the bubble nucleation start is expected

compared to when the nucleation starts at lower values. Future experiments should consider doing a linear sweep of the current (not the cathode potential) or a step increase of the current in constant intervals.

For less controlled experimental conditions (e.g., with cathode movement or fluctuating illumination levels), more generalized detection methods, such as blob characterization or machine learning algorithms, might offer superior robustness and accuracy. These methods can better handle variations in image data, making them more adaptable to diverse experimental setups.

When considering reactor design, a transparent H-type cell was advantageous for our experimental setup, as it facilitated the straightforward implementation of various cathode designs and simplified video recording. However, for practical and scalable applications, this specific reactor design is generally discouraged due to its significant mass transfer limitations at both laboratory and large scales [176], [206]. As previously emphasized, ensuring proper convection is critical, especially when working with porous or 3D electrode structures where efficient removal of dissolved H_2 is crucial. Consequently, compact flow-through cells are preferred in engineering applications due to their superior mass transfer capabilities, which allow for more efficient product removal and reactant delivery.

Nevertheless, integrating optical bubble measurement into these compact cell designs presents unique challenges. The constrained space often limits the ability to effectively capture images of the electrode surface, and the non-transparency of commonly employed construction materials further complicates optical access. To overcome these limitations, special observation windows can be ingeniously integrated into compact cell designs specifically for this purpose [150]. Furthermore, for the very early detection of bubbles where bubbles form slowly but do not rapidly depart from the surface, miniature cameras with low-speed capture capabilities, such as endoscopic cameras, might be particularly well-suited for integration into these compact cell designs, offering a promising tool for *in situ* monitoring. In other scenarios, such as turbid media, setups where bubbles do not necessarily form at the projected area first, or setups were bubble formation is desired, this tool can be used as a complimentary sensing device to other detection techniques such as operando high frequency impedance measurements for a more robust detection [157].

IV-5. Conclusion

In this chapter, the conditions enabling hydrogen production in the absence of visible bubble formation during water electroreduction were investigated. By combining optical video analysis, electrochemical measurements, and finite element modelling, the onset of H_2 bubble nucleation across different cathode materials and operating conditions was characterized. The optical detection method based on local brightness variations proved effective for fixed and well-illuminated electrodes, such as the stainless-steel plate (SSP), but encountered limitations with highly porous or mobile electrodes, particularly under agitation. This highlights the need for more robust image processing strategies when dealing with dynamic or heterogeneous electrode geometries. Among the tested cathodes, the stainless-steel porous foam (SSPF) exhibited the best performance in delaying bubble formation, allowing the highest bubble-free current densities. This advantage is attributed to its high surface area and favourable mass transport properties. Finite element simulations further revealed that hydrogen nucleation occurred at local supersaturation levels around $\sigma \approx 6$, consistent with values reported in the literature for macro-structured electrodes. Finally, the combined influence of hydrogen pre-saturation and medium agitation significantly impacted the critical current density at nucleation. These findings underline the importance of hydrodynamic conditions and local concentration gradients in the control of gas evolution. Overall, this work provides valuable insights for the design of electrochemical systems targeting efficient, bubble-free hydrogen delivery, particularly relevant in applications such as microbial electrosynthesis or membrane-less reactors.

Chapter V. Numerical simulation study on the mass transfer and current distribution of different cathode geometries for the solubilization of H_2 by water electroreduction

ABSTRACT

Water electroreduction offers a path to achieving high H_2 solubilization rates and efficiencies. However, to maximize the H_2 solubilization rate, large currents must be applied without causing bubble nucleation at the cathode surface. Bubble formation is influenced by uneven current distribution, which can arise from suboptimal cell geometry, kinetics, and mass transfer. Uneven current distribution is a known phenomenon in electrochemistry, with the primary current distribution being determined by the geometry and ohmic resistance. This is compounded by secondary and tertiary current distributions, which consider kinetic effects (activation overpotential) and mass transfer, respectively. Naturally, the following question arise when trying to optimize the cathode/cell structure to avoid bubble nucleation: What design constraints such as electrode shape and size ratios, electrode porosity and hydrodynamic flow (forced vs non-forced flow) arise when designing a water electroreduction cell with minimal current distribution heterogeneities and improved mass transfer?

To approach this question, numerical simulations were used in this chapter to evaluate different cathode characteristics (shape, size and porosity) providing a more affordable and faster alternative to experimental evaluation. To manage computational costs, mass transfer and current distribution were simulated separately, which also helped to understand the individual effect of hydrodynamics and cathode design. It was found that achieving geometrical symmetry in the sizing and shape of the electrodes and membranes is necessary to avoid hyperpolarization on edges. Moreover, when porous or 3D electrodes are used, it was also found by CFD simulations that forced flow might be more effective on achieving proper

mixing than agitation by stirring, which prompts the use of continuous flow cells over batch electrolysis designs.

V-1. Introduction

The potential for achieving supersaturated conditions and high solubilization efficiency was demonstrated while achieving H_2 solubilization rates comparable to gas injection in Chapter III. Nevertheless, in many hydrogenotrophic processes, besides improving the solubilization efficiency, the large scale production of metabolites of interest is still constrained by the slow H_2 solubilization rate, usually attributed to the slow gas-to-liquid mass transfer. Achieving larger H_2 solubilization rates by water electroreduction while maintaining high solubilization efficiencies implies being able to impose large currents without the nucleation of bubbles at the cathode surface. Unfortunately, the unevenness of the current density over the cathode surface can cause some areas of the electrode present significantly larger current densities and therefore become also nucleation sites (e.g., at electrode edges). Uneven current distributions can arise from suboptimal geometries, kinetics and mass transfer. As current moves through the electrolyte by ion/charge movement following the path that offers lower electrolyte (ohmic) resistance, it can be expected that nonsymmetrical electrode/cell geometries having paths with different electrolyte resistances present nonsymmetrical (uneven) current distributions as well. This is usually referred to as a primary current distribution, where the current density is highest at the electrode locations closest to the counter electrode [90]. The hyperpolarized points where current density is highest also experience higher activation overpotentials, which arise due to the slower charge exchange at the electrode-solution interface. It is referred as a secondary current distribution when considering the activation overpotential as well, which tends to “even out” the current distribution at the expense of an energy cost associated to the higher polarization. Finally, when considering the effect of the concentration profiles due to mass transfer, it is referred to as tertiary current distribution, where the ion and reacting species gradients influence the electrolyte conductivity and electrode kinetics respectively [93].

The importance of mass transfer and proper mixing around the cathode surface was also highlighted in Chapter IV as a fundamental phenomenon that prevents the nucleation of bubbles, where the current imposed free of bubbles could be ~2 times higher when the medium was agitated and already saturated with H_2. Nevertheless, it was also observed that vigorous stirring alone did not easily remove all H_2 bubbles attached to the carbon brushes of a cathode, and a better solubilization of H_2 was obtained during preliminary experimentation when the cathode was gently shaken by a servomotor instead of stirring agitation. Not surprisingly, rotating disk electrodes are commonly used in electrochemistry as a way to improve convective transport around the electrode surfaces due to its more controlled and predictable shear forces around the electrode surface [90].

Structural characteristics of the electrode also influence the mass transfer on the cathodic surface and therefore their capacity to work under a bubble-free regime. Although it is generally recognized that mass transfer in porous materials is more complex than in flat plates, it was demonstrated in Chapter IV that cathode structures with large surface areas such as porous materials, can allow larger currents in the absence of bubble formation. When using porous electrodes, it would be advantageous to choose a porous structure that allows a maximum dispersion of the fluid inside its porosity while still having a large surface area, as demonstrated by Rocha *et al* with the use of open cell Ni foams during alkaline water electrolysis [205].

It is therefore clear that for the solubilization of H_2, it becomes relevant to understand how mass transfer and current distribution can be influenced due to the cell/cathode design parameters with porous electrodes. As depicted in Fig. V.1, while the added area due to the cathode porosity impacts positively the solubilization of H_2 by lowering the current density, it also adds a current path of higher ohmic resistance and possibly complex mass transfer, which negatively impacts the current distribution.

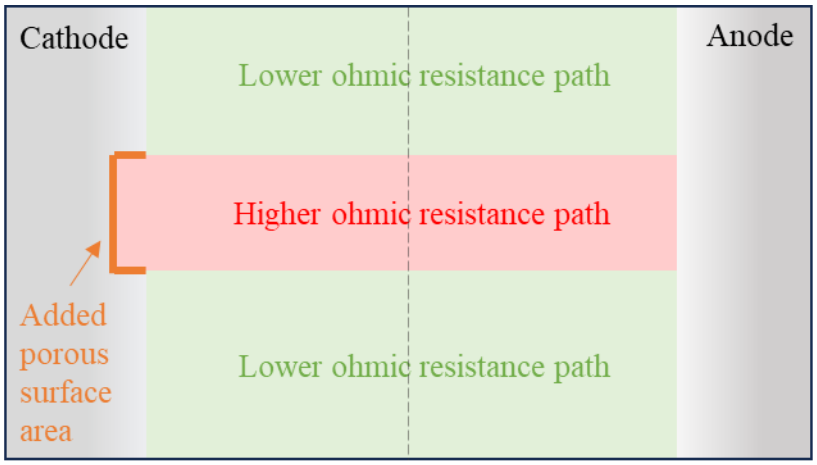

Fig. V.1. Schematic of a low and high ohmic resistance paths in a water electroreduction cell generated due to a nonsymmetric cathode geometry.

It is therefore essential to answer: What design constraints such as electrode shape and size ratios, electrode porosity and hydrodynamic flow (forced vs non-forced flow) arise when designing a water electroreduction cell with minimal current distribution heterogeneities and improved mass transfer?

Currently, the study of local variables such as the current density and dissolved H_2 concentrations cannot be straightforwardly measured experimentally in complex structures, and instead their study can be achieved through the simulation of both current distribution and mass transfer physics, which is a more affordable and faster alternative than the manufacturing and experimentally evaluating different designs. Nevertheless, the simulation of hydrodynamics is already highly computationally costly by itself, and the coupling of fluid flow with transport of species and current distribution physics raises the computational cost even further, severely limiting the number of simulations it can be performed within the design space for the optimization of the electrolyzer. Moreover, as concentration overpotentials can mask the uneven current distribution caused by geometric factors, both mass transfer and current distribution physics are simulated by separate in order to set design constraints that would reduce the number of simulations needed for the dimensioning of the electrolyzer through coupled Multiphysics. In the first part of this chapter, the current distribution is studied in different cathode size and geometries. Then, mass transfer is compared in two scenarios: unrestricted and restricted continuous flow, assuming the current distribution in the cathode is perfectly homogeneous and ignoring kinetic effects.

V-2. Methodology

V-2.1 Study of the current distribution of different cathode geometries during water electroreduction

To simulate the current distribution across the cathode surface, COMSOL Multiphysics 6.1 with the Secondary Current Distribution model of the cathodic chamber using a half cell model where the total current was imposed (galvanostatic boundary). While half cell (cathodic) mode with a galvanostatic boundary allows to calculate the current density distribution on the cathode surface on the cathodic chamber, the absence of an anode in the simulation impedes any conclusions on absolute values of electric potential (or energy) in the cathode or electrolysis cell [199]. The electrode reaction was modeled using Butler-Volmer kinetics with an anodic/cathodic transfer coefficient of $\alpha = 0.5$. The electrolyte conductivity (κ_l) and the exchange current density (J_0) used were 12.7 $mS \cdot cm^{-1}$ and 23.13 $A \cdot m^{-2}$ (See Fig. D3) as measured experimentally in Chapter IV. The geometry of the simulated system is shown in Fig. V.2.

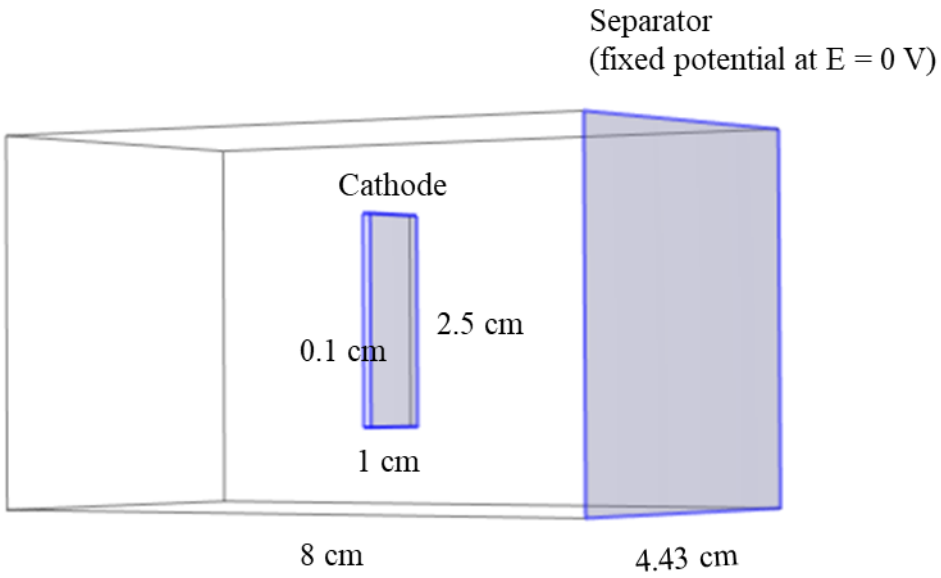

Fig. V.2. Schematic representation of the simulated geometry used for the study of the current distribution on a flat plate cathode.

The mesh was automatically generated by COMSOL through the physics-controlled option, where a triangular mesh is used with automatic size refinement near the boundaries. The

potential at the separator was fixed to 0 V. A first reference case simulation with a cathode size equal to the one used in the experimental part (2.5×1×0.1 cm^3) was used to compare the effect of different cathode geometries on the current distribution. For the reference case simulation, the total current was imposed on the cathode, at its value was equal to the maximum current obtained before nucleation occurred in the experimental part (4.5 mA on a stainless-steel plate, see Chapter IV). The maximum local current density in this scenario was used as a reference current density for estimating the total current that could be imposed in other cathode geometries. While maintaining the cathode thickness (0.1 cm), the width and height were also varied from 0.25 cm and 0.625 cm to 4.43 cm and 4.43 cm respectively to obtain different projected cathode areas and obtain the maximum current density that could be imposed before nucleation could occur (J_{bubble}), assuming nucleation occurs at the maximum local current density obtained on the reference case simulation. The size of the projected cathode surface area is also expressed as the fraction of the projected surface areas of the cathode to the separator (f_{area}).

V-2.2 Study of the H_2 mass transfer in a porous structure with different pore sizes and separation.

To simulate the mass transfer across the porous cathode, COMSOL Multiphysics 6.1 with the Transport of Diluted Species and Laminar Flow physics were used on the cathodic chamber. The H_2 diffusion coefficient was taken as 5.11×10^{-9} $m^2\cdot s^{-1}$. The cathodic chamber height and thickness simulated were 72 mm and 110 mm. These measurements were chosen arbitrarily small compared with a real application with the purpose of reducing the computational time of the hydrodynamic simulation and to be able to reuse some of the cathode geometries created during preliminary simulations. The width of the cathodic chamber was either 7.5 mm or 25.5 mm. The cathode bulk dimensions are 4.2×48.7 mm^2. The geometries of the cathodic chamber and cathode material are shown in Fig. V.3A for the wide cell and Fig. V.3B for the narrow cell.

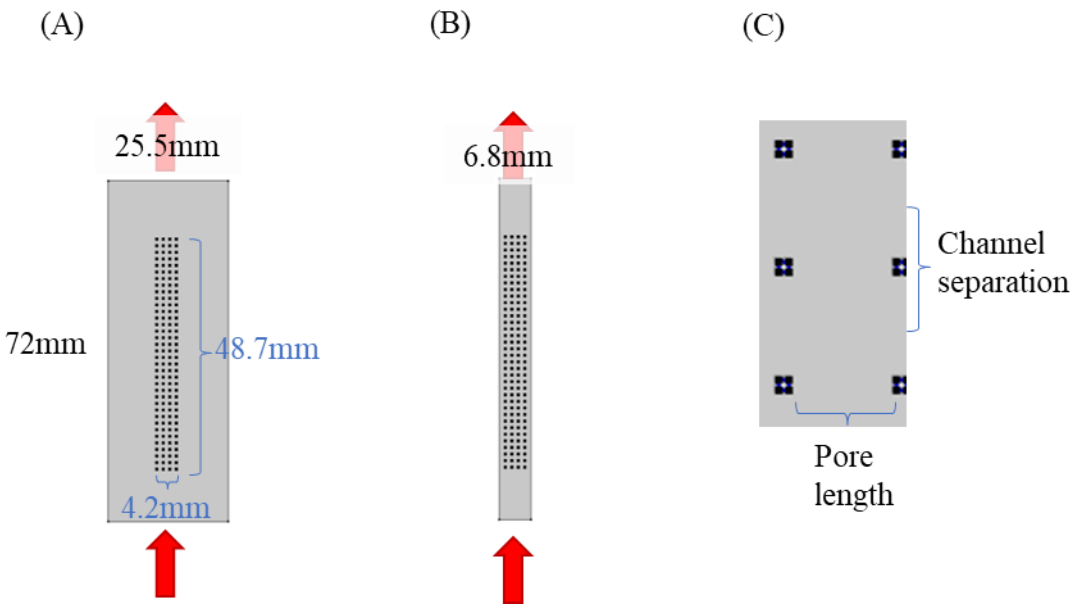

Fig. V.3. Schematic representation of the simulated geometry used for studying the mass transfer of a porous cathode.

The mesh was automatically generated by COMSOL through the physics-controlled option, where a triangular mesh is used with automatic size refinement near the boundaries. Four different pore per inch (ppi, based on open cell foams available at Recemat, www.recemat.nl) were used to create the channels of the cathode as well as three different channel separations as shown in Fig. V.3C. A combination of different ppi and channel separation values were simulated according to the Table V.1:

Table V.1. Parameters used for modeling the different porous cathode structures.

Run	Pores per inch (ppi, in^{-1})	Pore length (ppi^{-1}) [mm]	Channel separation (x times pore length)
1	10	2.54	1.1
2	20	1.27	1.1
3	30	0.847	1.1
4	10	2.54	1.5
5	20	1.27	1.5
6	30	0.847	1.5
7	10	2.54	1.9
8	20	1.27	1.9
9	30	0.847	1.9

10	40	0.635	1.1
11	40	0.635	1.5
12	40	0.635	1.9

For a coupling represented as shown in Fig. V.4, the inlet H_2 concentration ($C_{H_2}^{in}$ [mmol·L^{-1}]) to the electroreduction cell was taken as C_{H_2} at steady state in the gas fermentation reactor.

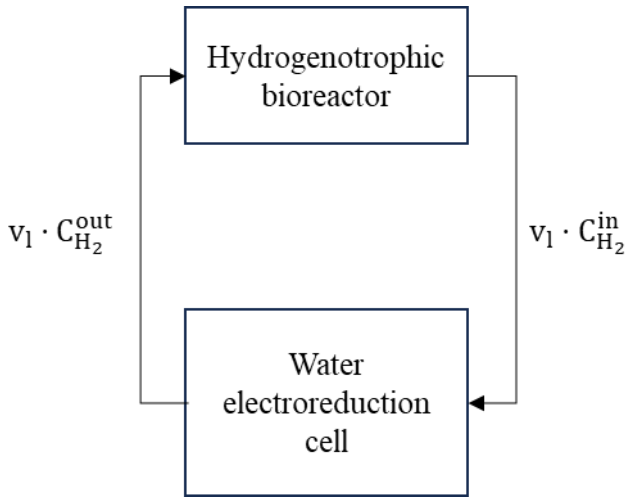

Fig. V.4. Schematic coupling of the gas fermentation reactor and the electrolyzer

The inlet concentrations of H_2 in the electrolyzer, $C_{H_2}^{in}$, was calculated based on a first order H_2 uptake rate $= k_1^x \cdot X \cdot C_{H_2}$, and taking k_1^x [h^{-1}·(g_{dw}·L^{-1})$^{-1}$] = 38.2 as reported by Muñoz *et al.* for *C. autoethanogenum* [166], X [g_{dw}·L^{-1}] = 0.2 according to the reported biomass in gas fermentation reactor of 2L at TBI with a H_2 uptake rate of 8.1 mmol·h^{-1}, resulting in $C_{H_2}^{in}$ = 0.53 mmol·L^{-1},

By making a mass balance of H_2 in both the gas fermentation reactor and the electrolyzer (equations 32 and 33), the H_2 solubilization rate must be equal to the H_2 uptake rate, and that the recycling flow rate (v_l) depends on $C_{H_2}^{out}$ which here was chosen as 1.21 mmol·L^{-1} based on the experimental results obtained in Chapter III.

$$v_l\left(C_{H_2}^{in} - C_{H_2}^{out}\right) = -H_2 \text{uptake rate (Hydrogenotrophic bioreactor)} \quad 32$$

$$v_l\left(C_{H_2}^{in} - C_{H_2}^{out}\right) = H_2 \text{solubilization rate (Water electroreduction cell)} \quad 33$$

Due to the small size simulated, it was decided to fix flow of H_2 as 1/10th of the flow calculated using the maximum consumption previously reported at TBI (8.1 mmol·h^{-1}). This H_2 flow was introduced in the model as a flux coming from the cathodic area. Therefore, the magnitude of the values obtained in this chapter are not scaled to target a real scenario but to study the physical behavior of the system. For every simulation, it was verified that the H_2 coming out minus the H_2 coming into the system was always equal to the desired H_2 flow rate. At the inlet boundary, $C_{H_2}^{in\ 1}$ was fixed together with a constant mass flow rate. The mass flow rate at the inlet boundary was also fixed and taken as $v_l \cdot (1kg \cdot L^{-1})$. The H_2 flow rate was imposed as a flux condition at the pore walls, where the flux corresponded to 8.1 mmol·h^{-1} divided by the total area of the pore walls for every case.

V-3. Results and discussion

V-3.1 Study of the current distribution of different cathode geometries during water electroreduction

V-3.1.1 Heterogeneities on the current distribution across the cathode surface

When using f_{area} = 0.127, the current density obtained presents a heterogeneous current distribution, with hyperpolarization around the edges of the cathode as seen in Fig. V.5A.

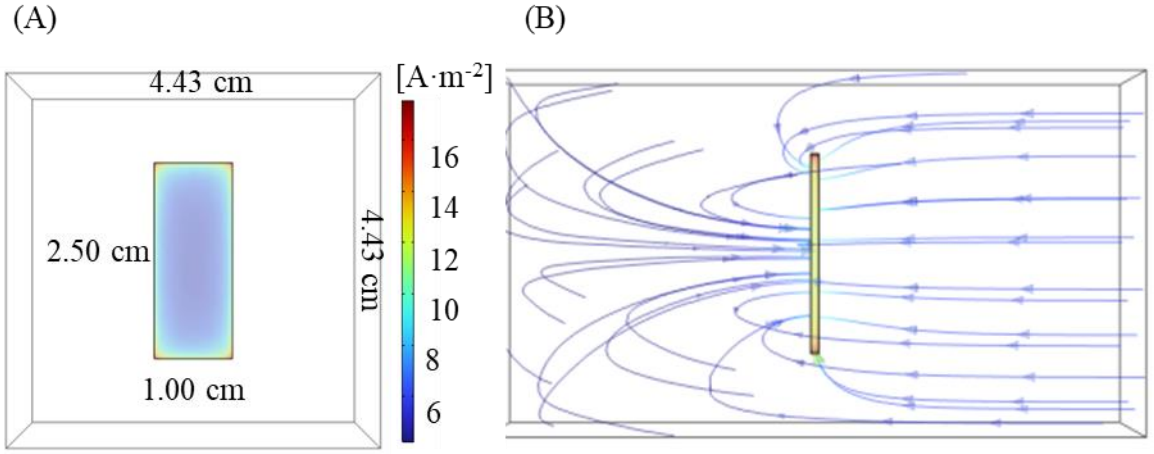

Fig. V.5. Current distribution on the (A) electrode and the (B) electrolyte for the reference case where f_{area} = 0.127.

The current density values ranged from ~ 6A·m^{-2} on the center of the projected face of the cathode, to ~18 A·m^{-2} around the edges. The origin of this heterogeneity comes from the mismatch between the projected surface area of the cathode and the separator. As shown in Fig. V.5B, the streamlines from the current density on the electrolyte coming from the separator area that does not have a parallel projection with the cathode surface either collapse on the edges (shortest path) or at the opposite surface (longer path). The longer path shown in the streamlines of the current distribution on the electrolyte directly translates into a higher ohmic resistance, which explains why the current density was ~ 2 A·m^{-2} lower on the opposite surface of the cathode. As H_2 would be produced at a faster rate in the hyperpolarized regions where the current density is ~18 A·m^{-2}, the nucleation of H_2 bubbles could be expected to preferentially start in these regions in a perfectly smooth cathodic surface. In this case, the total cathodic current imposed on the simulation was 4.5 mA, as it was the experimental current at which H_2 bubble nucleation was observed when using stainless-steel in the absence of H_2 pre-saturation or agitation (see Chapter IV). Therefore, the current density threshold can be taken as J_{bubble} = 18 A·m^{-2} and, for the specific case where f_{area} = 0.127 in a parallel plate cathode, I_{bubble} = 4.5 mA. In order to impose a larger I_{bubble} without surpassing the limit stablished by J_{bubble}, it would be tempting to try to remove the hyperpolarization on the edges by making the projected surface of the cathode larger than the separator surface as shown in Fig. V.6A, where f_{area} = 2. Although this would remove the hyperpolarization on the edges, it would still present a lower current density distribution on the opposite side of the cathode, besides presenting a poor electrochemical utilization of the added surface area.

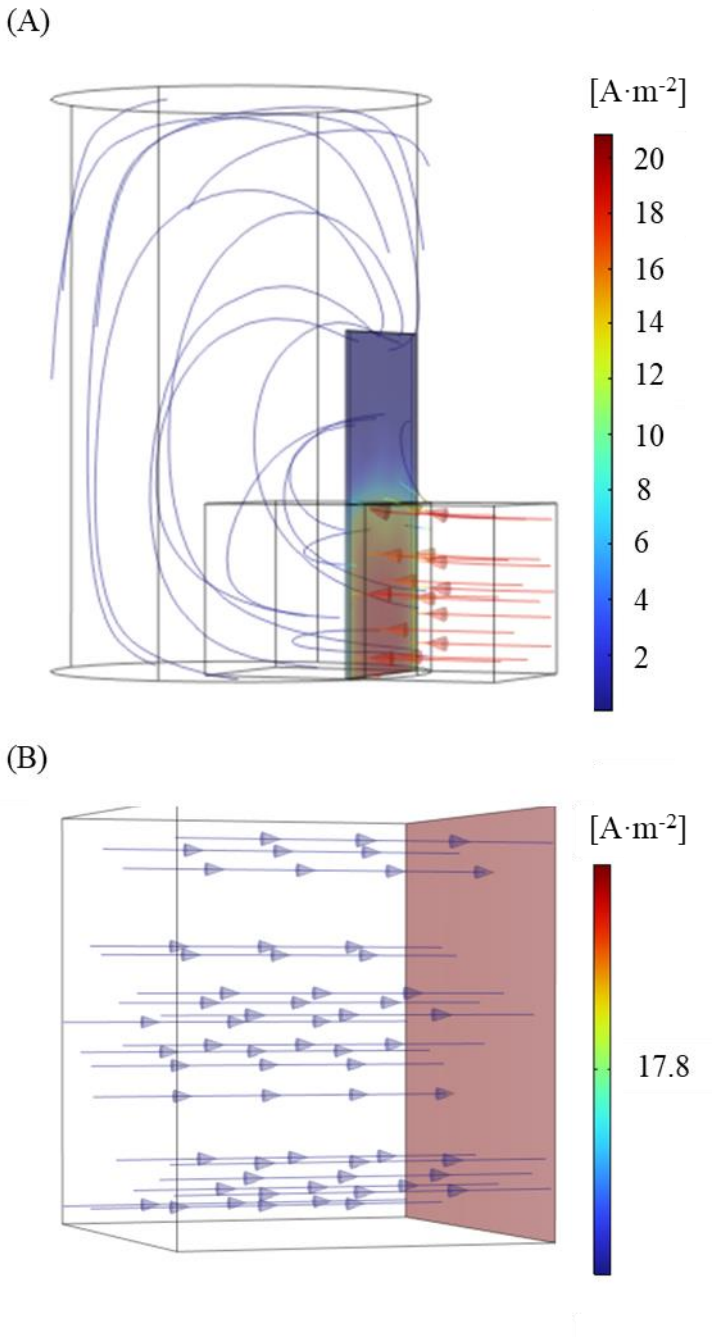

Fig. V.6. Current distribution streamlines on the electrolyte for (A) f_{area} = 2 and (B) f_{area} = 1.

In this case, 90% of the imposed current gets distributed in the cathode volume directly projected from the separator surface area, with an I_{bubble}=36 mA. The best utilization of the surface area is obtained when f_{area} = 1 as shown in Fig. V.6B. In this case, the current density distribution becomes homogeneous, avoiding hyperpolarization around the edges. As hyperpolarization facilitates the nucleation of bubbles on the cathode surface, the case where f_{area} = 1 becomes the best cathodic design for a parallel plate configuration when trying to

maximize the solubilization of H_2, with an I_{bubble}=35 mA, virtually equal to the case where f_{area} = 2.

V-3.1.2 Effect of the cathode positioning and electrode properties on the maximum imposed current before bubble nucleation

When using a parallel plate cathode, the best configuration is achieved when the surface area of the cathode projected relative to the separator is maximized up to f_{area} = 1. Nevertheless, other cathode designs such as 3D or porous electrodes allow having a higher surface area that is not necessarily projected into the separator surface area. In the following section, a cathode made of an array of perpendicular plates and a perforated plate is simulated during water electroreduction to evaluate the maximum total current that could be imposed before nucleation (I_{bubble}), and how it compares to the reference case when using a parallel plate cathode.

In perpendicular plates arranged as shown in Fig. V.7A and with the same dimensions of the parallel plate where f_{area} = 1, a higher current before the start of nucleation could be imposed (I_{bubble}), but the added (not projected) surface area becomes very inefficient on homogeneously distributing the current density, as observed in Fig. V.7B. This is attributed to the positioning of the electrodes, since most of the current density was distributed on the area closest to the separator as shown in Fig. V.7C. For example, while the current density was ~17.5 $A \cdot m^2$ at the cathode end closest to the separator, it quickly dropped to ~1.7 $A \cdot m^2$ at 1/3 of the cathode furthest from the separator.

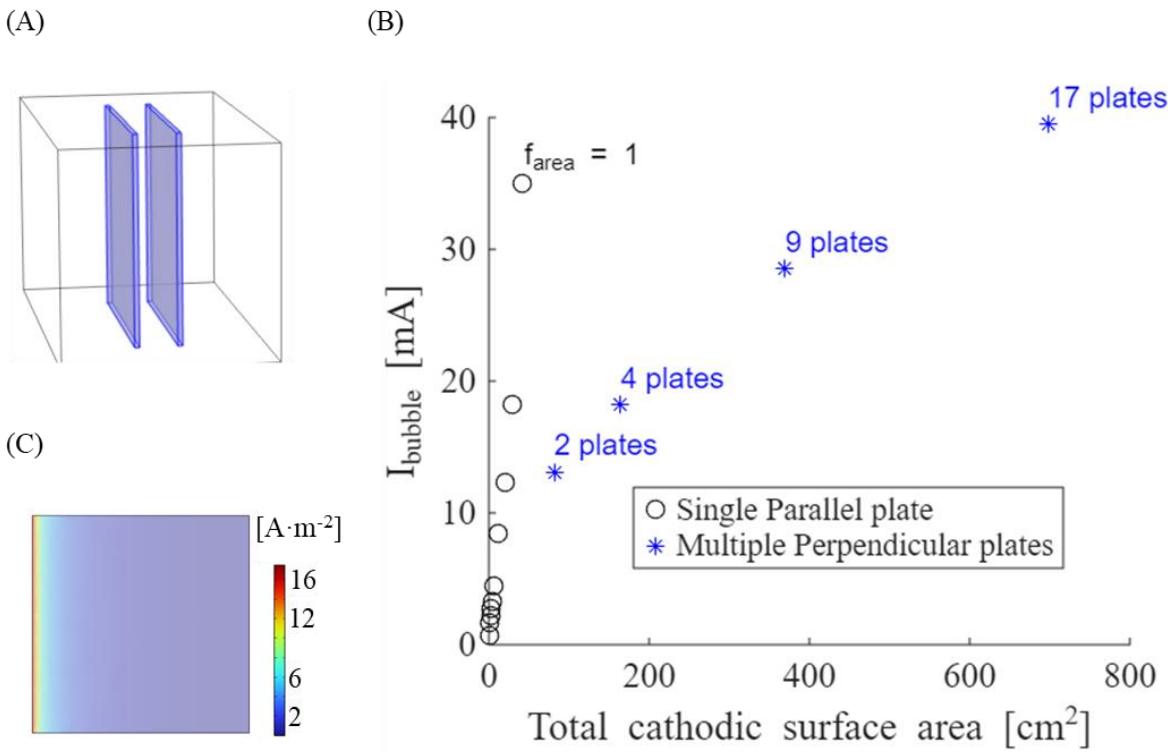

Fig. V.7. Comparison of the effect of the total cathodic projected surface area on the maximum total current that could be imposed before nucleation (I_{bubble}) for a single parallel plate and multiple perpendicular plates. (A) Two perpendicular plates array, each plate has dimensions of 4.43×4.43×0.1 cm^3. (B) Plot of I_{bubble} vs Total cathodic surface area. (C) Current density distribution in one of the two perpendicular plate arrays, where the separator is located on the left.

Next, a perforated plate with the same dimensions of the parallel plate where f_{area} = 1 was evaluated. Here, square holes of 5 mm of length were introduced to increase the total surface area as shown in Fig. V.8A. The porosity added by the holes allowed to increase the total surface area by 1.67 times compared with the parallel plate where f_{area} = 1, but the projected surface area got reduced 1.34 times. This design reduced the heterogeneity of the current density distribution with a better use of the added surface area as shown in Fig. V.8B compared with the perpendicular plate array shown in Fig. V.7C.

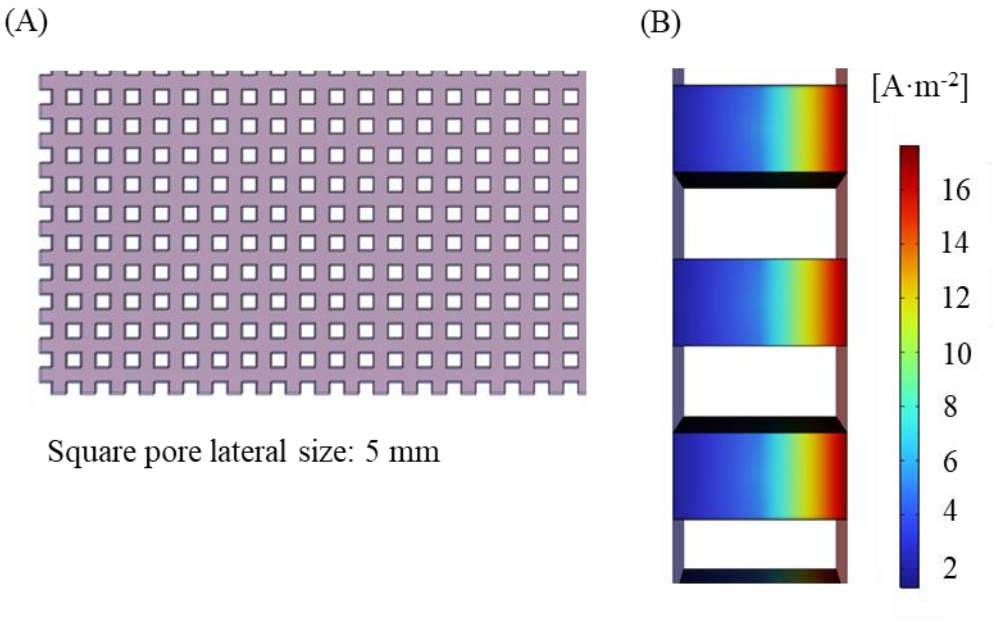

Fig. V.8. Current density distribution along a perforated plate cathode. (A) Perforated plate cathode design. (B) Current density distribution across the thickness of the perforated plate.

The current density distribution could be further improved when surrounding as much as possible the cathode surface area by separator surface, by adding a second separator surface on the opposite face as shown in Fig. V.9A. As expected, the current density distribution on the perforated plate becomes more homogenous as shown in Fig. V.9B. The addition of a second separator allows to impose a ~2 times higher I_{bubble} value in both perforated and parallel plates.

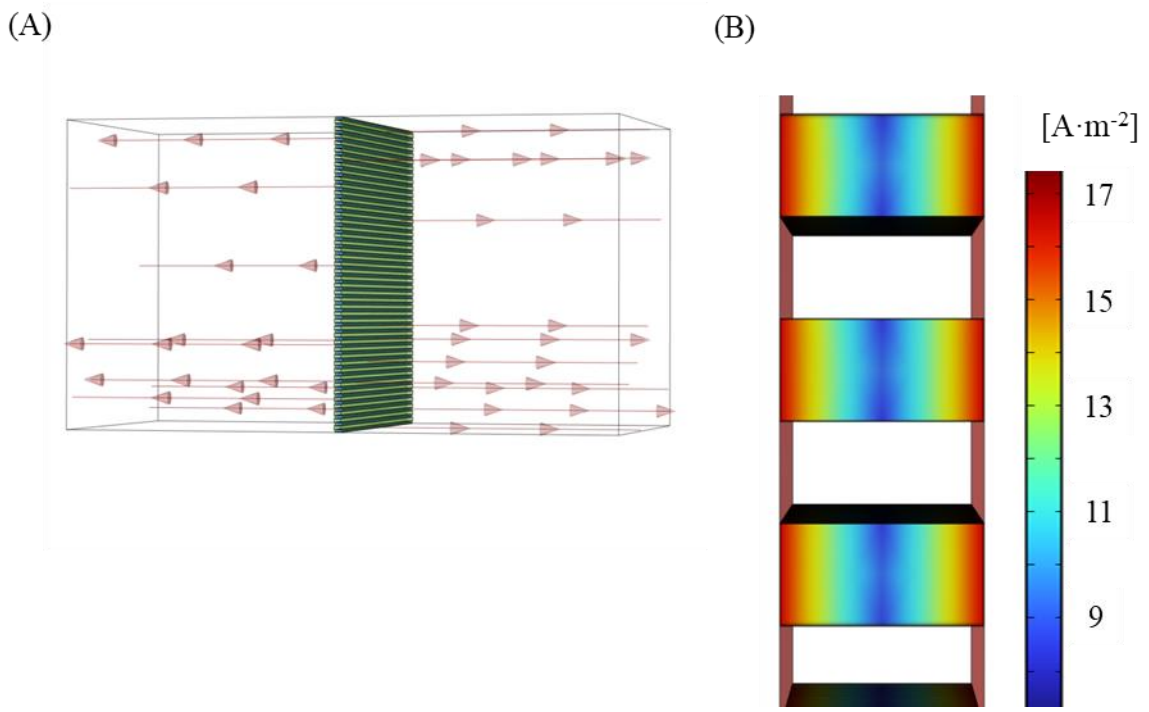

Fig. V.9. Current density distribution on the electrolyte when a second separator surface is introduced. (A)Two-separator configuration and (B) Current density distribution across the thickness of the perforated plate when a second separator surface is introduced.

For a fixed target of total current for operating an electrolyzer in the absence of bubbles, this would translate into a reduction in the cathode material by half, while maintaining the same anode and separator area.

Another factor to consider that affects the current distribution homogeneity is the electrolyte conductivity. In Chapter II, the conductivity of the electrolyte used during the experiments was of only 2.4 $mS \cdot cm^{-1}$ (below of the typical conductivity expected for MES, 10 $mS \cdot cm^{-1}$ [207]), and the H_2 solubilization kinetics were greatly improved when the electrolyte was increased to 12.7 $mS \cdot cm^{-1}$ (value used for the rest of the manuscript, see Supplemental Information C). For the perforated plate with double separator simulation, different salinities from 2.4-50 $mS \cdot cm^{-1}$ (The highest conductivity value tested here corresponds to a hypersaline medium effectively used for acetogenesis in a microbial electrosynthesis cell [208]) were evaluated based on the maximum total current that could be imposed before nucleation (I_{bubble}), and the results are shown in Fig. V.10.

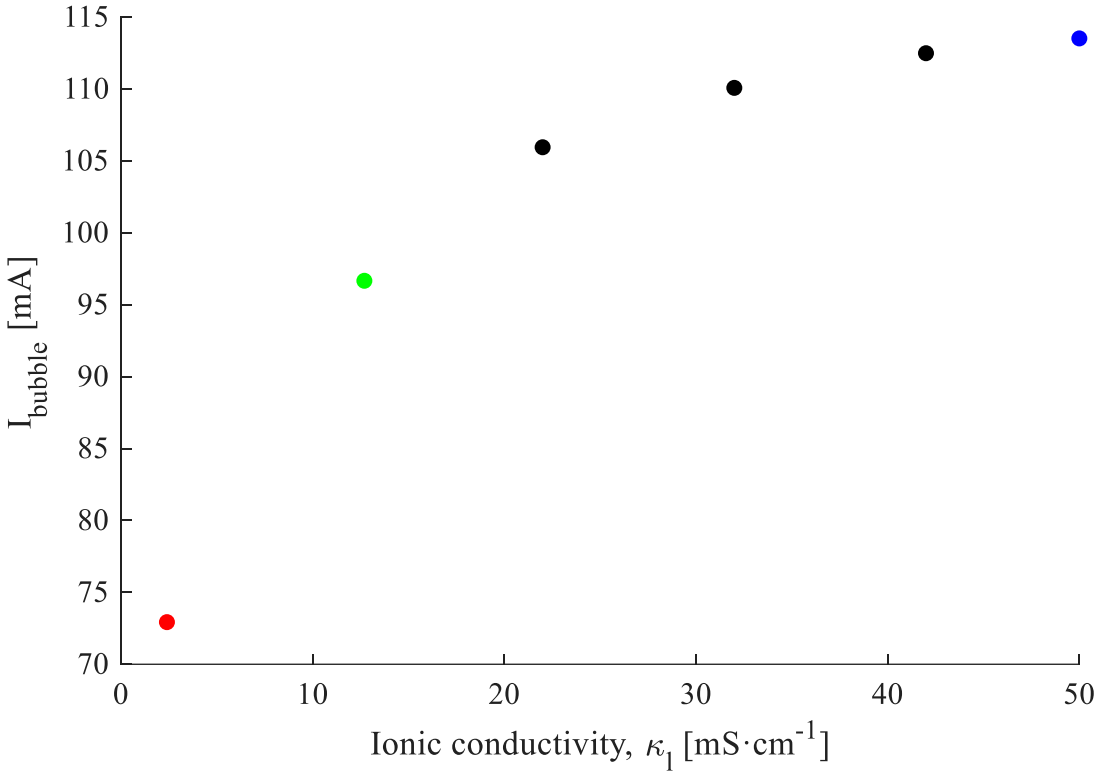

Fig. V.10. Comparison of the effect of the electrolyte conductivity (κ_l) on the maximum total current that could be imposed before nucleation (I_{bubble}) for a single perforated plate with double separator. Red: Low ionic conductivity (κ_l = 2.4 mS·cm^{-1}) corresponding to the minimum salt medium used as electrolyte in Chapter II; Green: Normal ionic conductivity (κ_l = 12 mS·cm^{-1}) used in the manuscript with a potassium phosphate buffer electrolyte (pH = 7.2, 0.1M); Blue: High ionic conductivity (50 mS·cm^{-1}) corresponding to a hypersaline medium used for acetate production in a microbial electrosynthesis cell [208].

The higher ionic conductivity of the medium allowed to reach higher values of I_{bubble} by reducing the heterogeneity in the current distribution across the cathodic surface, which could explain the inferior H_2 solubilization kinetics achieved experimentally when using a minimum salt medium (see Chapter II). This is expected, when considering that higher ionic conductivities allow higher Wagner values (see Chapter I). Similarly, by decreasing the exchange current density (j_0), higher Wagner numbers should be obtained that result in a more homogeneous current distribution. This inversely proportional relationship can be observed in in Fig. V.11, when varying the exchange current density values.

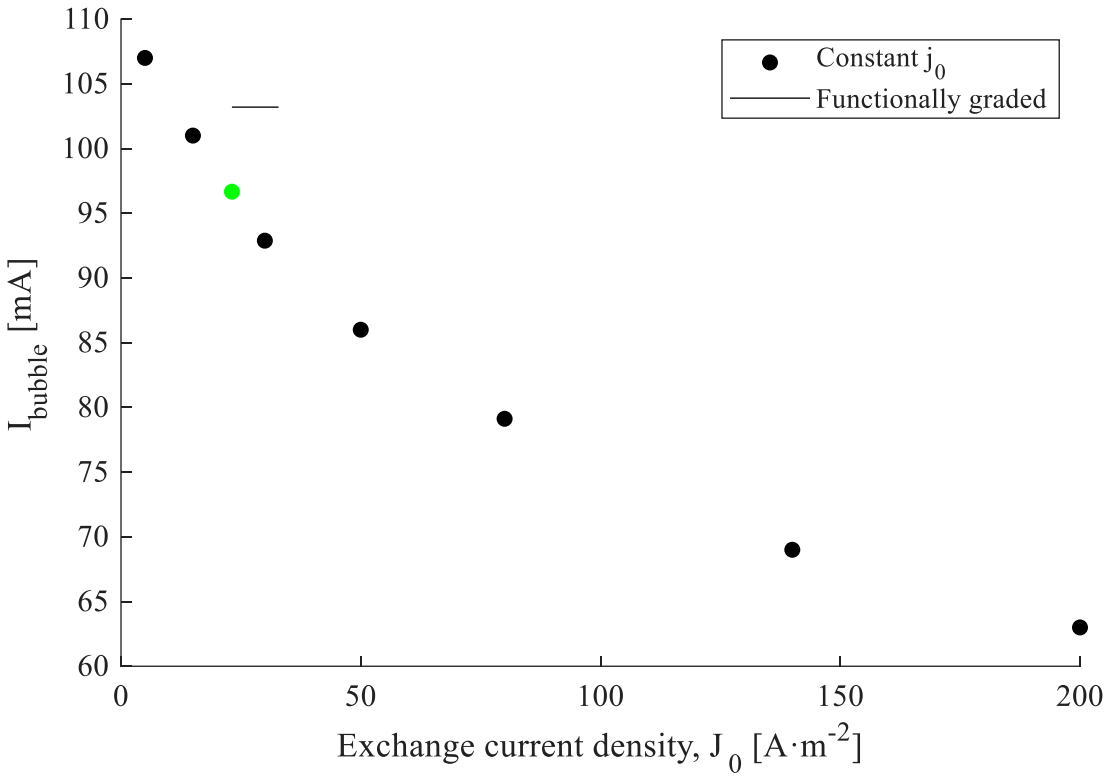

Fig. V.11. Comparison of the effect of the exchange current density of the cathode material (J_0) on the maximum total current that could be imposed before nucleation (I_{bubble}) for a single perforated plate with double separator. Green: Normal exchange current density (J_0 = 23.13 A·m^{-2}) used in the manuscript.

At first sight, it would look like only by reducing the exchange current density when using poor electrocatalytic materials would be favorable strategy for homogenizing the current distribution to avoid bubble nucleation, and that good electrocatalytic materials should be avoided. Nevertheless, an energy penalty can be expected from this approach, as it fails to recognize that the spatial variation of the current distribution can also be targeted by a spatial variation of the electrode properties, without worsening the electrocatalytic properties of the electrode. In the same way *brighteners* are used during electroplating to achieve a spatially variable exchange current density through a selective modification of the activation overpotential, a variable catalyst loading can also be used to homogenize the current distribution to create a functionally graded electrode [209]. The use of a functionally graded cathode was simulated by using a linearly variable exchange current density (j_0) across the cathode thickness as shown in Fig. V.12.

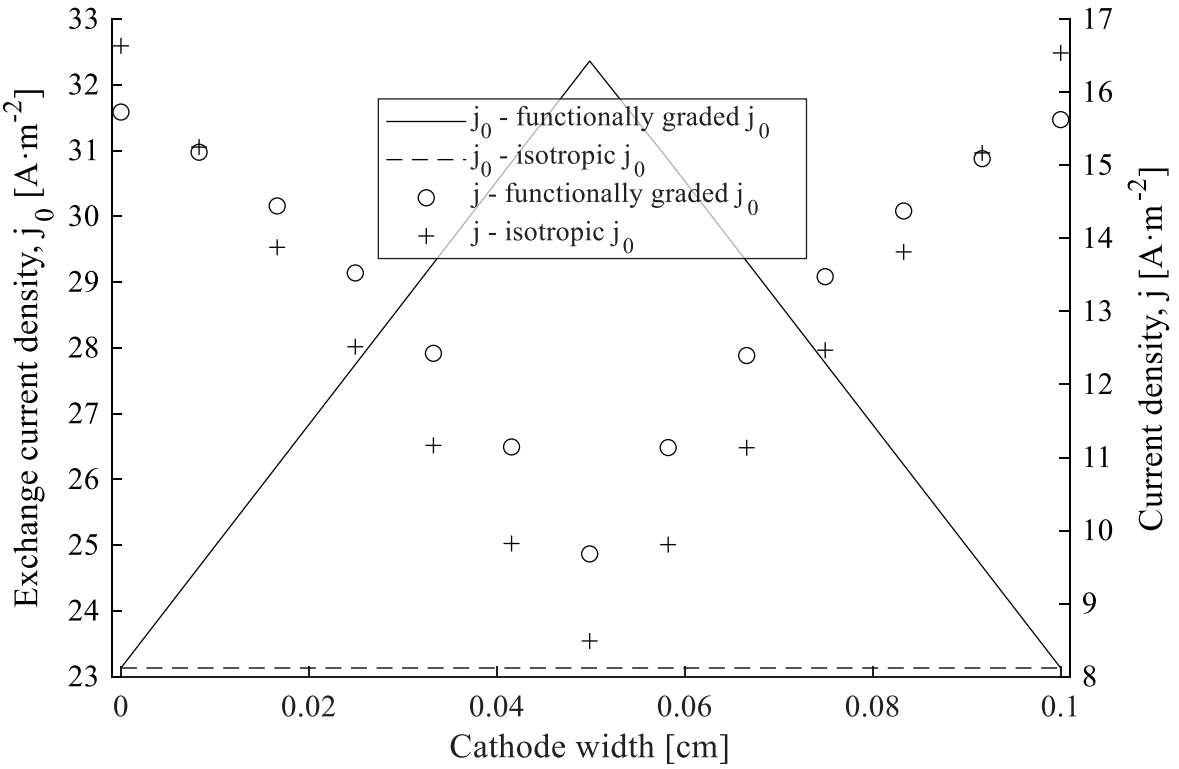

Fig. V.12. Effect of an anisotropic exchange current density (j_0) on the current distribution across the cathode thickness. Black line: Local exchange current density of the functionally graded cathode. Dashed line: Local exchange current density of the isotropic cathode. Circles: Local current density of the functionally graded cathode. Crosses: Local current density of the isotropic cathode. The current imposed in the system was 96.65 mA.

In this case, increasing the electrocatalytic activity through (j_0) as a function of the spatial length (thickness) also decreased the current density and improved the current distribution homogeneity, which should also contribute to a higher current imposed before the nucleation of bubble as shown in Fig. V.11. It is worth noting that here, a linear grading was used for j_0 which did not necessarily correspond to the best profile.

When comparing the single parallel plate, the perpendicular plates and the perforated plate as shown in Fig. V.13, it becomes evident that using porous structures in thin cathodes becomes the best choice to allow a higher I_{bubble} while maintaining a good current distribution. Nevertheless, this is only true if there is no limitation on the mass transfer, as the accumulation of H_2 near the cathodic surface promotes nucleation. It is easier to promote mixing near the cathode surface of a parallel plate compared to a porous structure. In a porous cathode,

although higher porosities allow adding larger total cathodic surface areas, a detrimental effect on the mass transfer should be expected.

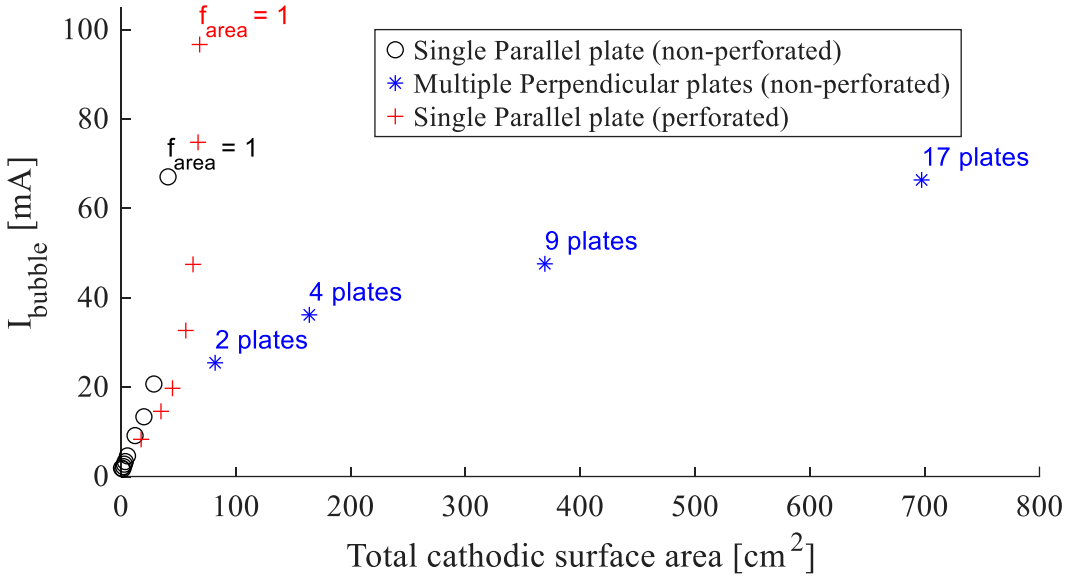

Fig. V.13. Comparison of the effect of the total cathodic projected surface area on the maximum total current that could be imposed before nucleation (I_{bubble}) for a single parallel plate, an array of perpendicular plates and a single perforated plate.

In summary, the use of porous cathodes can be advantageous to the specific goal of H_2 solubilization by water electroreduction. By analyzing the current density distribution alone in the absence of mass transfer effects, the following points should be considered when choosing/designing a porous cathode:

- The projected surface area of the cathode and the separator should be equal, with equidistant geometries (parallel) to avoid hyperpolarization on the cathode edges.
- Lower current densities can be achieved with thin, porous cathodes with a small compromise on the homogeneity of the current distribution.
- The use of a cell stack of thin electrodes with double separators (sandwich configuration) favors the homogeneity of the current distribution

These considerations could be applied to both bulk electrolysis and flow-through cell designs, with arrays of either parallel or concentric electrodes/separators for cubic and cylindrical cells. Besides the geometrical design of the cathode material, a potential approach to reduce uneven current distributions in porous electrodes should rely on maximizing the electrolyte

conductivity (considering the salinity tolerance of the selected hydrogenotrophs) and optimizing the catalytic activity of the cathodic surface through functionally graded materials. In the following section, design considerations for porous cathodes are studied on their impact on mass transfer, with the purpose of elucidating the differences in mass transfer that could arise in bulk electrolyzers (agitated) and flow-through cells.

V-3.2 Study of the H_2 mass transfer on cathodes with different porous characteristics

In Table V.2, the pores per inch (reciprocal of the pore size), the channel separation and the cell width were evaluated on their effect on the maximum local H_2 concentration in a continuous reactor at steady state.

Table V.2. Maximum local H_2 concentration achieved with different porous structures and cell width used in this work

					Maximum local H_2 concentration [mmol·L^{-1}]	
	Pores per inch	Channel separation	Reactive surface	Equivalent current density	Cell width [mm]	
Run	(ppi)	(times ppi^{-1})	area [cm^2]	[A·m^{-2}]	25.5 mm (wide)	7.5 mm (narrow)
1	10	1.1	38	11.43	10.34	4.17
2	20	1.1	75	5.79	11.92	2.06
3	30	1.1	113	3.84	12.83	1.63
4	10	1.5	145	2.99	12.55	3.86
5	20	1.5	224	1.94	13.97	2.16
6	30	1.5	299	1.45	14.21	1.72
7	10	1.9	108	4.02	13.71	6.68
8	20	1.9	267	1.63	15.98	2.44
9	30	1.9	377	1.15	16.55	1.91
10	40	1.1	151	2.88	13.30	1.46
11	40	1.5	433	1.00	14.96	1.54
12	40	1.9	485	0.90	16.76	1.67

To better understand the individual effect of these parameters, the simulation runs were grouped based on the cell width and are presented in the following sections.

V-3.2.1 Local H_2 accumulation at the cathode porosity design in a non-forced flow.

The local H_2 concentration obtained at steady state in Run 2 with a wide cell width of 25.5 mm is shown in Fig. V.14.

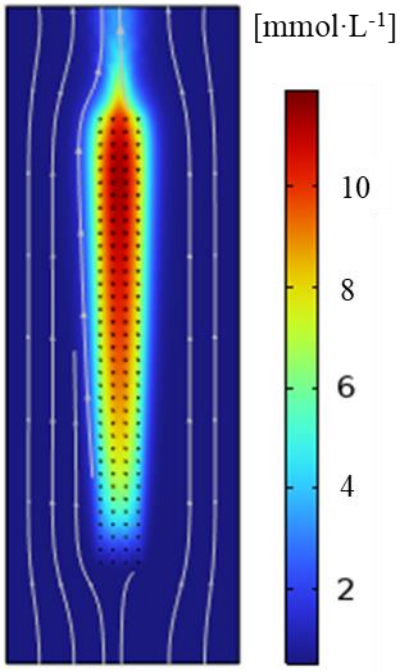

Fig. V.14. Spatial concentration profile of H_2 for the porous structure using 20 ppi and separation 1.1 in a cell of 25.5 mm of width.

At first sight, it can be seen that the H_2 accumulates in the porosity of the material and does not get properly mixed with the whole liquid volume, achieving a maximum H_2 concentration of 12 mmol·L^{-1}. As seen in Fig. V.15, a smaller separation and ppi (larger pore size) allowed to reduce the maximum local H_2 concentration.

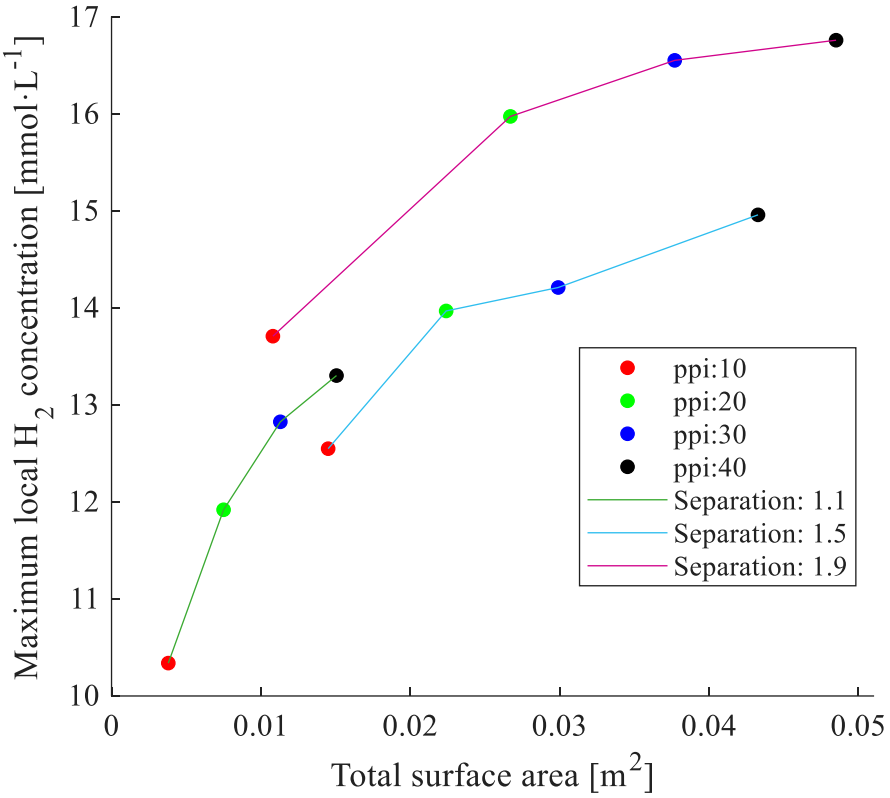

Fig. V.15. Effect of the cathodic surface area on the maximum concentration of H_2 achieved in a cell with 25.5 mm of width (wide).

Although it should be expected that the larger surface areas achieved with small pore sizes reduce the H_2 local accumulation, the opposite effect is obtained here, where larger pore sizes are preferred with a wide cell width.

V-3.2.2 Local H_2 accumulation at the cathode porosity design in a forced flow

The local H_2 concentration obtained at steady state in Run 2 with a narrow cell width of 7.5 mm is shown in Fig. V.16.

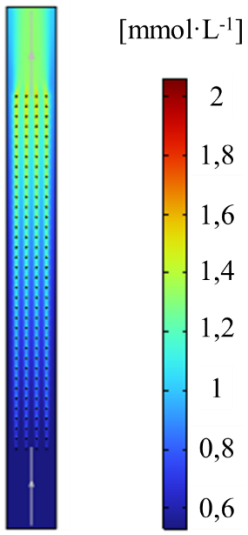

Fig. V.16. Spatial concentration profile of H_2 for the porous structure using 20 ppi and separation 1.1 1 in a cell of 7.5 mm of width.

In this case, the H_2 accumulation in the porosity of the material is much lower compared with the wide cell width, with the maximum local H_2 concentration being decreased by a factor of 6. Moreover, as seen in Fig. V.17, the use of larger surface areas with large ppi values (small pore sizes) effectively allowed to reduce the H_2 accumulation, approaching the limit stablished by a perfect mixing case at a maximum local H_2 concentration of 1.21 mmol·L^{-1}.

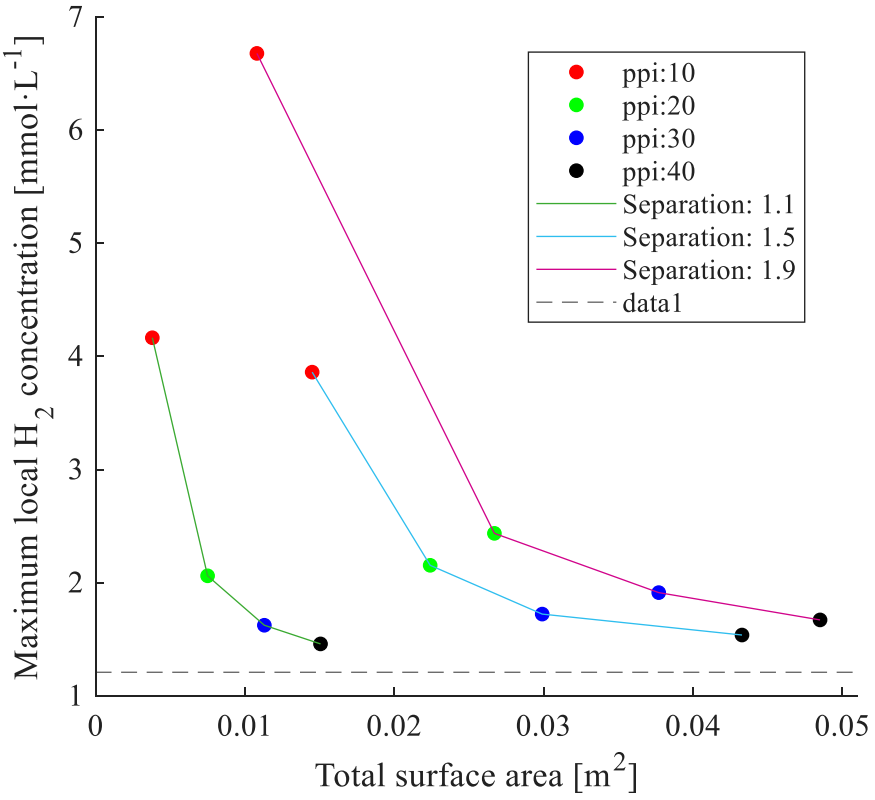

Fig. V.17. Effect of the cathodic surface area on the maximum concentration of H_2 achieved in a cell with 7.5 mm of width (narrow). The dashed line corresponds to the minimum achievable dissolved H_2 concentration in the simulation and equal to 1.21 mmol·L^{-1}.

This opposite effect of the total surface area on the local accumulation of H_2 can be explained by analyzing the velocity attained inside the porosity. As show in Table V.3, although increasing values of ppi meant larger total surface areas, the fluid velocity was significantly decreased, which contributed to the poor mixing and local accumulation of H_2. For in the forced flow type, this effect is reversed, which highlights the importance of working with porous structures that allow for high fluid penetration besides their large surface areas.

Table V.3. Maximum fluid velocity inside the porous structure for different ppi values at 1.1 separation. The values reported here are taken from the fluid velocity measured at the middle height of the cell.

	Maximum fluid velocity inside the porous structure [m·s^{-1}]			
Flow type	10 ppi	20 ppi	30 ppi	40 ppi
Non-forced	2.4×10^{-5}	8.3×10^{-6}	5.1×10^{-6}	3.5×10^{-6}
Forced	6.2×10^{-4}	6.9×10^{-4}	7.1×10^{-4}	7.3×10^{-4}

In summary, to take advantage of the large surface areas of porous cathodes per volume of material for H_2 solubilization during water electroreduction, a forced flow through the porosity of the cathode should be employed. In this sense, a flow through cell should be the preferred design, since the agitation used in bulk electrolyzers might be insufficient to enforce the proper mass transfer of species in the porosity of the electrode.

V-4. Conclusions

To avoid current heterogeneities and maximize the use of the cathode area, the projected cathode surface area should be equal and equidistant from the separator. Moreover, the larger surface area of porous cathodes can offset the heterogeneities on the current distribution, allowing higher currents in the absence of bubble formation. In this sense, thin porous electrodes should be favored for taking advantage of both higher surface areas with a less

heterogeneous current distribution. A potential approach to reduce the current distribution heterogeneities could also arise from the manufacturing of functionally graded electrodes, but further research should be undertaken to validate these results.

Nevertheless, for the dimensioning of a water electroreduction cell, other design restrictions should be considered, as the use of integrated sensors could restrict the minimum cell thickness. To avoid the accumulation of H_2 inside the porous cathode, a forced flow cell (continuous electrolyzer) should be preferred over an agitated cell (batch electrolyzer). The use of cell stacks, besides adding compactness to the water electroreduction cell design, can also favor the use of less cathode material due to a better current distribution over the cathodic surface but at the cost of a more complex setup. In Chapter VI, the dimensioning of the cathode/cell size and geometry will be done based on the principles established in this chapter: working with a thin porous cathode with a continuous forced-flow operation and a symmetrical cathode-separator design, with the purpose of supply the necessary dissolved H_2 to a hydrogenotrophic bioreactor.

Chapter VI. Electrolytic H_2 supply for hydrogenotrophic bioreactors: A feasibility study on a coupled reactor system

ABSTRACT

Water electroreduction can be used to directly produce dissolved H_2 with high solubilization efficiency and even achieve supersaturated concentrations in the liquid medium. Based on the operational and design principles established in previous chapters (forced fluid flow, cathode/cell geometrical symmetry, thin porous cathode design and local dissolved H_2 concentration and current density thresholds), This chapter addressed the question of whether it would be feasible to couple a water electroreduction cell with a hydrogenotrophic bioreactor. This feasibility is studied through numerical simulation and evaluated in terms of the required dimensions of the water electroreduction cell and the recycling rate necessary to maintain a continuous operation at steady state in two different H_2 uptake scenarios. Results show that for a low H_2 uptake scenario (8.1 mmol·h^{-1}, real case scenario for a hydrogenotrophic bioreactor running at TBI) in a 2 L bioreactor, a 2×15×15 cm^3 porous cathode in an electroreduction cell operated at 0.77 A and a recycling rate of 47.1 L·h^{-1}. This system could maintain a dissolved H_2 concentration of 0.53 mmol·L^{-1} in the bioreactor, avoiding bubble nucleation by keeping the maximum local H_2 concentration at 0.91 mmol·L^{-1} and maximum current density at 17.53 A·m^{-2}, both below the threshold limits estimated before of 5.5 mmol·L^{-1} and 18 A·m^{-2}, respectively. However, enabling H_2 supersaturation from 0.78 mmol·L^{-1} up to 1.21 mmol·L^{-1} at the exit of the water electroreduction cell reduced the recycling rate by 1.8 times compared to the baseline, which would also probably require over-pressurization of the system to avoid larger H_2 losses.

For a high H_2 uptake rate scenario (84 mmol·h^{-1}, hypothetical case), an initial single-cell design was unfeasible, requiring a prohibitively large cathode size of 2×60×223 cm^3 operating at 45 A. However, utilizing a stack of three 2×30×40 cm^3 cells and achieving a H_2 supersaturation of 2.42 mmol·L^{-1} could be more feasible if H_2 loss measurements are implemented. This

optimized design reduced the required current by 4.8 times (to 9.24 A), total cathode volume by 3.7 times (to 7200 cm^3), and recycling rate by 13.6 times (to 92 $L \cdot h^{-1}$). As the working dissolved H_2 concentration was targeted at the saturation limit, scenarios of high H_2 uptake rate could be more practically implemented in a microbial electrosynthesis cell configuration where electrolytic H_2 production and biological uptake occur in the same physical space.

VI-1. Introduction

H_2 gas injection, as a traditional technique for H_2 supply, is severely limited by its low solubility in water and the slow gas-to-liquid mass transfer, restricting microbial uptake kinetics and overall productivity in hydrogenotrophic bioreactors and therefore necessitating the injection of large H_2 quantities with low solubilization efficiency.

Water electroreduction offers a promising alternative as it directly produces dissolved H_2 within the liquid medium, thereby entirely bypassing the gas-to-liquid mass transfer bottleneck. This direct production allows for the reach of supersaturated concentrations of dissolved H_2 (up to 1.21 $mmol \cdot L^{-1}$ observed in Chapter III), significantly exceeding the saturation limit achievable by gas injection at 1 bar (0.78 $mmol \cdot L^{-1}$). These elevated H_2 concentrations could be crucial for enhancing metabolite production rates, improving selectivity in hydrogenotrophic processes, and potentially shifting metabolic pathways towards higher-value products. Furthermore, water electroreduction can achieve significantly higher H_2 solubilization efficiencies, and being more energy-efficient compared with gas injection.

However, using water electroreduction cells for H_2 solubilization presents its own set of challenges, primarily focused on preventing the nucleation and growth of H_2 gas bubbles at the cathode surface. Bubble formation is a major cause of reduced overall efficiency: it reduces solubilization rate and H_2 bioavailability and introduces additional energetic penalties when re-solubilization by gas recirculation is implemented. In previous chapters, it was shown that H_2 bubble nucleation could be avoided when working at current densities lower than ~18 $A \cdot m^{-2}$ and dissolved H_2 concentrations under ~5.5 $mmol \cdot L^{-1}$.

While the principles for bubble-free operation have been established, a key question remains: can an electroreduction cell be designed with feasible dimensions and operational conditions to effectively couple with and supply the demands of a hydrogenotrophic bioreactor? This chapter aims to demonstrate that a continuous electrolysis design can be scaled to meet the specific H_2 requirements for hydrogenotrophic bioreactors.

The research done in previous chapters has shown that high-surface-area cathodes enhance mass transfer by preventing bubble nucleation and achieving high H_2 solubilization efficiency. Furthermore, it has been proposed that continuous forced flow electrolysis designs are preferred at scale due to improved flow hydrodynamics, which in turn leads to a better use of the cathode surface area. Also, critical geometrical factors such as cathode/separator positioning have an effect on the current distribution. Building on these findings, this chapter addressed the question of whether it would be feasible to couple a water electroreduction cell operated in continuous with a forced-flow thin porous cathode, with a hydrogenotrophic bioreactor at steady state. This feasibility is studied through numerical simulation and evaluated in terms of the required dimensions of the water electroreduction cell and the recycling rate necessary to maintain a continuous operation at steady state in two different H_2 uptake scenarios

The simulations are divided into several cases that reflect real-world hydrogenotrophic processes. The proposed cell designs are analyzed when coupled with both low and high H_2 uptake rate scenarios. This approach allows to determine the feasibility of the system and its potential for practical application.

VI-2. Methodology

The numerical simulation study was based on a system design that couples a water electroreduction cell with a hydrogenotrophic bioreactor, as depicted in Fig. VI.1.

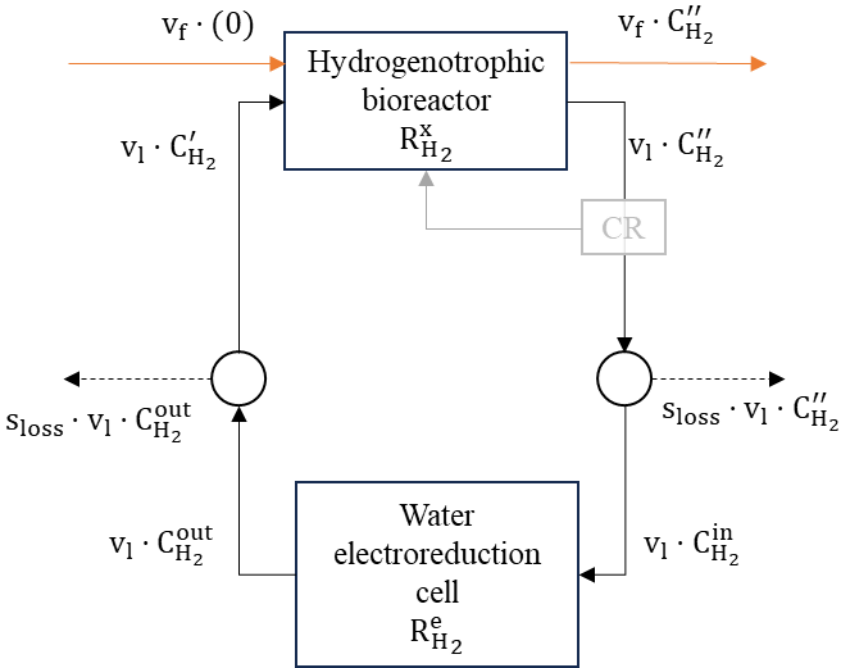

Fig. VI.1. Schematic of a water electroreduction cell and a hydrogenotrophic bioreactor coupling. The nutrient feed and purge flows are shown with orange arrows, the recycling cycle is shown with black arrows and H_2 losses due to leaking and bubbling during other processes (e.g., fluid transport, CO_2 gas injection, cell retention) is shown with dashed arrows. The equations represent the H_2 flow through the system. In grey, a cell recycling system is shown although it was not considered for the H_2 balance.

The electrolytic H_2 production and the biologic H_2 uptake rates are denoted as $R^e_{H_2}$ and $R^x_{H_2}$ [mmol·h^{-1}]. The recycle and nutrient feed/purge flow rates are defined as v_l and v_f [L·h^{-1}]. Concentrations of dissolved H_2 at the inlet and outlet of the hydrogenotrophic bioreactor are C'_{H_2} and C''_{H_2} [mmol·L^{-1}], while concentrations at the inlet and outlet of the electroreduction cell are $C^{in}_{H_2}$ and $C^{out}_{H_2}$ [mmol·L^{-1}]. The percentage of H_2 lost after exiting the electroreduction cell and the hydrogenotrophic bioreactor is represented by s_{loss}.

To find the appropriate dimensions for the water electroreduction cell, two distinct scenarios were evaluated, representing a high and low H_2 uptake rate ($R^x_{H_2}$). It was assumed that the bioreactor was primarily populated by *C. autoethanogenum*, a strain with both industrial relevance and a high presence in the gas fermentation reactor at TBI. For both scenarios, experimentally reported values of $R^x_{H_2}$ were used to calculate C''_{H_2}, assuming a first order uptake kinetics as shown in equation 34.

$$R^{x}_{H_2} = k^{x}_{1} \cdot X \cdot C''_{H_2} \quad 34$$

Where the reported biomass concentration (X, [g_{dw}·L^{-1}]) and $R^{x}_{H_2}$ for each scenario are tabulated in Table VI.1. The value for k^{x}_{1} was taken as 38.2 [h^{-1}·(g_{dw}·L^{-1})$^{-1}$] as reported by Muñoz *et al.* for *C. autoethanogenum* [166].

Table VI.1. H_2 uptake kinetic parameters at steady state of the hydrogenotrophic bioreactor to be coupled with the water electroreduction reactor

Scenario	Biomass X [g_{dw}·L^{-1}]	Dilution rate D [day^{-1}]	H_2 uptake rate $R^{x}_{H_2}$ [mmol·h^{-1}]	H_2 concentration C''_{H_2} [mmol·L^{-1}]
1. Low H_2 uptake*	0.2	0.2	8.1	0.53***
2. High H_2 uptake**	1.4	1.0	84	0.78***

* Experimental values reported in gas fermentation reactor of 2 L (2000 cm^3) at TBI.

** Experimental values reported by Valgepea *et. al.* [43]. $R^{x}_{H_2}$ was reported by volume of reactor, here it was multiplied by V_R = 2 L (2000 cm^3).

*** Calculated from $R^{x}_{H_2} = k^{x}_{1} \cdot X \cdot C_{H_2}$. For both scenarios, k^{x}_{1} [h^{-1}·(g_{dw}·L^{-1})$^{-1}$] = 38.2 as reported by Muñoz *et al.* for *C. autoethanogenum* [166].

For a hydrogenotrophic reactor volume (V_R) of 2 L (2000 cm^3), v_f is calculated using the dilution rate D as $v_f = V_R \cdot D$. Here, the volume of the bioreactor and not the total volume of the working fluid was taken. This is due to the fact that the system assumes there is a cell retention mechanism within the bioreactor, that prevents its biomass crossing the boundaries of the bioreactor and diluting it in the electroreduction cell volume. Moreover, the $R^{x}_{H_2}$ value at steady state from the reactor at TBI could only be maintained in the coupled system if X and C''_{H_2} are also maintained as described in equation 34. While X is maintained through the cell retention system, C''_{H_2} is maintained by mass balances from Fig. VI.1 and compiled in equations 35-38 in Table VI.2.

Table VI.2. Mass balances from the coupled system shown in Fig. VI.1 used to calculate $C^{in}_{H_2}$, C'_{H_2}, $R^{e}_{H_2}$ and v_l.

$v_l \cdot C_{H_2}^{out} = v_l \cdot C'_{H_2} + s_{loss} \cdot v_l \cdot C_{H_2}^{out}$	(H_2 loss before water electroreduction cell)	35
$v_l \cdot C''_{H_2} = v_l \cdot C_{H_2}^{in} + s_{loss} \cdot v_l \cdot C''_{H_2}$	(H_2 loss before hydrogenotrophic bioreactor)	36
$v_l \cdot C_{H_2}^{in} + R_{H_2}^{e} = v_l \cdot C_{H_2}^{out}$	(Water electroreduction cell)	37
$v_l \cdot C'_{H_2} = v_f \cdot C''_{H_2} + v_l \cdot C''_{H_2} + R_{H_2}^{x}$	(Hydrogenotrophic bioreactor)	38

The parameters $C_{H_2}^{in}$, C'_{H_2} , $R_{H_2}^{e}$ and v_l were calculated from the mass balances compiled in according to the seven simulation cases proposed for different $R_{H_2}^{x}$, $C_{H_2}^{out}$, s_{loss} and cathode thickness, as shown in Table VI.3.

Table VI.3. Parameters used for the simulation of different cases for the dimensioning of the water electroreduction reactor.

	$R_{H_2}^{x} = 8.1\ [mmol \cdot h^{-1}]$				$R_{H_2}^{x} = 84\ [mmol \cdot h^{-1}]$		
Parameters	Case 1	Case 2	Case 3	Case 4*	Case 5	Case 6*	Case 7*
$C_{H_2}^{out}$ [mmol·L^{-1}]	0.78	0.78	1.21	1.21	1.21	2.42	1.21
s_{loss} [%]	10	30	30	30	30	30	30
Cathode thickness [cm]	2	2	2	2	2	2	1

* Case 4 (3 cells) and Case 6 (3 cells) and Case 7 (3 cells) were dimensioned as a stack of cells, where the dimensions and parameters reported in the results section correspond to a single unit.

It is worth noting that maintaining H_2 supersaturation can be highly challenging, and reactor pressurization in Case 3-7 would probably be needed to avoid degassing.

The system's solubilization efficiency (SEE) [%] was calculated using equation 39, where $R_{H_2}^{e100\%}$ is the electrolytic H_2 production at s_{loss} = 0:

$$SEE = \frac{R_{H_2}^{e100\%}}{R_{H_2}^{e}} = 1 - \frac{s_{loss} \cdot v_l (C_{H_2}^{out} + C_{H_2})}{R_{H_2}^{e}} \quad 39$$

The current I [A] imposed in the simulation was calculated from $R_{H_2}^{e}$ as shown in equation 40.

$$I = \frac{2\ mol\ e^-}{mol\ H_2} \cdot \frac{96485\ C}{mol\ e^-} \cdot R_{H_2}^{e}[mmol\ H_2 \cdot h^{-1}] \cdot \frac{1\ mol\ H_2}{1000\ mmol\ H_2} \cdot \frac{1\ h}{3600\ s} \quad 40$$

Each case was simulated to calculate the dimensions of the water electroreduction cell necessary to maintain its operation free of bubbles. For this, the maximum local concentration of dissolved H_2 ($C_{H_2}^{max}$) was kept below 5.5 mmol·L^{-1} and the local maximum current density (j^{max}) below 18 [A·m^{-2}] according to the limits found in Chapter IV. For every simulated case, $R_{H_2}^{e}$, $C_{H_2}^{out}$ and $C_{H_2}^{in}$ were compared with the expected values obtained from the mass balances from Table VI.2 to check for the correct formulation.

A single electroreduction cell is made of a cathodic chamber surrounded by two anodic chambers as shown in Fig. VI.2A. The chambers were taken of equal height and width, but the anodic chamber was taken as 1 cm thick, where the anodes are DSA plates (Di Noer Technology Co. Ltd, China). To dimension the size of the porous cathode needed, only the cathodic chamber was simulated as shown in Fig. VI.2B.

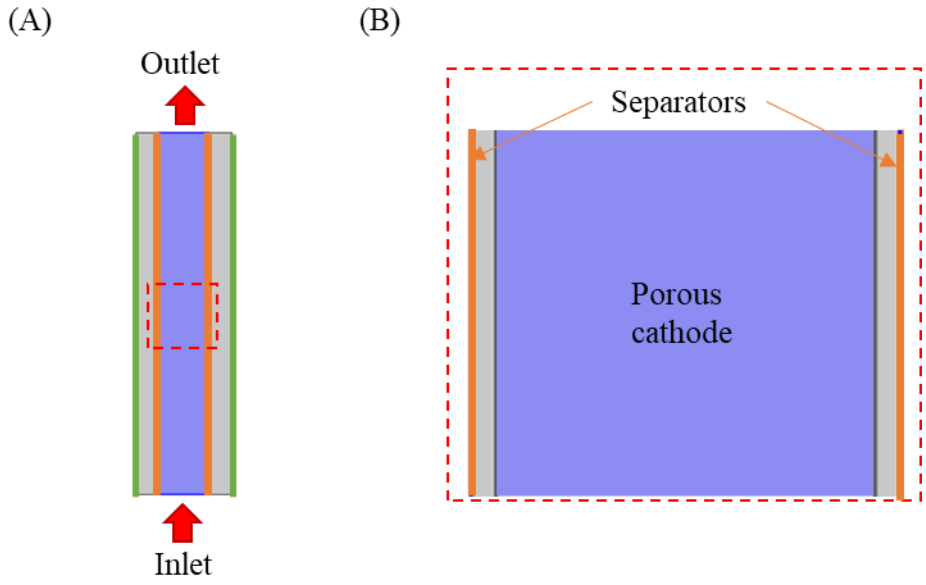

Fig. VI.2. Schematic representation of the water electroreduction cell design. (A) complete single cell, where the anodes are shown in green, the cathode in blue and the separator in orange. The red dashed line corresponds to a zoomed view (B) of the simulated geometry.

The simulations were performed using COMSOL Multiphysics 6.1 with the Secondary Current Distribution model coupled with Free and Porous Media Flow and Transport of Diluted Species physics using a half cell model of the cathodic chamber where the total current was imposed (galvanostatic boundary). While half cell (cathodic) mode with a galvanostatic boundary allows

to calculate the current density distribution on the cathode surface and mass transfer on the cathodic chamber, the absence of an anode in the simulation impedes any conclusions on absolute values of electric potential (or energy) in the cathode or electrolysis cell [199]. The mesh was automatically generated by COMSOL through the physics-controlled option, where a triangular mesh is used with automatic size refinement near the boundaries.

The electrode reaction was modeled using Butler-Volmer kinetics with a cathodic transfer coefficient of 0.5. The electrolyte conductivity (κ_l = 12.7 mS·cm^{-1}) and the exchange current density (J_0 = 23.13 A·m^{-2}, see Fig. D3) were taken from the experimental measurements from Chapter IV. The equilibrium potential in the secondary current distribution model was described by the Nernst equation to account for the H_2 concentration effect on the Butler-Volmer kinetic rate through the overpotential calculation. The potential at the separator was fixed at 0 V. At the inlet boundary, $C_{H_2}^{in}$ was fixed together with a constant mass flow rate. The mass flow rate at the inlet boundary was also fixed and taken as $v_l \cdot (1\mathrm{kg} \cdot \mathrm{L}^{-1})$.

The structural properties of the cathode were based on the Grade 1116 metal open-cell foam from Recemat (www.recemat.nl) due to its range of available thicknesses and large pore size, which should facilitate the escape of undesirable bubbles. Key properties of the foam include a pore diameter of 1.4 ×10^{-3} m, a porosity of 0.90, a permeability of 2.76×10^{-8} m^2, and a specific surface area of 1000 m^2·m^{-3}[210]) Although other grades offer larger specific surface areas (theoretically requiring less material), the larger pores should offer an easier escape route for undesirable bubble formation. A thickness of 2 cm was chosen for the simulation except for Case 7 (1 cm). It was considered that 2 cm was large enough for the use of small sensors in the cell such as small endoscopic cameras for bubble detection as well as data sampling. A space equal to the pore diameter (1.4 ×10^{-3} m) was left between the separators and the porous cathode. The dispersion inside the porosity of the cathode due to the fluid velocity was estimated based on the literature review of dispersion models and experimental data compiled for porous media [211], [212] (the dispersity values used here were interpolated from a collection of data on porous materials which included ceramic foams, see Supplemental Information F).

The mixing index (MI) at the outlet of the cell was also reported and calculated as shown in equation 41:

$$MI = 1 - \frac{\sqrt{\frac{1}{N}\sum_{i=1}^{N}(c_i - < c >)^2}}{< c >} \quad 41$$

To calculate the power required for moving the fluid while overcoming the pressure drop across the porous cathode, the following equation 42 was used as follows:

$$P_{hyd} = \left(v_l \cdot \frac{1\ m^3}{1000\ L} \cdot \frac{1\ h}{3600}\right) \cdot \Delta P \quad 42$$

Where ΔP [Pa] is the pressure drop across the length of the cathodic chamber volume. To compare with an equivalent power required for the mixing of a 2 L (2000 cm^3) hydrogenotrophic bioreactor with gas injection, an impeller diameter of 4.5 cm (1/3 of the bioreactor diameter) was used at a stirring speed of 600 rpm, a fluid viscosity of 1 centipoise and density of 1000 $kg \cdot m^{-3}$ (assuming water properties). By using the methodology followed by McCabe *et. al.* with a conservative power number of 1 [213], a mixing power of 0.2 W is calculated.

VI-3. Results

VI-3.1 Reducing imposed current and recycling rate through H_2 supersaturation

This section begins by examining the relationship between the imposed current, recycling rate (v_l), and the dissolved H_2 outlet concentration from the electroreduction cell ($C_{H_2}^{out}$) by solving the mass balances from Table VI.2. A summary of the numeric results obtained from each simulation case is tabulated, serving as a basis for the subsequent analysis in the following sections.

To reduce the volumetric flow rate without altering the dissolved H_2 flow rate, it is necessary to allow for a larger accumulation of H_2 in the medium, as shown in Fig. VI.3.

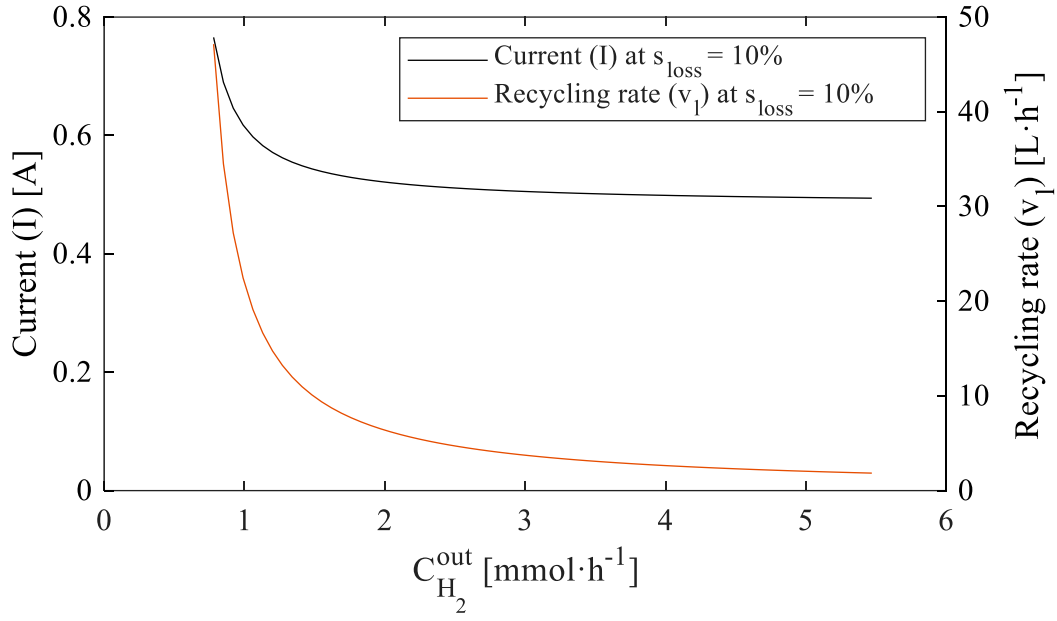

Fig. VI.3. Effect of the outlet concentration of dissolved H_2 ($C_{H_2}^{out}$) on the recycling rate of electrolyte (v_l) and the current applied to the water electroreduction cell (I). The recycling rate is shown in orange (right axis) while the current is shown in black (left axis) for Case 1.

The results clearly show that retaining a higher H_2 supersaturation within the system significantly reduces the imposed current and, even more notably, the recycling rate. Consequently, a reduction in the physical dimensions of the electroreduction cell through a smaller cathode size could also be expected. The extent of this reduction, along with the effects of other parameters such as H_2 losses (s_{loss}), H_2 uptake rate ($R_{H_2}^x$) and cell stacking, is analyzed through the simulation results. The most important parameters for evaluating each simulation case are compiled in Table VI.4. Nonetheless, their analysis can be more easily interpreted with a more visual representation and a detailed description of these results as presented in sections VI-3.3 and VI-3.4.

Table VI.4. Summary of the global simulation results from the low (Cases 1-5) and high (Cases 6-7) H_2 uptake scenarios.

	Case	1	2	3	4	5	6	7
Parameters**					Simulation results			

Number of stacked cells	1	1	1	3	1	3	6
Cathode thickness [cm]	2.0	2.0	2.0	2.0	2.0	2.0	1.0
Cathode width [cm]	15	60	20	11.8	60	30	50.5
Cathode height [cm]	15	60	20	11.8	223	40	50.5
Cathode volume (stack) [cm^{-3}]	450	7200	800	835	26760	7200	15301
$C_{H_2}^{in}[mmol \cdot L^{-}1]$ *	0.48	0.37	0.37	0.37	0.55	0.55	0.55
$C_{H_2}^{out}[mmol \cdot L^{-}1]$ *	0.78	0.78	1.21	1.21	1.21	2.43	1.21
$C_{H_2}^{max}[mmol \cdot L^{-1}]$	0.91	0.90	1.49	1.61	1.24	2.78	1.64
$j^{max}[A \cdot m^{-2}]$	17.5	17.2	17.8	17.4	17.9	17.7	17.5
Mixing index, MI [%]	91	91	87	84	99	88	80
Péclet number, Pe	11821	2454	4810	2717	78649	3843	31148
Pressure drop [Pa]	12.5	133	6.74	2.25	1272	10.7	73.0
P_{hyd} (stack) [$W \cdot 10^{-6}$]	163	18844	48	16	443423	274	25456
			Mass balances results				
Current (stack) [A]	0.77	11.11	1.15	1.15	44.66	9.24	44.66
Recycling rate (stack), $v_l\ [L \cdot h^{-1}]$	47.1	506.8	25.6	25.6	1254.7	92.0	1254.7
$C_{H_2}^{in}[mmol \cdot L^{-}1]$	0.48	0.37	0.37	0.37	0.55	0.55	0.55
$C_{H_2}^{out}[mmol \cdot L^{-}1]$	0.78	0.78	1.21	1.21	1.21	2.42	1.21
$C'_{H_2}[mmol \cdot L^{-}1]$	0.70	0.55	0.85	0.85	0.85	1.69	0.85
H_2 loss, s_{loss} [%]	10	30	30	30	30	30	30
SSE [%]	57	4	38	38	10	49	10

* Concentrations calculated as an averaged value at the exit of the water electroreduction cell.

** The values tabulated correspond to a single cell from the stack otherwise stated

VI-3.2 Case 1 - Water electroreduction cell for coupling with hydrogenotrophic bioreactor at TBI (low H_2 uptake rate)

This subsection presents the detailed results for Case 1, a low H_2 uptake scenario based on the operational conditions of a hydrogenotrophic bioreactor at TBI. The analysis focuses on the current distribution and H_2 concentration profiles across the cathodic chamber, as well as on the top (exit) cross-section and projected surface of the cathode. Additionally, the velocity

profile at the central cross-section of the cathode is examined, along with the effect of the chosen cathode-separator spacing.

Fig. VI.4 shows the H_2 concentration and current distribution profiles across the porous cathode for Case 1. The first observation is that while most of the variation in H_2 concentration occurs along the cathode's height, the majority of the current density variation occurs along its width. In this case, a local maximum dissolved H_2 concentration of 0.91 mmol·L^{-1} and local maximum current density of 17.53 A·m^2 were achieved, both of which were below the estimated bubble nucleation limits ($C_{H_2}^{crit} = 5.5\ \mathrm{mmol \cdot L^{-1}}$ and $J_{bubble} = 18\ \mathrm{A \cdot m^{-2}}$).

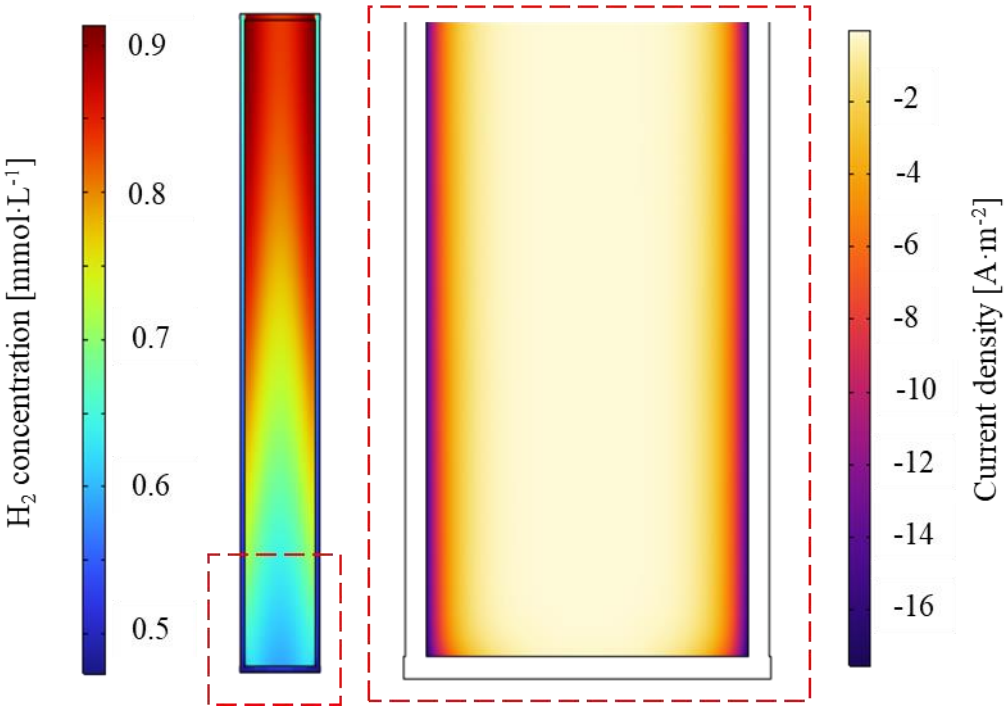

Fig. VI.4. H_2 concentration profile and current distribution across the surface of the porous cathode for the simulation Case 1.

The current distribution remained heterogeneous across the cathode's thickness. This relationship with the dissolved H_2 concentration is further evidenced by analyzing the profiles at the top of the cathode surface, as shown in Fig. VI.5A. As the fluid moves up through the porous cathode, the H_2 concentration increases, causing a decrease in current density due to concentration polarization. However, as seen in Fig. VI.5B, the current distribution heterogeneity along the vertical axis is much lower than that across the cathode thickness at the outlet, which is primarily attributed to ohmic losses. Based on these profiles, it can be

expected that bubble formation might occur in the upper half of the cathode height, where the H_2 concentration becomes supersaturated.

(A)

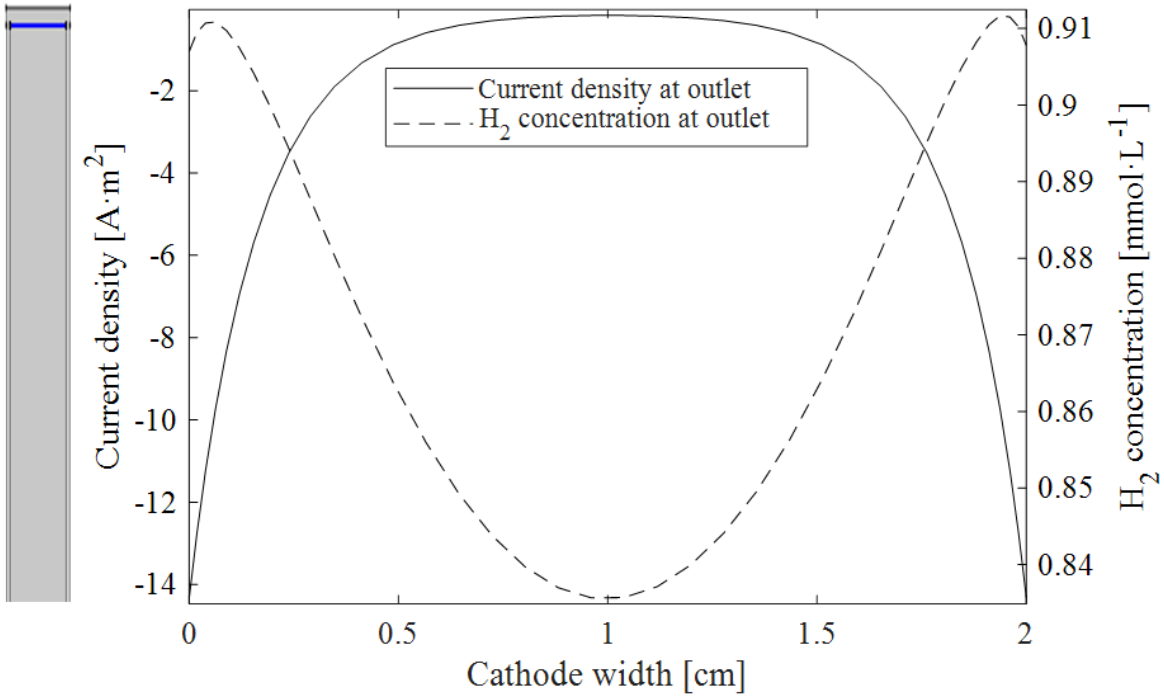

(B)

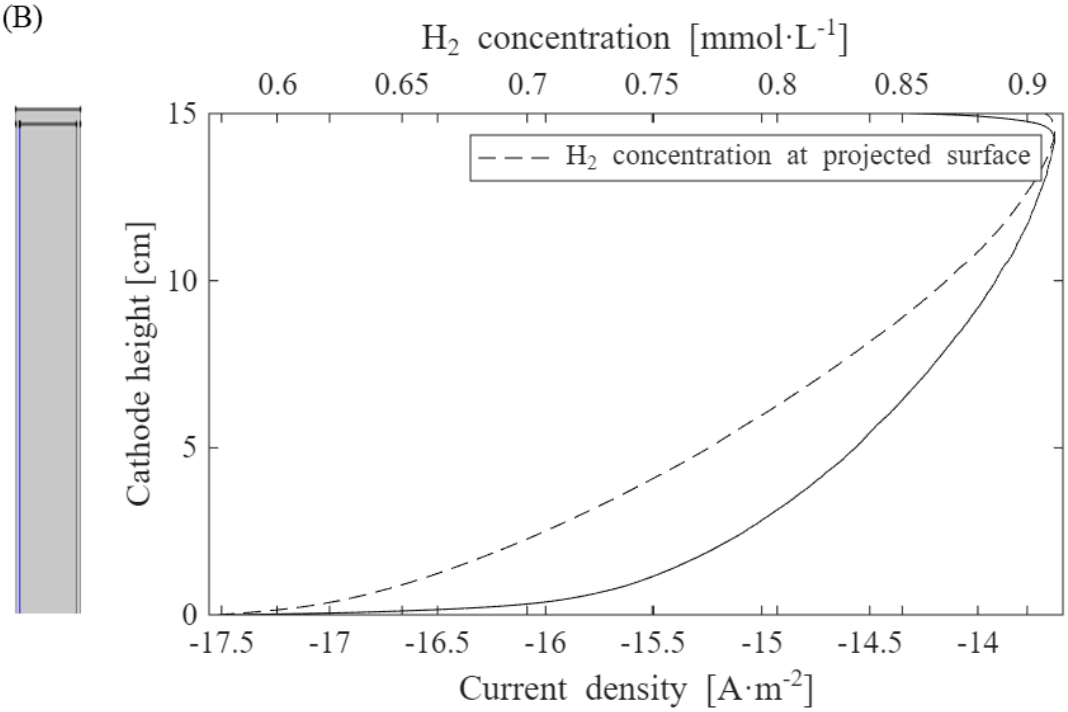

Fig. VI.5. H_2 concentration profile and current density distribution along the (A) cathode width at the exit and (B) the cathode height on the projected surface area of the porous cathode for the simulation Case 1.

The shape of the velocity profile also depended on the space between the cathode's projected surface and the separator. For this simulation, the space was set equal to the cathode's pore diameter ($1.4 \cdot 10^{-3}$ [m^{-1}]), as this allowed for a high velocity magnitude near the projected surface of the cathode, where the current density is at its highest, as shown in Fig. VI.6.

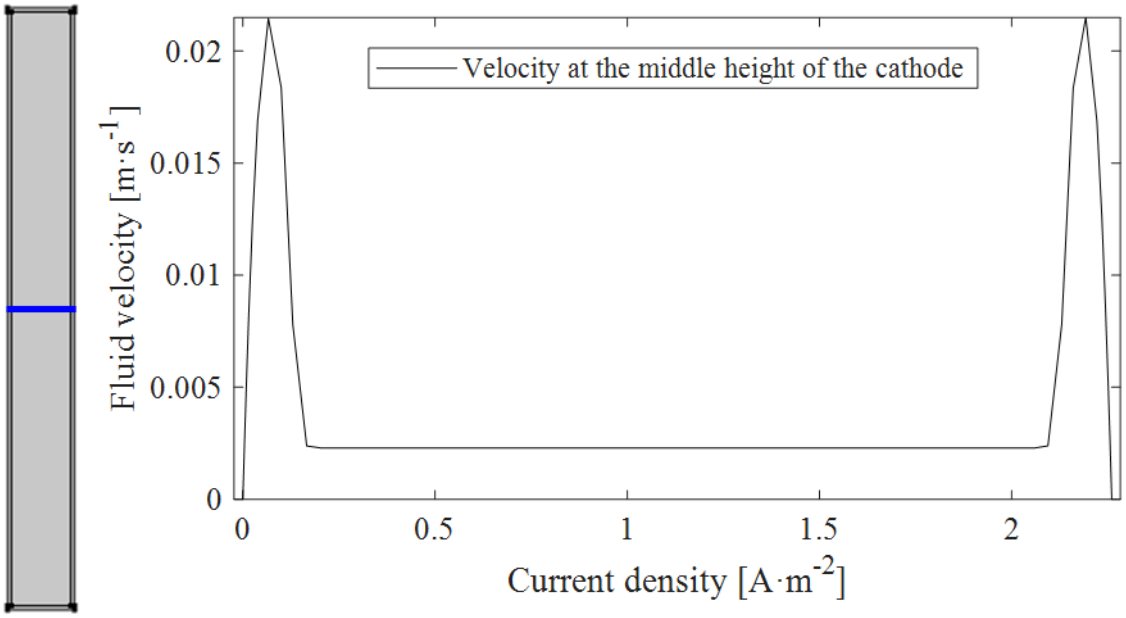

Fig. VI.6. Fluid velocity (y- component) profile along the cell width from the middle height of the cell for the simulation Case 1.

It was also found that this spacing was near the optimal point for minimizing both the maximum local current density and H_2 concentration, as seen in Fig. VI.7. While smaller separations might seem better overall, the precise positioning at such small distances becomes impractical. These results further confirm the suitability of flow-through cell designs for H_2 solubilization.

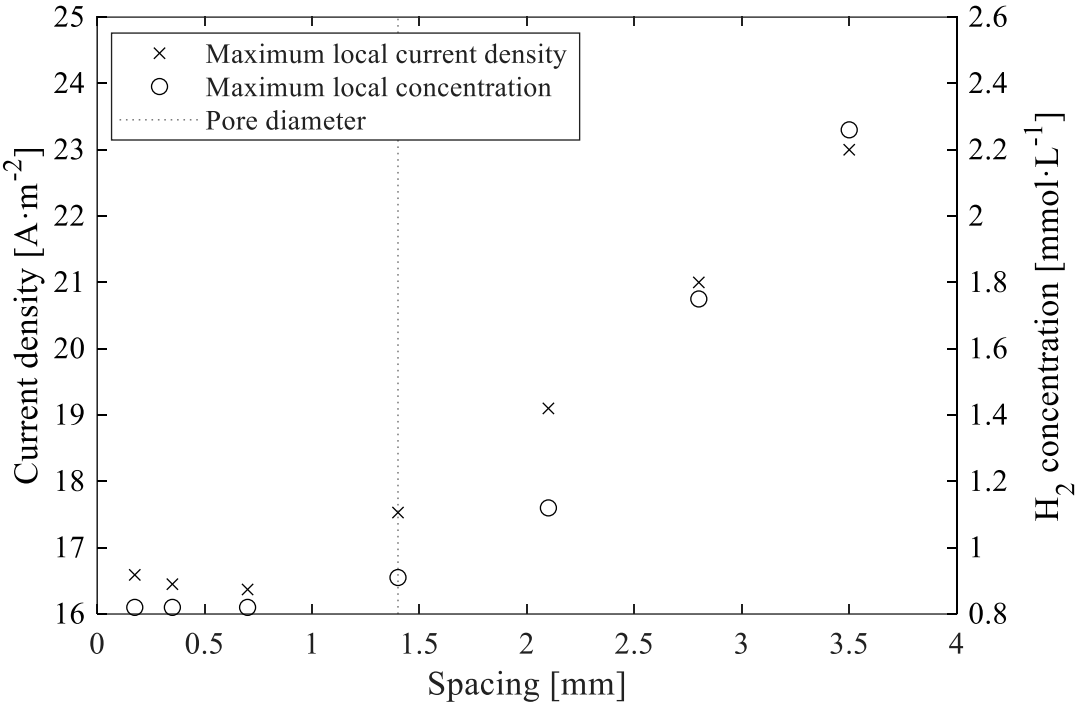

Fig. VI.7. Effect of the separator-cathode spacing on the maximum local current density and local concentration of H_2.

VI-3.3 Cases 2-5 - Effect of H_2 supersaturation ($C_{H_2}^{out}$) and H_2 loss percentage (s_{loss}) on cell dimensions at low H_2 uptake rate

This subsection expands on the low H_2 uptake rate scenario ($R_{H_2}^{x} = 8.1\ [\mathrm{mmol \cdot h^{-1}}]$) by examining the effects of H_2 supersaturation, H_2 loss percentage and a cell stacking on cell dimensions and operational parameters such as current, recycling rate, and cathode volume. This analysis involves a comparison of simulation results from Cases 2-5, using Case 1 as a baseline.

Using Case 1 (current of 0.77 A, cathode volume of 450 cm^3 and recycling rate (v_l) of 47 $L \cdot h^{-1}$) as a reference, an increase in H_2 loss (s_{loss}) from 10% to 30% dramatically increased the required current by 15 times, the cathode volume by 17 times, and the recycling rate by 11 times, as shown in Fig. VI.8. This was caused by a sharp drop in the system solubilization efficiency (SSE) from 57% to 4%. Higher H_2 losses are likely to occur from improper handling of the liquid medium, such as the development of heavy turbulence and agitation, and are also expected in systems with supersaturated liquid.

In contrast, Case 3, which allowed the water electroreduction cell to reach a supersaturation concentration of 1.21 mmol·h^{-1} while maintaining a high s_{loss} of 30%, required only a 1.5-fold increase in current and a 1.8-fold increase in cathode volume compared to Case 1. The recycling rate was also reduced by 1.8 times. This highlights the potential benefits of allowing higher H_2 concentrations, although experimental data on H_2 losses at different supersaturation levels are still needed.

The power required for the pump to overcome the pressure drop in the electrolyzer in Case 3 was 3.4 times lower than in Case 1. While using a cell stack in Case 4 showed no change in the parameters compared to Case 3, the power for the cell stack was reduced by a further 3 times compared to the non-stacked cell (Case 3) due to the larger cross sectional area of the stack (reduced fluid velocity), demonstrating that to reduce the pressure drop, a cell stack of thin porous electrodes should be used for a more compact design.

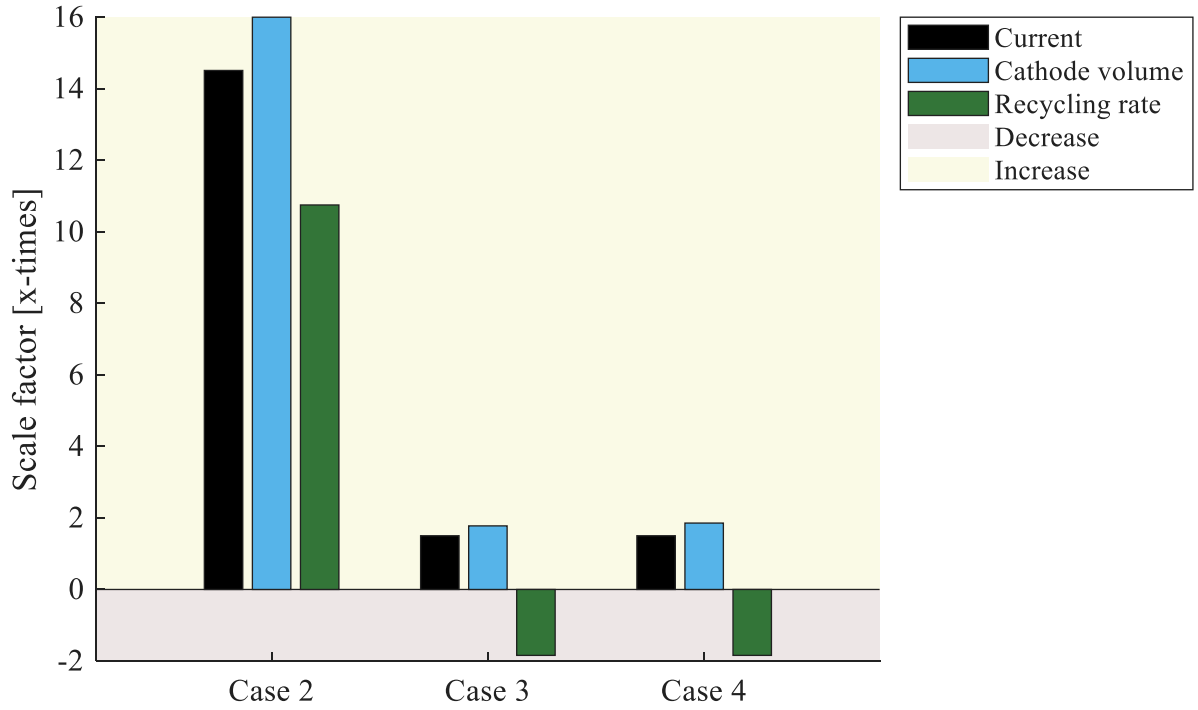

Fig. VI.8. Scale factors for simulation cases with low H_2 uptake. The scale factors are based on three key parameters: current, recycling rate, and cathode volume, taking the results from Case 1 as baseline. The yellow region indicates a parameter increase relative to the baseline, while the red region shows a decrease. Case 4 was omitted since the plotted parameters were identical to Case 3. The baseline parameters were: Current of 0.77 A, cathode volume of 450 cm^3 and recycling rate of 47 L·h^{-1}

VI-3.4 Cases 6-8 - Water electroreduction cell for coupling with hydrogenotrophic bioreactor at high biomass cell density (high H_2 uptake rate)

This subsection shifts the focus to a high H_2 uptake rate scenario, representing a bioreactor with a high biomass cell density. The objective is to determine whether the proposed cell design can be feasibly scaled to meet the significantly higher H_2 demand ($R^{x}_{H_2} = 84\ [mmol \cdot h^{-1}]$).The primary challenges are the excessively large cathode volume and operational conditions required and through a comparative analysis of the simulation results for Cases 6 and 7, strategies like using a cell stack and achieving higher supersaturation are highlighted due to their potential to dramatically reduce the required current, cathode volume, and recycling rate.

In the second scenario, a higher H_2 uptake rate was simulated, where $R^{x}_{H_2}$ = 84 mmol·h^{-1} (10.4 times larger than in scenario 1). As the concentration in the bioreactor had to be maintained at the saturation point (0.78 mmol·h^{-1}), achieving supersaturation in the electrolyzer becomes inevitable for the coupling. For Case 5, a cathode size of 2×60×223 cm^3 would be required to operate at a current of 45 A (s_{loss} of 30%, SSE of 10%), a recycling rate of 1255 L·h^{-1}, and an outlet concentration of $C^{out}_{H_2}$ = 1.21 [mmol·L^{-1}]. This concentration was chosen based on the experiments from Chapter III. However, the excessively large cathode volume and operational conditions would make its practical implementation unfeasible.

Nevertheless, by using a stack of three cells and a $C^{out}_{H_2}$ = 2.42 [mmol·L^{-1}] as in Case 6, the current, cathode volume and recycling rate were reduced 4.8, 3.7 and 13.6 times respectively, as shown in Fig. VI.9. This was achieved by allowing an increase in SSE from 10% to 49%. These significant reductions highlight the necessity of a more rigorous evaluation of H_2 losses and solubilization efficiencies at different conditions, especially when operating hydrogenotrophic bioreactors with higher H_2 uptake rates.

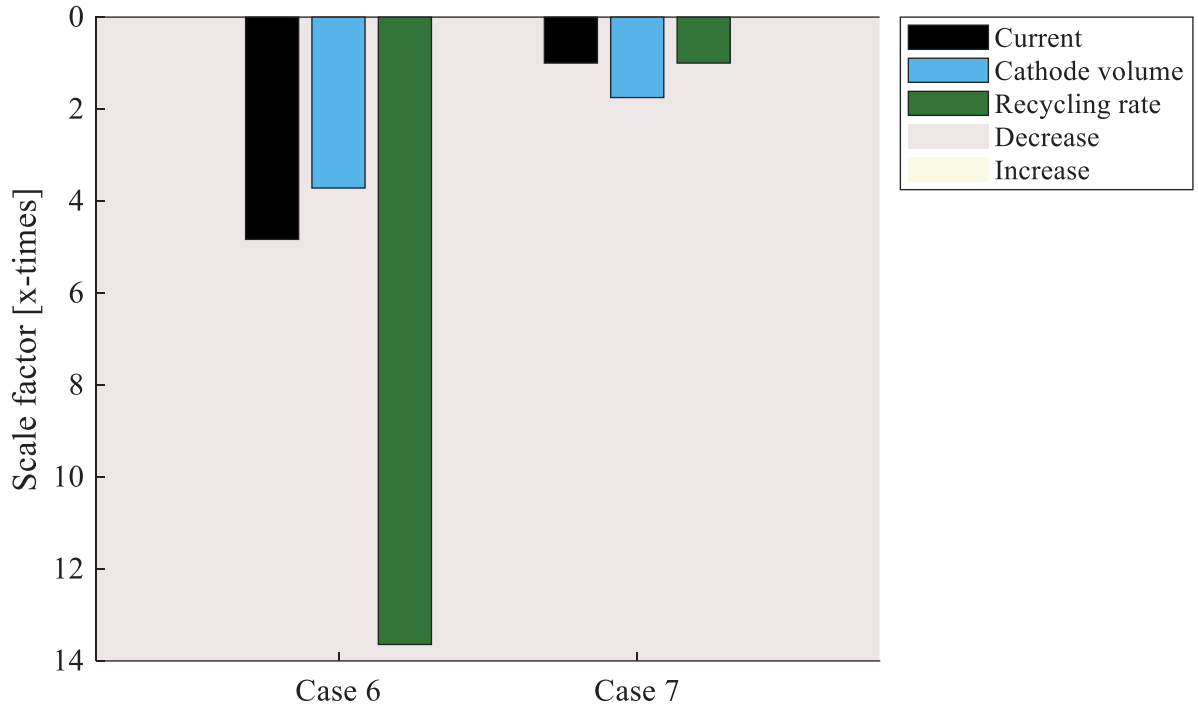

Fig. VI.9. Scale factors for simulation cases with high H_2 uptake. The scale factors are based on three key parameters: current recycling rate, and cathode volume, taking the results from Case 5 as baseline. The red region indicates that the parameters shown had a decrease on their scale factors relative to the baseline Case 5. The baseline parameters were: Current of 45 A, cathode volume of 26760 cm^3 and recycling rate of 1255 $L \cdot h^{-1}$

Lastly, although working with reduced-thickness cathode foams and a large cell stack might be inconvenient, Case 7 (1 cm thickness and a stack of six cells) showed that the total cathode volume was cut by half. This was attributed to a more efficient current distribution, as shown in Fig. VI.10. The implications of this improvement for the current distribution show that thin cathodes should be chosen as small as the design and operational restrictions allow it, and compactness should be pursued by using a stack of thin porous electrodes instead of a single cell thick electrode.

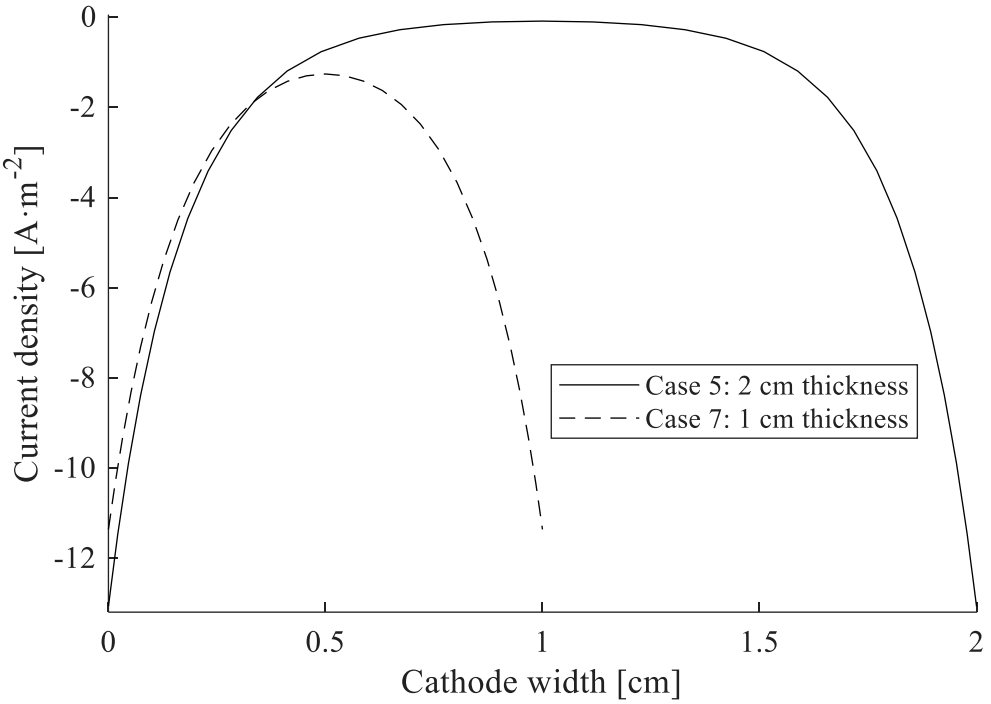

Fig. VI.10. Current density distribution along the cathode width at the exit of the cathode for Cases 5 (cathode thickness of 2 cm) and Case 7 (stack of 6 cells with cathode thickness of 1 cm).

VI-4. Discussion and closing remarks

VI-4.1 Key findings and system feasibility

This chapter demonstrates the feasibility of coupling a water electroreduction cell with a hydrogenotrophic bioreactor, particularly for the low H_2 uptake rate scenario based on experimental data from TBI. At steady state, a gas consumption rate of 8.1 mmol·h^{-1} of H_2, would correspond to an acetate production rate of 2.0 mmol·h^{-1} (1.8 mmol·h^{-1} reported) with a reported biomass concentration of 0.2 g·L^{-1} in a 2 L (2000 cm^3) reactor can be sustained. The proposed system, with a cathode size of 2×15×15 cm^3 (Case 1), would operate at a cathodic current of 0.77 A, achieving a System solubilization efficiency (SSE) of 57% and a recycling rate of 47.1 L·h^{-1}. A volumetric comparison of the proposed water electroreduction cell next to the coupled hydrogenotrophic bioreactor is shown in Fig. VI.11. This system would provide an outlet dissolved H_2 concentration of 0.78 mmol·L^{-1} from the electroreduction cell, necessary to maintain a dissolved H_2 concentration in the bioreactor of 0.53 mmol·L^{-1}.

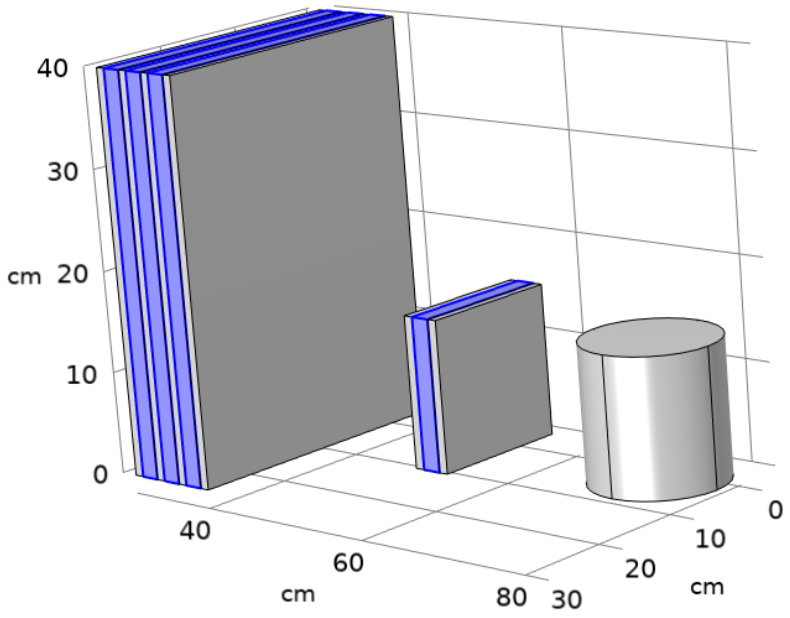

Fig. VI.11. Comparison of the dimensions of the resulting water electroreduction cells from Case 6 (left) with a cathodic volume of 7200 cm^3, Case 1 (middle) with a cathodic volume of 450 cm^3 and a hydrogenotrophic bioreactor of 2000 cm^3. The cathode volumes are shown in blue.

Another important finding is the low power consumption required for the proposed system's fluid movement. The power needed to overcome the pressure drop across the cell at the specified recycling rate would be only 0.164×10^{-3} W. This is considerably lower than the approximately 0.2 W required for moderate mixing in a traditional 2 L (2000 cm^3) gas injection tank (at 600 rpm).

The coupling with a hydrogenotrophic bioreactor at high H_2 uptake rate might become more challenging. An electroreduction stack of three cells, each with a cathode size of $2\times30\times40$ cm^3 (Case 6), would operate at a total cathodic current of 9.24 A, achieving a system solubilization efficiency (SSE) of 51% and a recycling rate of 92 $L\cdot h^{-1}$. Nevertheless, this would require the handling of supersaturation concentrations (2.43 $mmol\cdot L^{-1}$ at the electroreduction cell), which needs to be further validated through experimentation and probably require over-pressurization of the system to prevent low solubilization efficiency values (SSE). A simpler approach would be maintaining the design considerations used here (geometric symmetry,

flow through cell and thin porous electrodes) to make a MES system with a liquid loop recycling, where electrolytic H_2 production and biological uptake occur in the same physical space.

The fundamental principles followed here for simulating a forced flow through the porous cathode, although it considers dispersity factors for correcting mainly the transverse diffusion (across the cathode thickness), could not truly simulate the apparition of dead zones, which would require a real 3D reconstruction of the porous structure and an increased computational power. Nevertheless, a possible strategy to overcome this hydrodynamic limitation would be to impose a forced fluid flow with alternating direction, where dead zones formed by the forward direction are removed by the backwards directional flow [214].

VI-4.2 Practical challenges and operational considerations

For the proposed system to function effectively, the microbial retention time must be decoupled from the recycling cycle to prevent biofilm growth on the cathode. It should also be independent of the nutrient feed/purge retention time, as hydrogenotrophic microorganisms are slow-growing compared with aerobic heterotrophs [11], [44], [182]. Typical methods for cell retention or recycling, such as micro-filtration and centrifugation, would need to be implemented [10], [215]. The energy costs and retention efficiency of these methods, as well as potential H_2 losses during the processes, must be considered.

Additionally, while CO_2 can be assumed to be near saturation under most operational conditions (see Chapter III), its solubilization and transport are also coupled with the recycling cycle. A larger liquid volume in the complete system would necessitate a higher CO_2 supply rate to maintain the required dissolved H_2 concentrations. Since controlling the dissolved CO_2 concentration may have a lesser effect on the process compared to H_2, it can be argued that the biggest impact is on H_2 solubilization. If CO_2 is to be dissolved from the gas phase, a method like molecular diffusion through hollow fiber membranes is preferable to bubble injection [9], [216]. This not only improves gas-to-liquid CO_2 transfer but also avoids the purging effect that CO_2 bubbling might have. Moreover, the surfactant activity of dissolved CO_2 is a well-known effect that can favor nucleation [120]. At a CO_2 applied pressure of 1 atm, the surface tension of the media should drop from ~72 to ~70 in water [129]. Although this might seem insignificant, others have experimentally shown that a lower (~65%) dissolved H_2

concentrations is obtained in the presence of dissolved CO_2 when electrolytic microbubbles and traditional gas injection is used [16].

The kinetics of H_2 solubilization should be evaluated in an optimized growth medium. A good starting point for the exploration of a growth medium that favors H_2 solubilization should be the optimized media for microbial electrosynthesis cells (MES) since they are usually more ionically conductive than gas fermentation media.

Besides providing dissolved H_2 for the hydrogenotrophic bacteria, the cell must also be designed to prevent the O_2 crossover from the anodic to the cathodic chamber, due to its toxic effects in anaerobic hydrogenotrophs. The obvious drawback of using ion exchange membranes/separators that efficiently restrict O_2 diffusion is their added resistance of ion crossover between the two chambers. This added internal resistance is a common energy penalty that needs to be avoided for the scale-up of these reactors. In preliminary experiments (see Supplemental Information E), there was no significant difference between the O_2 diffusion to the catholyte crossing the cation exchange membrane (CMI 7000S, Membranes International Inc, USA) and the solubilization of O_2 from the atmosphere. Unfortunately, the reactor setup used here was not gas-tight and the O_2 crossover effect could have been masked by the atmospheric O_2 diffusion. Nonetheless, it is important to remark that the opposite efforts of solubilizing H_2 in the catholyte should be applied to avoid solubilization of O_2 in the anolyte. This means the use of anodes that promote fast detachment and removal of O_2 bubbles. Other common approaches to avoid O_2 solubilization include the use of alternative oxidation reactions such as carbon oxidation [217], the passive removal of O_2 by hydrophobic membranes [218] or the active removal of O_2 by N_2 flushing [219], although their feasibility to be implemented at large- implementation needs to be further addressed.

VI-4.3 Implications in a microbial electrosynthesis system (MES) setup

The design principles explored in this work for efficient H_2 solubilization also support the operation of a Microbial Electrosynthesis (MES) cell. While the electrolytic production of micro/nano bubbles in MES has been proposed to enhance H_2 solubilization kinetics, bubble-free and flow-through MES systems with porous cathodes have also been previously investigated. This work advances that concept by demonstrating how reactor and electrode

geometries can be optimized to maintain bubble-free operation through a study of current distribution and hydrodynamics, rather than simply limiting the imposed current.

A key argument for physically decoupling H_2 production from the bioprocess is to prevent microbial colonization of the cathode, which competes for the electroactive surface area needed for the hydrogen evolution reaction (HER). A potential solution is to explore cathode materials with reduced affinity for biofilm attachment. A simpler approach, however, might be to leverage the effect that even gentle bubble formation has on preventing biofilm growth. Following the design principles proposed here, an optimized cell could operate at higher total currents before the onset of controlled, gentle bubbling for biofilm prevention [18], [220], [221]. Future work could explore managing biofilm formation through the sporadic, careful release of bubbles via current control.

General Conclusion

The efficient and controlled delivery of dissolved H_2 stands as a critical bottleneck in advancing hydrogenotrophic bioprocesses, particularly for the sustainable production of valuable metabolites such as organic acids and alcohols. Traditional H_2 gas injection methods are severely constrained by the inherently low solubility of H_2 in water and the sluggish gas-to-liquid mass transfer, which collectively restrict biological H_2 uptake kinetics and overall bioreactor productivity. This limitation prompts the injection of substantial H_2 volumes with characteristically low solubilization efficiencies, or the need for gas recirculation to extend the residence time of the slow dissolving bubbles. To circumvent these bottlenecks, the integration of water electroreduction as an alternative H_2 supply mechanism has emerged as a promising strategy in parallel to microbial electrosynthesis systems, demanding precise monitoring and careful reactor design to maximize solubilization rates and efficiency by avoiding H_2 bubble nucleation. This conclusion summarizes some prospects in sensing technologies for dissolved H_2 and bubble detection (Chapter II), evaluates the comparative advantages of water electroreduction over gas injection (Chapter III), elucidates the critical role of cathode design in preventing bubble nucleation (Chapter IV), identifies the underlying principles for the operation of bubble-free water electroreduction (Chapter V) and outlines the feasibility and future trajectory for coupling these electrochemical systems with hydrogenotrophic bioreactors (Chapter VI).

Accurate and real-time measurement of dissolved H_2 concentration and the detection of H_2 bubble nucleation are fundamental for avoiding H_2 loss during different biological H_2 uptake rates and for possibly help into elucidate and control the desired product spectrum of CO_2 reduction by hydrogenotrophs. The inherent challenges in measuring dissolved H_2, reinforced by the non-equilibrium conditions that can occur between the liquid and gas phase of the bioreactor, render traditional headspace gas fraction estimations unreliable. In this context, the development of robust sensing technologies is indispensable for process control and stability. In Chapter II, the following questions were aborded: what are the limitations of existing sensing technologies for monitoring dissolved H_2 concentrations and bubble nucleation events during water electroreduction? and what are the most suitable technologies for real-time H_2 sensing to be implemented in the control of a water electroreduction cell? In

this regard, the headspace gas chromatography (HS-GC) method developed in this work demonstrated high precision for dissolved H_2 concentration measurements (R^2 = 0.99) , which was used for effectively validating H_2 pre-saturation conditions in experimental setups. Although the method used here requires significant liquid sampling volumes (50 mL) and manual manipulation, which can be cumbersome for continuous, in-situ monitoring in laboratory-scale experiments, its accuracy and lack of frequent sensing element replacement offer a reliable ex-situ alternative. For dynamic process control, however, future efforts should focus on a more automatized version of the HS-GC for the profiling of different dissolved gases in the liquid medium.

When operating the water electroreduction cell in the absence of H_2 nucleation, it was also proved here that the potential of employing optical methods for the detection of bubbles. It was shown that unlike semiconducting metal oxide (SMO) sensors, which only detect bubbles after their detachment from the electrode surface, introducing significant detection delays and signal saturation issues, a digital camera provides direct, non-invasive, and timely signals of nucleation events at the cathode surface. Through traditional image processing techniques implemented in MATLAB, nucleation events were successfully identified on various electrode materials. While its efficacy is highest for fixed and well-illuminated electrodes (e.g., stainless-steel porous foam and plates), limitations were observed with mobile electrodes (e.g., carbon brush), underscoring the necessity for more sophisticated image processing algorithms to handle dynamic geometries if necessary. Nevertheless, this optical approach emerges as a reliable feedback mechanism, enabling a future sensor-actuator coupling for real-time control of the imposed current to maintain bubble-free conditions and maximize solubilization efficiency in water electroreduction cells.

Using the headspace gas chromatography method developed together with the amperometric H_2 sensor, the following question was aborded in Chapter III. How do water electroreduction and traditional gas injection compare in terms of H_2 solubilization rate, maximum concentration achieved in the medium and energy consumption per mole of H_2 solubilized? The comparative evaluation of water electroreduction against traditional H_2 gas injection highlights the superior potential of water electroreduction for hydrogenotrophic bioprocesses was done in this chapter. Gas injection methods are inherently limited by the low solubility of H_2 in water and slow gas-to-liquid mass transfer kinetics. This leads to low solubilization

efficiencies (e.g., ~2% observed for gas injection) and a maximum dissolved H_2 concentration constrained by the saturation limit at 1 bar (0.78 mmol·L^{-1}) , regardless of the H_2 supply rate. Efforts to overcome these limitations through high pressures introduce operational complexities and safety concerns, while the industrial implementation of micro/nanobubbles remains challenging due to issues like sparger fouling and stability. In stark contrast, water electroreduction directly produces dissolved H_2 within the liquid medium, entirely bypassing the gas-to-liquid mass transfer bottleneck. This direct production allows for the achievement of supersaturated concentrations of dissolved H_2, reaching up to 1.21 mmol·L^{-1} experimentally, significantly exceeding the saturation limit of gas injection. Water electroreduction also demonstrates significantly higher H_2 solubilization efficiencies, achieving 35% efficiency, an 18-fold improvement over gas injection in a single pass for a CSTR configuration, which could avoid the use of large columns. Even with H_2 supply rates approximately 18 times lower than gas injection, water electroreduction achieved comparable H_2 solubilization rates (0.67 mmol·L^{-1}·h^{-1} for water electroreduction versus 0.79 mmol·L^{-1}·h^{-1} for gas injection). This translates into substantial energy efficiency benefits: Water electroreduction required approximately 4.6 times less energy per mol of H_2 solubilized compared to H_2 produced via steam methane reforming used for gas injection, and 3.6 times less compared to H_2 produced by an ideal water electrolyzer producing H_2 gas. The ability to achieve and maintain high H_2 concentrations is fundamental for hydrogenotrophic bioprocesses where alcohols or reduced organic acids are desired, as these elevated levels can provide enough reducing equivalents to allow large metabolite production rates, improve selectivity (e.g., shifting acetogenesis to solventogenesis for ethanol production), and modulate microbial competition, favoring strains with higher H_2 thresholds and enabling thermodynamically challenging metabolic pathways. This capacity to finely control H_2 concentration opens new avenues for optimizing product yields and guiding complex microbial consortia towards desired metabolic outcomes.

However, the effective utilization of water electroreduction for H_2 solubilization critically depends on preventing H_2 bubble nucleation and growth at the cathode surface. Bubble formation is highly detrimental, as it reduces solubilization rates, interrupts H_2 bioavailability, introduces energetic penalties, and masks active electrode surface area. The critical threshold for bubble-free operation was established at local H_2 concentrations below 5.5 mmol·L^{-1} and current densities below 18 A·m^{-2}. These thresholds were determined in Chapter IV and it was

also studied how agitation and the accumulation of dissolved H_2 affect the nucleation events at different cathode structures.

Porous cathode materials provide a high surface area, which effectively distributes the applied current over a larger region, thereby reducing local current densities and slowing H_2 accumulation at the electrode-electrolyte interface. For instance, a stainless-steel porous foam exhibited the highest current density before nucleation, particularly under agitated and H_2 pre-saturated conditions. However, the efficacy of porous materials is not solely dependent on surface area; electrolyte permeability within the porous structure is equally critical. Open-cell foams with larger pores generally offer higher permeability, lower pressure drops, and improved H_2 removal, preventing H_2 accumulation within the porosity that could otherwise lead to nucleation. This highlights that porosity alone is insufficient without adequate flow.

The implementation of forced flow, typically achieved through flow-through cell designs, is essential for mitigating local H_2 supersaturation in the most inner sections of the cathode. Experiments showed that agitation, although it significantly counteracted the effects of H_2 pre-saturation by promoting the removal of dissolved H_2 from the electrode surface, although it could be problematic for porous or 3D electrodes. This prompts the question of what other considerations should be taken when implementing a bubble-free operation of a water electroreduction cell. In Chapter V, design constraints such as electrode shape and size ratios, electrode porosity and hydrodynamic flow (forced vs non-forced flow) were studied by Multiphysics simulations, with the purpose of aiding the design of a water electroreduction cell with minimal current distribution heterogeneities and improved mass transfer. Flow-through cells, with their improved hydrodynamics, are demonstrably superior to agitated bulk electrolyzers in ensuring efficient H_2 solubilization and bubble-free operation, particularly by enforcing proper mass transfer within the cathode's porosity.

Furthermore, thin cathodes contribute significantly to the homogeneity of current distribution, which is a critical factor in avoiding hyperpolarized regions prone to bubble nucleation. A homogeneous current distribution is best achieved when the projected cathode surface area is equal to and equidistant from the separator/counter electrode. Higher electrolyte conductivities (e.g., 50 $mS \cdot cm^{-1}$) also enhances current distribution homogeneity in the simulations, allowing for higher currents before nucleation occurs. The use of cell stacks and double separators (sandwich configuration) further promotes current distribution

homogeneity and reduces total cathode volume and pump power requirements, making the system more energy-efficient and compact. The combination of thin, porous cathodes with forced flow represents an optimized strategy for sustained, bubble-free H_2 delivery in microbial electrosynthesis systems. These design principles are fundamental for maximizing bubble-free H_2 solubilization and ensuring continuous H_2 bioavailability for hydrogenotrophic microorganisms, directly improving the efficiency and productivity of bioprocesses.

Finally, it is important to approach the question of whether it would be feasible to couple a water electroreduction cell with a hydrogenotrophic bioreactor. This feasibility was evaluated for low and high H_2 uptake scenarios in Chapter VI, offering compelling design considerations and clear directions for future research. For a low H_2 uptake rate scenario (8.1 $mmol \cdot h^{-1}$), a feasible system was identified comprising a 2×15×15 cm^3 porous cathode operating at 0.77 A with a recycling rate of 47.1 $L \cdot h^{-1}$. This setup would maintain a dissolved H_2 concentration of 0.53 $mmol \cdot L^{-1}$ in a 2 L bioreactor while avoiding bubble nucleation by keeping local H_2 concentrations and current densities below critical thresholds established. A significant advantage of this coupled system is the remarkably low power consumption for fluid movement (~0.0002 W) , substantially less than the ~0.2 W typically required for mixing in traditional gas injection systems. Enabling H_2 supersaturation (up to 1.21 $mmol \cdot L^{-1}$) at the electroreduction cell exit further reduced the recycling rate by 1.8 times, although this might necessitate system over-pressurization to mitigate H_2 losses.

Scaling to a high H_2 uptake rate scenario (84 $mmol \cdot h^{-1}$) initially posed significant challenges, with single-cell designs proving unfeasible due to prohibitive cathode volumes and current requirements. However, an optimized design involving a stack of three 2×30×40 cm^3 cells, operating at a higher H_2 supersaturation of 2.42 $mmol \cdot L^{-1}$, dramatically reduced the required current by 4.8 times, total cathode volume by 3.7 times, and recycling rate by 13.6 times, while simultaneously increasing the system solubilization efficiency from 10% to 49%. This highlights the role of cell stacking and higher supersaturation in achieving feasibility at industrial scales. Furthermore, reducing cathode thickness from 2 cm to 1 cm in a six-cell stack halved the total cathode volume due to a more efficient current distribution, emphasizing the preference for thin cathodes where design and operational constraints allow. For high H_2 uptake rates, the implementation of a microbial electrosynthesis system (MES) configuration, where H_2

production and biological uptake occur in the same physical space, could be more practical, especially when targeting dissolved H_2 concentrations over the saturation limit.

Several design considerations and practical challenges must be addressed for the successful implementation of these coupled systems. The microbial retention time must be decoupled from the recycling cycle to prevent biofilm growth on the cathode, necessitating robust cell retention mechanisms such as micro-filtration or centrifugation, whose energy costs and retention efficiencies need thorough evaluation. The transport and solubilization of CO_2 are also intertwined with the recycling cycle, requiring higher CO_2 supply rates for larger liquid volumes; here, molecular diffusion via hollow fiber membranes is preferable to bubble injection to avoid purging effects and consequently degassing H_2. Exploring cathode materials with reduced affinity for biofilm attachment or managing biofilm formation through sporadic, controlled bubble release could be promising alternatives proposed in this work. Furthermore, optimization of the growth medium for enhanced ionic conductivity (hypersaline media) with the use of halotolerant microorganisms could also benefit H_2 solubilization due to the more homogeneous current distribution over the cathodic surface.

Looking forward, future research should focus on obtaining reliable experimental data on the difficulties of stabilizing supersaturated solutions, and investigating microbial growth kinetics, product yields, and selectivity under these elevated H_2 concentrations to fully harness the potential for shifting metabolic pathways. The integration of real-time bubble detection with advanced electrochemical control systems would allow for dynamic optimization of current and microbial growth. High-fidelity simulations incorporating hydrodynamics, mass transport, and reaction kinetics will be instrumental in guiding the design of hierarchical electrode structures and optimized flow field geometries. These endeavors collectively could pave the way for a shift in hydrogenotrophic bioprocesses, driven by the precision and efficiency offered by coupled water electroreduction systems with optimal current distribution.

REFERENCES

[1] United Nations General Assembly, “Progress towards the Sustainable Development Goals,” May 2024.

[2] United Nations Environment Programme *et al.*, *Emissions Gap Report 2024: No more hot air … please! With a massive gap between rhetoric and reality, countries draft new climate commitments*. United Nations Environment Programme, 2024. doi: 10.59117/20.500.11822/46404.

[3] United Nations Environment Programme, “Emissions Gap Report 2022: The Closing Window — Climate crisis calls for rapid transformation of societies,” Nairobi, 2022. [Online]. Available: https://www.unep.org/emissions-gap-report-2022

[4] P. C. Psarras, S. Comello, P. Bains, P. Charoensawadpong, S. Reichelstein, and J. Wilcox, “Carbon Capture and Utilization in the Industrial Sector,” *Environ. Sci. Technol.*, vol. 51, no. 19, pp. 11440–11449, 2017, doi: 10.1021/acs.est.7b01723.

[5] H. L. Drake, Ed., *Acetogenesis*. in Chapman & Hall microbiology series. New York, NY: Chapman & Hall, 1994.

[6] J. Bae *et al.*, “Valorization of C1 gases to value-added chemicals using acetogenic biocatalysts,” *Chem. Eng. J.*, vol. 428, no. July 2021, p. 131325, 2022, doi: 10.1016/j.cej.2021.131325.

[7] P. Linstrom, “NIST Chemistry WebBook, NIST Standard Reference Database 69.” National Institute of Standards and Technology, 1997. doi: 10.18434/T4D303.

[8] L. A. Alves, J. B. Almeida E Silva, and M. Giulietti, “Solubility of D -Glucose in Water and Ethanol/Water Mixtures,” *J. Chem. Eng. Data*, vol. 52, no. 6, pp. 2166–2170, Nov. 2007, doi: 10.1021/je700177n.

[9] F. Ale Enriquez and B. K. Ahring, “Strategies to overcome mass transfer limitations of hydrogen during anaerobic gaseous fermentations: A comprehensive review,” *Bioresour. Technol.*, vol. 377, p. 128948, Jun. 2023, doi: 10.1016/j.biortech.2023.128948.

[10] M. D. Bredwell, P. Srivastava, and R. M. Worden, “Reactor Design Issues for Synthesis-Gas Fermentations,” *Biotechnol. Prog.*, vol. 15, no. 5, pp. 834–844, Jan. 1999, doi: 10.1021/bp990108m.

[11] M. Kircher and T. Schwarz, Eds., *CO2 and CO as Feedstock: Sustainable Carbon Sources for the Circular Economy*. in Circular Economy and Sustainability. Cham: Springer International Publishing, 2023. doi: 10.1007/978-3-031-27811-2.

[12] P. Izadi and F. Harnisch, “Microbial | electrochemical CO2 reduction: To integrate or not to integrate?,” *Joule*, vol. 6, no. 5, pp. 935–940, May 2022, doi: 10.1016/j.joule.2022.04.005.

[13] P. L. Tremblay, L. T. Angenent, and T. Zhang, “Extracellular Electron Uptake: Among Autotrophs and Mediated by Surfaces,” *Trends Biotechnol.*, vol. 35, no. 4, pp. 360–371, 2017, doi: 10.1016/j.tibtech.2016.10.004.

[14] E. Blanchet, F. Duquenne, Y. Rafrafi, L. Etcheverry, B. Erable, and A. Bergel, “Importance of the hydrogen route in up-scaling electrosynthesis for microbial CO2 reduction,” *Energy Environ. Sci.*, vol. 8, no. 12, pp. 3731–3744, 2015, doi: 10.1039/c5ee03088a.

[15] S. T. Boto, B. Bardl, F. Harnisch, and M. A. Rosenbaum, “Microbial electrosynthesis with *Clostridium ljungdahlii* benefits from hydrogen electron mediation and permits a greater

variety of products," *Green Chem.*, vol. 25, no. 11, pp. 4375–4386, 2023, doi: 10.1039/D3GC00471F.

[16] K. Cui, K. Guo, J. M. Carvajal-Arroyo, J. Arends, and K. Rabaey, "An electrolytic bubble column with an external hollow fiber membrane gas–liquid contactor for effective microbial electrosynthesis of acetate from CO2," *Chem. Eng. J.*, vol. 471, p. 144296, Sep. 2023, doi: 10.1016/j.cej.2023.144296.

[17] E. V. LaBelle and H. D. May, "Energy Efficiency and Productivity Enhancement of Microbial Electrosynthesis of Acetate," *Front. Microbiol.*, vol. 8, p. 756, May 2017, doi: 10.3389/fmicb.2017.00756.

[18] I. Vassilev, P. Dessì, S. Puig, and M. Kokko, "Cathodic biofilms – A prerequisite for microbial electrosynthesis," *Bioresour. Technol.*, vol. 348, p. 126788, Mar. 2022, doi: 10.1016/j.biortech.2022.126788.

[19] O. Alšauskas, "World Energy Outlook 2024".

[20] T. M. Gür, "Carbon Dioxide Emissions, Capture, Storage and Utilization: Review of Materials, Processes and Technologies," *Prog. Energy Combust. Sci.*, vol. 89, p. 100965, Mar. 2022, doi: 10.1016/j.pecs.2021.100965.

[21] S. Gross, "The challenge of decarbonizing heavy industry," Jun. 2021.

[22] P. Fennell, J. Driver, C. Bataille, and S. J. Davis, "Going net zero for cement and steel".

[23] C. Bataille *et al.*, "A review of technology and policy deep decarbonization pathway options for making energy-intensive industry production consistent with the Paris Agreement," *J. Clean. Prod.*, vol. 187, pp. 960–973, Jun. 2018, doi: 10.1016/j.jclepro.2018.03.107.

[24] G. P. Thiel and A. K. Stark, "To decarbonize industry, we must decarbonize heat," *Joule*, vol. 5, no. 3, pp. 531–550, Mar. 2021, doi: 10.1016/j.joule.2020.12.007.

[25] F. M. Baena-Moreno, M. Rodríguez-Galán, F. Vega, B. Alonso-Fariñas, L. F. Vilches Arenas, and B. Navarrete, "Carbon capture and utilization technologies: a literature review and recent advances," *Energy Sources Part Recovery Util. Environ. Eff.*, vol. 41, no. 12, pp. 1403–1433, Jun. 2019, doi: 10.1080/15567036.2018.1548518.

[26] L. Gonsalvi, A. Guerriero, and S. Kostera, "Homogeneously Catalyzed CO 2 Hydrogenation to Formic Acid/Formate with Non-precious Metal Catalysts," in *CO2 Hydrogenation Catalysis*, 2021, pp. 53–88. doi: 10.1002/9783527824113.ch3.

[27] W. Li *et al.*, "A short review of recent advances in CO_2 hydrogenation to hydrocarbons over heterogeneous catalysts," *RSC Adv.*, vol. 8, no. 14, pp. 7651–7669, 2018, doi: 10.1039/C7RA13546G.

[28] S. Saeidi *et al.*, "Recent advances in CO2 hydrogenation to value-added products — Current challenges and future directions," *Prog. Energy Combust. Sci.*, vol. 85, p. 100905, Jul. 2021, doi: 10.1016/j.pecs.2021.100905.

[29] R. Sen, A. Goeppert, and G. K. Surya Prakash, "Homogeneous Hydrogenation of CO2 and CO to Methanol: The Renaissance of Low-Temperature Catalysis in the Context of the Methanol Economy," *Angew. Chem. Int. Ed.*, vol. 61, no. 42, p. e202207278, Oct. 2022, doi: 10.1002/anie.202207278.

[30] F. Gong, H. Zhu, Y. Zhang, and Y. Li, "Biological carbon fixation: From natural to synthetic," *J. CO2 Util.*, vol. 28, pp. 221–227, Dec. 2018, doi: 10.1016/j.jcou.2018.09.014.

[31] I. Sánchez-Andrea *et al.*, "The reductive glycine pathway allows autotrophic growth of Desulfovibrio desulfuricans," *Nat. Commun.*, vol. 11, no. 1, p. 5090, Oct. 2020, doi: 10.1038/s41467-020-18906-7.

[32] N. J. Claassens *et al.*, “Engineering the Reductive Glycine Pathway: A Promising Synthetic Metabolism Approach for C1-Assimilation,” in *One-Carbon Feedstocks for Sustainable Bioproduction*, vol. 180, A.-P. Zeng and N. J. Claassens, Eds., in Advances in Biochemical Engineering/Biotechnology, vol. 180. , Cham: Springer International Publishing, 2022, pp. 299–350. doi: 10.1007/10_2021_181.

[33] E. Kurt, J. Qin, A. Williams, Y. Zhao, and D. Xie, “Perspectives for Using CO2 as a Feedstock for Biomanufacturing of Fuels and Chemicals,” *Bioengineering*, vol. 10, no. 12, p. 1357, Nov. 2023, doi: 10.3390/bioengineering10121357.

[34] B. Liang, Y. Zhao, and J. Yang, “Recent Advances in Developing Artificial Autotrophic Microorganism for Reinforcing CO2 Fixation,” *Front. Microbiol.*, vol. 11, p. 592631, Nov. 2020, doi: 10.3389/fmicb.2020.592631.

[35] S. W. Ragsdale, “*Enzymology of the Wood–Ljungdahl Pathway of Acetogenesis*,” *Ann. N. Y. Acad. Sci.*, vol. 1125, no. 1, pp. 129–136, Mar. 2008, doi: 10.1196/annals.1419.015.

[36] H. L. Drake, A. S. Gößner, and S. L. Daniel, “*Old Acetogens, New Light*,” *Ann. N. Y. Acad. Sci.*, vol. 1125, no. 1, pp. 100–128, Mar. 2008, doi: 10.1196/annals.1419.016.

[37] S. Wiley *et al.*, “An alcove at the acetyl-CoA synthase nickel active site is required for productive substrate CO binding and anaerobic carbon fixation,” *J. Biol. Chem.*, vol. 300, no. 8, p. 107503, Aug. 2024, doi: 10.1016/j.jbc.2024.107503.

[38] F. Liew, M. E. Martin, R. C. Tappel, B. D. Heijstra, C. Mihalcea, and M. Köpke, “Gas Fermentation—A Flexible Platform for Commercial Scale Production of Low-Carbon-Fuels and Chemicals from Waste and Renewable Feedstocks,” *Front. Microbiol.*, vol. 7, May 2016, doi: 10.3389/fmicb.2016.00694.

[39] R. Takors *et al.*, “Using gas mixtures of CO, CO2 and H2 as microbial substrates: the do’s and don’ts of successful technology transfer from laboratory to production scale,” *Microb. Biotechnol.*, vol. 11, no. 4, pp. 606–625, 2018, doi: 10.1111/1751-7915.13270.

[40] H. Lee, J. Bae, S. Jin, S. Kang, and B. K. Cho, “Engineering Acetogenic Bacteria for Efficient One-Carbon Utilization,” *Front. Microbiol.*, vol. 13, no. May, 2022, doi: 10.3389/fmicb.2022.865168.

[41] R. Kourist and S. Schmidt, Eds., *The autotrophic biorefinery: raw materials from biotechnology*. Berlin Boston: De Gruyter, 2021. doi: 10.1515/9783110550603.

[42] F. Kracke *et al.*, “Efficient Hydrogen Delivery for Microbial Electrosynthesis via 3D-Printed Cathodes,” *Front. Microbiol.*, vol. 12, p. 696473, Aug. 2021, doi: 10.3389/fmicb.2021.696473.

[43] K. Valgepea *et al.*, “H2 drives metabolic rearrangements in gas-fermenting Clostridium autoethanogenum,” *Biotechnol. Biofuels*, vol. 11, no. 1, p. 55, Dec. 2018, doi: 10.1186/s13068-018-1052-9.

[44] V. G. Debabov, “Acetogens: Biochemistry, Bioenergetics, Genetics, and Biotechnological Potential,” *Microbiology*, vol. 90, no. 3, pp. 273–297, May 2021, doi: 10.1134/S0026261721030024.

[45] B. E. Rittmann and P. L. McCarty, “Environmental biotechnology : principles and applications,” *Curr. Opin. Biotechnol.*, vol. 7, no. 3, pp. 357–365, 2001, doi: 10.1016/S0958-1669(96)80047-4.

[46] V. Müller, N. P. Chowdhury, and M. Basen, “Electron Bifurcation: A Long-Hidden Energy-Coupling Mechanism,” *Annu. Rev. Microbiol.*, vol. 72, no. 1, pp. 331–353, Sep. 2018, doi: 10.1146/annurev-micro-090816-093440.

[47] E. Biegel, S. Schmidt, J. M. González, and V. Müller, “Biochemistry, evolution and physiological function of the Rnf complex, a novel ion-motive electron transport complex

in prokaryotes," *Cell. Mol. Life Sci.*, vol. 68, no. 4, pp. 613–634, Feb. 2011, doi: 10.1007/s00018-010-0555-8.

[48] L. Westphal, A. Wiechmann, J. Baker, N. P. Minton, and V. Müller, "The Rnf Complex Is an Energy-Coupled Transhydrogenase Essential To Reversibly Link Cellular NADH and Ferredoxin Pools in the Acetogen Acetobacterium woodii," *J. Bacteriol.*, vol. 200, no. 21, Nov. 2018, doi: 10.1128/JB.00357-18.

[49] H. L. Drake, K. Küsel, and C. Matthies, "Acetogenic Prokaryotes," in *The Prokaryotes*, M. Dworkin, S. Falkow, E. Rosenberg, K.-H. Schleifer, and E. Stackebrandt, Eds., New York, NY: Springer New York, 2006, pp. 354–420. doi: 10.1007/0-387-30742-7_13.

[50] F. Min, M. Kopke, and S. Dennis, "Gas Fermentation for Commercial Biofuels Production," in *Liquid, Gaseous and Solid Biofuels - Conversion Techniques*, Z. Fang, Ed., InTech, 2013. doi: 10.5772/52164.

[51] K. Valgepea *et al.*, "Arginine deiminase pathway provides ATP and boosts growth of the gas-fermenting acetogen Clostridium autoethanogenum," *Metab. Eng.*, vol. 41, pp. 202–211, May 2017, doi: 10.1016/j.ymben.2017.04.007.

[52] V. Mahamkali *et al.*, "Redox controls metabolic robustness in the gas-fermenting acetogen *Clostridium autoethanogenum*," *Proc. Natl. Acad. Sci.*, vol. 117, no. 23, pp. 13168–13175, Jun. 2020, doi: 10.1073/pnas.1919531117.

[53] R. K. Thauer, K. Jungermann, and K. Decker, "Energy conservation in chemotrophic anaerobic bacteria," *Bacteriol. Rev.*, vol. 41, no. 1, pp. 100–180, Mar. 1977, doi: 10.1128/br.41.1.100-180.1977.

[54] H. L. Drake, *Acetogenesis*. Chapman & Hall, 1994.

[55] L. Laguillaumie *et al.*, "Controlling the microbial competition between hydrogenotrophic methanogens and homoacetogens using mass transfer and thermodynamic constraints," *J. Clean. Prod.*, vol. 414, p. 137549, Aug. 2023, doi: 10.1016/j.jclepro.2023.137549.

[56] C. M. Spirito, H. Richter, K. Rabaey, A. J. Stams, and L. T. Angenent, "Chain elongation in anaerobic reactor microbiomes to recover resources from waste," *Curr. Opin. Biotechnol.*, vol. 27, pp. 115–122, Jun. 2014, doi: 10.1016/j.copbio.2014.01.003.

[57] T. A. Lynch, Y. Wang, B. Van Brunt, D. Pacheco, and P. H. Janssen, "Modelling thermodynamic feedback on the metabolism of hydrogenotrophic methanogens," *J. Theor. Biol.*, vol. 477, pp. 14–23, Sep. 2019, doi: 10.1016/j.jtbi.2019.05.018.

[58] M. Laura and P. Jo, "No acetogen is equal: Strongly different H_2 thresholds reflect diverse bioenergetics in acetogenic bacteria," *Environ. Microbiol.*, vol. 25, no. 10, pp. 2032–2040, Oct. 2023, doi: 10.1111/1462-2920.16429.

[59] R. Ganigué, P. Sánchez-Paredes, L. Bañeras, and J. Colprim, "Low Fermentation pH Is a Trigger to Alcohol Production, but a Killer to Chain Elongation," *Front. Microbiol.*, vol. 7, May 2016, doi: 10.3389/fmicb.2016.00702.

[60] T. Antukh, I. Lee, S. Joo, and H. Kim, "Hydrogenotrophs-Based Biological Biogas Upgrading Technologies," *Front. Bioeng. Biotechnol.*, vol. 10, p. 833482, Apr. 2022, doi: 10.3389/fbioe.2022.833482.

[61] I. Kerkhof, L. Puiman, and A. J. J. Straathof, "Understanding microbial syngas fermentation rates," *Appl. Microbiol. Biotechnol.*, vol. 108, no. 1, p. 540, Dec. 2024, doi: 10.1007/s00253-024-13364-3.

[62] T. Hübert, L. Boon-Brett, and W. Buttner, *Sensors for Safety and Process Control in Hydrogen Technologies*, 0 ed. CRC Press, 2018. doi: 10.1201/b19141.

[63] J. Dang, N. Wang, and H. K. Atiyeh, “Review of Dissolved CO and H2 Measurement Methods for Syngas Fermentation,” *Sensors*, vol. 21, no. 6, p. 2165, Mar. 2021, doi: 10.3390/s21062165.

[64] T. Hübert, L. Boon-Brett, G. Black, and U. Banach, “Hydrogen sensors – A review,” *Sens. Actuators B Chem.*, vol. 157, no. 2, pp. 329–352, Oct. 2011, doi: 10.1016/j.snb.2011.04.070.

[65] R. B. Bird, W. E. Stewart, and E. N. Lightfoot, *Transport phenomena*, Revised ed. New York: Wiley, 2007.

[66] P. A. Ramachandran, *Advanced transport phenomena: analysis, modeling and computations*. Cambridge: Cambridge University Press, 2014.

[67] I. K. Stoll, N. Boukis, and J. Sauer, “Syngas Fermentation to Alcohols: Reactor Technology and Application Perspective,” *Chem. Ing. Tech.*, vol. 92, no. 1–2, pp. 125–136, Jan. 2020, doi: 10.1002/cite.201900118.

[68] M. Alheshibri, J. Qian, M. Jehannin, and V. S. J. Craig, “A History of Nanobubbles,” *Langmuir*, vol. 32, no. 43, pp. 11086–11100, Nov. 2016, doi: 10.1021/acs.langmuir.6b02489.

[69] S. R. German, M. A. Edwards, Q. Chen, and H. S. White, “Laplace Pressure of Individual H_2 Nanobubbles from Pressure–Addition Electrochemistry,” *Nano Lett.*, vol. 16, no. 10, pp. 6691–6694, Oct. 2016, doi: 10.1021/acs.nanolett.6b03590.

[70] W. Fan *et al.*, “A modelling approach to explore the optimum bubble size for micro-nanobubble aeration,” *Water Res.*, vol. 228, p. 119360, Jan. 2023, doi: 10.1016/j.watres.2022.119360.

[71] F. Y. Ushikubo *et al.*, “Evidence of the existence and the stability of nano-bubbles in water,” *Colloids Surf. Physicochem. Eng. Asp.*, vol. 361, no. 1–3, pp. 31–37, May 2010, doi: 10.1016/j.colsurfa.2010.03.005.

[72] P. S. Epstein and M. S. Plesset, “On the Stability of Gas Bubbles in Liquid-Gas Solutions,” *J. Chem. Phys.*, vol. 18, no. 11, pp. 1505–1509, Nov. 1950, doi: 10.1063/1.1747520.

[73] P. B. Duncan and D. Needham, “Test of the Epstein−Plesset Model for Gas Microparticle Dissolution in Aqueous Media: Effect of Surface Tension and Gas Undersaturation in Solution,” *Langmuir*, vol. 20, no. 7, pp. 2567–2578, Mar. 2004, doi: 10.1021/la034930i.

[74] D. Lohse and X. Zhang, “Surface nanobubbles and nanodroplets,” *Rev. Mod. Phys.*, vol. 87, no. 3, pp. 981–1035, Aug. 2015, doi: 10.1103/RevModPhys.87.981.

[75] K. Kikuchi, Y. Tanaka, Y. Saihara, M. Maeda, M. Kawamura, and Z. Ogumi, “Concentration of hydrogen nanobubbles in electrolyzed water,” *J. Colloid Interface Sci.*, vol. 298, no. 2, pp. 914–919, Jun. 2006, doi: 10.1016/j.jcis.2006.01.010.

[76] X. Zhu, R. Verzicco, X. Zhang, and D. Lohse, “Diffusive interaction of multiple surface nanobubbles: shrinkage, growth, and coarsening,” *Soft Matter*, vol. 14, no. 11, pp. 2006–2014, 2018, doi: 10.1039/C7SM02523H.

[77] B. H. Tan, H. An, and C.-D. Ohl, “Stability of surface and bulk nanobubbles,” *Curr. Opin. Colloid Interface Sci.*, vol. 53, p. 101428, Jun. 2021, doi: 10.1016/j.cocis.2021.101428.

[78] N. Nirmalkar, A. W. Pacek, and M. Barigou, “On the Existence and Stability of Bulk Nanobubbles,” *Langmuir*, vol. 34, no. 37, pp. 10964–10973, Sep. 2018, doi: 10.1021/acs.langmuir.8b01163.

[79] S. Wang, Z. Wang, P. Lv, L. Jiang, C. Shi, and Y. Song, “CO_2 Micro–Nanobubble Technology in Carbon Capture, Utilization, and Storage: A Mini Review,” *Energy Fuels*, vol. 39, no. 5, pp. 2381–2395, Feb. 2025, doi: 10.1021/acs.energyfuels.4c05183.

[80] J. R. T. Seddon, D. Lohse, W. A. Ducker, and V. S. J. Craig, “A Deliberation on Nanobubbles at Surfaces and in Bulk,” *ChemPhysChem*, vol. 13, no. 8, pp. 2179–2187, Jun. 2012, doi: 10.1002/cphc.201100900.

[81] N. Matsuki, T. Ishikawa, S. Ichiba, N. Shiba, Y. Ujike, and T. Yamaguchi, “Oxygen supersaturated fluid using fine micro/nanobubbles,” *Int. J. Nanomedicine*, p. 4495, Sep. 2014, doi: 10.2147/IJN.S68840.

[82] M. Soyluoglu, D. Kim, Y. Zaker, and T. Karanfil, “Stability of Oxygen Nanobubbles under Freshwater Conditions,” *Water Res.*, vol. 206, p. 117749, Nov. 2021, doi: 10.1016/j.watres.2021.117749.

[83] S. Xue, Y. Zhang, T. Marhaba, and W. Zhang, “Aeration and dissolution behavior of oxygen nanobubbles in water,” *J. Colloid Interface Sci.*, vol. 609, pp. 584–591, Mar. 2022, doi: 10.1016/j.jcis.2021.11.061.

[84] Y. Jiang, Z. Ma, Z. Gu, F. Liu, P. Shen, and C. S. Poon, “A novel approach for improving aqueous carbonation kinetics with CO2 micro- and nano-bubbles,” *Chem. Eng. J.*, vol. 500, p. 157363, Nov. 2024, doi: 10.1016/j.cej.2024.157363.

[85] M. Nsenga Kumwimba *et al.*, “Micro/nanobubble aeration promotes rapid and stable partial nitrification by strengthening the synergistic activity of functional microbial communities in the treatment of low-strength rural wastewater,” *Chem. Eng. J.*, vol. 519, p. 165552, Sep. 2025, doi: 10.1016/j.cej.2025.165552.

[86] P. Pal and H. Anantharaman, “CO2 nanobubbles utility for enhanced plant growth and productivity: Recent advances in agriculture,” *J. CO2 Util.*, vol. 61, p. 102008, Jul. 2022, doi: 10.1016/j.jcou.2022.102008.

[87] A. Tekile, I. Kim, and J.-Y. Lee, “Extent and persistence of dissolved oxygen enhancement using nanobubbles,” *Environ. Eng. Res.*, vol. 21, no. 4, pp. 427–435, Sep. 2016, doi: 10.4491/eer.2016.028.

[88] S. H. Oh, J. G. Han, and J.-M. Kim, “Long-term stability of hydrogen nanobubble fuel,” *Fuel*, vol. 158, pp. 399–404, Oct. 2015, doi: 10.1016/j.fuel.2015.05.072.

[89] W. Cai *et al.*, “An electrolytic-hydrogen-fed moving bed biofilm reactor for efficient microbial electrosynthesis of methane from CO2,” *Chem. Eng. J.*, vol. 428, p. 132093, Jan. 2022, doi: 10.1016/j.cej.2021.132093.

[90] A. J. Bard and L. R. Faulkner, *Electrochemical methods: fundamentals and applications*, 2nd ed. New York: Wiley, 2001.

[91] L. Zhang, “Electrochemical Water Electrolysis; Fundamentals and Technologies”.

[92] T. Naito, T. Shinagawa, T. Nishimoto, and K. Takanabe, “Water Electrolysis in Saturated Phosphate Buffer at Neutral pH,” *ChemSusChem*, vol. 13, no. 22, pp. 5921–5933, Nov. 2020, doi: 10.1002/cssc.202001886.

[93] E. Yeager, J. O. Bockris, B. E. Conway, and S. Sarangapani, Eds., *Comprehensive Treatise of Electrochemistry: Electrodics: Transport*. Boston, MA: Springer US, 1983. doi: 10.1007/978-1-4615-6690-8.

[94] G. F. Swiegers, R. N. L. Terrett, G. Tsekouras, T. Tsuzuki, R. J. Pace, and R. Stranger, “The prospects of developing a highly energy-efficient water electrolyser by eliminating or mitigating bubble effects,” *Sustain. Energy Fuels*, vol. 5, no. 5, pp. 1280–1310, 2021, doi: 10.1039/D0SE01886D.

[95] A. L. Hoang, R. E. Owen, G. Tsekouras, and D. J. L. Brett, “Bubble Detection on the Cathode and Anode of a High-Performing Capillary- Fed Water Electrolysis Cell”.

[96] P. Tiwari, G. Tsekouras, K. Wagner, G. F. Swiegers, and G. G. Wallace, “A new class of bubble-free water electrolyzer that is intrinsically highly efficient,” *Int. J. Hydrog. Energy*, vol. 44, no. 42, pp. 23568–23579, Sep. 2019, doi: 10.1016/j.ijhydene.2019.07.100.

[97] A. R. Zeradjanin, J. Grote, G. Polymeros, and K. J. J. Mayrhofer, “A Critical Review on Hydrogen Evolution Electrocatalysis: Re-exploring the Volcano-relationship,” *Electroanalysis*, vol. 28, no. 10, pp. 2256–2269, Oct. 2016, doi: 10.1002/elan.201600270.

[98] S. D. Simpson, R. J. Conrado, C. D. Mihalcea, and M. E. Martin, “Integrated fermentation and electrolysis process.” Google Patents, Jul. 23, 2019.

[99] K. Scott and E. H. Yu, *Microbial Electrochemical and Fuel Cells. Fundamentals and Applications*. Woodhead publishing series in energy, 2015.

[100] B. E. Logan, *Microbial Fuel Cells*, 1st ed. Wiley, 2007. doi: 10.1002/9780470258590.

[101] D. R. Lovley, “Powering microbes with electricity: direct electron transfer from electrodes to microbes,” *Environ. Microbiol. Rep.*, vol. 3, no. 1, pp. 27–35, Feb. 2011, doi: 10.1111/j.1758-2229.2010.00211.x.

[102] L. Luan *et al.*, “Bioelectrocatalysis for CO2 reduction: recent advances and challenges to develop a sustainable system for CO2 utilization,” *Biotechnol. Adv.*, vol. 63, p. 108098, Mar. 2023, doi: 10.1016/j.biotechadv.2023.108098.

[103] D. R. Lovley, “Electromicrobiology,” *Annu. Rev. Microbiol.*, vol. 66, pp. 391–409, 2012, doi: 10.1146/annurev-micro-092611-150104.

[104] P.-L. Tremblay, L. T. Angenent, and T. Zhang, “Extracellular Electron Uptake: Among Autotrophs and Mediated by Surfaces,” *Trends Biotechnol.*, vol. 35, no. 4, pp. 360–371, Apr. 2017, doi: 10.1016/j.tibtech.2016.10.004.

[105] K. P. Nevin, T. L. Woodard, A. E. Franks, Z. M. Summers, and D. R. Lovley, “Microbial Electrosynthesis: Feeding Microbes Electricity To Convert Carbon Dioxide and Water to Multicarbon Extracellular Organic Compounds,” *mBio*, vol. 1, no. 2, pp. e00103-10, Jun. 2010, doi: 10.1128/mBio.00103-10.

[106] J. S. Deutzmann, M. Sahin, and A. M. Spormann, “Extracellular Enzymes Facilitate Electron Uptake in Biocorrosion and Bioelectrosynthesis,” *mBio*, vol. 6, no. 2, pp. e00496-15, May 2015, doi: 10.1128/mBio.00496-15.

[107] E. Marsili and X. Zhang, “Shuttling via soluble compounds,” in *Bioelectrochemical Systems: from extracellular electron transfer to biotechnological application*, K. Rabaey, L. Angenent, P. Lens, U. Schroder, J. Keller., IWAP Publishing, UK, 2009.

[108] K. J. J. Steinbusch, H. V. M. Hamelers, J. D. Schaap, C. Kampman, and C. J. N. Buisman, “Bioelectrochemical Ethanol Production through Mediated Acetate Reduction by Mixed Cultures,” *Environ. Sci. Technol.*, vol. 44, no. 1, pp. 513–517, Jan. 2010, doi: 10.1021/es902371e.

[109] E. Marsili, D. B. Baron, I. D. Shikhare, D. Coursolle, J. A. Gralnick, and D. R. Bond, “*Shewanella* secretes flavins that mediate extracellular electron transfer,” *Proc. Natl. Acad. Sci.*, vol. 105, no. 10, pp. 3968–3973, Mar. 2008, doi: 10.1073/pnas.0710525105.

[110] A. Okamoto, K. Hashimoto, and K. H. Nealson, “Flavin Redox Bifurcation as a Mechanism for Controlling the Direction of Electron Flow during Extracellular Electron Transfer,” *Angew. Chem. Int. Ed.*, vol. 53, no. 41, pp. 10988–10991, Oct. 2014, doi: 10.1002/anie.201407004.

[111] S. Freguia, S. Tsujimura, and K. Kano, “Electron transfer pathways in microbial oxygen biocathodes,” *Electrochimica Acta*, vol. 55, no. 3, pp. 813–818, Jan. 2010, doi: 10.1016/j.electacta.2009.09.027.

[112] D. R. Lovley, “Microbial nanowires,” *Curr. Biol.*, vol. 32, no. 3, pp. R110–R112, 2022, doi: 10.1016/j.cub.2021.12.019.

[113] N. S. Malvankar and D. R. Lovley, “Electronic Conductivity in Living Biofilms: Physical Meaning, Mechanisms, and Measurement Methods,” in *Biofilms in Bioelectrochemical Systems*, 2015, pp. 211–248. doi: 10.1002/9781119097426.ch7.

[114] J. S. Deutzmann, M. Sahin, and A. M. Spormann, “Extracellular Enzymes Facilitate Electron Uptake in Biocorrosion and Bioelectrosynthesis,” *mBio*, vol. 6, no. 2, pp. e00496-15, May 2015, doi: 10.1128/mBio.00496-15.

[115] K. A. Vincent, A. Parkin, and F. A. Armstrong, “Investigating and Exploiting the Electrocatalytic Properties of Hydrogenases,” *Chem. Rev.*, vol. 107, no. 10, pp. 4366–4413, Oct. 2007, doi: 10.1021/cr050191u.

[116] H. Beyenal and J. T. Babauta, *Biofilms in Bioelectrochemical Systems*. 2015.

[117] B. S. Jayathilake *et al.*, “Developing reactors for electrifying bio-methanation: a perspective from bio-electrochemistry,” *Sustain. Energy Fuels*, vol. 6, no. 5, pp. 1249–1263, 2022, doi: 10.1039/D1SE02041B.

[118] E. V. Labelle, C. W. Marshall, and H. D. May, “Microbiome for the Electrosynthesis of Chemicals from Carbon Dioxide,” *Acc. Chem. Res.*, vol. 53, no. 1, pp. 62–71, 2020, doi: 10.1021/acs.accounts.9b00522.

[119] E. Blanchet, F. Duquenne, Y. Rafrafi, L. Etcheverry, B. Erable, and A. Bergel, “Importance of the hydrogen route in up-scaling electrosynthesis for microbial CO2 reduction,” *Energy Environ. Sci.*, vol. 8, no. 12, pp. 3731–3744, Dec. 2015, doi: 10.1039/c5ee03088a.

[120] S. D. Lubetkin, “Why Is It Much Easier To Nucleate Gas Bubbles than Theory Predicts?,” *Langmuir*, vol. 19, no. 7, pp. 2575–2587, Apr. 2003, doi: 10.1021/la0266381.

[121] K. Kikuchi *et al.*, “Hydrogen particles and supersaturation in alkaline water from an Alkali–Ion–Water electrolyzer,” *J. Electroanal. Chem.*, vol. 506, no. 1, pp. 22–27, Jun. 2001, doi: 10.1016/S0022-0728(01)00517-4.

[122] V. B. Svetovoy, R. G. P. Sanders, and M. C. Elwenspoek, “Transient nanobubbles in short-time electrolysis,” *J. Phys. Condens. Matter*, vol. 25, no. 18, p. 184002, May 2013, doi: 10.1088/0953-8984/25/18/184002.

[123] A. V. Postnikov, I. V. Uvarov, N. V. Penkov, and V. B. Svetovoy, “Collective behavior of bulk nanobubbles produced by alternating polarity electrolysis,” *Nanoscale*, vol. 10, no. 1, pp. 428–435, 2018, doi: 10.1039/C7NR07126D.

[124] N. Ibl, “Some theoretical aspects of pulse electrolysis,” *Surf. Technol.*, vol. 10, no. 2, pp. 81–104, Feb. 1980, doi: 10.1016/0376-4583(80)90056-4.

[125] Á. Molina and J. González, *Pulse Voltammetry in Physical Electrochemistry and Electroanalysis: Theory and Applications*. in Monographs in Electrochemistry. Cham: Springer International Publishing, 2016. doi: 10.1007/978-3-319-21251-7.

[126] S. D. Lubetkin, “The fundamentals of bubble evolution,” *Chem. Soc. Rev.*, vol. 24, no. 4, p. 243, 1995, doi: 10.1039/cs9952400243.

[127] S. R. German, M. A. Edwards, Q. Chen, Y. Liu, L. Luo, and H. S. White, “Electrochemistry of single nanobubbles. Estimating the critical size of bubble-forming nuclei for gas-evolving electrode reactions,” *Faraday Discuss.*, vol. 193, pp. 223–240, 2016, doi: 10.1039/C6FD00099A.

[128] S. R. German, M. A. Edwards, H. Ren, and H. S. White, “Critical Nuclei Size, Rate, and Activation Energy of H_2 Gas Nucleation,” *J. Am. Chem. Soc.*, vol. 140, no. 11, pp. 4047–4053, Mar. 2018, doi: 10.1021/jacs.7b13457.

[129] S. Lubetkin, “The motion of electrolytic gas bubbles near electrodes,” *Electrochimica Acta*, vol. 48, no. 4, pp. 357–375, Dec. 2002, doi: 10.1016/S0013-4686(02)00682-5.

[130] M. E. Tawfik and F. J. Diez, “On the relation between onset of bubble nucleation and gas supersaturation concentration,” *Electrochimica Acta*, vol. 146, pp. 792–797, Nov. 2014, doi: 10.1016/j.electacta.2014.08.147.

[131] Y. Zhang, X. Zhu, J. A. Wood, and D. Lohse, “Threshold current density for diffusion-controlled stability of electrolytic surface nanobubbles,” *Proc. Natl. Acad. Sci.*, vol. 121, no. 21, p. e2321958121, May 2024, doi: 10.1073/pnas.2321958121.

[132] C. Jin, Y.-L. Liu, Y. Shan, and Q.-J. Chen, “Scanning Electrochemical Cell Microscope Study of Individual H2 Gas Bubble Nucleation on Platinum: Effect of Surfactants,” *Chin. J. Anal. Chem.*, vol. 49, no. 4, pp. e21055–e21064, Apr. 2021, doi: 10.1016/S1872-2040(21)60096-8.

[133] M. Suvira and B. Zhang, “Effect of Surfactant on Electrochemically Generated Surface Nanobubbles,” *Anal. Chem.*, vol. 93, no. 12, pp. 5170–5176, Mar. 2021, doi: 10.1021/acs.analchem.0c05067.

[134] J. Hanwright, J. Zhou, G. M. Evans, and K. P. Galvin, “Influence of Surfactant on Gas Bubble Stability,” *Langmuir*, vol. 21, no. 11, pp. 4912–4920, May 2005, doi: 10.1021/la0502894.

[135] L. Puiman, M. P. Elisiário, L. M. L. Crasborn, L. E. C. H. Wagenaar, A. J. J. Straathof, and C. Haringa, “Gas mass transfer in syngas fermentation broths is enhanced by ethanol,” *Biochem. Eng. J.*, vol. 185, p. 108505, Jul. 2022, doi: 10.1016/j.bej.2022.108505.

[136] R. Iwata *et al.*, “Bubble growth and departure modes on wettable/non-wettable porous foams in alkaline water splitting,” *Joule*, vol. 5, no. 4, pp. 887–900, Apr. 2021, doi: 10.1016/j.joule.2021.02.015.

[137] T. Fujimura, W. Hikima, Y. Fukunaka, and T. Homma, “Analysis of the effect of surface wettability on hydrogen evolution reaction in water electrolysis using micro-patterned electrodes,” *Electrochem. Commun.*, vol. 101, pp. 43–46, Apr. 2019, doi: 10.1016/j.elecom.2019.02.018.

[138] Y. Tanaka and K. Kikuchi, “Dissolution of hydrogen produced by water electrolysis: Effects of electrode roughness factor and current density,” *Results Chem.*, vol. 5, p. 100984, Jan. 2023, doi: 10.1016/j.rechem.2023.100984.

[139] H. C. Lim, “Fed-Batch Cultures”.

[140] V. Sivalingam, T. Haugen, A. Wentzel, and C. Dinamarca, “Effect of Elevated Hydrogen Partial Pressure on Mixed Culture Homoacetogenesis,” *Chem. Eng. Sci. X*, vol. 12, p. 100118, Nov. 2021, doi: 10.1016/j.cesx.2021.100118.

[141] Stoll I.K. *et al.*, “Fermentation of h2 and co2 with clostridium ljungdahlii at elevated process pressure first experimental results,” *Chem. Eng. Trans.*, vol. 64, pp. 151–156, May 2018, doi: 10.3303/CET1864026.

[142] I. K. Stoll, N. Boukis, and J. Sauer, “Syngas Fermentation at Elevated Pressure - Experimental Results,” *Proc. 27th Eur. Biomass Conf. Exhib.*, vol. 27-30 May 2019, p. 7 Pages, 2019, doi: 10.5071/27THEUBCE2019-3CV.3.4.

[143] C. Kantzow and D. Weuster-Botz, “Effects of hydrogen partial pressure on autotrophic growth and product formation of Acetobacterium woodii,” *Bioprocess Biosyst. Eng.*, vol. 39, no. 8, pp. 1325–1330, Aug. 2016, doi: 10.1007/s00449-016-1600-2.

[144] K. Valgepea *et al.*, “Maintenance of ATP Homeostasis Triggers Metabolic Shifts in Gas-Fermenting Acetogens,” *Cell Syst.*, vol. 4, no. 5, pp. 505-515.e5, May 2017, doi: 10.1016/j.cels.2017.04.008.

[145] A. Katsyv and V. Müller, “Overcoming Energetic Barriers in Acetogenic C1 Conversion,” *Front. Bioeng. Biotechnol.*, vol. 8, no. December, pp. 1–23, 2020, doi: 10.3389/fbioe.2020.621166.

[146] A. Lasia, “Mechanism and kinetics of the hydrogen evolution reaction,” *Int. J. Hydrog. Energy*, vol. 44, no. 36, pp. 19484–19518, Jul. 2019, doi: 10.1016/j.ijhydene.2019.05.183.

[147] X. Zhao, H. Ren, and L. Luo, “Gas Bubbles in Electrochemical Gas Evolution Reactions,” *Langmuir*, vol. 35, no. 16, pp. 5392–5408, Apr. 2019, doi: 10.1021/acs.langmuir.9b00119.

[148] P. A. Kempler, R. H. Coridan, and L. Luo, “Gas Evolution in Water Electrolysis,” *Chem. Rev.*, vol. 124, no. 19, pp. 10964–11007, Oct. 2024, doi: 10.1021/acs.chemrev.4c00211.

[149] B. T. Sangtam and H. Park, “Review on Bubble Dynamics in Proton Exchange Membrane Water Electrolysis: Towards Optimal Green Hydrogen Yield,” *Micromachines*, vol. 14, no. 12, p. 2234, Dec. 2023, doi: 10.3390/mi14122234.

[150] J. Mo, Z. Kang, G. Yang, W. Barnhill, F.-Y. Zhang, and D. Talley, “Visualization on rapid and micro-scale dynamics of oxygen bubble evolution in PEMECs,” in *2017 IEEE 12th International Conference on Nano/Micro Engineered and Molecular Systems (NEMS)*, Los Angeles, CA, USA: IEEE, Apr. 2017, pp. 101–105. doi: 10.1109/NEMS.2017.8016983.

[151] Y. Li *et al.*, “Wettability effects of thin titanium liquid/gas diffusion layers in proton exchange membrane electrolyzer cells,” *Electrochimica Acta*, vol. 298, pp. 704–708, Mar. 2019, doi: 10.1016/j.electacta.2018.12.162.

[152] L. Laguillaumie, “Study of the competition between homoacetogens and hydrogenotrophic methanogens in anaerobic mixed cultures for acetate production from H2/CO2: an experimental and modeling approach,” 2022.

[153] “Practical and Theoretical Basis for Redox-measurements in Compacted Bentonite A Literature Survey.pdf.”

[154] P. R. Teasdale, A. I. Minett, K. Dixon, T. W. Lewis, and G. E. Batley, “Practical improvements for redox potential (EH) measurements and the application of a multiple-electrode redox probe (MERP) for characterising sediment in situ,” *Anal. Chim. Acta*, vol. 367, no. 1–3, pp. 201–213, Jul. 1998, doi: 10.1016/s0003-2670(98)00171-8.

[155] A. V. Vershinin and A. G. Rozanov, “The platinum electrode as an indicator of redox environment in marine sediments,” *Mar. Chem.*, vol. 14, no. 1, pp. 1–15, Nov. 1983, doi: 10.1016/0304-4203(83)90065-8.

[156] I. M. Piskarev, V. A. Ushkanov, N. A. Aristova, P. P. Likhachev, and T. S. Myslivets, “Establishment of the redox potential of water saturated with hydrogen,” *Biophysics*, vol. 55, no. 1, pp. 13–17, Feb. 2010, doi: 10.1134/s0006350910010033.

[157] K. Dastafkan *et al.*, “*Operando* monitoring of gas bubble evolution in water electrolysis by single high-frequency impedance,” *EES Catal.*, vol. 1, no. 6, pp. 998–1008, 2023, doi: 10.1039/D3EY00182B.

[158] K. Cui, X. Xue, Z. Pan, J. Yu, W. Cai, and K. Guo, “Selective enrichment of homoacetogens and optimization of the operational conditions for effective acetate production in hydrogen-mediated microbial electrosynthesis reactors,” *Biochem. Eng. J.*, vol. 198, p. 109035, Sep. 2023, doi: 10.1016/j.bej.2023.109035.

[159] S. F. Jones, G. M. Evans, and K. P. Galvin, “Bubble nucleation from gas cavities a review,” 1999.

[160] A. Battistel, C. R. Dennison, A. Lesch, and H. H. Girault, “Local Study on Hydrogen and Hydrogen Gas Bubble Formation on a Platinum Electrode,” *J. Phys. Chem. C*, vol. 123, no. 17, pp. 10849–10856, May 2019, doi: 10.1021/acs.jpcc.8b10920.

[161] R. K. Thauer, “The Wolfe cycle comes full circle,” *Proc. Natl. Acad. Sci.*, vol. 109, no. 38, pp. 15084–15085, Sep. 2012, doi: 10.1073/pnas.1213193109.

[162] H. L. Drake, “Acetogens,” *Harold Drake*, 1994.

[163] P. Dessì *et al.*, “Microbial electrosynthesis: Towards sustainable biorefineries for production of green chemicals from CO2 emissions,” *Biotechnol. Adv.*, vol. 46, no. July 2020, 2021, doi: 10.1016/j.biotechadv.2020.107675.

[164] P. Albina, N. Durban, A. Bertron, A. Albrecht, J.-C. Robinet, and B. Erable, “Influence of Hydrogen Electron Donor, Alkaline pH, and High Nitrate Concentrations on Microbial Denitrification: A Review,” *Int. J. Mol. Sci.*, vol. 20, no. 20, p. 5163, Oct. 2019, doi: 10.3390/ijms20205163.

[165] O. R. Kotsyurbenko, M. V. Glagolev, A. N. Nozhevnikova, and R. Conrad, “Competition between homoacetogenic bacteria and methanogenic archaea for hydrogen at low temperature,” *FEMS Microbiol. Ecol.*, vol. 38, no. 2–3, pp. 153–159, Dec. 2001, doi: 10.1111/j.1574-6941.2001.tb00893.x.

[166] L. Muñoz-Duarte, S. Chakraborty, L. V. Grøn, M. F. Bambace, J. Catalano, and J. Philips, “H_2 Consumption by Various Acetogenic Bacteria Follows First-Order Kinetics up to H_2 Saturation,” *Biotechnol. Bioeng.*, vol. 122, no. 4, pp. 804–816, Apr. 2025, doi: 10.1002/bit.28904.

[167] IEA (2024), “Global Hydrogen Review 2024,” IEA, Paris, 2024. [Online]. Available: https://www.iea.org/reports/global-hydrogen-review-2024

[168] V. Linek, M. Kordač, and T. Moucha, “Mechanism of mass transfer from bubbles in dispersions,” *Chem. Eng. Process. Process Intensif.*, vol. 44, no. 1, pp. 121–130, Jan. 2005, doi: 10.1016/j.cep.2004.05.009.

[169] E. Kadic and T. J. Heindel, *An Introduction to Bioreactor Hydrodynamics and Gas-Liquid Mass Transfer*, 1st ed. Wiley, 2014. doi: 10.1002/9781118869703.

[170] W. Chuenchart, R. Karki, T. Shitanaka, K. R. Marcelino, H. Lu, and S. K. Khanal, “Nanobubble technology in anaerobic digestion: A review,” *Bioresour. Technol.*, vol. 329, p. 124916, Jun. 2021, doi: 10.1016/j.biortech.2021.124916.

[171] R. Karthikeyan, R. Singh, and A. Bose, “Microbial electron uptake in microbial electrosynthesis: a mini-review,” *J. Ind. Microbiol. Biotechnol.*, vol. 46, no. 9–10, pp. 1419–1426, Oct. 2019, doi: 10.1007/s10295-019-02166-6.

[172] Z. Liu, X. Xue, W. Cai, K. Cui, S. A. Patil, and K. Guo, “Recent progress on microbial electrosynthesis reactor designs and strategies to enhance the reactor performance,” *Biochem. Eng. J.*, vol. 190, p. 108745, Jan. 2023, doi: 10.1016/j.bej.2022.108745.

[173] P. L. Spath and M. K. Mann, “Life Cycle Assessment of Hydrogen Production via Natural Gas Steam Reforming,” NREL/TP-570-27637, 764485, Sep. 2000. doi: 10.2172/764485.

[174] M. Schalenbach, G. Tjarks, M. Carmo, W. Lueke, M. Mueller, and D. Stolten, “Acidic or Alkaline? Towards a New Perspective on the Efficiency of Water Electrolysis,” *J. Electrochem. Soc.*, vol. 163, no. 11, pp. F3197–F3208, 2016, doi: 10.1149/2.0271611jes.

[175] J. J. Reed, “The NBS Tables of Chemical Thermodynamic Properties: Selected Values for Inorganic and C1 and C2 Organic Substances in SI Units.” National Institute of Standards and Technology, 2020. doi: 10.18434/M32124.

[176] D. Pletcher, R. A. Green, and R. C. D. Brown, “Flow Electrolysis Cells for the Synthetic Organic Chemistry Laboratory,” *Chem. Rev.*, vol. 118, no. 9, pp. 4573–4591, May 2018, doi: 10.1021/acs.chemrev.7b00360.

[177] M. A. Lever, “Acetogenesis in the Energy-Starved Deep Biosphere – A Paradox?,” *Front. Microbiol.*, vol. 2, 2012, doi: 10.3389/fmicb.2011.00284.

[178] A. Regueira, J. M. Lema, and M. Mauricio-Iglesias, “Microbial inefficient substrate use through the perspective of resource allocation models,” *Curr. Opin. Biotechnol.*, vol. 67, pp. 130–140, Feb. 2021, doi: 10.1016/j.copbio.2021.01.015.

[179] M. Pavan *et al.*, “Advances in systems metabolic engineering of autotrophic carbon oxide-fixing biocatalysts towards a circular economy,” *Metab. Eng.*, vol. 71, pp. 117–141, May 2022, doi: 10.1016/j.ymben.2022.01.015.

[180] H. Richter, B. Molitor, H. Wei, W. Chen, L. Aristilde, and L. T. Angenent, “Ethanol production in syngas-fermenting Clostridium ljungdahlii is controlled by thermodynamics rather than by enzyme expression,” *Energy Environ. Sci.*, vol. 9, no. 7, pp. 2392–2399, 2016, doi: 10.1039/C6EE01108J.

[181] M. T. Agler, C. M. Spirito, J. G. Usack, J. J. Werner, and L. T. Angenent, “Development of a highly specific and productive process for n-caproic acid production: applying lessons from methanogenic microbiomes,” *Water Sci. Technol.*, vol. 69, no. 1, pp. 62–68, Jan. 2014, doi: 10.2166/wst.2013.549.

[182] J. De Jesús Montoya-Rosales, P. Núñez-Valenzuela, A. Ontiveros-Valencia, M. Morales-Ibarría, S. Revah, and E. Razo-Flores, “From Syngas Fermentation to Chain Elongation: the Role of Key Microorganisms and Multi-omics Analysis,” *BioEnergy Res.*, vol. 17, no. 2, pp. 897–911, Nov. 2023, doi: 10.1007/s12155-023-10696-2.

[183] C. M. Spirito, H. Richter, K. Rabaey, A. J. Stams, and L. T. Angenent, “Chain elongation in anaerobic reactor microbiomes to recover resources from waste,” *Curr. Opin. Biotechnol.*, vol. 27, pp. 115–122, Jun. 2014, doi: 10.1016/j.copbio.2014.01.003.

[184] C. Quintela *et al.*, “Excessive Ethanol Oxidation Versus Efficient Chain Elongation Processes,” *Waste Biomass Valorization*, vol. 15, no. 4, pp. 2545–2558, Apr. 2024, doi: 10.1007/s12649-023-02323-0.

[185] S. Kobayashi *et al.*, “Reversible Hydrogenase Activity Confers Flexibility to Balance Intracellular Redox in Moorella thermoacetica,” *Front. Microbiol.*, vol. 13, p. 897066, May 2022, doi: 10.3389/fmicb.2022.897066.

[186] M. Demler and D. Weuster-Botz, “Reaction engineering analysis of hydrogenotrophic production of acetic acid by *Acetobacterium woodii*,” *Biotechnol. Bioeng.*, vol. 108, no. 2, pp. 470–474, Feb. 2011, doi: 10.1002/bit.22935.

[187] P. M. Wilkinson, A. P. Spek, and L. L. Van Dierendonck, “Design parameters estimation for scale-up of high-pressure bubble columns,” *AIChE J.*, vol. 38, no. 4, pp. 544–554, Apr. 1992, doi: 10.1002/aic.690380408.

[188] J.-Y. Gao *et al.*, “Strengthening H2 gas–liquid mass transfer using superaerophobic cathodes for enhanced methane production from CO2 in H2-mediated microbial electrosynthesis system,” *Bioresour. Technol.*, vol. 417, p. 131850, Feb. 2025, doi: 10.1016/j.biortech.2024.131850.

[189] P. Dessì *et al.*, “Microbial electrosynthesis of acetate from CO2 in three-chamber cells with gas diffusion biocathode under moderate saline conditions,” *Environ. Sci. Ecotechnology*, vol. 16, p. 100261, Oct. 2023, doi: 10.1016/j.ese.2023.100261.

[190] A. R. Zeradjanin, J. Grote, G. Polymeros, and K. J. J. Mayrhofer, “A Critical Review on Hydrogen Evolution Electrocatalysis: Re-exploring the Volcano-relationship,” *Electroanalysis*, vol. 28, no. 10, pp. 2256–2269, Oct. 2016, doi: 10.1002/elan.201600270.

[191] W. Zhou *et al.*, “Recent developments of carbon-based electrocatalysts for hydrogen evolution reaction,” *Nano Energy*, vol. 28, pp. 29–43, Oct. 2016, doi: 10.1016/j.nanoen.2016.08.027.

[192] A. Ursua, L. M. Gandia, and P. Sanchis, “Hydrogen Production From Water Electrolysis: Current Status and Future Trends,” *Proc. IEEE*, vol. 100, no. 2, pp. 410–426, Feb. 2012, doi: 10.1109/JPROC.2011.2156750.

[193] J. Chi and H. Yu, “Water electrolysis based on renewable energy for hydrogen production,” *Chin. J. Catal.*, vol. 39, no. 3, pp. 390–394, Mar. 2018, doi: 10.1016/S1872-2067(17)62949-8.

[194] S. A. Grigoriev, V. N. Fateev, D. G. Bessarabov, and P. Millet, “Current status, research trends, and challenges in water electrolysis science and technology,” *Int. J. Hydrog. Energy*, vol. 45, no. 49, pp. 26036–26058, Oct. 2020, doi: 10.1016/j.ijhydene.2020.03.109.

[195] M. Carmo, D. L. Fritz, J. Mergel, and D. Stolten, “A comprehensive review on PEM water electrolysis,” *Int. J. Hydrog. Energy*, vol. 38, no. 12, pp. 4901–4934, Apr. 2013, doi: 10.1016/j.ijhydene.2013.01.151.

[196] P. Dessì *et al.*, “Microbial electrosynthesis: Towards sustainable biorefineries for production of green chemicals from CO2 emissions,” *Biotechnol. Adv.*, vol. 46, p. 107675, Jan. 2021, doi: 10.1016/j.biotechadv.2020.107675.

[197] F. Scholz *et al.*, Eds., *Electroanalytical Methods*. Berlin, Heidelberg: Springer Berlin Heidelberg, 2010. doi: 10.1007/978-3-642-02915-8.

[198] P. J. Sides, “Phenomena and Effects of Electrolytic Gas Evolution,” in *Modern Aspects of Electrochemistry*, vol. 18, R. E. White, J. O. Bockris, and B. E. Conway, Eds., in Modern Aspects of Electrochemistry, vol. 18. , Boston, MA: Springer US, 1986, pp. 303–354. doi: 10.1007/978-1-4613-1791-3_6.

[199] COMSOL AB, *Electrochemistry Module User’s Guide*, Version: COMSOL 6.1. Stockholm, Sweden: COMSOL AB, 2022.

[200] Q. Chen and L. Luo, “Correlation between Gas Bubble Formation and Hydrogen Evolution Reaction Kinetics at Nanoelectrodes,” *Langmuir*, vol. 34, no. 15, pp. 4554–4559, Apr. 2018, doi: 10.1021/acs.langmuir.8b00435.

[201] Q. Chen, L. Luo, H. Faraji, S. W. Feldberg, and H. S. White, “Electrochemical Measurements of Single H_2 Nanobubble Nucleation and Stability at Pt Nanoelectrodes,” *J. Phys. Chem. Lett.*, vol. 5, no. 20, pp. 3539–3544, Oct. 2014, doi: 10.1021/jz501898r.

[202] K. V. Dapkus and P. J. Sides, “Nucleation of electrolytically evolved hydrogen at an ideally smooth electrode,” *J. Colloid Interface Sci.*, vol. 111, no. 1, pp. 133–151, May 1986, doi: 10.1016/0021-9797(86)90014-7.

[203] J. A. Hammons *et al.*, “Nanobubble Formation and Coverage during High Current Density Alkaline Water Electrolysis,” *Nano Lett.*, vol. 24, no. 43, pp. 13695–13701, Oct. 2024, doi: 10.1021/acs.nanolett.4c03657.

[204] N. P. Brandon and G. H. Kelsall, “Growth kinetics of bubbles electrogenerated at microelectrodes,” *J. Appl. Electrochem.*, vol. 15, no. 4, pp. 475–484, Jul. 1985, doi: 10.1007/BF01059288.

[205] F. Rocha, R. Delmelle, C. Georgiadis, and J. Proost, “Effect of pore size and electrolyte flow rate on the bubble removal efficiency of 3D pure Ni foam electrodes during alkaline water electrolysis,” *J. Environ. Chem. Eng.*, vol. 10, no. 3, p. 107648, Jun. 2022, doi: 10.1016/j.jece.2022.107648.

[206] Z. J. Oliver *et al.*, “Scaling Organic Electrosynthesis: The Crucial Interplay between Mechanism and Mass Transport,” *ACS Cent. Sci.*, vol. 11, no. 4, pp. 528–538, Apr. 2025, doi: 10.1021/acscentsci.4c01733.

[207] P. Dessì *et al.*, “Microbial electrosynthesis of acetate from CO2 in three-chamber cells with gas diffusion biocathode under moderate saline conditions,” *Environ. Sci. Ecotechnology*, vol. 16, p. 100261, Oct. 2023, doi: 10.1016/j.ese.2023.100261.

[208] X. Zhang, T. Arbour, D. Zhang, S. Wei, and K. Rabaey, “Microbial electrosynthesis of acetate from CO2 under hypersaline conditions,” *Environ. Sci. Ecotechnology*, vol. 13, p. 100211, Jan. 2023, doi: 10.1016/j.ese.2022.100211.

[209] Y. Zhang, A. Smirnova, A. Verma, and R. Pitchumani, “Design of a proton exchange membrane (PEM) fuel cell with variable catalyst loading,” *J. Power Sources*, vol. 291, pp. 46–57, Sep. 2015, doi: 10.1016/j.jpowsour.2015.05.002.

[210] M. Medraj, E. Baril, V. Loya, and L.-P. Lefebvre, “The effect of microstructure on the permeability of metallic foams,” *J. Mater. Sci.*, vol. 42, no. 12, pp. 4372–4383, Jun. 2007, doi: 10.1007/s10853-006-0602-x.

[211] A. A. Khrapitchev and P. T. Callaghan, “Reversible and irreversible dispersion in a porous medium,” *Phys. Fluids*, vol. 15, no. 9, pp. 2649–2660, Sep. 2003, doi: 10.1063/1.1596914.

[212] J. C. F. Pereira, I. Malico, T. C. Hayashi, and J. Raposo, “Experimental and numerical characterization of the transverse dispersion at the exit of a short ceramic foam inside a pipe,” *Int. J. Heat Mass Transf.*, vol. 48, no. 1, pp. 1–14, Jan. 2005, doi: 10.1016/j.ijheatmasstransfer.2004.08.001.

[213] W. L. McCabe, J. C. Smith, and P. Harriott, *Unit operations of chemical engineering*, 7. ed., Internat. ed. in McGraw-Hill chemical engineering series. Boston, Mass.: McGraw-Hill Higher Education, 2005.

[214] S. M. De Smit, J. J. H. Langedijk, J. H. Bitter, and D. P. B. T. B. Strik, “Alternating direction of catholyte forced flow-through 3D-electrodes improves start-up time in microbial electrosynthesis at applied high current density,” *Chem. Eng. J.*, vol. 464, p. 142599, May 2023, doi: 10.1016/j.cej.2023.142599.

[215] C. Kantzow, A. Mayer, and D. Weuster-Botz, “Continuous gas fermentation by Acetobacterium woodii in a submerged membrane reactor with full cell retention,” *J. Biotechnol.*, vol. 212, pp. 11–18, Oct. 2015, doi: 10.1016/j.jbiotec.2015.07.020.

[216] J. Bae *et al.*, “Valorization of C1 gases to value-added chemicals using acetogenic biocatalysts,” *Chem. Eng. J.*, vol. 428, p. 131325, Jan. 2022, doi: 10.1016/j.cej.2021.131325.

[217] N. Rohbohm, “Investigation of Carbon Capture Technology–Optimization of Microbial Electrochemical Cells: A Study on Single-Chamber, Flow Cell, and Zero-Gap Reactor Configurations,” PhD Thesis, Eberhard-Karls-Universität Tübingen, Germany, 2025.

[218] P. Tiwari, G. Tsekouras, K. Wagner, G. F. Swiegers, and G. G. Wallace, “A new class of bubble-free water electrolyzer that is intrinsically highly efficient,” *Int. J. Hydrog. Energy*, vol. 44, no. 42, pp. 23568–23579, Sep. 2019, doi: 10.1016/j.ijhydene.2019.07.100.

[219] A. Kuchenbuch *et al.*, “Reducing Oxygen Stress and Improving Hydrogen Availability Boosts Microbial Electrosynthesis by *Clostridium ljungdahlii*,” *ChemSusChem*, vol. 18, no. 21, p. e202501118, Nov. 2025, doi: 10.1002/cssc.202501118.

[220] E. Blanchet, F. Duquenne, Y. Rafrafi, L. Etcheverry, B. Erable, and A. Bergel, “Importance of the hydrogen route in up-scaling electrosynthesis for microbial CO_2 reduction,” *Energy Environ. Sci.*, vol. 8, no. 12, pp. 3731–3744, 2015, doi: 10.1039/C5EE03088A.

[221] S. Bajracharya *et al.*, “Carbon dioxide reduction by mixed and pure cultures in microbial electrosynthesis using an assembly of graphite felt and stainless steel as a cathode,” *Bioresour. Technol.*, vol. 195, pp. 14–24, Nov. 2015, doi: 10.1016/j.biortech.2015.05.081.

Supplemental Information

A. Headspace-gas chromatograph method

To measure the dissolved H_2 concentration at the end of the H_2 pre-saturation step, a double syringe configuration was used as shown in Fig. A1.

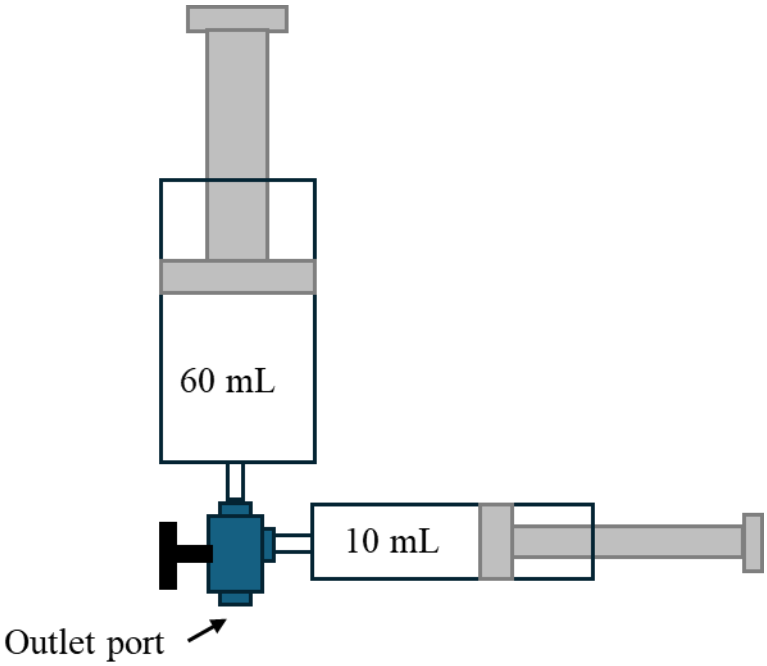

Fig. A1. Double syringe configuration for measuring the dissolved H_2 concentration by the headspace-gas chromatography method made of a 60 mL and 10 mL syringe connected with a 3-way valve.

The steps used on this method are described as follows:

1) A 50 mL liquid sample is collected through the outlet port into the 60 mL syringe while the port to the 10 mL syringe remains closed. Undesired introduced air is eliminated by turning upside-down the syringe and pushing out the undesired gas phase.
2) The 3-way valve is turned into the configuration where only the outlet port and the 10 mL port are open. 5 mL of air is collected with the 10 mL syringe.
3) The 3-way valve is turned again to let the two syringe ports open while the outlet port is closed. The 5 mL of air collected is transferred to the 60 mL syringe.
4) The 3-way valve is turned around where the 60 mL port is closed. Vigorous agitation is done for 1 minute to strip the dissolved H_2 out of the liquid phase and reach the partition equilibrium between the liquid and gas phase.

5) The 3-way valve is turned to connect the two syringes' ports again while the outlet port is closed. With the 60 mL syringe turned upside down, only the gas phase is transferred from the 60 mL to the 10 mL syringe.
6) Finally, the 3-way valve is turned to close the 10 mL syringe and contain the gas sample, which is then further injected into the gas chromatograph.

The following calculation is done to obtain the dissolved concentration of H_2 in the liquid sample from the headspace concentration obtained by the gas chromatograph:

First, the moles of air (n_{air}, N_2 + O_2) introduced in step 2) are calculated from the ideal gas law:

$$n_{air} = \frac{P \cdot V_1}{R \cdot T} = \ 2.04x10^{-4} \text{ moles}$$

Where P is the pressure inside the syringe (1 atm), V_1 is 5 mL, T is 25 C and R is the ideal gas constant, 8.3145 $m^3 \cdot Pa \cdot mol^{-1} \cdot K^{-1}$. From the gas chromatograph reading, the H_2-to-air fraction ratio (equal to a molar ratio) was used to obtain the moles of H_2 in the headspace (n_{H_2}) striped from the liquid phase in step 4):

$$n_{H_2} = 2.04x10^{-4} \cdot \frac{{f_{H_2}}^{GC}}{{f_{air}}^{GC}}$$

As the piston of the syringe will move to maintain the inside of the syringe at atmospheric pressure, the new volume (V_2) of the headspace after striping H_2 in step 4) is calculated:

$$V_2 = \frac{\left(n_{H_2} + n_{air}\right) \cdot R \cdot T}{P}$$

Using Henry's law, the ratio of dissolved H_2 in the liquid phase to the partial pressure of H_2 in the gas phase is calculated as follows:

$$k_H(T) = k_H^0 \cdot \exp\left(C \cdot \left(\frac{1}{T} - \frac{1}{298.15 \text{ K}}\right)\right)$$

Where k_H^0 is the Henry's law constat for the solubility of H_2 in water at 25 C ($k_H^0 = 0.00078 \ (\text{mol} \cdot \text{kg}^{-1}) \cdot \text{bar}^{-1}$) and C is the temperature dependence constant ($C = 500$ K). $k_H(T)$ has units of $(\text{mol} \cdot \text{kg}^{-1}) \cdot \text{bar}^{-1}$ [webbook.nist.gov]. With the partial pressure of H_2 in the headspace calculated as $P_{H_2} = 101325 \text{ Pa} \cdot {f_{H_2}}^{GC}$ and using appropriate units, the moles of dissolved H_2 (n_{dH_2}) are calculated as:

$$n_{dH_2} = k_H(T) \cdot P_{H_2}$$

Finally, the dissolved H_2 concentration is obtained by dividing the moles of total H_2 ($n_{dH_2} + n_{H_2}$) by the liquid sample volume, 50 mL.

As an example, the theoretical saturation concentration of dissolved H_2 in equilibrium with 1 atm of headspace pressure is 0.78 mmol·L^{-1}. which would be obtained when the fraction of H_2 in the headspace from step 6) is ${f_{H_2}}^{GC} = 0.142$.

At the end of the experiments done in Chapter III, , the dissolved H_2 concentration measured with the amperometric H_2 probe was compared with the headspace GC method, and their values are shown in Table A1.

Table A1. Validation of the dissolved H_2 concentration measured with the amperometric H_2 sensor and the headspace gas chromatography technique. The sampled points were taken close to the end of each experiment.

H_2 solubilization technique	Dissolved H_2 concentration [mmol·L^{-1}]	
Water electroreduction	Amperometric H_2 sensor	Headspace gas chromatography
20 mA	0.51	0.54
60 mA	0.83	0.77
100 mA	1.21	1.16
H_2 gas injection		
1 L·h^{-1}	0.58	0.65
2 L·h^{-1}	0.66	0.63
3 L·h^{-1}	0.62	0.63

B. Current control interface developed for the BioLogic VSP potentiostat

The imposed voltage/current by industrial rectifiers and lab scale DC power supplies can usually be controlled by simple communication protocols such as analog 0-10V or 4-20 mA signals. Nevertheless, most of the research in electrochemistry is performed on commercial potentiostats that are usually controlled by the manufacturer's software. With the goal of expanding available research tools that close the gap between the electrolyzer operation at lab scale and industrial scale, a simple communication protocol was developed as a proof of concept to easily control the current of a potentiostat based on analog signals that could be triggered by external sensors/software such as the detection of H_2 nucleation by a digital camera, or the measurement of dissolved H_2 by an amperometric H_2 probe. A simple schematic of the proposed system is shown in Fig. B1.

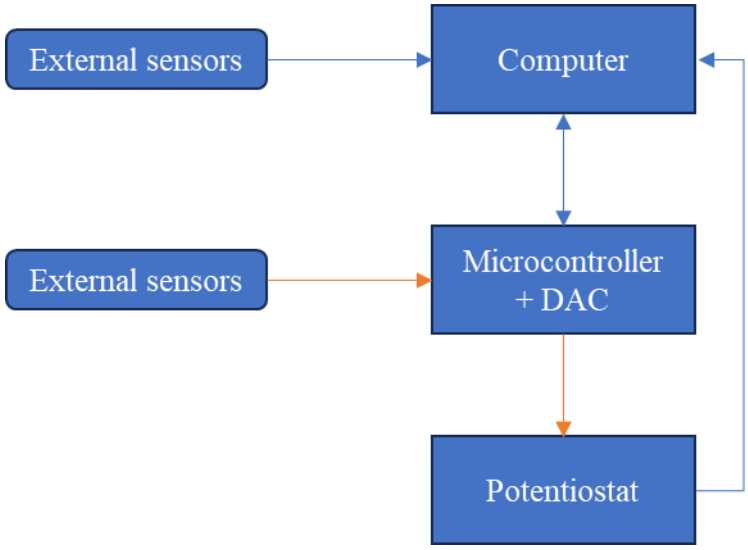

Fig. B1. Schematic representation of the proposed communication system for the current control of a potentiostat. Blue arrows represent digital signals while orange arrows represent analog signals. DAC: digital-to-analog converter.

The elements of the system proposed here were a microcontroller Arduino UNO (Arduino, Italy), a digital-to-analog converter (DAC MCP4922, MicroChip, USA) and a potentiostat (VSP Biologic). A simple example of current control is described as follows. In the operation of an electrolyzer designed to maximize the rate of H_2 solubilization, a digital camera could be used as an external sensor to maximize the current imposed by the potentiostat while avoiding the

nucleation of bubbles at the cathode surface. When bubbles are detected by the analysis of the video fed to the computer, a digital signal (Serial COM communication) is sent to the microcontroller, that converts it to an analog signal with the attached digital-to-analog converter (0-5V, see Fig. B2).

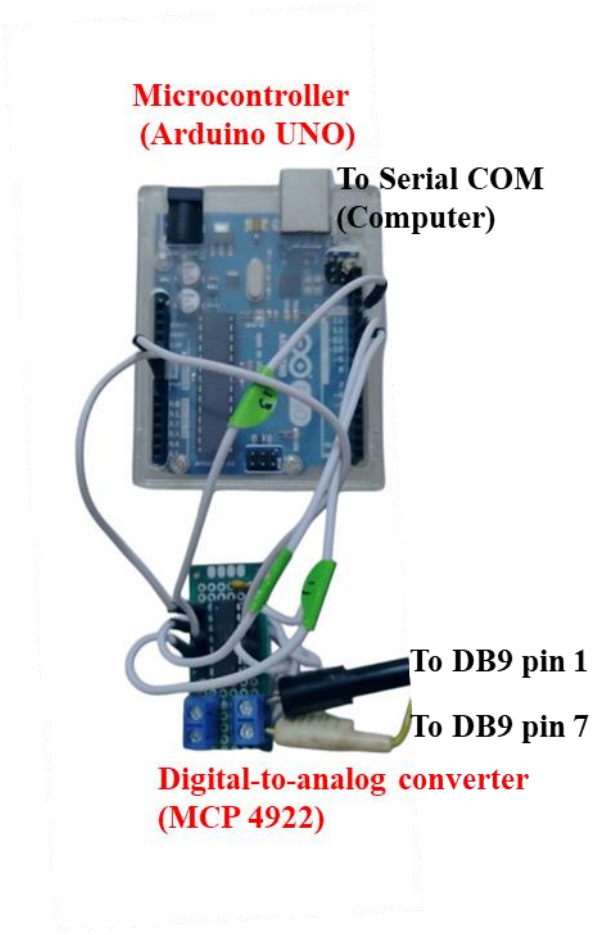

Fig. B2. Microcontroller and digital-to-analog converter (DAC) setup

This analog signal is sent to the potentiostat by a DB9 connection through the Analog In and Ground connector (pins 1,7, see Fig. Fig. B3).

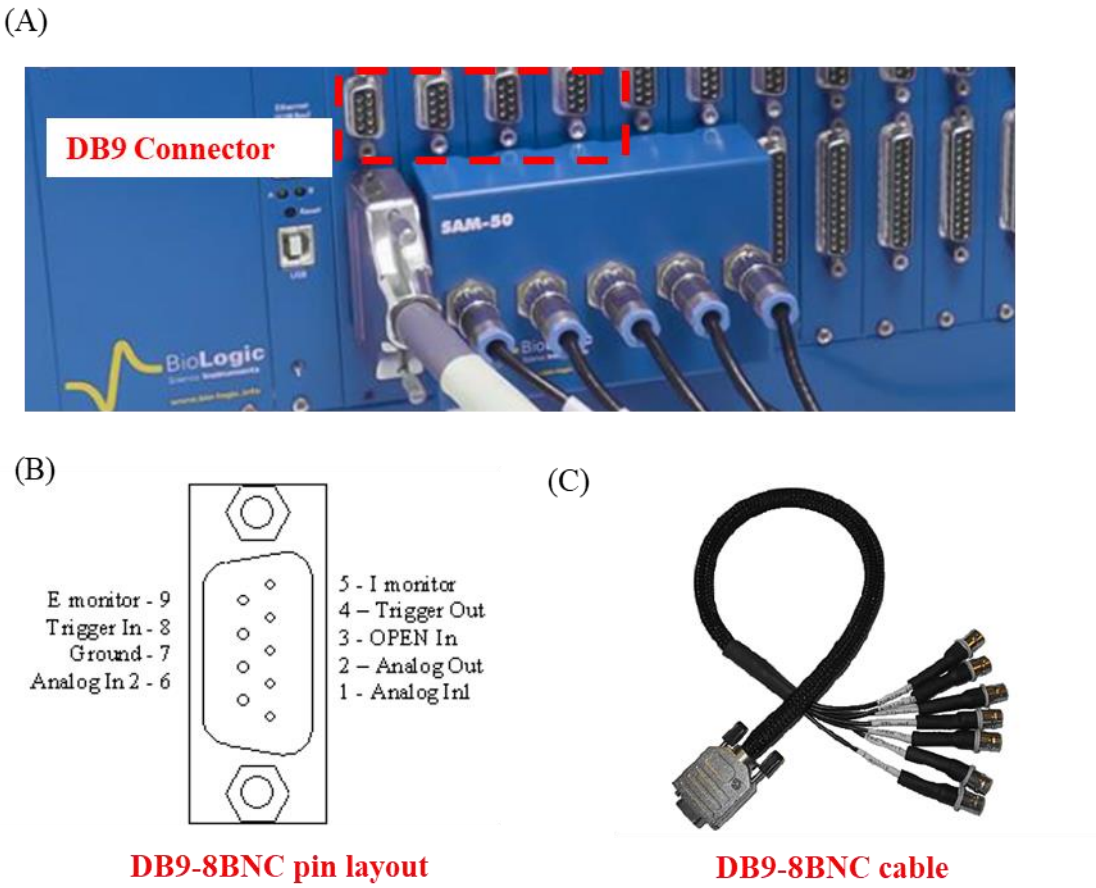

Fig. B3. DB9 connection on a VSP biologic potentiostat for analog communication. (A) DB9 connector on the potentiostat. (B) Pin layout of the DB9 connection. Here, only Analog In 1 and Ground connections were used. (C) DB9-8BNC cable for the analog communication between the microcontroller + DAC.

Finally, this analog signal (0-5V) is linearly converted to a current value (e.g., -1400 – 0 mA) according to the desired range of operation. This conversion is done by the EC-Lab software in the Modulo Bat technique under the External Devices tab as shown in Fig. B4.

(A)

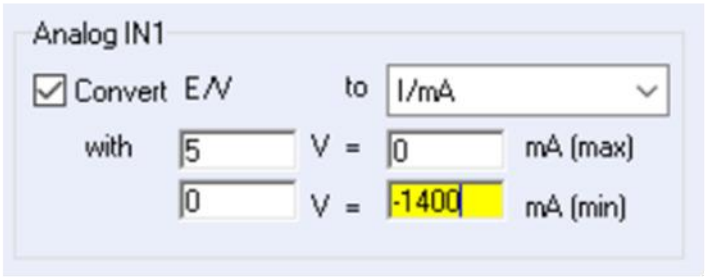

(B)

State	Controls		
» 0	CC	Dis	(I=-1400,000 mA)
» 1	CC	Dis	(I=-1390,000 mA)
» 2	CC	Dis	(I=-1380,000 mA)
» 3	CC	Dis	(I=-1370,000 mA)
...	...	...	...
» 138	CC	Dis	(I=-20,000 mA)
» 139	CC	Dis	(I=-10,000 mA)
» 140	CC	Dis	(I=0,000 mA)

Fig. B4. Modulo Bat interface on the EC-lab software. (A) Linear conversion of the analog signal sent by the microcontroller + DAC (0-5V) to a current value in the range of the desired operation (here, 0 to -1400 mA). (B) States of the Module Bat technique, where current steps of 10 mA are used to switch to the desired current.

The Modulo Bat technique contains 140 steps to switch to discrete values of current, here with current steps of 10 mA to cover the -1400-0 mA range (Fig S2-4B). To avoid the manual creation of the 140 steps necessary for the current control, a MATLAB script was written and attached at the end of this section (ModBat.m). Similarly, the script loaded into the microcontroller to send the analog signal to the potentiostat is included as well (DAC_general.ino).

ModBat.m

```
% This script processes technical parameters from an Excel file and an MPS setup template file,

% generating a new MPS file with formatted data for further analysis or control.
```

```
% Inputs:
% - tech_filepath: Path to the Excel file containing technical parameters.
% - setup_filepath: Path to the MPS setup file.
%
% Outputs:
% - NewTech: A new MPS file created in the specified directory, containing the
%            formatted technical parameters and setup information.
[tech_file,tech_path] = uigetfile('*.xls*','Select excel with tech parameters');
tech_filepath = [tech_path,tech_file];
[setup_file,setup_path] = uigetfile([tech_path,'*.mps'],'Select mps with setup');
setup_filepath = [setup_path,setup_file];
tech = 'CC'; %% Constant Current option, other configurations such as Constat Voltage (CV) could be implemented.
Irange = [-1400,0];%Desired mA Range
colwidth = 20;
Vrange = [0,5];%V
step_size = 10;
Ns = 1 + (max(Irange)-min(Irange))/step_size;
I_vector = linspace(min(Irange),max(Irange),Ns);
max_V_flag = field_gen(max(Vrange),0,3);%V
min_V_flag = field_gen(min(Vrange),0,3);%V
max_I_flag = field_gen(max(Irange),0,3);%mA
min_I_flag = field_gen(min(Irange),0,3);%mA
seq_order = 0:1:(Ns-1);
opts = detectImportOptions(tech_filepath);
opts.DataRange = "A2";
opts.Sheet = tech;
tech_table = readtable(tech_filepath,opts);
```

```
setupID = fopen(setup_filepath);
setup_str = textscan(setupID,'%s','Delimiter',newline);
fclose(setupID);
setup_str = cellfun(@replace,setup_str,{{'max_I_flag','min_I_flag','max_V_flag','min_V_flag'}},...
   {{max_I_flag,min_I_flag,max_V_flag,min_V_flag}},'UniformOutput',false);
var_vector = cell(10,2);
var_vector(1,:) = [{'Ns'},{field_vector(seq_order,colwidth,0)}];
[ctrl1_val,charge_vector] = field_vector(I_vector,colwidth,3);
var_vector(2,:) = [{'ctrl1_val'},{ctrl1_val}];
var_vector(3,:) = [{'N'},{field_vector([0,0*ones(1,Ns-1)],colwidth,2)}];
var_vector(4,:) = [{'charge/discharge'},{charge_vector}];
var_vector(5,:) = [{'N1'},var_vector(3,2)];
var_vector(6,:) = [{'lim_nb'},{field_vector([2,2*ones(1,Ns-2),2],colwidth,0)}];
var_vector(7,:) = [{'lim1_value'},{field_vector(I_vector+diff(I_vector(1:2)/2),colwidth,3)}];
var_vector(8,:) = [{'lim2_value'},{field_vector(I_vector-diff(I_vector(1:2)/2),colwidth,3)}];
var_vector(9,:) = [{'lim1_seq'},{field_vector([seq_order(1:end-1)+1,9999],colwidth,0)}];
var_vector(10,:) = [{'lim2_seq'},{field_vector([9999,seq_order(2:end)-1],colwidth,0)}];
tech_lines = cell(height(tech_table),1);
for m = 1:height(tech_table)
   line_m_name = tech_table.Name{m};
   name_idx = strcmpi(line_m_name,var_vector(:,1));
   if any(name_idx)
      line_m_var = var_vector(name_idx,2);
      line_m_var = line_m_var{1};
   else
      if isempty(tech_table.Value{m})
         tag = ' ';
```

```
      else
         tag = tech_table.Value{m};
      end
      line_m_var = field_vector(tag,colwidth,Ns);
   end
   line = [field_gen(line_m_name,colwidth),line_m_var];
   tech_lines{m} = line;
end
NewTech = fopen(sprintf('%sNewTech_%s.mps',tech_path,string(datetime('now','Format','dd_MM_uuuu
HH_mm_ss'))),'w','n','windows-1252');
%fprintf(NewTech,'%s\n',setup_str{1}{:});
fprintf(NewTech,'%s\n',tech_lines{:});
fclose(NewTech);
```

DAC_general.ino

```
#include <MCP_DAC.h>
#include <SPI.h>
#include <Adafruit_ADS1X15.h>
#include <Servo.h>
MCP4922 MCP;
Adafruit_ADS1115 ads1115;
Servo servopar;
// DAC = 1D
// Servo = 1S
// Relay = 1R
float ptA_initial = 0,pt_lim = 500;
int avg = 20, del = 10, DAC_pin = 10, servo_pin = 9, Servo_speed = 0, Servo_delay = 200, led_state = 0;
```

```
int relay_pin[4] = {2,4,7,8};

int relay_state[4] = {0,0,0,0};

String ini = "Z", string_in = "";

int aPin[6] = {0};

int ADSpin[6] = {0};

int MCP_flag = 0, servo_flag = 0, relay_flag = 0;


void setup() {
 Serial.begin(9600);
 delay(100);
 pinMode(LED_BUILTIN, OUTPUT);
 while (Serial.available() == 0){
 }
 aBool(aPin,ADSpin,MCP_flag,servo_flag,relay_flag);
 int ADS_flag = any(ADSpin);
 if (ADS_flag){
  ads1115.begin(0x48);
  delay(100);
 }
 if (MCP_flag){
  SPI.begin();
  MCP.begin(DAC_pin);
  delay(100);
  MCP.write(ptA_initial, 0);
  delay(100);
 }
 if (servo_flag > 0){
```

```
   servopar.attach(servo_pin);
   delay(100);
  }
  if (relay_flag > 0){
   for (int i=0; i < 4;i++){
     digitalWrite(relay_pin[i],HIGH);
     pinMode(relay_pin[i], OUTPUT);

   }
  }
}

void loop() {
  if (led_state == 0){
   digitalWrite(LED_BUILTIN, HIGH);
   led_state = 1;
  }
  else if (led_state == 1){
   digitalWrite(LED_BUILTIN, LOW);
   led_state = 0;
  }

  Serial.print(ini);
  for (int i=0; i < 6; i++){
   if (aPin[i]){
     String pinValue = getpinB(i, avg, del, 0);
     Serial.print("A");
```

```
    Serial.print(i);
    Serial.print("_");
    Serial.print(pinValue);
    Serial.print("_");
    Serial.print("A");
    Serial.print(i);
   }
   if (ADSpin[i]){
    String pinValue = getpinB(i, avg, del, 1);
    Serial.print("ADS");
    Serial.print(i);
    Serial.print("_");
    Serial.print(pinValue);
    Serial.print("_");
    Serial.print("ADS");
    Serial.print(i);
   }
  }
  Serial.println();
  if (Serial.available() != 0) {
   String string_in = Serial.readStringUntil('\n');
   sendCommand(string_in,ptA_initial,pt_lim,Servo_speed,Servo_delay,relay_pin,relay_state);
  }

  if (servo_flag == 1){
   if (Servo_speed != 0){
    servopar.writeMicroseconds(1500-Servo_speed);
```

```
    if (Servo_delay != 0){
      delay(Servo_delay);
      servopar.writeMicroseconds(1500+Servo_speed);
      delay(round(Servo_delay*0.7));
    }
  }
  else {
    servopar.writeMicroseconds(1500);
    delay(500);
  }
 }
 else if (servo_flag == 2) {
  if (Servo_speed != 0 && Servo_delay != 0){
    servopar.write(0);
    delay(2*Servo_delay);
    servopar.write(Servo_speed*20/14);
    delay(2*Servo_delay);
  }
  else {
    delay(500);
  }
 }
 else {
  delay(500);
 }
}
```

```
String getpinB(int pin, int avg, int del, int ads){
 int16_t byt = 0;
 for (int i=0; i < avg; i++) {
  if (ads) {
   if (pin<4){
    byt = byt + ads1115.readADC_SingleEnded(pin);
   }
   else if (pin == 4) {
    byt = byt + ads1115.readADC_Differential_0_1();
   }
   else {
    byt = byt + ads1115.readADC_Differential_2_3();
   }
  }
  else {
   byt = byt + analogRead(pin);
  }
  delay(del);
 }
 float bytavg = byt/avg;
 if (ads && pin < 4){
  bytavg = ads1115.computeVolts(bytavg);
 }
 else if (ads && pin >= 4){
  float multiplier = 0.1875F;
  bytavg = bytavg*multiplier*1000.0;
 }
```

```
  return String(bytavg);
}



void sendDAC(String subs_in, float (&ptA_initial), int pt_lim){
  float point = subs_in.toFloat();
  float pt_diff = point-ptA_initial;
  float pt_ratio = ceil(abs(pt_diff)/pt_lim);
  if (pt_ratio > 1){
    for (int i = 1; i < pt_ratio; i++){
      float pt_step = ptA_initial + i*(pt_diff/pt_ratio);
      int p_send = round(pt_step);
      MCP.write(p_send, 0);
      delay(300);
      //Serial.println(pt_step);
    }
  }
  delay(300);
  //Serial.println(point);
  int p_send = round(point);
  MCP.write(p_send, 0);
  ptA_initial = point;
}
void Servoconfig(String string_in,int (& Servo_speed), int (& Servo_delay)){
  String speed_str = string_in.substring(0,1);
  int speed = speed_str.toInt();
  Servo_speed = 14*speed;
```

```
  String del_str = string_in.substring(1,2);
  int del = del_str.toInt();
  if (del == 0){
    Servo_delay = 0;
  }
  else{
    Servo_delay = round(500/del);
  }
}
void Relayconfig(String relay_str,int (& relay_pin)[4], int (& relay_state)[4]){
  for (int i=0; i < 4;i++){
    String ri = String(relay_str[i]);
    int rint = ri.toInt();
    if (relay_state[i] != rint){
      relay_state[i] = rint;
      if (relay_state[i] == 1){
        digitalWrite(relay_pin[i], LOW);
      }
      else {
        digitalWrite(relay_pin[i], HIGH);
      }
    }
  }
}
int any(int x[6]){
  int y = 0;
  for (int i=0; i < 6;i++){
```

```
    if (x[i] == 1){
      return 1;
    }
  }
  return 0;
}

void aBool(int (& aPin)[6],int (& ADSpin)[6],int (& MCP_flag),int (& servo_flag),int (& relay_flag)){
  String aPins_in = Serial.readStringUntil('\n'), Ap = "A";
  if (aPins_in.indexOf("MCP") != -1){
    MCP_flag = 1;
  }
  if (aPins_in.indexOf("Relay") != -1){
    relay_flag = 1;
  }
  if (aPins_in.indexOf("ServoC") != -1){
    servo_flag = 1;
  }
  else if (aPins_in.indexOf("ServoA") != -1){
    servo_flag = 2;
  }
  for (int i=0; i < 6; i++){
    String i_s = String(i);
    if (aPins_in.indexOf(Ap+i_s) != -1){
      aPin[i] = 1;
    }
  }
```

```
 for (int i=0; i<6; i++){
  String i_d = String(i);
  if (aPins_in.indexOf("ADSs"+i_d) != -1 && i <4){
   ADSpin[i] = 1;
  }
  else if (aPins_in.indexOf("ADSd01") != -1 && i == 4){
   ADSpin[4] = 1;
  }
  else if (aPins_in.indexOf("ADSd23") != -1 && i == 5){
   ADSpin[5] = 1;
  }
 }
}

void sendCommand(String string_in, float (& ptA_initial), int pt_lim, int (& Servo_speed), int (& Servo_delay),int (& relay_pin)[4], int (& relay_state)[4]){
 int idx = string_in.indexOf("Z");
 int idx2 = string_in.indexOf("?");
 String substr = string_in, str2;
 while (idx != -1) {
  str2 = substr.substring(idx+1,idx2);
  sortCommand(str2, ptA_initial, pt_lim, Servo_speed, Servo_delay, relay_pin, relay_state);
  delay(3000);
  substr = substr.substring(idx2+1);
  idx = substr.indexOf("Z");
  idx2 = substr.indexOf("?");
 }
```

```
}

void sortCommand(String string_in, float (& ptA_initial), int pt_lim, int (& Servo_speed), int (& Servo_delay),int (& relay_pin)[4], int (& relay_state)[4]){
  String ID = string_in.substring(0,2);
  String command = string_in.substring(2);
  if (ID == "1D"){
    sendDAC(command, ptA_initial, pt_lim);
  }
  else if (ID =="1S"){
    Servoconfig(command,Servo_speed,Servo_delay);
  }
  else if (ID =="1R"){
    Relayconfig(command,relay_pin,relay_state);
  }
  else {
    // do nothing
  }
}
```

C. Medium conductivity and H_2 solubilization

Two experiments were done with a KCl solution at 10g·L^{-1} (0.13 M) and a potassium phosphate buffered solution (0.1 M, pH = 7.2) with the initial purpose of preliminary study the H_2 solubilization kinetics at a higher cathodic current (60 mA) on the carbon brush used in Chapter II. The phosphate buffered medium composition was chosen to simulate the buffering capacity of a growth medium used for acetogenesis in a microbial electrosynthesis cell [17].

Although the medium composition was not studied in depth in this work, some insights could be obtained from this preliminary testing of these electrolytes. The minimum salt medium used in experiments from Chapter II had a low ionic conductivity of κ_l = 2.4 mS·cm^{-1}, which prevented the imposition and testing of higher currents in a H-type cell configuration. As mentioned in Chapter II, at 30 mA, the catholyte pH rose by 2 units, which could be further affecting the H_2 solubilization characteristics. When the catholyte was changed to a more conductive electrolyte, such as the KCl (0.13 M, κ_l = 13.6 mS·cm^{-1}) and the potassium phosphate buffered medium (0.1 M, 12.7 mS·cm^{-1}), higher currents were able to be imposed. The H_2 solubilization kinetics of both mediums at 60 mA on the carbon brush appeared to be very similar, as shown in Fig. C1, despite the differences in the final pH reached in the KCl medium (pH = 12.2) and the potassium phosphate buffered medium (pH = 7.3).

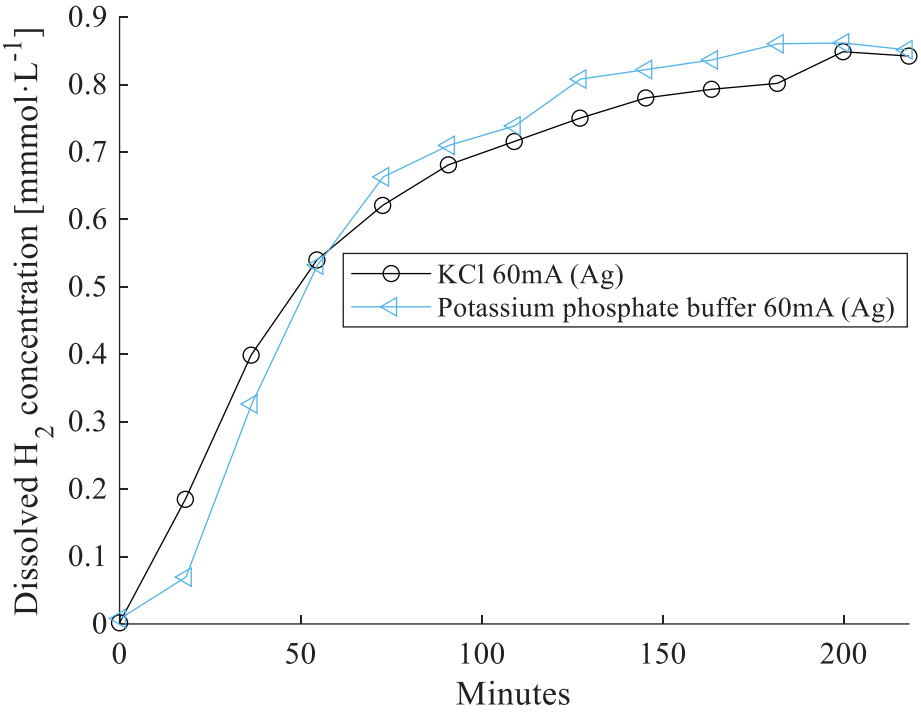

Fig. C1. H_2 solubilization kinetics during water electroreduction in a carbon brush cathode with a cathodic current of 60 mA in two different liquid mediums. Black circles: KCl medium (10 $g \cdot L^{-1}$, 13.6 $mS \cdot cm^{-1}$). Blue triangles: Potassium phosphate buffered medium (0.1 M, 12.7 $mS \cdot cm^{-1}$).

Besides the capacity to impose higher cathodic currents at higher catholyte conductivities, the maximum H_2 concentration obtained here was around 4.3 times higher than the one obtained with the minimum salt medium at 30 mA. In Chapter III, the maximum dissolved H_2 concentration achieved at 20 mA with the potassium phosphate buffered solution was still 2.5 times higher than the one obtained with the minimum salt medium at 30 mA presented in Chapter II, highlighting an important role of the electrolyte conductivity on the solubilization of H_2.

D. Bubble detection

The two videos presented here correspond to the stainless-steel plate (SSP) at the configuration of no agitation and no H_2 pre-saturation. The first video titled "bubble_detection.avi" shows the two criteria used to help identify the current at which the bubble nucleation starts. The second video titled "stamped_video.avi" shows in a separate window, a larger image of the electrode, which was used also to visually aid the determination of the bubble nucleation current. Using both videos, the current at which bubble nucleation started was identified at -4.01 mA. In the first video, it can also be seen that there is a small plateau between -1.0 and -1.15 V vs SCE. The start of the plateau matches the start of the bubble nucleation detected. This can be explained as bubbles start covering the electrode surface, they remain pinned, and less electrode surface area is available for the water electroreduction reaction and therefore, the decrease of the potential (increase of energy used) does not increase the current produced. At -1.15 V, it can be seen on the video that bubbles start to quickly detach from the electrode surface, increasing again the available electrochemical surface area which also matches with the end of the plateau in the voltammogram. This effect was only clearly observed in the SSP under no agitation, due to the more homogeneous bubble nucleation and detachment compared with the configuration under agitation or the stainless-steel porous foam (SSPF) and the carbon brush (CB) electrode. Therefore, the criteria used to tune the classification of pixels corresponding to bubbles was based on the stainless steel plate under no agitation.

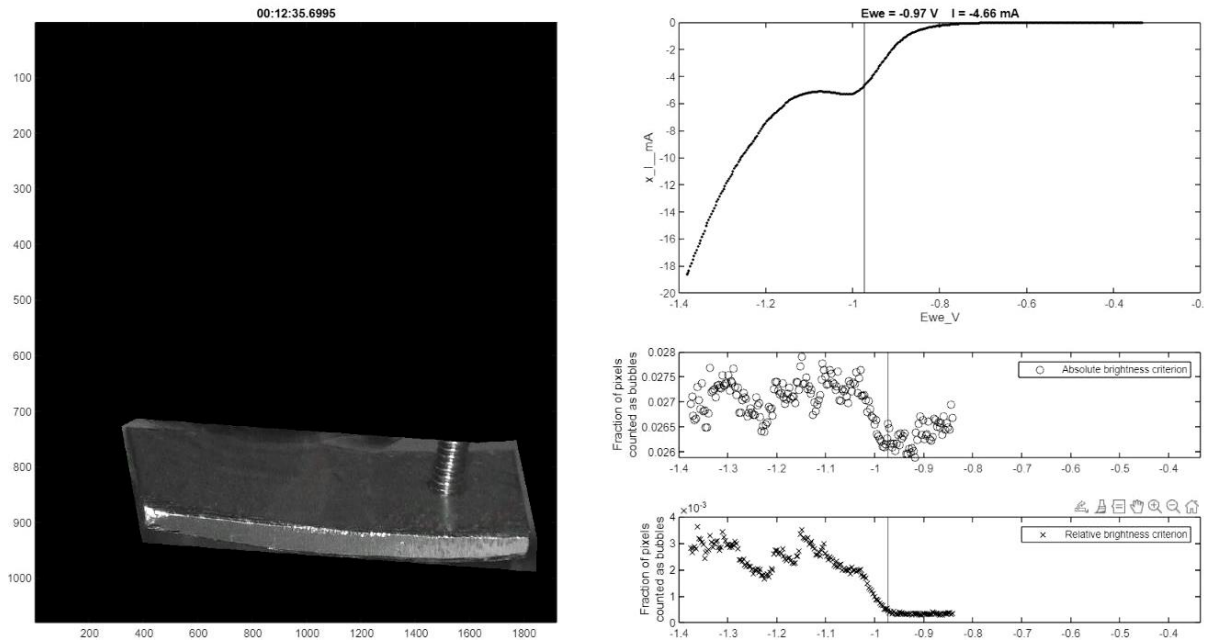

Fig. D1.Image of the graphical interface for the bubble detection algorithm used with the stainless-steel plate (SSP) under no agitation and no H_2 pre-saturation. The plateau on the voltammogram matches with the signal increase on the bubble detection algorithm.

In Fig. D2, SSP, SSPF and CB at the end of the experiment are shown in the conditions of no agitation and no H_2 pre-saturation.

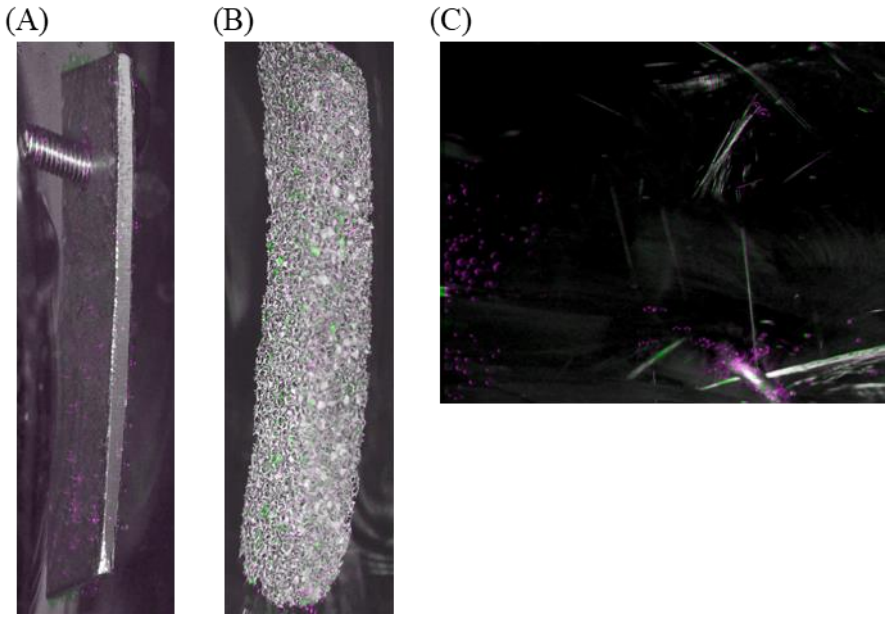

Fig. D2.Image of the (A) stainless-steel plate, SSP; (B) stainless-steel porous foam, SSPF, and (C) carbon brush, CB, at the end of the experiment in the conditions of no agitation and no

H_2 pre-saturation. The electrode potentials correspond to -1.37 V, -1.53 V and -1.28 V vs SCE respectively. The separator/anode is situated to the left of the frame.

From the LSV of the SSP at the agitated condition, the exchange current density was found to be around J_0 = 23.13 A·m^{-2} by using the linear Tafel approximation described in equation 16. The Tafel plot for these cases is shown in

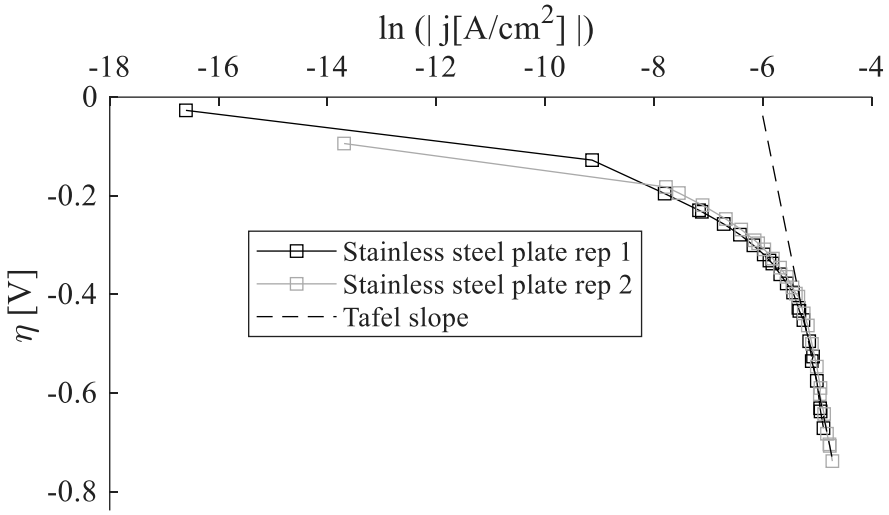

Fig. D3. Graphical representation of the Tafel equation for the agitated SSP setup. A corresponding exchange current density of J_0 = 23.13 A·m^{-2} is obtained from the plotted data.

E. O_2 crossover across the separator

The objective of this setup was to quantify the rate of oxygen crossover across the separator used in the manuscript (CMI 7000S, Membranes International Inc, USA) to validate its barrier effect against O_2 contamination in the recycling medium. To evaluate this crossover, the following experiment was set as follows. A three-chamber setup was built with a left (empty) chamber where O_2 concentration is to be measured, a middle chamber (anodic) where the electrolyte is saturated with O_2 by the anodic oxidation of water, and a right (cathodic) chamber where H_2 is produced by the reduction of water. This setup is depicted in Fig. E1(A).

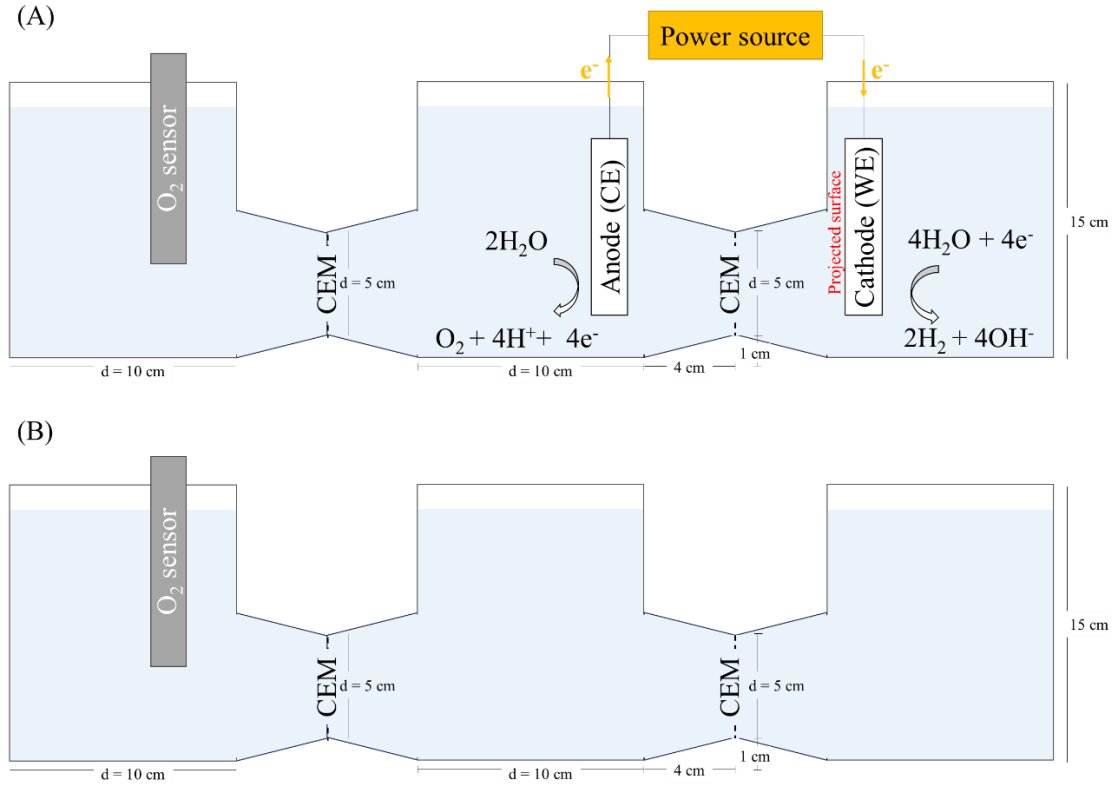

Fig. E1. Experimental setup to measure the O_2 crossover effect in a (A) three chamber water electroreduction cell and (B) three chamber control system. The anode used was a platinum grid of 3×1×0.1 cm^3 while the cathode was a retriculated vitreous carbon of 5×4×0.5 cm^3, 20 ppi (BASi, United States).

The anode used was a platinum grid of 3×1×0.1 cm^3 while the cathode was a reticulated vitreous carbon of 5×4×0.5 cm^3, 20 ppi (BASi, United States).

A potentiostat (VSP, BioLogic) was used as a power source to perform chronopotentiometry at 60 mA. A control was also tested where no polarization was applied as shown in Fig. E1(B), to see the effect of the possible O_2 diffusion from air due to the setup not being gas-tight. For both setups, the left and middle chambers were initially purged with N_2 until concentration dropped from ~0.3 mmol·L^{-1} to ~0.01 mmol·L^{-1}. Afterwards, the O_2 concentration on the left chamber was followed for 20 hours as shown in Fig. E2.

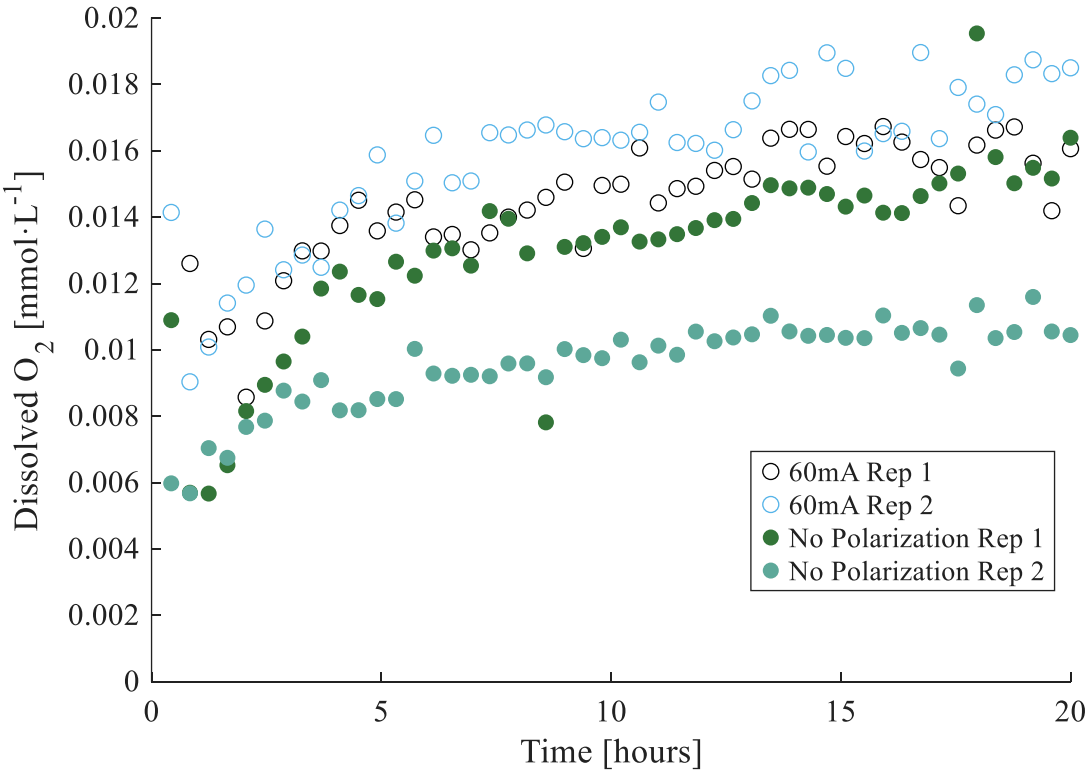

Fig. E2. O_2 concentration over the left and middle chamber of the setup depicted in Fig. E1. Empty markers represent the polarization setups where the middle chamber was saturated with O_2, while the filled markers represent the non-polarized setups.

Taking the dissolved O_2 concentrations from 10-20 hours of operation (to ensure that the O_2 concentration in the anodic chamber was saturated, measured with an external O_2 sensor in the anodic chamber), the rate of the O_2 dissolution was calculated for each repetition. The dissolution rate for the polarized duplicates was 1.15·± 0.79 [×10^{-4} mmol·L^{-1}·h^{-1}] while for the non-polarized duplicates was 1.73·± 1.58 [×10^{-4} mmol·L^{-1}·h^{-1}], showing no significant difference in the O_2 crossover rate ($p = 0.69$).

F. Longitudinal and transverse dispersity

The dispersity was calculated based on the extracted data from the dispersity values collected by Khrapitchev *et. al.* and Pereira *et. al.* [211], [212]. The extracted data is plotted in Fig. F1.

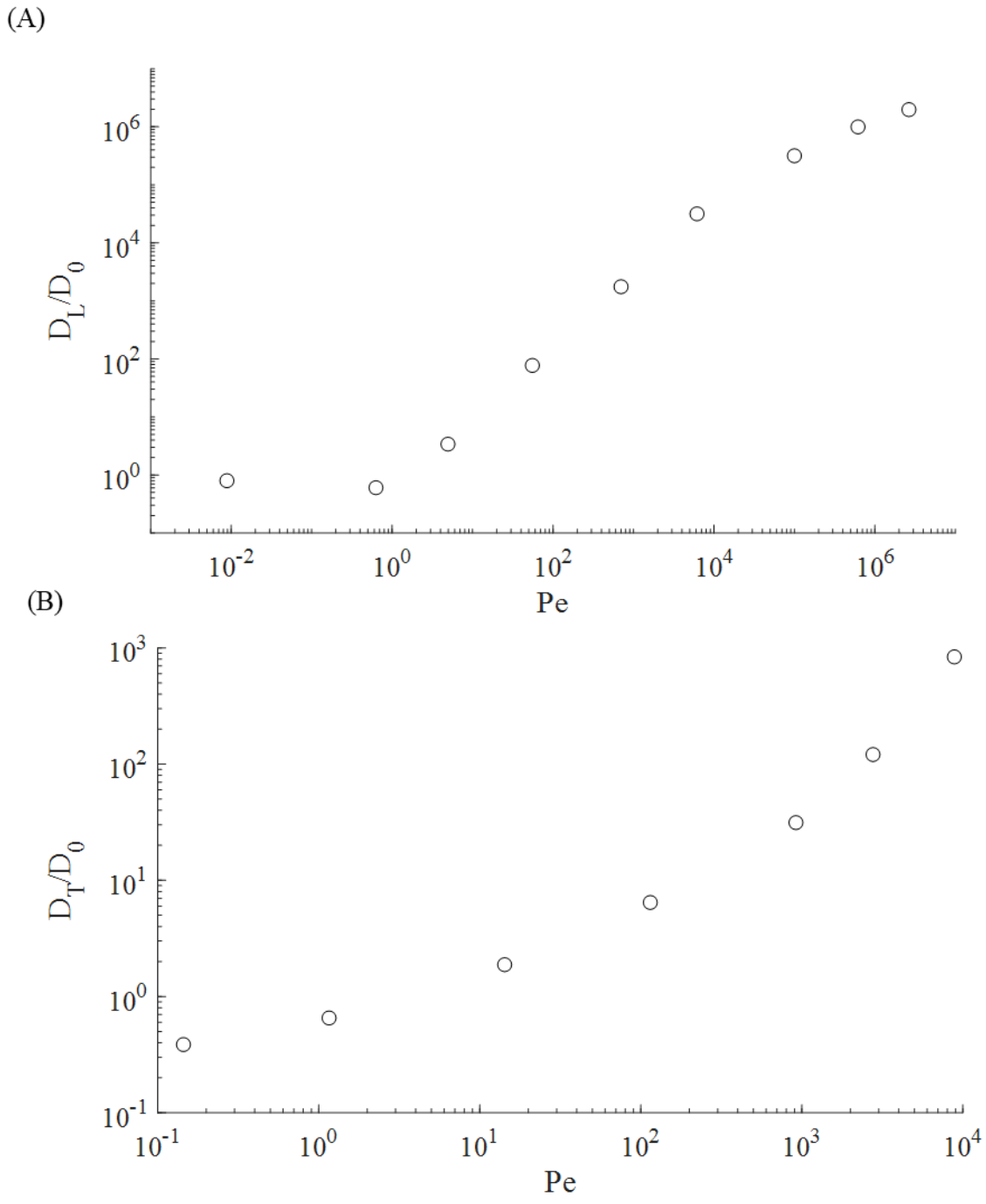

Fig. F1. Effective (A) longitudinal and (B) transverse dispersity as a function of the Péclet number (Pe).

The Péclet number (Pe) was calculated as $\mathrm{Pe} = \left(\frac{\theta \cdot \mathrm{d}}{1-\theta}\right) \cdot \frac{\mathrm{v}}{\mathrm{D}_{\mathrm{H}_2}}$, where θ is the cathode porosity, v is the effective longitudinal velocity [m·s^{-1}], d is the pore diameter [m] and $\mathrm{D}_{\mathrm{H}_2}$ is the molecular diffusion coefficient of H_2 in the fluid [m^2·s^{-1}].